Doctoral theses at NTNU, 2023:450

Daniel dos Santos Mota

Control and Stability of Isolated Grids with Synchronous and Non-Synchronous Generation

Doctoral thesis

NTNU
Norwegian University of Science and Technology
Thesis for the Degree of
Philosophiae Doctor
Faculty of Information Technology and Electrical
Engineering
Departement of Electric Energy

NTNU
Norwegian University of
Science and Technology

Daniel dos Santos Mota

Control and Stability of Isolated Grids with Synchronous and Non-Synchronous Generation

Thesis for the Degree of Philosophiae Doctor

Trondheim, December 2023

Norwegian University of Science and Technology
Faculty of Information Technology and Electrical Engineering
Departement of Electric Energy

NTNU
Norwegian University of
Science and Technology

NTNU
Norwegian University of Science and Technology

Thesis for the Degree of Philosophiae Doctor

Faculty of Information Technology and Electrical Engineering
Departement of Electric Energy

ISBN 978-82-326-7604-0 (printed ver.)
ISBN 978-82-326-7603-3 (electronic ver.)
ISSN 1503-8181 (printed ver.)
ISSN 2703-8084 (online ver.)

Doctoral theses at NTNU, 2023:450

Printed by NTNU Grafisk senter

To my family

Don’t panic!

The Hitchhiker’s Guide to the Galaxy
Douglas Adams

Abstract

This thesis explores the challenges and opportunities associated with integrating offshore wind turbines into a geographically compact power-intensive isolated electric grid that is currently supplied by gas-powered synchronous generators. To explore the best power and energy characteristics of different energy storage devices, a hybrid energy storage system is evaluated as the means of mitigating the negative effects of wind intermittency. In this hybrid system, batteries are employed as fast energy storage devices providing inertial and primary frequency control reserves, whereas a pair of electrolyzers and fuel cells are used as slower secondary reserve providers. These storage devices are coupled via dc/dc converters to a common dc link which, in turn, is connected to the isolated grid's main ac high-voltage busbar through an active front-end converter. Large converter-interfaced flexible loads in the isolated grid are also expected to act as primary power reserve providers.

In addition to frequency control problems introduced by non-synchronous intermittent renewable energy sources, the power electronic converters of wind turbines, flexible loads, and energy storage systems tend to operate as constant power devices. This is known to cause stability issues in micro and large grids. Within this context, three goals have been defined for this PhD research: (1) identify and address causes of converter-induced instabilities, (2) propose robust control strategies to exploit efficiently existing and new assets added to the grid, and (3) assess and validate experimentally in the laboratory the proposed control strategies. These goals led to five research questions, namely: (1) which phenomena may lead to converter-driven instabilities and how can one mitigate them, (2) how can one build a robust control structure for regulating frequency in the time scale of seconds to minutes and for providing reactive or voltage support, (3) how can one share fast power reserves among traditional generators and converter-interfaced sources in the time scales of seconds to minutes, (4) what are the consequences of shifting primary frequency control reserves from slower synchronous generation to faster converter-interfaced ones, and (5) how can one properly reproduce the phenomena under study in a reduced-scale laboratory setup.

The pursuit for answers to these research questions led to a number of contributions to the scientific literature, which were presented at academic conferences and published in journals. Among them, the five main contributions compiled in this thesis are as follows: (1) a set of control structures for energy storage systems for providing inertial, primary, and secondary power reserves, (2) identification and analysis of the root cause of an oscillation phenomenon occurring in power converters operating with dual rotating reference frames, (3) the description of a sequence separation method applied to the direct and quadrature axes of the rotating reference frames, (4) the expansion of a requirement for frequency reserves stemming from interconnected systems and application of this extended concept to an isolated grid dominated by constant power loads, and (5) a method for matching preexisting reduced-scale laboratory converters to specific characteristics of real-life large power converters.

In conclusion, this thesis sheds light on the complex dynamics and interactions that arise when non-synchronous converter-interfaced renewable energy sources are connected to existing power-intensive isolated electric grids previously dominated by traditional synchronous generation.

Preface

This thesis is submitted as a partial fulfillment of the requirements for acquiring a Philosophiae Doctor (PhD) Degree at the Norwegian University of Science and Technology (NTNU). This doctoral work has been carried out at the Power Electronic Systems and Components research group in the Department of Electric Energy, with Professor Elisabetta Tedeschi and Dr. Santiago Sanchez-Acevedo as main supervisor and co-supervisor, respectively.

This work was supported through the PETROSENTER scheme under the LowEmission Research Centre grant number 296207 and was carried out in the period between February 2020 and January 2023. Educating 19 PhD students is one of the many goals of the LowEmission center. This doctoral dissertation was prepared by one of these students.

Outline

The thesis is divided into three parts:

Part I – Main Matter
Core of the thesis divided into chapters.

Part II – Appendices
Complimentary discussions divided into appendices.

Part III – Lists and Supplementary Information
Lists of figures, tables, abbreviations, acronyms, and symbols.

Navigating this Document

Sources are cited in the following format: [number]. They are numbered sequentially as mentioned in the text starting from one at the beginning of each chapter/appendix. References are active links in the electronic version of this document. You should be able to click on the [number] and go to the reference list at the end of the respective chapter/appendix. From this list, you should be able to click your way back to the page where the reference was cited.

Figures and tables are numbered as follows: chapter number.sequential number. Cross-references along the text are typeset in blue and are active links that lead you back to the respective figures and tables. However, there is no active link in each figure and table to bring you back to the page you were on previously. You will find lists of figures and tables for entire document in Part III.

Equations that are mentioned across this document are numbered in the following format: (chapter number.sequential number). Cross-references to equations in the text are typeset in blue and are "clickable". Symbols are also typeset in blue with active links to the list of symbols in Part III. From the list of symbols, you should be able to click your way back to the page you were previously reading.

Abbreviations and acronyms are active links and are typeset in blue. They typically appear in first time they are mentioned in each chapter/appendix as: long version (short version). After that, they tend to appear only in the short version. Some abbreviations and acronyms, however, may appear only in their short form. Notice that they are also active links. For instance, if you click in the words "ac/dc" in this sentence, you should be directed to the list of abbreviations and acronyms, from there you should be able to return to this page (number x).

Acknowledgements

Thank you Professor Elisabetta Tedeschi and Research Scientist Santiago Sanchez-Acevedo for your guidance and support throughout my PhD research. Your keen eyes for detail and rigorous approaches to research have helped me navigate through the PhD life. Thank you faculty and staff at the Department of Electric Energy of NTNU for your unwavering support and academic resources that have contributed to the completion of this thesis. Thank you SINTEF Researchers Harald Svendsen, Andrzej Holdyk, Til Kristian Vrana, Jon Are Suul, Olve Mo, Kjell Ljøkelsøy, and Salvatore D'Arco. Your expertise guided and refined my work.

Thank you co-authors and all who supported me with discussions that shaped my research. Although some of you have already been mentioned, some still haven't. Thank you Professor Gilbert Bergna-Diaz, Augusto Matheus dos Santos Alonso, Babak Abdolmaleki, Spyridon Chapaloglou, Ayotunde Adekunle Adeyemo, Joseph Kiran Banda, Erick Fernando Alves, and many others. Erick, thank you for tempting me to take the leap back to academia.

Thank you my fellow PhD candidates for the jovial working environment, for the insistence to play football (although I haven't played), for the scientific interesting colloquia, and for the warm conversations during coffee breaks. I will miss those times.

Thank you professors at the *Escola Politécnica da Universidade de São Paulo*. You invited me with your lectures to follow the electric power systems' path. Thank you my dear Professor Clovis Goldemberg for guiding me towards voltage regulators of synchronous generators. Thank you Professor Walter Kaiser for supporting me from São Paulo, while I was already in Norway, during the final stages of my work on power system stabilizers.

To those who thought me my mother tongue, *agradeço a vocês meu pai e minha mãe por me ensinarem a bater asas e por me incentivarem a voar buscando meus sonhos. Hoje sinto um misto de preocupação e orgulho quando vejo minhas crias tomando suas próprias decisões*. To my brother, thank you for the paths we shared and for the paths we will still share. And to my wife and two children, thank you for enduring a stressed husband and a grumpy father working evenings and weekends on his personal project. I am forever grateful.

Contents

PART I MAIN MATTER

PART II APPENDICES

PART III LISTS AND SUPPLEMENTARY INFORMATION

Part I

MAIN MATTER

CHAPTER 1

Introduction

This doctoral dissertation gathers the main results of the investigations that I, with the help of professors, researchers, and fellow PhD candidates, performed within the electrical engineering field of control structures for the stability guarantee of offshore oil and gas (O&G) platforms isolated from the continent and fed by traditional natural-gas driven turbogenerators (GTs) which are expected to be connected to an offshore wind farm (WF), equipped with converter-interface flexible loads, and supported by converter-interfaced energy storage systems (ESSs) employing battery, fuel cells, and electrolyzers as energy storage devices (ESDs). In broader terms, complex power-intensive isolated electrical grids with synchronous and non-synchronous generation.

This dissertation was written under LowEmission Research Centre (LowEmission) framework for petroleum activities on the Norwegian continental shelf (NCS), which gathers Norwegian and international industrial entities including vendors, operators, and energy companies with research groups at SINTEF and NTNU. The mission of the LowEmission Centre is to pave the road towards zero-emission production of O&G from the NCS. The LowEmission activities, which span from 2019 to 2026, are subdivided into nine subprojects covering, among other topics, efficiency enhancement of gas turbines, improvements to the energy systems, investigations of carbon-free firing sources, research into fuel cells and heat sources, the discovery of more efficient processing techniques, optimization of logistics, and a greater understanding of zero-emission vessels.

The PhD research presented herein was executed under the umbrella of the LowEmission "Subproject 5 Energy Systems - Digital Solutions", which aims to develop generic methods, models, and digital tools for the analysis and optimization of integrated offshore energy systems with renewable energy supply. The goal is to enable the cost-effective, reliable, and stable operation of the O&G platforms' energy systems with low or zero CO_2 emissions.

1.1 MOTIVATION AND RESEARCH GOALS

Rapid climate change is among the biggest global challenges today. The general roadmap to tackle this challenge includes country-specific paths that depend on the types of national energy resources. The petroleum sector accounts for a considerable portion of many countries' nitrogen oxides (NO_x) and greenhouse gas (GHG) emissions. At the same time, it is a key element of their socio-economic development. In Norway, for instance, 20 % of the GHG emissions come from GTs in operation in the O&G fields in the NCS [1]. A similar situation, with considerable emissions from the offshore O&G sector, is observed in other European states, such as the United Kingdom [2] and the Netherlands [3].

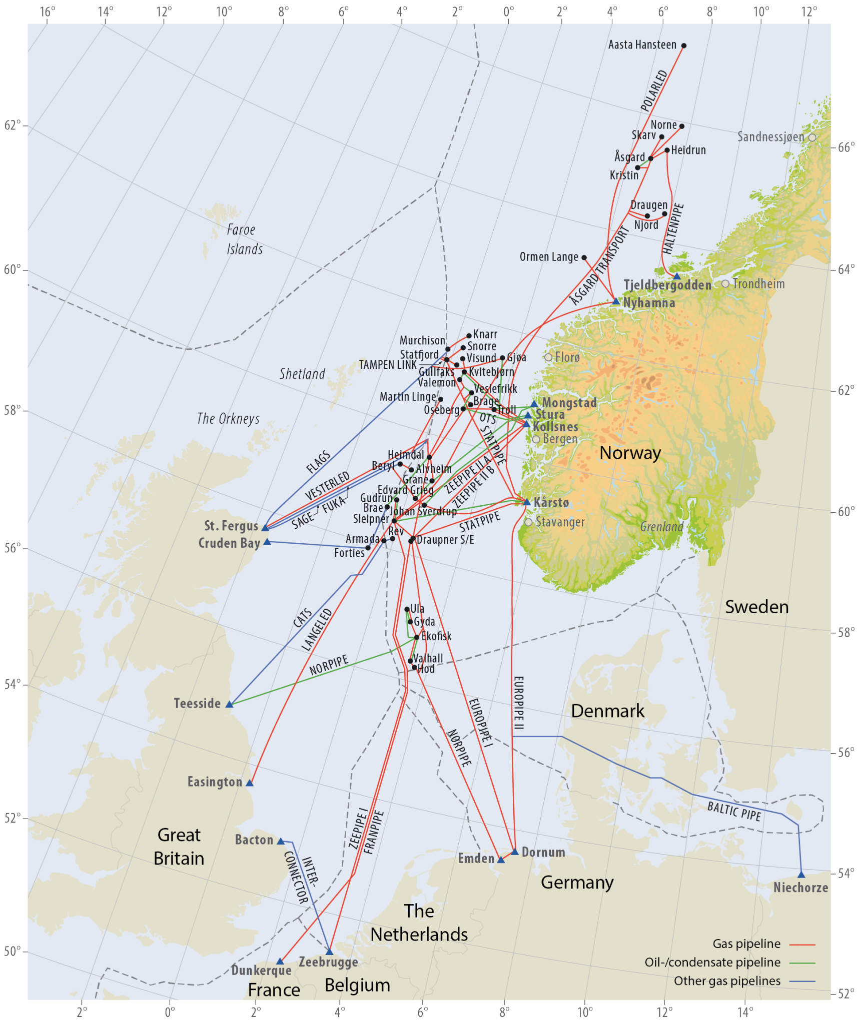

FIGURE 1.1 Gas grid in the Norwegian continental shelf.

© Norwegian Ministry of Petroleum and Energy 2023 | Reproduced with permission from: www.norskpetroleum.no/wp-content/uploads/09-Rorledninger-E-1.png. "Maps, illustrations, graphs and tables can be reused, given that the material is marked with the source and link."

Figure 1.1 illustrates the scale of the offshore O&G activities in the NCS with its grid of pipelines connecting the production fields to continental Norway and Great Britain, Belgium, the Netherlands, Germany, and Poland. Natural gas produced by the 93 active fields [4] in the NCS corresponded to 52 % of the total value of goods exported by Norway in 2022 [5]. However, not all natural gas extracted from the NCS is transported to land. A relevant part of it is used for heat and electricity generation in the O&G platforms on the Barents, North and Norwegian Seas. These platforms rely mostly on aeroderivative single-cycle GTs for power and heat supply [6]. For instance, in 2008, the total installed capacity of the 167 gas turbines on the NCS summed up to approximately 3 GW. Most of those turbines were rated between 20 and 30 MW, whereas only 41 of them were rated below 10 MW [7].

Feasible approaches for reducing emissions related to offshore O&G production include the optimization of energy efficiency, carbon capture and storage, electrification from cleaner sources located onshore, and the use of renewable energy sources. Among the local cleaner sources, the abundance of offshore wind [8] is extremely promising when economic and environmental aspects are considered. However, technical challenges shall be addressed when integrating wind energy to the isolated power system of an O&G platform. The compact single-cycle aeroderivative turbines employed for heat and electricity generation in these platforms operate at relatively stable loads, however out of their best efficiency points due to redundancy requirements. Introducing a new but intermittent energy source such as wind has positive (+) and negative (−) consequences for the GTs [9, 10]. Among the consequences, one can mention:

(+) operation of one GT at a higher load and better efficiency range if the redundant one can stay in cold standby;
(−) increased number of start-stop operations and more variable load profile for the GTs, i.e., higher wear and tear and NO_x emissions;
(−) overall degradation of the electric power quality and grid frequency stability, resulting in higher wear and tear of motors without variable frequency drives.

Integrating wind energy into isolated O&G industrial systems presents several challenges that need to be addressed from the early design stage by possibly adapting the control of generation units and best exploiting both existing and new assets. Within this context, three goals were established for my three-year PhD project at the LowEmission Centre.

Research Goal I — Identify and address causes of converter-induced instability

Intermittent renewable energy sources (RES) like wind and solar photovoltaic (PV) farms are typically connected to the electrical grid through full-power back-to-back power electronic converters (PECs) [11]. The increased participation of such converter-interfaced sources is responsible for a new type of instability phenomenon that is becoming relevant both in micro and large electric grids [12, 13]. Therefore, the first goal defined for my PhD-project was to identify and address root causes of converter-driven instabilities in a power-intensive isolated grid fed by traditional synchronous generation, connected to converter-interfaced intermittent RES, and supported by an ESS and fast-acting converter-interfaced flexible loads.

Research Goal II — Propose robust control strategies

Introducing converter-interfaced ESSs, which are capable of reacting faster than the traditional turbine governors of GTs [13] in an isolated industrial grid, demands the use of effective coordination strategies for sharing frequency control power reserves. Within this context, the second goal defined for my PhD project was to propose robust control strategies to exploit efficiently the existing and new assets added to the grid. As there are many industrial partners in the LowEmission Research Centre, the following constraints were adopted for the control strategies: they should aim for modularity allowing for the maintenance and replacement of parts with equipment from different suppliers; be independent from fast communication links between different converters of the ESS and between the ESS and the platform's power management system (PMS); and preferably be based on established robust control techniques such as, for example, proportional, integral, and derivative (PID) regulators.

Research Goal III — Assess and validate experimentally the proposed control strategies

The National Smart Grid Laboratory (NSGL) at NTNU provides state-of-the-art research, development, and testing infrastructure that features real-time simulators (RTSs) and power hardware-in-the-loop (PHIL) assets with ratings up to 200 kVA, 400 V ac, and 700 V dc. The NSGL facilities are available for the PhD candidates of the LowEmission Research Centre. With this in mind, the third goal defined for my PhD project was to assess the possibilities and establish procedures for employing NSGL's ac and dc grid emulators coupled with a reduced-scale 60 kVA converter to reproduce a full-scale energy storage system grid converter (ESSGC) and assess the efficacy of the proposed control strategies from Research Goal II.

1.2 RESEARCH METHODOLOGY

With the Research Goals I to III defined, a research methodology was proposed in agreement with the PhD supervisor and co-supervisor. The research was divided into five main stages, which are illustrated in figure 1.2.

Phase 1 — Conceptualization

The knowledge frontier was investigated in this phase with a comprehensive literature review on the topics concerning this PhD project. The object of

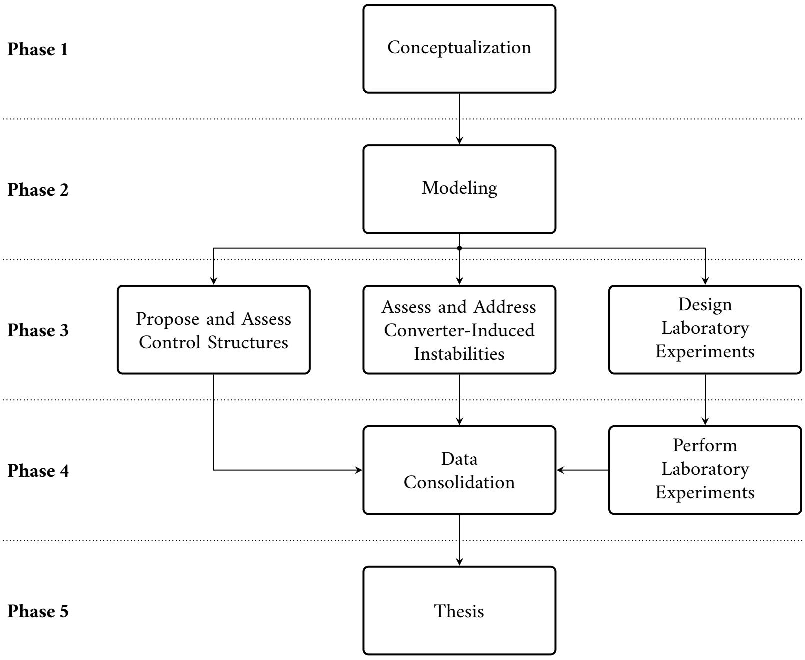

FIGURE 1.2 Research methodology.

the research was conceptualized and the coverage and limitations were established.

Phase 2 — Modeling

In phase 1, the problem was defined; now it was time to start solving it. Real-life tests in an existing O&G platform were not included in the scope. Therefore, computer simulation models were key for achieving the research goals. Models based on a real platform expected to be connected to an offshore wind farm were constructed in partnership with fellow PhD candidates and were curated by members of the LowEmission project. Although the direct application on site of the research findings was a target, opportunities for generalizing conclusions and, ultimately, proposing analytical solutions were continuously considered.

Phase 3 — Propose, address, assess, and design

Once the first computer simulation models were operational, a new phase involving three parallel activities started.

Propose and assess control structures: variants of existing control structures were proposed as the assessment of existing ones progressed.

Assess and address converter-induced instabilities: during the evaluation of the different control structures, root causes of instabilities were assessed and addressed.

Design experiments: the PhD candidate was introduced to the facilities at the NSGL and started design experiments for validating the theoretical and computer simulated results.

During phase 3, the computer simulation models were continuously refined and updated. With the goal of documenting and allowing reproducibility, the models were made publicly available in online data repositories, see section 1.6.

Phase 4 — Experiment and consolidate

The three complementary activities of phase 3 were followed by two activities in this phase. The designed experiments were executed at the NSGL. Computer simulations and experimental data were consolidated while the good control structures were selected and the bad ones discarded.

Phase 5 — Thesis

This dissertation was sketched throughout all research phases. However, it was mainly written after phase 4 when all scientific manuscripts were already submitted for publication.

Although not represented in figure 1.2, a publication plan was established and target conferences and scientific journals were defined. The publication plan included at least three conference papers and two journal papers to be written and submitted along the phases 2 to 4 of this PhD project. The list of scientific publications will be presented later in section 1.5.

1.3 RESEARCH QUESTIONS

As the research progressed from phase 1 of conceptualization and the first scientific manuscripts began to be sketched, the following research questions were proposed:

Research Question I — Which phenomena may lead to converter-driven instabilities and how can one mitigate oscillations in isolated grids with traditional synchronous generation complemented by converter-interfaced intermittent RES and supported by converter-interfaced ESS?

Research Question II — How can one build a robust control structure for regulating frequency in the time scale of seconds to minutes, as well as provide reactive or voltage support, in isolated grids equipped with fast converter-interfaced ESS?

Research Question III — How can one share frequency control power reserves among traditional synchronous generators and converter-interfaced sources and loads in the time scales of seconds to minutes in isolated grids?

Research Question IV — What are the consequences of shifting primary frequency control reserves from traditional slower synchronous generation to faster converter-interfaced ESSs?

Research Question V — How can one properly reproduce the phenomena under study in this work in a PHIL laboratory setup employing ac and dc grid emulators and reduced scale PECs?

1.4 CONTRIBUTIONS TO THE SCIENTIFIC LITERATURE

The five main contributions to the scientific literature proposed in the pursuit of answering the Research Questions are compiled into this dissertation. The contributions are enumerated in the sequence they are discussed in the chapters. Notice that this is not the chronological sequence in which the contributions were published or submitted for publication in academic conferences and journals. The relationship between chapters and contributions is illustrated in figure 1.3 in page 13.

Contribution I — Control structures for an energy storage system providing inertial, primary, and secondary frequency reserves.
A control strategy for providing inertial, primary, and secondary frequency reserves with a hybrid ESS employing battery, fuel cells, and electrolyzers as ESDs in an isolated electric grid was described and tested with computer simulations and PHIL laboratory setups. This strategy is based on established PID techniques and does not rely on fast communication links between different ESDs nor with the grid's PMS. It also allows for voltage and reactive power support to be provided by the energy storage system grid converter.

Contribution II — Identification and analysis of an oscillation phenomenon occurring in PECs operating with dual rotating reference frame (RRF) current controllers.
The cause of voltage oscillations with the fundamental frequency observed in the dc-link of the study case's ESS, when the energy storage system grid converter (ESSGC) operated with a dual RRF inner current controller scheme, was identified and analyzed. These oscillations are directly tied to exponentially decaying dc currents that appear in three-phase systems with high reactance-resistance ratio (X/R) and the way dual RRF controllers split the positive and negative sequence measurements. An evaluation of the expected range of X/R seen from the ESSGC terminals towards the isolated ac grid was also provided.

Contribution III — Positive and negative sequence separation with delayed signal cancellation applied directly to the RRF.
A simplified delayed signal cancellation (DSC) technique, denoted as DSC_{dq} in this work, is presented. This technique is applied directly to the RRFs and removes an intermediate step with filtering in the stationary reference frame (SRF) demanded by the traditional $\text{DSC}_{\alpha\beta}$ method. A mathematical

proof of the equivalence between the traditional DSC$_{\alpha\beta}$ applied in the SRF and the DSC$_{dq}$ is provided. An assessment of the performance of dual sequence current controllers employing known sequence isolation methods and employing the proposed DSC$_{dq}$ is also presented. This assessment is performed in a scenario with high X/R consistent with the study case used as a base in this dissertation.

Contribution IV — Extended FCR$_{\mathrm{I}}$ concept applied to autonomous grids. An expansion of the single slope power-frequency curve of the Nordic frequency containment reserves for isolated operation (FCR$_{\mathrm{I}}$) concept was proposed. The new expanded FCR$_{\mathrm{I}}$ employs a segmented-slope droop curve with different regions for the normal operation of power reserves and large disturbance operation. The advantages, from a frequency control viewpoint, of replacing slower GTs by faster converter-interfaced ESSs as the main provider of normal operation primary reserves were demonstrated with numerical simulations and reduced-scale PHIL tests of an industrial isolated grid dominated by constant power loads (CPLs). It showed, moreover, that this replacement caused a non-critical reduction in the damping of oscillation modes associated with measurement transducers and controllers of constant power devices. These numerical simulations and PHIL tests took into consideration the negative effects caused by CPLs in the electrical grid, an issue commonly overlooked in the literature of power-intensive isolated grids.

Contribution V — Scaling method for laboratory power hardware-in-the-loop test beds. A scaling method and guidelines were proposed for matching specific characteristics of ready-to-use laboratory converters in PHIL test beds with real-life full-size PECs. The method and guidelines exploit the base kVA of the reduced-scale laboratory converters and can be adapted to academic and industrial laboratories. This method was proposed while aiming at Research Goal III and, simultaneously, targeting a future research topic of assessing the effects of the harmonics introduced by the grid converters (GCs) of wind turbines and ESSs on isolated grids.

1.5 SCIENTIFIC PUBLICATIONS

The contributions were published in the following academic papers. The publications themselves are not a part of this dissertation; however, their contents have been compiled and harmonized in the different chapters. The relationships among contributions, publications, and chapters are illustrated in figure 1.3 in page 13.

Publication I — Offshore Wind Farms and Isolated Oil and Gas Platforms: Perspectives and Possibilities. Daniel dos Santos Mota, Erick

Fernando Alves, Santiago Sanchez-Acevedo, Harald G. Svendsen, and Elisabetta Tedeschi. *ASME 2022 41st International Conference on Ocean, Offshore and Arctic Engineering (OMAE)*, Hamburg, Germany. October 3, 2022. ©2022 ASME. DOI: 10.1115/OMAE2022-80645. ISBN: 978-0-7918-8595-6.

Publication II — Sizing of Hybrid Energy Storage Systems for Inertial and Primary Frequency Control. Erick Fernando Alves, Daniel dos Santos Mota, Elisabetta Tedeschi. *Frontiers in Energy Research*, Volume 9, 2021. Frontiers Media SA, Lausanne, Switzerland. May 28, 2021. ©2021 Alves, Mota, Tedeschi. DOI: 10.3389/fenrg.2021.649200. ISSN: 2296-598X.

Publication III — Understanding the Effects of Exponentially Decaying DC Currents on the Dual dq Control of Power Converters in Systems with High X/R. Daniel dos Santos Mota and Elisabetta Tedeschi. *IEEE 15th International Conference on Compatibility, Power Electronics and Power Engineering (CPE-POWERENG)*, Florence, Italy. August 10, 2021. ©2021 IEEE. DOI: 10.1109/CPE-POWERENG50821.2021.9501204. ISBN: 978-1-7281-8071-7.

Publication IV — Dual Sequence Controller with Delayed Signal Cancellation in the Rotating Reference Frame. Daniel Dos Santos Mota, Erick Fernando Alves, and Elisabetta Tedeschi. *IEEE 22nd Workshop on Control and Modelling of Power Electronics (COMPEL)*, Cartagena, Colombia. December 23, 2021. Copyright ©2021 IEEE. ISSN: 1093-5142.
DOI: 10.1109/COMPEL52922.2021.9646023.

Publication V — On Adaptive Moving Average Algorithms for the Application of the Conservative Power Theory in Systems with Variable Frequency. Daniel dos Santos Mota and Elisabetta Tedeschi. *Energies*, Volume 14, Issue 4, MDPI Open Access Journals, Basel, Switzerland. February 23, 2021. ©2021 Mota, Tedeschi. DOI: 10.3390/en14041201. ISSN: 1996-1073.

Publication VI — Coordination of Frequency Reserves in an Isolated Industrial Grid Equipped with Energy Storage and Dominated by Constant Power Loads. Daniel dos Santos Mota, Erick Fernando Alves, Salvatore D'Arco, Santiago Sanchez-Acevedo, and Elisabetta Tedeschi. *IEEE Transactions on Power Systems*. August 11, 2023. ©2023 Mota, Alves, D'Arco, Sanchez-Acevedo, Tedeschi. DOI: 10.1109/TPWRS.2023.3304319. Print ISSN: 0885-8950. Online ISSN: 1558-0679.

Publication VII — Harmonic-Invariant Scaling Method for Power Electronic Converters in Power Hardware-in-the-Loop Test Beds. Daniel dos Santos Mota, Joseph Kiran Banda, Ayotunde Adekunle Adeyemo, and Elisabetta Tedeschi. *IEEE Open Journal of Industry Applications*, Volume 4, Pages 139 - 148, April 2023. April 23, 2023. ©2023 IEEE. ISSN: 2644-1241. DOI: 10.1109/OJIA.2023.3266882.

1.6 REPRODUCIBILITY AND DATA REPOSITORIES

With the goals of documenting the work, allowing reproducibility, and increasing science dissemination, online publicly available data repositories associated with the different publications have been created throughout this PhD research. These repositories are hosted by Zenodo[1] and GitHub.

Repository I — Data Set and Simulation Files used in the Manuscript Offshore Wind Farms and Isolated Oil and Gas Platforms: Perspectives and Possibilities. Daniel dos Santos Mota. For Publication I. February 15, 2022. DOI: 10.5281/zenodo.6095757

Repository II — efantnu/hybrid-ess-design: Review 1 release. Erick F. Alves, Daniel dos Santos Mota, Elisabetta Tedeschi. For Publication II. March 12, 2021. DOI: 10.5281/zenodo.4601067

Repository III — Frequency Adaptive Delayed Signal Cancellation Applied Directly to the Rotating Reference Frames of Dual-Sequence Current Controllers of Power Converters. Daniel dos Santos Mota. For Publication IV. October 1, 2021. DOI: 10.5281/zenodo.5588091

Repository IV — On Adaptive Moving Average Algorithms for the Application of the Conservative Power Theory in Systems with Variable Frequency. Daniel dos Santos Mota. For Publication V. February 22, 2021. DOI: 10.5281/zenodo.4555392.

Repository V — Data Repository for Manuscript Submission to IEEE TPWRS. Daniel dos Santos Mota. For Publication VI. October 1, 2022. DOI: 10.5281/zenodo.7113316

Repository VI — Data repository for the article Harmonic-Invariant Scaling Method for Power Electronic Converters in Power Hardware-in-the-Loop Test Beds. Daniel Dos Santos Mota, Joseph Kiran Banda, Ayotunde Adekunle Adeyemo. For Publication VII. May 9, 2023. DOI: 10.5281/zenodo.7912825

Repository VII — Data Repository for this Dissertation. Daniel dos Santos Mota. August 25, 2023. GitHub: github.com/santosmota/PhD_Daniel_Mota_Data. DOI: 10.5281/zenodo.8282628.

Repository VIII — Repository for the Figures of this Dissertation that were Composed with LaTeX. Daniel dos Santos Mota. August 1, 2023. GitHub: github.com/santosmota/PhD_Daniel_Mota_Data_StandAlonePics. DOI: 10.5281/zenodo.8282714.

---

[1] Zenodo is operated by CERN and OpenAIRE.

1.7 OUTLINE OF THE DISSERTATION

This doctoral dissertation is divided into seven chapters that introduce the work, contextualize it, present the main contributions, and list the final remarks. The contents of the different scientific articles published throughout this PhD research have been compiled into the different chapters. Some chapters are dedicated mainly to one specific publication, whereas others may include the contents of more than one publication. The relationships among chapters, contributions, and publications are illustrated in figure 1.3.

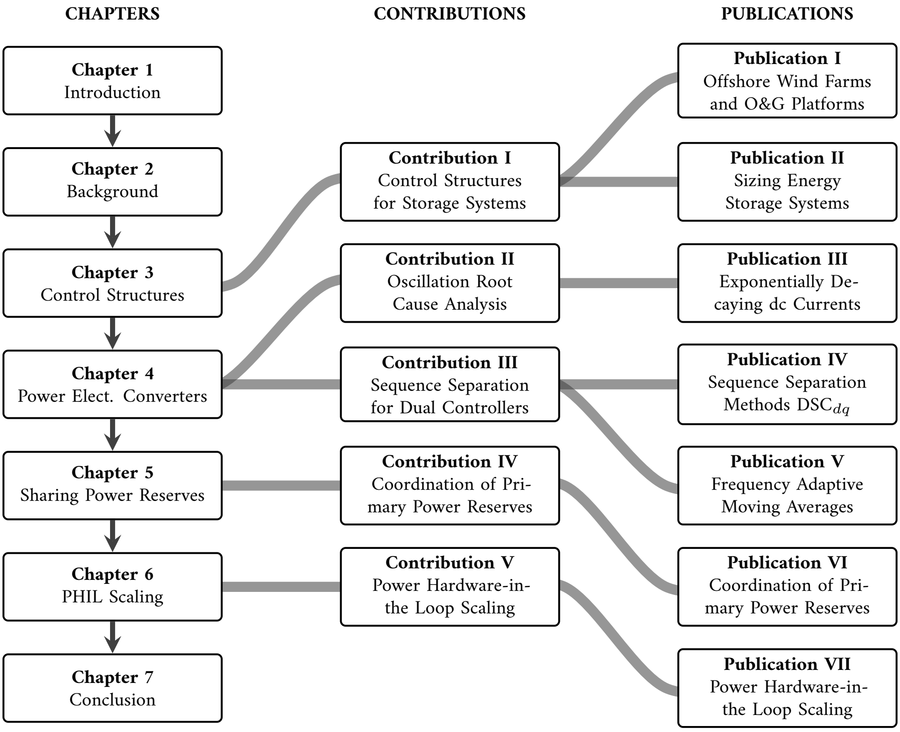

FIGURE 1.3 Chapters, Contributions, and Publications.

© Daniel Mota 2023 | Source code information at Part III.

CHAPTER 1 — INTRODUCTION

This chapter.

CHAPTER 2 — BACKGROUND

This chapter lays the foundation upon which the discussion of control and stability of autonomous grids with synchronous and non-synchronous generation is based. Contents of Publications I to III and VI are compiled and extended in this chapter.

CHAPTER 3 — CONTROL STRUCTURES FOR ESSS

Control structures for isolated grids in which traditional synchronous generation is complemented by intermittent RES are proposed in this chapter, which is tied to Research Goal II and aims to answer Research Question II. The focus is on the outer control loops of a converter-interfaced ESS that provides frequency control support for an isolated grid. Contribution I to the scientific literature is presented in this chapter, which compiles the contents of Publication I.

CHAPTER 4 — CURRENT CONTROL IN POWER CONVERTERS

This chapter is tied to Research Goal I, which addresses possible causes of instability, and to Research Goal II, which proposes control structures. It focuses on the PECs' fast inner current controllers operating in single or dual rotating reference frames. Contribution II from Publication III and Contribution III from Publication IV, as well as passages from Publication V, are compiled in this chapter.

CHAPTER 5 — SHARING OF PRIMARY POWER RESERVES

This chapter is tied to Research Goal II, which proposes control structures, as well as Research Goal III, which validates them in the laboratory. It stems from Research Questions III and IV and focuses on the sharing of primary power reserves for the frequency control in an isolated grid fed by traditional synchronous generation, connected to converter-interfaced generation, and dominated by CPLs. Contribution IV to the scientific literature is presented in this chapter, which compiles the contents of Publication VI.

CHAPTER 6 — SCALING METHOD FOR PHIL TEST BEDS

This chapter is tied to the Research Goal III, which validates in the laboratory the control structures proposed in this dissertation. It stems from Research Question V and focuses on a scaling method for matching specific characteristics of laboratory PECs used in PHIL tests to the characteristics of real-life full-scale converters. Contribution V to the scientific literature is presented in this chapter, which compiles the contents of Publication VII.

CHAPTER 7 — CONCLUSION

Conclusion, discussion, and final remarks on this dissertation.

It is important to remark that the original nomenclatures of the publications have been harmonized to better fit this dissertation. Moreover, the original published figures have been completely redrawn, reformatted, and harmonized to fit the nomenclature, color scheme, font, and page size of this document. Some figures are completely original and others were meant to be published, but were not due to diverse reasons, such as editorial page limitations defined by academic conferences and journals. The LaTeX and Python source codes for drawing the figures in this dissertation are made publicly available, see Part III.

1.8 SCOPE LIMITATIONS

The complex interactions between the controllers of traditional frequency containment power reserves, conventional and converter-interfaced loads, and converter-interface storage systems in the first seconds to minutes after a transient disturbs the grid are investigated in this work. The focus is on the initial phases right after disturbances that cause power unbalances, namely the inertial and primary phases of the frequency control. In these phases, the voltage controllers of the synchronous generators, the governors of the gas turbines, the slower outer loops and the faster inner control loops of converter-interfaced loads and sources interact and can give rise to instability issues. An illustration of the time scale of the control phenomena in electrical grids is provided later in section 2.3; a definition of the phases of the frequency control in electrical grids is available at section 2.2; the PEC's outer loops are addressed in chapter 3; and the inner loops are examined in chapter 4. It is important to remark that secondary and tertiary frequency control dynamics, long term (hours to days) estimation of optimal levels of energy reserves, and techno-economical or risk-based forecasting tools for power management are considered outside the scope of this dissertation.

1.9 READER'S BACKGROUND

This thesis is written by an electrical engineer for readers with a background in electrical systems that are familiar with Fortescue's method of symmetrical components applied to ac three-phase circuits [14], more commonly known as the positive, negative, and zero sequences, and Park's two-reaction theory of circuit analysis [15], which is commonly referred to as the direct and quadrature rotating reference frame. It is also assumed that the readers are familiar with the expression "per unit", denoted as pu, which means that a variable has been divided by a base value and is, therefore, dimensionless.

1.10 REFERENCES

[1] OED. Norwegian Petroleum Emissions to Air. Online. Norwegian Ministry of Petroleum and Energy and the Norwegian Petroleum Directorate Oslo, Norway (January 2023). URL https://www.norskpetroleum.no/en/environment-and-technology/emissions-to-air/, accessed on 2023-01-11. Cited on page(s) 4.

[2] OGUK. North Sea Transition Deal. Report NSTD Department for Business, Energy & Industrial Strategy and Oil and Gas UK (OGUK) London, United Kingdom (March 2021). URL https://assets.publishing.service.gov.uk/government/uploads/system/uploads/attachment_data/file/972520/north-sea-transition-deal_A_FINAL.pdf, accessed on 2023-01-10. Cited on page(s) 4.

[3] Adrian Serna Tamez and Stijn Dellaert. Decarbonisation Options for the Dutch Offshore Natural Gas Industry. Report PBL 416 PBL Netherlands Environmental Assessment Agency and

TNO Energy Transition (2020). URL https://www.pbl.nl/sites/default/files/downloads/pbl-2020-decarbonisation-options-for-the-dutch-offshore-natural-gas-industry_4161.pdf, accessed on 2023-01-11. Cited on page(s) 4.

[4] OED. Norsk Petroleum Fakta. Online Norwegian Ministry of Petroleum and Energy and the Norwegian Petroleum Directorate Oslo, Norway (January 2023). URL https://www.norskpetroleum.no/fakta/, accessed on 2023-06-06. Cited on page(s) 5.

[5] SSB. External trade in goods, main figures (NOK million), by trade flow 1960-2022. Statistikkbanken Table 08800 Statistisk Sentralbyrå Oslo, Norway (June 2023). URL https://www.ssb.no/en/statbank/table/08800, accessed on 2023-06-23. Cited on page(s) 5.

[6] Håvard Devold. Oil and Gas Production Handbook, an Introduction to Oil and Gas Production, Transport, Refining and Petrochemical Industry. ABB Oil and Gas Oslo, Norway 3.0 edition (2013). ISBN 978-82-997886-3-2. URL https://library.e.abb.com/public/34d5b70e18f7d6c8c1257be500438ac3/Oil%20and%20gas%20production%20handbook%20ed3x0_web.pdf, accessed on 2023-02-17. Cited on page(s) 5.

[7] OED. Kraft fra Land til Norsk Sokkel. Teknisk Rapport Oljedirektoratet, Norges vassdrags og energidirektorat, Petroleumtilsynet, Statens forurensningstilsyn Oslo, Norway (January 2008). URL https://www.npd.no/globalassets/1-npd/publikasjoner/rapporter/kraft-fra-land-rapport.pdf, accessed 2023-01-11. Cited on page(s) 5.

[8] IEA. Offshore Wind Outlook 2019. Report WEO STO 2019 International Energy Agency Paris, France (November 2019). URL https://iea.blob.core.windows.net/assets/495ab264-4ddf-4b68-b9c0-514295ff40a7/Offshore_Wind_Outlook_2019.pdf, accessed on 2023-03-17. Cited on page(s) 5.

[9] Magnus Korpås, Leif Warland, Wei He, and John Olav Giæver Tande. A case-study on offshore wind power supply to oil and gas rigs. *ELSEVIER Energy Procedia* **24** (January 2012). ISSN 1876-6102. DOI 10.1016/j.egypro.2012.06.082. Cited on page(s) 5.

[10] Luca Riboldi, Erick F. Alves, Marcin Pilarczyk, Elisabetta Tedeschi, and Lars O. Nord. Optimal Design of a Hybrid Energy System for the Supply of Clean and Stable Energy to Offshore Installations. *Frontiers in Energy Research* **8**, 346 (December 2020). ISSN 2296-598X. doi: 10.3389/fenrg.2020.607284. DOI 10.3389/fenrg.2020.607284. Cited on page(s) 5.

[11] Remus Teodorescu, Marco Liserre, and Pedro Rodriguez. Grid Converters for Photovoltaic and Wind Power Systems | IEEE eBooks | IEEE Xplore. Wiley-IEEE Press (December 2010). ISBN 978-0-470-05751-3. DOI 10.1002/9780470667057. Cited on page(s) 5.

[12] Mostafa Farrokhabadi, *et al.* Microgrid Stability Definitions, Analysis, and Examples. *IEEE Transactions on Power Systems* **35** (1) (January 2020). ISSN 1558-0679. DOI: 10.1109/TPWRS.2019.2925703. Cited on page(s) 5.

[13] Nikos Hatziargyriou, *et al.* Definition and Classification of Power System Stability – Revisited & Extended. *IEEE Transactions on Power Systems* **36** (4), 3271–3281 (July 2021). ISSN 1558-0679. DOI: 10.1109/TPWRS.2020.3041774. Cited on page(s) 5, 6.

[14] Charles Legeyt Fortescue. Method of Symmetrical Co-ordinates Applied to the Solution of Polyphase Networks. *Proceedings of the American Institute of Electrical Engineers* **37** (6), 629–716 (June 1918). ISSN 2376-7758. DOI 10.1109/PAIEE.1918.6594104. Cited on page(s) 15.

[15] Robert H. Park. Two-reaction Theory of Synchronous Machines Generalized Method of Analysis-part I. *Transactions of the American Institute of Electrical Engineers* **48** (3), 716–727 (July 1929). ISSN 2330-9431. DOI 10.1109/T-AIEE.1929.5055275. Cited on page(s) 15.

CHAPTER 2

Background

RESEARCH GOALS AND SCIENTIFIC PUBLICATIONS

This chapter lays the foundation upon which the discussion on the control and stability of isolated grids with synchronous and non-synchronous generation is based. Contents of Publications I to III and VI are compiled and extended in this chapter.

A generalized version of the isolated grid under study in this dissertation is shown in figure 2.1. This grid features traditional synchronous generation provided by turbogenerators (GTs). It is expected to be connected to a wind farm (WF) and be supported by a converter-interfaced energy storage system (ESS). The loads of the grid are composed of constant impedance loads (CZLs) and constant power loads (CPLs). Among the CPLs, a reasonable set of converter-interfaced flexible loads (FLX) are expected to be able to provide frequency control support. The devices of this grid are located in a reasonably limited geographical region and can be directly, or indirectly, connected to the main ac busbar, which operates at voltages on the range of 10 kV.

One critical aspect for operating an isolated system like the one illustrated in figure 2.1 is the frequency control, which demands a continuous compensation of imbalances between consumption and generation. However, before further investigating the challenges of controlling and maintaining the stability on such a grid, it is important to introduce a few key concepts.

2.1 STABILITY IN ELECTRIC POWER GRIDS

An electrical power system is considered stable if it is able to return to the previous or reach a new acceptable equilibrium state after being subjected to a perturbation. A new acceptable state of equilibrium is characterized by new bounded levels for the system's variables and possible changes to the system's topology. The definitions for acceptable new levels for the variables and acceptable new topologies vary from application to application. Traditionally, the stability of large country-wide electrical systems has been classified into three categories [1].

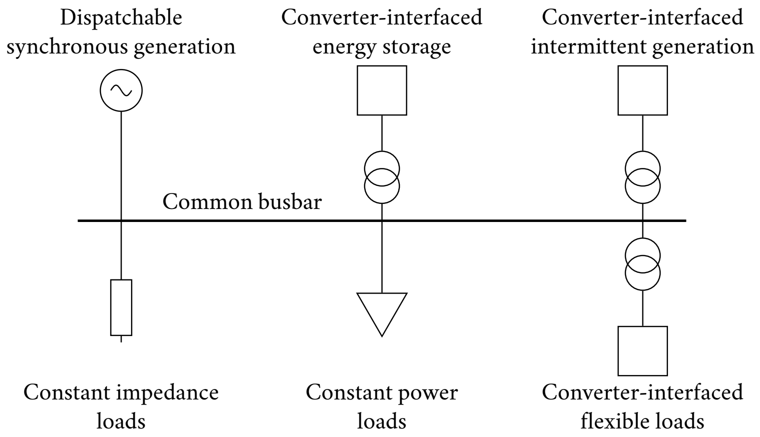

FIGURE 2.1 Generalized version of the isolated grid under study in this dissertation.

© Daniel Mota 2023 | Source code information at Part III.

1. **Rotor angle stability**: the ability of each synchronous machine to remain in synchronism despite inherent low-frequency electromechanical oscillations in the power system.
2. **Voltage stability**: the capacity of maintaining steady voltage levels at the different buses in the power system during changes to the power flow and despite the effects of the impedances of the elements in the electrical grid.
3. **Frequency stability**: the ability to reach a steady frequency level by correcting imbalances between generation and load.

Intermittent renewable energy sources (RES) like wind and solar photo-voltaic (PV) farms are typically connected to the electrical grid through full-power back-to-back power electronic converters (PECs). These converters interact with the electrical system in a considerably different way when compared to traditional synchronous generators driven by gas, steam, or hydraulic turbines [2]. In this context, a new root-cause for instabilities becomes relevant in both micro and large grids [3, 4].

> **Converter-induced or converter-driven instabilities** arise from the interactions of different control loop layers of grid connected converters with each other or other elements of the system. They should not be overlooked when integrating intermittent RES in isolated grids.

2.2 FREQUENCY CONTROL IN AN ISOLATED GRID

To understand the dynamic behavior of the frequency of an isolated ac electric grid, the simplified model of a spinning flywheel can be used. In this model, shown in figure 2.2, all rotating masses of the synchronous generators are aggregated into a single rotating mass with moment of inertia J. The kinetic energy stored in this rotating mass stabilizes the system. On the "generation side" axle, the aggregated turbines of the system apply mechanical torque τ_m that accelerates the angular frequency ω of the rotating mass. On the "load side" axle, the aggregated loads apply electrical torque τ_e that reduces ω.

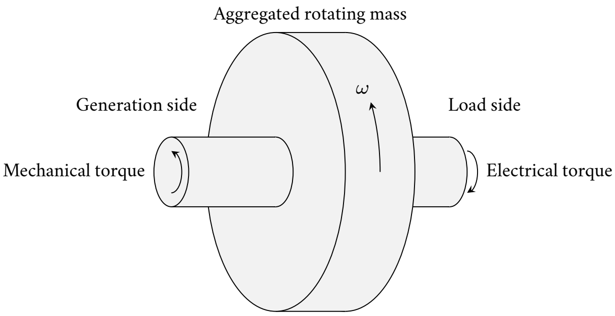

FIGURE 2.2 Rotating mass model.

© Daniel Mota 2023 | Source code information at Part III.

The balance of torques of the rotating mass model can be written as

$$\underbrace{J\frac{\mathrm{d}\omega(t)}{\mathrm{d}t}}_{\text{Accelerating torque}} = \underbrace{\tau_m(t)}_{\text{Turbines' torque}} - \underbrace{\tau_e(t)}_{\text{Loads' torque}} .$$

When expressed in terms of power, the balance of torque becomes

$$\omega(t)J\frac{\mathrm{d}\omega(t)}{\mathrm{d}t} = P_m(t) - P_e(t) \tag{2.1}$$

where P_m is the mechanical power delivered by the turbines to the rotating mass and P_e is the electrical power consumed by the grid. Notice that the balance of power in equation (2.1) is nonlinear. Whenever there is an excess of power generation compared to the load, the angular frequency of the rotating mass increases. When there is underproduction, the frequency decreases. Due to the stochastic behavior of the loads, the mechanical power supplied to the rotating mass must be continuously adapted by the turbine governors.

There is no fast direct communication between loads and governors. The balance of power happens indirectly via control of the ac frequency, which is performed by the activation, in a hierarchic manner, of power reserves. Primary reserves perform a droop-based frequency control responding automatically after power imbalances limiting frequency deviations in a time scale of seconds. Secondary reserves are subordinated to the grid's automatic generation control (AGC), which brings the frequency back to its rated value within seconds to minutes after power imbalances [5]. In the European context, primary reserves are named frequency containment reserves (FCR) and are coordinated nationally by transmission system operators (TSOs) [6]. The FCR concept will be explored later in chapter 5.

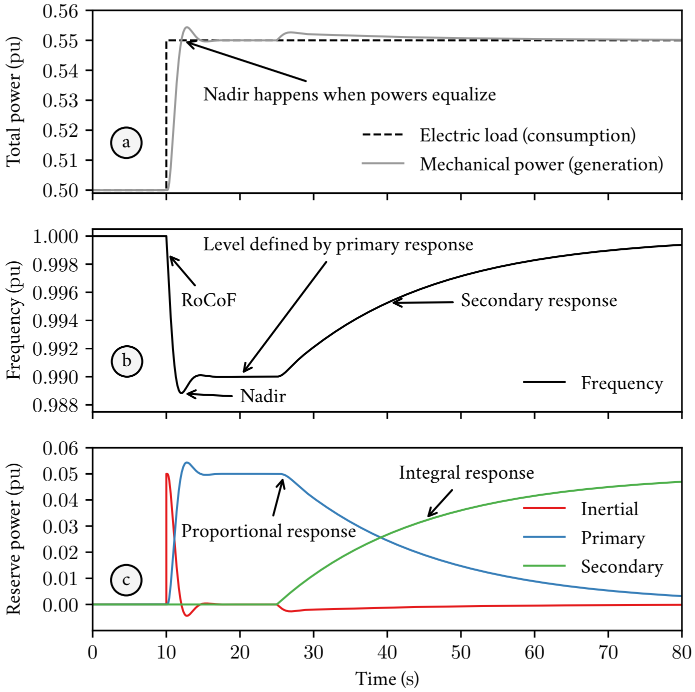

FIGURE 2.3 Phases of frequency control.

© Daniel Mota 2023 | Source code information at Part III.

Figure 2.3 illustrates the phases of the frequency control and the activation of the reserves after a sudden increase in the electric load consumed in the isolated grid. Initially, electric load and mechanical power (dashed black and solid gray, respectively, in figure 2.3a) are in balance at 0.5 pu and the frequency (solid black in figure 2.3b) is constant at 1 pu. At $t = 10$ s, the load increases in a step by 0.05 pu. The mismatch between electric load and mechanical power is covered, initially, only by the inertial reserves (solid red in figure 2.3c) leading the frequency to drop. The initial rate of change of frequency (RoCoF) depends on the aggregated moment of inertia J from equation (2.1). The turbine governors sense the frequency drop and react proportionally by supplying the primary power reserves (in solid blue in figure 2.3c). When the primary response matches the power unbalance, the frequency stops to decrease and reaches its minimum value, called nadir. The proportional response of the primary providers stops the ac frequency fall and brings it to a steady-state level that is below rated as annotated in figure 2.3b.

By the end of the primary response phase, the grid's AGC or power management system (PMS) activate the secondary power reserves (solid green in figure 2.3c). The integral response of the secondary reserves brings the frequency back to the rated. Notice that the total mechanical power in figure 2.3a needs to be slightly higher than the electric load for the frequency to increase. Furthermore, the inertial power always reacts against frequency change. During the secondary phase, part of the mechanical power is used to replenish the kinetic energy stored in the rotating masses.

By the end of the secondary response (not shown in figure 2.3), the AGC or PMS may decide to slowly replace the secondary power reserves initially used for frequency control by other more efficient measures. This is typically achieved through redispatching of generators and loads in the tertiary response phase. The time scales of the frequency control phases are typically: a few seconds for the inertial, seconds to few minutes for the primary, minutes for the secondary, and from a quarter to a full hour for tertiary [2, 4]. The tertiary phase, however, is considered outside the scope of this dissertation.

2.3 Time Scales of Phenomena in Electric Power Grids

A constellation of control loops, directly or indirectly connected to each other, is necessary to keep in operation the electric system of an isolated industrial grid. The dynamics of those control loops happen in different time scales, as illustrated in figure 2.4. Isolated industrial installations feature numerous loads as pumps, compressors, and heaters that may be interfaced by PECs. Traditional voltage regulators and speed governors of synchronous generators work in time scales from 100 ms to 1000 s, whereas the control structures of modern PECs operate in time scales down to 10 µs or lower [4]. On one hand, these faster responses can be beneficial and add new possibilities for frequency control such as inertia emulation and other forms of fast regulation [7]. On the other hand, detrimental interactions such as the converter-driven instabilities mentioned in section 2.1 can also be introduced.

Offshore wind turbines (WTs) feature, for instance, low-frequency oscillation modes due to the slow swinging of their tall floating towers [9]. These low-frequency mechanical oscillations are, ultimately, reflected as variations in the power delivered by the WT to the grid. In the case of large WF with several WTs, these low frequency oscillations can be evened out. However, in the scenario with a few WTs, they might not be negligible. Combined with short-term and long-term wind variations, low frequency power oscillations from the WF increase the burden of synchronous machines' GTs for controlling the frequency, which can lead to higher wear and tear of turbine governors. It is therefore important to investigate the possibilities and consequences of increasingly shifting primary power reserves from the slower GTs to the faster converter-interfaced ESS.

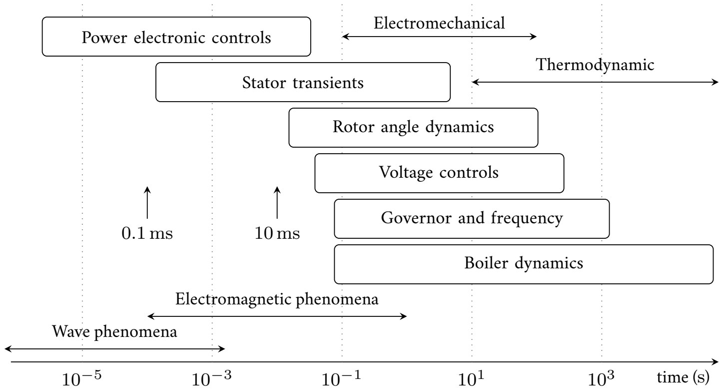

FIGURE 2.4 Time scale of phenomena in electrical systems, adapted from [8].

© Daniel Mota 2023 | Redrawn and recomposed from Publication I | Source code information at Part III.

2.4 THE ISOLATED GRID OF THE STUDY CASE

Figure 2.5 shows a simplified single line diagram of the study case used in this dissertation, which is based on an existing oil and gas (O&G) platform in the North Sea expected to be connected to a floating WF.

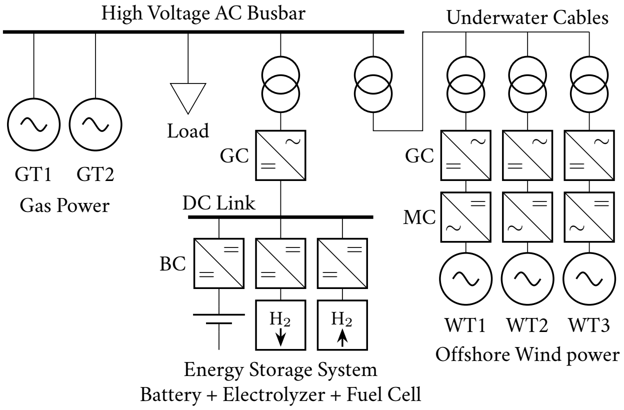

FIGURE 2.5 Simplified single-line diagram of the study case.

© Daniel Mota 2023 | Redrawn and recomposed from Publication I | Source code information at Part III.

Variants of this study case were used throughout this PhD-research. These are available at the following repositories.

- Repository I: DIgSILENT PowerFactory 2020 SP2A models used for Publication I. These models are a version featuring pulse-width modulation (PWM) switching in the grid converters (GCs) of the ESS and WTs of the models in Repository II.

- Repository II: MathWorks MATLAB Simulink R2016a models used in Publication II with averaged representations [10] for all the PECs (no PWM switching). Notice that, despite their numbering, which fits the sequence of chapters of this dissertation, Repository II was published earlier than Repository I.
- Repository V: MathWorks MATLAB Simulink R2018a and DIgSILENT PowerFactory 2020 SP2A versions of the model in Repository I. The models in Repository V include an aggregated constant power load representing part of the platform's electric load and a fast converter-interfaced flexible load representing the water injection system. All PECs are represented with averaged models. In addition to that, Python scripts for controlling the PowerFactory model and performing automatic eigenvalue analysis are also available in this repository.

In the following subsections, the main devices of this grid will be briefly presented.

2.4.1 Synchronous Generation

The study case platform illustrated in figure 2.5 operates isolated from the continent and is fed, in normal operation, by two 35.2 MW aero-derivative single-cycle GTs. The gas turbines are connected to 4-pole synchronous generators of 44 MVA each directly connected to the platform's main high-voltage (HV) busbar at 11 kV. Real-life examples of such turbines and generators can be found at [11, 12], respectively. One single 35.2 MW GTs is not able to feed the platform as the average electrical load of the study case platform is 44 MW. Additionally, the thermal load of the industrial processes [13] requires one of the GTs to be in operation at all times. Therefore, this platform always operates with at least one GT, which provides a kinetic energy buffer for stabilizing the frequency of the grid.

Due to safety concerns, the prospective scenario investigated in Publications I to III and VI assumed that two GTs would still operate simultaneously even with full production from the WF. The premise of two GTs operating at all times is kept in this dissertation. The presence of the GTs also guarantees that the grid is "formed" [14]. Therefore, the energy storage system grid converter (ESSGC) operates in grid following mode.

The angular frequency of the synchronous generators is controlled by turbine governors. The stator voltage is controlled by excitation systems. The interested reader may find more information on the modeling of generators in [15], turbine governors in [16], excitation systems in [17], and tuning techniques for proportional, integral, and derivative (PID) regulators in [18].

2.4.2 Wind Farm

Riboldi *et al.* [19] suggested in a techno-economical study that a reduction of approximately 30 % of the annual CO_2 emissions can be achieved if the study-case platform were connected to a 12 MW floating offshore WF. The reduction, however, depended on the installation of a centralized hybrid ESS with 4 MW proton exchange membrane (PEM) fuel cells and 6 MW PEM electrolyzers. In Publication II, a set of three 4 MW WTs was used as a prospective scenario for proposing a sizing methodology for the platform's hybrid ESS. This same scenario was used in Publications I, III, and VI and is, therefore, adopted in this dissertation.

Figure 2.5 shows the WTs with their HV underwater cables forming the collector system that feeds the platform. To minimize losses, the collector system operates at 33 kV. The three WTs employ full-power back-to-back PECs that isolate the mechanical oscillation modes on the turbine side from the electrical oscillation modes on the platform's grid side [20]. This fact allows for a simplified representation of the wind turbine units in the study case model. Different strategies for modelling the WTs were used in Publications I, II, and VI. These will be detailed later in chapter 3 and chapter 5.

2.4.3 Energy Storage System

As suggested by Riboldi *et al.* [19] and illustrated in figure 2.5, a hybrid ESS is employed in the study case for counteracting the effects of wind variability and intermittency. A fast energy storage device (ESD) composed of a battery and a dc/dc converter provides reserves for the short term wind and load variations. The main purpose of the battery is to reduce the burden on the turbine governors due to fast frequency regulation. The paired electrolyzer and fuel cell with their own dc/dc converters form one single ESD. Energy is stored as hydrogen when there is wind overproduction. Hydrogen is transformed into electricity when there is little production from the WF. The control structure chosen for the converters of the ESS will be detailed in chapters 3 and 4.

2.4.4 Loads

The local loads in figure 2.5 represent a mix of CPL and CZL that can be changed in steps for testing the dynamic characteristics of the model. A substantial part of the loads are interfaced to the grid via PECs. The level of details with which these loads are modeled varies throughout this dissertation and is explained in greater detail in each chapter. It is, nonetheless, important to remark that the platform's water injection system is assumed to operate as fast converter-interfaced flexible loads that can provide primary power reserves. The operation of the water injection system in conjunction with wind power has, for instance, been assessed by [21–24].

2.5 NEXT STEPS

After this brief presentation of key concepts such as stability in electric grids, a simplified rotating mass model, time scales of the control phenomena, and an introduction to the study-case employed throughout this dissertation, the next chapter studies a control structure for providing inertial, primary, and secondary power reserves for frequency regulation from converter-interfaced ESSs.

2.6 REFERENCES

[1] Prabha Kundur, *et al.* Definition and Classification of Power System Stability IEEE/CIGRE Joint Task Force on Stability Terms and Definitions. *IEEE Transactions on Power Systems* **19** (3) (August 2004). ISSN 1558-0679. DOI: 10.1109/TPWRS.2004.825981. Cited on page(s) 17.

[2] Federico Milano, Florian Dörfler, Gabriela Hug, David J. Hill, and Gregor Verbič. Foundations and Challenges of Low-Inertia Systems (Invited Paper). In *2018 Power Systems Computation Conference (PSCC)* Dublin, Ireland (June 2018). IEEE. DOI: 10.23919/PSCC.2018.8450880. Cited on page(s) 18, 21.

[3] Mostafa Farrokhabadi, *et al.* Microgrid Stability Definitions, Analysis, and Examples. *IEEE Transactions on Power Systems* **35** (1) (January 2020). ISSN 1558-0679. DOI: 10.1109/TPWRS.2019.2925703. Cited on page(s) 18.

[4] Nikos Hatziargyriou, *et al.* Definition and Classification of Power System Stability – Revisited & Extended. *IEEE Transactions on Power Systems* **36** (4), 3271–3281 (July 2021). ISSN 1558-0679. DOI: 10.1109/TPWRS.2020.3041774. Cited on page(s) 18, 21.

[5] Erik Ela, Michael Milligan, and Brendan Kirby. Operating Reserves and Variable Generation. Technical Report NREL/TP-5500-51978 National Renewable Energy Lab. (NREL) Golden, Colorado, USA (August 2011). DOI 10.2172/1023095. Cited on page(s) 19.

[6] EU. Establishing a Guideline on Electricity Transmission System Operation. Commission regulation (EU) 2017/1485. European Union (2017). URL https://eur-lex.europa.eu/eli/reg/2017/1485/oj, accessed on 2023-01-09. Cited on page(s) 20.

[7] ENTSO-E. Fast Frequency Reserve – Solution to the Nordic Inertia Challenge. Summary Report ENTSO-E / Statnett Oslo, Norway (December 2019). URL https://www.statnett.no/globalassets/for-aktorer-i-kraftsystemet/utvikling-av-kraftsystemet/nordisk-frekvensstabilitet/ffr-stakeholder-report_13122019.pdf, accessed on 2023-01-09. Cited on page(s) 21.

[8] N. Hatziargyriou, *et al.* Stability Definitions and Characterization of Dynamic Behavior in Systems with High Penetration of Power Electronic Interfaced Technologies, TR-77 — Definition and Classification of Power System Stability Revisited. Technical Report PES-TR77 IEEE Power & Energy Society (May 2020). URL: resourcecenter.ieee-pes.org/technical-publications/technical-reports/PES_TP_TR77_PSDP_stability_051320.html, accessed on 2023-01-10. Cited on page(s) 22.

[9] T. J. Larsen and T. D. Hanson. A Method to Avoid Negative Damped Low Frequent Tower Vibrations for a Floating, Pitch Controlled Wind Turbine. *Journal of Physics: Conference Series* **75** (July 2007). DOI: 10.1088/1742-6596/75/1/012073. Cited on page(s) 21.

[10] Seddik Bacha, Iulian Munteanu, and Antoneta Iulinana Bratcu. Power Electronic Converters Modelling and Control with Case Studies. Advanced Textbooks in Control and Signal Process-

ing. Springer London, England (2013). ISBN 978-1-4471-5478-5. URL https://link.springer.com/book/10.1007/978-1-4471-5478-5, accessed on 2023-06-09. Cited on page(s) 23.

[11] GE. LM2500 aeroderivative gas turbine 50/60Hz. Product specifications GEA32937B General Electric Company Boston, MA, USA (March 2022). URL https://www.ge.com/content/dam/gepower-new/global/en_US/downloads/gas-new-site/products/gas-turbines/lm2500-fact-sheet-product-specifications.pdf, accessed on 2023-02-17. Cited on page(s) 23.

[12] ABB. High Power 4-pole Generators from 50 to 85 MVA for Mid-Size Steam and Gas Turbines. Product Note 9AKK106497 ABB Zürich, Switzerland (February 2015). URL https://library.abb.com/d/9AKK106497, accessed on 2023-02-17. Cited on page(s) 23.

[13] Håvard Devold. Oil and Gas Production Handbook, an Introduction to Oil and Gas Production, Transport, Refining and Petrochemical Industry. ABB Oil and Gas Oslo, Norway 3.0 edition (2013). ISBN 978-82-997886-3-2. URL https://library.e.abb.com/public/34d5b70e18f7d6c8c1257be500438ac3/Oil%20and%20gas%20production%20handbook%20ed3x0_web.pdf, accessed on 2023-02-17. Cited on page(s) 23.

[14] Frede Blaabjerg, Remus Teodorescu, Marco Liserre, and Adrian V. Timbus. Overview of Control and Grid Synchronization for Distributed Power Generation Systems. *IEEE Transactions on Industrial Electronics* **53** (5), 1398–1409 (October 2006). ISSN 1557-9948. DOI 10.1109/TIE.2006.881997. Cited on page(s) 23.

[15] Prabha Kundur, Neil J. Balu, and Mark G. Lauby. Power System Stability and Control. EPRI power system engineering series. McGraw-Hill New York, USA (1994). ISBN 978-0-07-035958-1. Cited on page(s) 23.

[16] Pouyan Pourbeik, *et al.* Dynamic Models for Turbine-Governors in Power System Studies. Technical Report PES-TR1 IEEE Power & Energy Society (January 2013). URL https://site.ieee.org/fw-pes/files/2013/01/PES_TR1.pdf, accessed on 2023-02-17. Cited on page(s) 23.

[17] IEEE Std 421.5-2016. IEEE Recommended Practice for Excitation System Models for Power System Stability Studies. IEEE Power & Energy Society New York, NY, USA (August 2016). DOI 10.1109/IEEESTD.2016.7553421. Cited on page(s) 23.

[18] Friederich Fröhr and Fritz Orttenburger. Introduction to Electronic Control Engineering. Siemens Aktiengesellschaft; Heyden & Son LTD. Berlin and München, Germany; London, UK (1982). ISBN 0-85501-290-0. Cited on page(s) 23.

[19] Luca Riboldi, Erick F. Alves, Marcin Pilarczyk, Elisabetta Tedeschi, and Lars O. Nord. Optimal Design of a Hybrid Energy System for the Supply of Clean and Stable Energy to Offshore Installations. *Frontiers in Energy Research* **8**, 346 (December 2020). ISSN 2296-598X. doi: 10.3389/fenrg.2020.607284. DOI 10.3389/fenrg.2020.607284. Cited on page(s) 24.

[20] Linash P. Kunjumuhammed, Bikash C. Pal, Colin Oates, and Kevin J. Dyke. Electrical Oscillations in Wind Farm Systems: Analysis and Insight Based on Detailed Modeling. *IEEE Transactions on Sustainable Energy* 7 (1), 51–62 (January 2016). ISSN 1949-3037. DOI 10.1109/TSTE.2015.2472476. Cited on page(s) 24.

[21] Jesus Silva, Muhammad Jafar, A Marichalar, and Elisabetta Tedeschi. Integration of Wind Power to Supply Water Injection Systems as Controllable Loads in Offshore Oil and Gas Facilities. In *Offshore Energy & Storage Symposium (OSES 2016)* Malta (July 2016). URL https://www.researchgate.net/publication/312134034, accessed on 2023-02-17. Cited on page(s) 25.

[22] Santiago Sanchez, Elisabetta Tedeschi, Jesus Silva, Muhammad Jafar, and Alexandra Marichalar. Smart load management of water injection systems in offshore oil and gas platforms integrating wind power. *IET Renewable Power Generation* **11** (9), 1153–1162 (7 2017). ISSN 1752-1416, 1752-1424. DOI 10.1049/iet-rpg.2016.0989. Cited on page(s) 25.

[23] DNV. WIN WIN joint industry project: Wind-powered water injection. Public report DNV GL AS Høvik, Norway (May 2019). URL https://www.dnv.com/news/making-wind-powered-water-injection-a-commercial-reality-148049, accessed on 2023-02-17. Cited on page(s) 25.

[24] Khalid S. Khan, Isabelle V. M. dos Santos, Guilherme B. dos Santos, Maurício B. C. Salles, and

Renato M. Monaro. Evaluation of deep-water floating wind turbine to power an isolated water injection system. In *ASME 2021 3rd International Offshore Wind Technical Conference*. ASME (April 2021). DOI 10.1115/IOWTC2021-3522. Cited on page(s) 25.

CHAPTER 3

Control Structures for Converter-Interfaced Energy Storage Systems

RESEARCH GOALS AND CONTRIBUTIONS TO THE SCIENTIFIC LITERATURE

Control structures for isolated grids in which traditional synchronous generation is complemented by intermittent renewable energy sources (RES) are proposed in this chapter, which is tied to Research Goal II and aims to answer Research Question II. The focus is on the outer control loops of a converter-interfaced energy storage system (ESS) that provides frequency control support for an isolated grid. Contribution I to the scientific literature is presented in this chapter, which compiles the contents of Publication I.

Power and energy demands vary during the different frequency control phases. Secondary reserves require the largest energy storage, followed by primary reserves and inertial support. However, inertial support demands the steepest rates of change of power, followed by primary and secondary reserves. Today's energy storage solutions vary considerably in peak power capacity, rate of change of power limitations, and energy density. There is no one-size-fits-all energy storage device (ESD) that is able to store the necessary energy, provide the required peak power, and change the power as fast as required to provide frequency control support during all phases. Therefore, hybrid solutions combining different types of ESDs are becoming a preferred choice in transportation and power system applications [1].

Figure 3.1 illustrates the centralized hybrid ESS employed in study cases by Publications I, II, and VI to counteract the negative effects of wind intermittency in the stability and frequency control of an oil and gas (O&G) platform expected to be connected to an offshore wind farm (WF). The ESS combines the specific characteristics of different ESDs. The electrolyzer and fuel cell produce or consume hydrogen for providing the slower secondary reserves for frequency control. The battery acts as a fast ESD for the short-term variations supplying inertial and primary reserves. The ESDs operate in dc and are interfaced to the grid via a bidirectional ac-dc converter. An inductive-capacitive-inductive (LCL) filter stage connects the ESS to the platform's main high-voltage (HV) busbar. The step-up transformer serves as the grid-side inductance of the LCL filter. Although not listed among the main contributions of this dissertation, it is worth remarking that an analytical sizing method for hybrid ESSs and a literature review on designing the LCL filter were presented in Publication II.

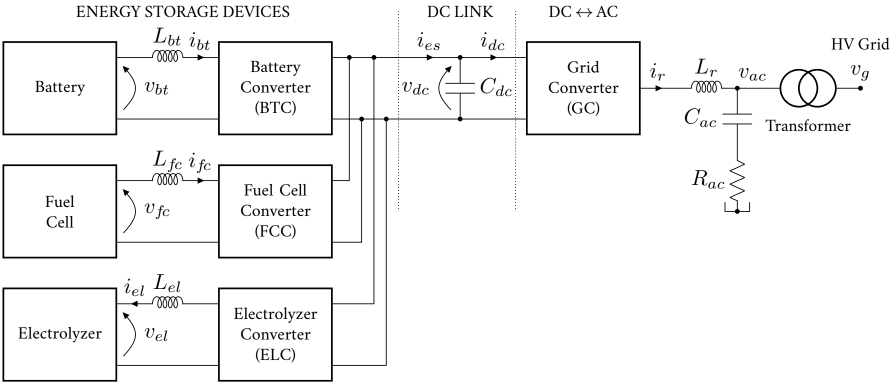

FIGURE 3.1 Schematic diagram of a hybrid ESS.

© Daniel Mota 2023 | Redrawn and recomposed from Publication I | Source code information at Part III.

The power consumed by the industrial processes and the power supplied to the study case's grid must be continuously equalized. Albeit in a different time scale, the ESS in figure 3.1 features an analogous power balancing problem. The power provided by the ESDs and the power extracted from the dc-link by the grid converter (GC) must be continuously equalized. Therefore, a set of control structures for this hybrid ESS must take both power balancing problems into consideration. In this chapter, the control strategy described in Publication I for providing inertial, primary, and secondary frequency reserves with a hybrid ESS in an isolated electric grid is presented. This strategy is based on established proportional, integral, and derivative (PID) techniques and does not rely on fast communication links between different ESDs or the platform's power management system (PMS). It also provides the means for the ESS to deliver voltage and reactive power support.

The chapter is organized as follows: the power balancing problem within the ESS is discussed in section 3.1; the control structures for the hybrid ESS are presented in section 3.2; the dynamic performance of these structures for supporting the frequency control of the study case's isolated grid is analyzed in section 3.3; a discussion is made in section 3.4; and, finally, the concluding remarks are listed in section 3.5.

3.1 POWER BALANCING WITHIN THE ESS

At the core of the ESS shown in figure 3.1, in the dc link, there is a capacitor bank represented by C_{dc}. In a way similar to the rotating masses of the ac grid, the capacitor bank maintains an energy buffer given by equation (3.1). The amount of energy stored in the dc link divided by the GC's rated apparent power will later be used for scaling purposes in chapter 6.

$$E = \frac{C_{dc}\, {v_{dc}}^2}{2}. \tag{3.1}$$

Variations in the dc-link voltage (v_{dc}) indicate a power imbalance between the ESDs and the GC. In other words, if the power supplied by the ESDs and the power transferred from the dc link to the ac grid by the GC are in equilibrium, the voltage at C_{dc} is constant. If the net power supplied to the dc link is positive, v_{dc} increases in conjunction with the energy E. Conversely, if the net power is negative, v_{dc} decreases. Assuming that losses on the converters and dc link of the ESS are negligible, the dynamic behavior of v_{dc} described in terms of the net current provided by the ESDs to the dc-link (i_{es}) and the dc current entering the GC (i_{dc}) is

$$\underbrace{C_{dc}\frac{\mathrm{d}v_{dc}}{\mathrm{d}t}}_{\text{Buffer}} = \underbrace{i_{es}}_{\text{from the ESDs}} - \underbrace{i_{dc}}_{\text{to the ac side}}. \tag{3.2}$$

Like a turbine governor controlling the ac grid frequency, the ESS features an internal dc voltage regulator acting on either the ESD or GC power flow to constrain v_{dc} variations. Naturally, this dc voltage regulator acts in a fraction of the time scales for ac grid frequency control, see section 2.3. Failure to control v_{dc} results in a voltage collapse of the ESS or significant power oscillations. However, note that the larger the capacitance C_{dc}, the larger the energy buffer E and the more forgiving the system is to imbalances between the ESDs and GC. Therefore, sizing C_{dc} becomes a techno-economical task that has consequences to the tuning and dynamics of the dc voltage controller. Although considered outside the scope of this dissertation, this issue is discussed in the algebraic method for sizing the ESS proposed in Publication II.

In the next sections, the ESS control structures for ac grid frequency support and internal v_{dc} regulator described in Publication I are presented.

3.2 ESS CONTROL STRUCTURE

The main control structures employed in the battery converter (BC) and GC of the hybrid ESS shown in figure 3.1 are presented in this section. Notice that the term battery is used for ESDs in general in this section. The concepts presented herein are also applicable to fuel cells and electrolyzers with only minor adaptations. It is important to emphasize that an approach based on traditional PID controllers is adopted as those are well-proven and usually available in commercial products. Moreover, a structure that does not rely on a fast communication link between the different converters of the ESS or with the platform's PMS is chosen. Finally, all power electronic converters (PECs) of the ESS operate with a pulse-width modulation (PWM) technique [2] and use cascaded control structures with a fast inner current control loop and a slower outer loop. The faster inner current control of the ESS converters will be further discussed in chapter 4. The PWM techniques, however, are considered outside the scope of this dissertation.

The quantities controlled by the outer loops of the PECs in figure 3.1 are the grid frequency (f), the dc-link voltage (v_{dc}), and the ac voltage at the middle of the LCL filter (v_{ac}). Each of these loops will be described in the following subsections.

3.2.1 Grid Frequency Control

Figure 3.2 shows the control structure for the ac frequency support provided by the ESDs of the ESS. This structure uses the measurement of the grid frequency $\widehat{f}$ to generate the reference $\overset{*}{i}_{bt}$ for the BC inner current control loop. Note that all measurements (denoted as $\widehat{x}$) in the control structures are assumed to have been properly conditioned, filtered, and scaled.

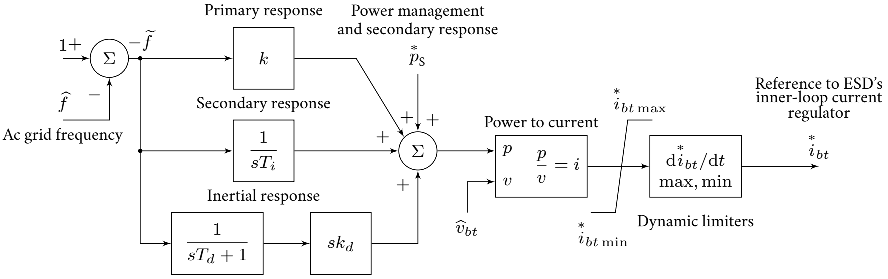

FIGURE 3.2 Grid frequency control support with the ESS.

© Daniel Mota 2023 | Redrawn and recomposed from Publication I | Source code information at Part III.

The structure in figure 3.2 is divided into three branches that correspond to the different phases of the frequency control of ac grids.

Primary response — This branch features a proportional regulator with a gain k that defines the active power change for a given frequency deviation. This gain is the equivalent of the inverse of the frequency droop. The higher the gain k, the higher the contribution of the battery for a given grid frequency deviation.

Secondary response — This branch contains an integrator with a parameter T_i. If the battery is the only device in the system supplying secondary reserves, the integral branch can be enabled, and it will work towards removing the steady-state error left by the droop based control of the primary response. However, if a turbogenerator (GT) or another ESD is also a source of secondary reserves, the T_i

branch is disabled. Then, the input $\overset{*}{p}_S$ is used by the PMS to coordinate the delivery of reserves between GTs and ESDs. Notice that the input $\overset{*}{p}_S$ can also be used for controlling the state of charge (SOC) of the battery. Although not represented in figure 3.2, this branch contains anti-windup features that block the integration in case the minimum and maximum output values are achieved. See more on anti-windup in appendix C.

Inertial response — This is the derivative branch with a gain k_d that establishes the active power response to a given time derivative of the grid frequency. Contrary to the "real" inertial response provided by rotating masses, the inertia emulation from the battery relies on a frequency measurement that is inherently noisy. Therefore, a low-pass filter (LPF) stage with a time constant T_d is necessary in the derivative branch. The dynamic contribution of this branch will be analyzed in section 3.3.1.

The minimum and maximum values ($\overset{*}{i}_{bt\max}$ and $\overset{*}{i}_{bt\min}$) in figure 3.2 provide the means for dynamically limiting the operation based on SOC, temperature, or other conditions of the ESD. The rate-of-change limiters are not necessarily static nor symmetric. Moreover, the power-to-current block compensates for variations in the battery voltage. It turns the BC into a constant power device (CPD). Due to the possible detrimental effects of this nonlinear feature, it was not implemented for Publication I and is not present in the results shown in section 3.3. It will be, nonetheless, activated for the results presented later in chapter 5.

3.2.2 Dc Voltage Control

The energy storage system grid converter (ESSGC) ensures, indirectly by controlling the dc-link voltage, that the net power provided by the ESDs is transferred to the ac grid. Figure 3.3 shows the dc-voltage control loop of the GC, which is performed with a proportional and integral (PI) regulator. More information on the structure of the PI regulators used throughout this dissertation with their anti-windup features is available at the appendix C. The measured value of the dc-link voltage in pu is subtracted by one and is used as input to a PI regulator.

Given the conventions adopted in this work, the dc-voltage PI regulator implements the following logic with the reference $\overset{*}{i}_{rd}$, which is always kept within minimum and maximum limits:

- when $\widehat{v}_{dc} > 1$ pu, then $\overset{*}{i}_{rd}$ increases, resulting in more power transferred from the dc to the ac side of the converter;
- when $\widehat{v}_{dc} < 1$ pu, then $\overset{*}{i}_{rd}$ decreases.

For improving the dc-voltage dynamics, a feed-forward path ($\widehat{i}_{es}$) is employed for the net current provided by the ESDs. Notice that this feed-forwarding scheme does not require a fast communication link between the converter of the ESDs and the GC. If a dc-current measurement transducer is connected at the electrical point marked by i_{es} in figure 3.1 and interfaced with the GC controller, then no direct communication with the different ESDs is necessary. The output of the PI regulator added to the feed-forward component $\widehat{i}_{es}$ becomes the reference $\overset{*}{i}_{rd}$ in the direct axis of the rotating reference frame (RRF). This reference is forwarded to the GC's fast inner current controller. See appendix A for information on the reference frames and transformations adopted in this dissertation.

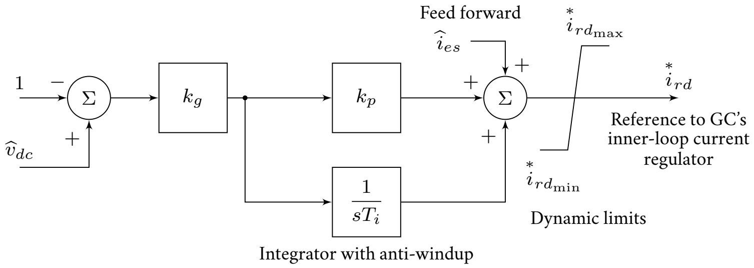

FIGURE 3.3 Control of the dc-link voltage of the ESS. Although implemented, the anti-windup features are not represented in this block diagram for clarity purposes.

© Daniel Mota 2023 | Redrawn and recomposed from Publication I | Source code information at Part III.

It is worth mentioning that the performance of current controllers operating in RRFs is affected by unbalanced three-phase loads, i.e., when the loads on each of the phases of the system are considerably different. Within the scope of this dissertation, a strategy known as dual RRF current controller has been investigated. This strategy relies on splitting three-phase measurements into two components, one called positive sequence and the other negative sequence. A literature review and a comparison of controllers with different sequence separation strategies was done in Publication III. A method for sequence separation applied directly to the RRF was described in Publication IV. The contents of these two publications are compiled in chapter 4.

3.2.3 *Ac Voltage Control*

The root-mean-square (RMS) value of the three-phase voltage at the center of the LCL filter in figure 3.1 (v_{ac}) is controlled by the PI regulator shown in figure 3.4. See more on the anti-windup features of the PI in appendix C. The measured value $\widehat{v}_{ac}$ is subtracted by the reference $\overset{*}{v}_{ac}$, which can be set to a fixed value, for instance, 1 pu, or can be controlled by a reactive power outer loop. Given the conventions adopted in this work, the ac-voltage PI regulator implements the following logic:

- when $\widehat{v}_{ac} > \overset{*}{v}_{ac}$, then $\overset{*}{i}_{rq}$ increases, resulting in more reactive power supplied by the converter;

- when $\widehat{v}_{ac} < \overset{*}{v}_{ac}$, then $\overset{*}{i}_{rq}$ decreases.

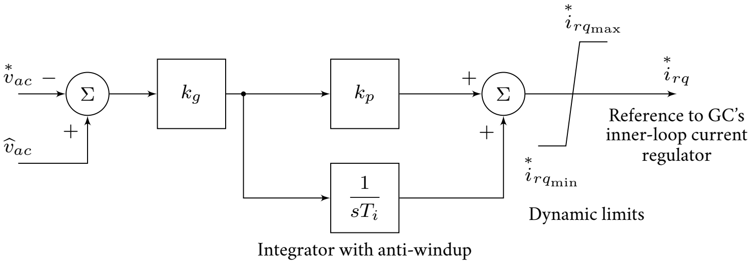

FIGURE 3.4 Control of the ac voltage in the ESS.

© Daniel Mota 2023 | Source code information at Part III.

In chapter 5, the ac voltage control outer loop uses as feedback the amplitude of the positive sequence content of the voltage. Sequence isolation methods will later be discussed in chapter 4.

3.2.4 Reactive Power Control

The GCs of the isolated grid under study in this work have, within their capacity limits, control over the RMS value of the voltage in the middle of their LCL filters (marked with v_{ac} in figure 3.1). The reactive power exchange through the converter transformer is dictated mainly by the difference in the amplitudes of v_{ac} and v_g. Even without a direct measurement of v_g in figure 3.1, the reactive power exchange can be controlled by increasing or decreasing the reference voltage $\overset{*}{v}_{ac}$ in figure 3.4. This can be implemented by a PI regulator placed in an outer loop.

In chapter 5, the wind turbine grid converters (WTGCs) run in reactive power control mode, whereas the ESSGC runs only in ac voltage control mode. However, for the results shown in this chapter section 3.3, all WTGCs of the study-case grid run in voltage control model, whereas the ESSGC runs with its reference $\overset{*}{i}_{rq}$ forced to zero, providing no voltage nor reactive power support.

3.3 DYNAMIC BEHAVIOUR OF ESS SUPPORTING AN ISOLATED GRID

In this section, an analysis of the dynamic behaviour of a hybrid ESS equipped with the control structures described in section 3.2 is presented. Results of computer simulations illustrate the discussion. The simulation models were originally developed in MathWorks MATLAB Simulink R2016a for Publication II (Repository II). However, for Publication I and for this chapter, these original models were re-written in DIgSILENT PowerFactory 2020 SP2A (Repository I).

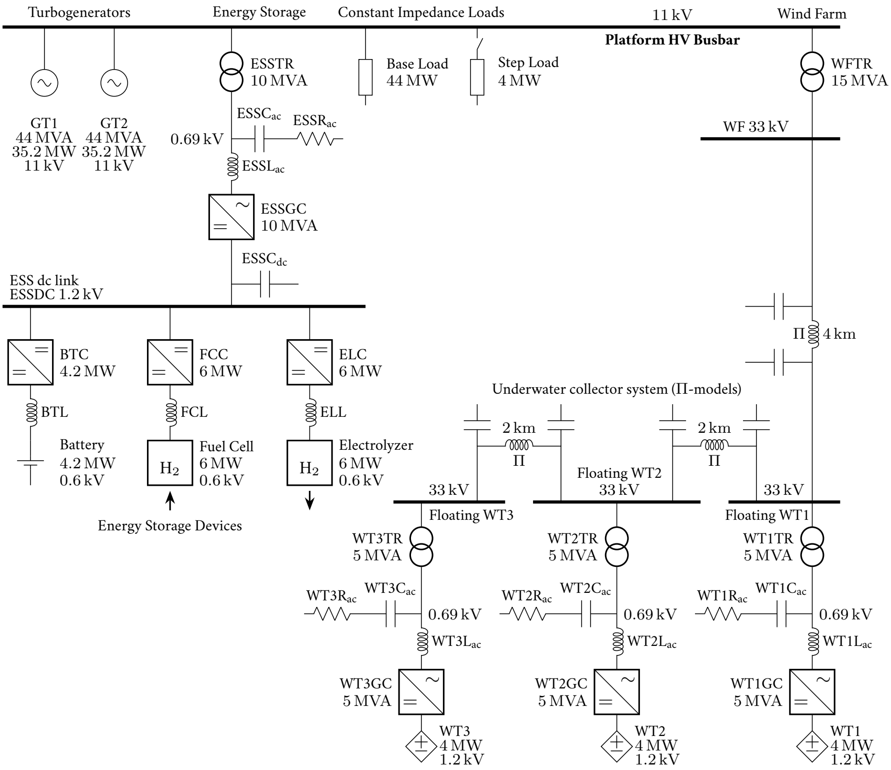

FIGURE 3.5 Single line diagram of the study case used to evaluate the dynamic behavior of a hybrid ESS connected to an isolated grid supplied by synchronous and non-synchronous generation.

© Daniel Mota 2023 | Source code information at Part III.

Figure 3.5 shows a single-line diagram of the study case analyzed in Publication I and presented in this chapter. Two gas-powered GTs feed the platform's main HV busbar. The platform's power consumers are modeled as two constant impedance loads (CZLs), one for the base load and one for a "step load". Three type 4 [3] offshore floating wind turbines (WTs) are connected to the main busbar via an HV underwater collector system. PowerFactory's detailed model with PWM switching with built-in fast current controllers in the RRF [4] are used for the GCs of the ESS and WTs. A simplified average model of the ESD's dc/dc converters is used. For details on PECs modeling strategies, see [5]. The converters' outer loops were manually programmed in PowerFactory.

Three cases are used for analysis and discussion in this chapter:

Case 1 — ESS is connected but does not provide support power reserves.

Case 2 — ESS provides primary reserves;

Case 3 — ESS provides inertial and primary reserves.

For all three cases, the following conditions apply. The base load is 44 MW and, at instant $t = 1$ s, the step load of 4 MW is connected to the platform's HV busbar. The turbine governors (GT1,GT2) are represented by a GAST model [6] and run in speed control with a droop of 4.7 %. The excitation systems (GT1, GT2) are represented by an AC1C model [7] and control the HV busbar voltage. Each of the wind turbine converters (WT1GC, WT2GC, WT3GC) supplies a constant power of 4 MW and regulates the voltage at the 690 V side of the converter transformers (WT1TR, WT2TR, WT3TR) to 1 pu. The ac/dc converter of the ESS (ESSGC) runs in dc voltage control mode, as illustrated in figure 3.3. The ac voltage support provided by the ESSGC is forced to zero, i.e., with $\overset{*}{i}_{rq} = 0$ in figure 3.4. The fuel cell converter (FCC) is set to supply a slow secondary response to frequency variations. This response, however, is not significant within the time scales analyzed in this chapter.

3.3.1 Frequency Support Provided by the ESS

Figure 3.6 shows the responses to the connection of the 4 MW step load at $t = 1$ s. The responses for case 1 are shown in solid green, the ones for case 2 in solid red, and the ones for case 3 in solid blue. Notice that, as the loads are modeled as CZLs, the total power consumed (figure 3.6a) varies with the platform's main busbar voltage (figure 3.6f). It is also possible to notice that there is room for improvement if the ac voltage support were to be provided by the ESSGC. The power supplied by the WTs that arrives at the platform's busbar is also affected by the voltage variations caused by the step load, as shown in figure 3.6e. The following remarks are worth making regarding the differences in the dynamic responses of the cases 1 to 3 in figures 3.6b, c, and d.

- Case 1 (solid green): the GTs supply the totality of the extra power demanded by step load. The generator speed drops after $t = 1$ s and reaches the minimum, known as nadir, at $t = 1.8$ s. The primary response of the GTs, i.e., the droop of 4.7 %, brings the generator speed up to 49.85 Hz. The behaviour of the generator speed is noticeably oscillatory but still damped.
- Case 2 (solid red): the GTs and the ESS share the burden of providing the extra power to the step load. The primary frequency control support provided by the ESS improves the nadir, which happens at $t = 1.6$ s. The primary responses of the GTs and ESS together bring the frequency up to 49.9 Hz.
- Case 3 (solid blue): the GTs and the ESS share the extra power demanded by the step load. The fast response of the ESS due to the derivative term manages to improve the nadir. The behavior of the generator speed is considerably less oscillatory than the ones observed for cases 1 and 2.

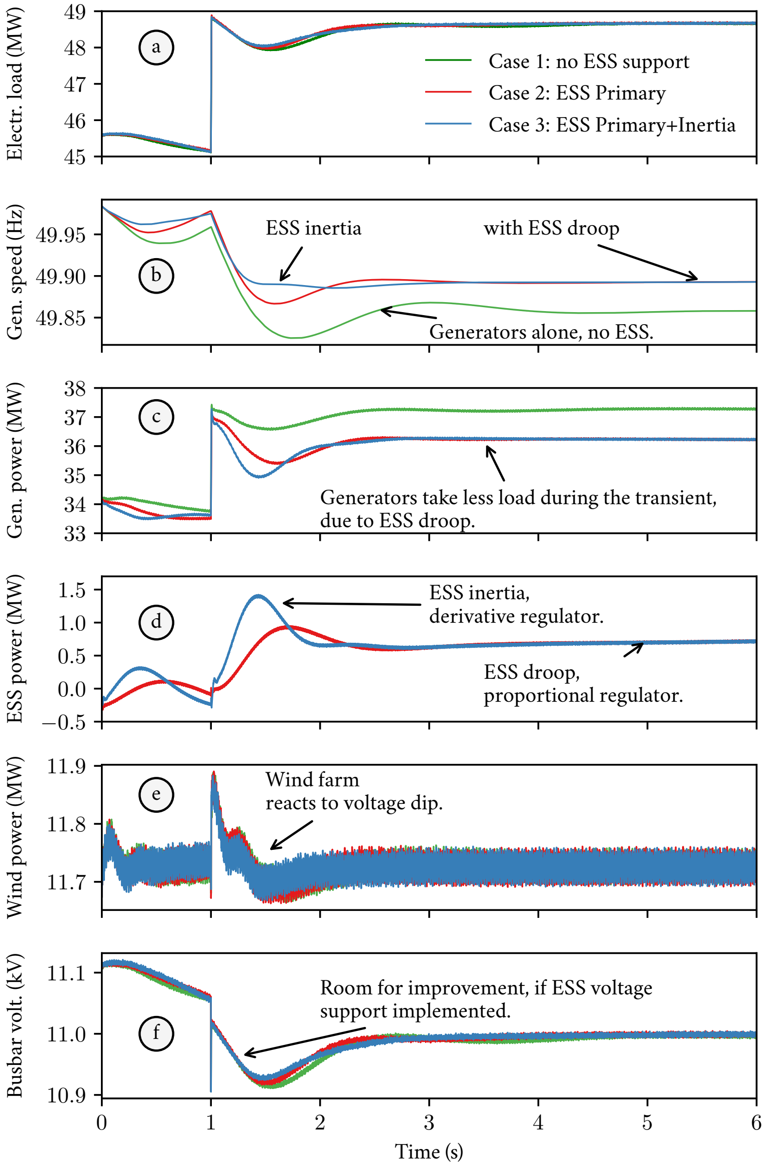

FIGURE 3.6 Dynamic response after the connection of a 4 MW step load to the platform's main busbar. Case 1 in green, case 2 in red, and case 3 in blue.

3.3.2 Dc Voltage Control within the ESS

Figure 3.7 shows the effect on the dc voltage of operating with or without the feed-forward scheme during the transient with ESS inertial and primary support (case 3). It is clear that the dc voltage control becomes worse without the feed-forward scheme. The differences are, however, considerably small. Nevertheless, the lower the capacitance connected to the dc link, the higher the dc voltage variations will be during transients. Therefore, the improved dynamic provided by the feed-forward can be necessary when a reduction of the capacitance bank is desirable.

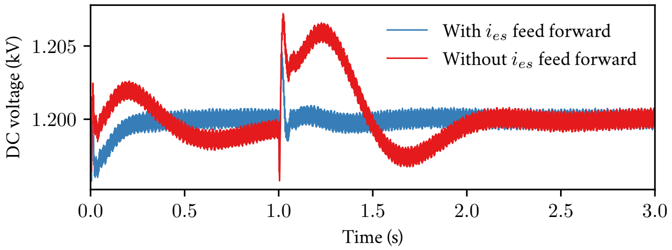

FIGURE 3.7 Influence of the feed-forwarding i_{es} in the control of the ESS dc-link voltage. Case 3 with inertial and primary support provided by the ESS. The response with feed-forwarding scheme active is shown in blue, and inactive is shown in red.

© Daniel Mota 2023 | Redrawn and recomposed from Publication I | Source code information at Part III.

3.3.3 Frequency as a Global Variable

The theoretical framework adopted in this dissertation assumes that the electrical frequency across the whole platform and the mechanical rotating speed of the GTs can be treated as one unique variable. A comparison is made for case 3 to test the validity of the “global frequency” assumption. Figure 3.8 shows, in Hz, the electrical frequency at the low-voltage (LV)-side of the ESS transformer (ESS 690V) and at the LV-side of the WT3 transformer (WT3 690V). The WT number 3 is the one farthest from the platform. The electrical measurement is performed with PowerFactory’s built-in phase-locked loops (PLLs) [4, 8]. The mechanical rotating speeds of the GTs, scaled to match 50 Hz, are also shown. They are almost identical to each other. There are, however, small differences between the measured electrical frequencies and the mechanical speeds right after the step load is applied. The sudden change in the voltage profile at the platform’s HV busbar (not shown in Figure 3.8 but visible in figure 3.6f) is detected by the PLL at the LV-side of the ESS transformer as a small but sharp frequency dip. For WT3, which is farther from the transient source, the measured electrical frequency features a smoother dip. The derivative part of the frequency support provided by fast ESD might respond poorly to these dips in the electrical frequency measured with PLLs.

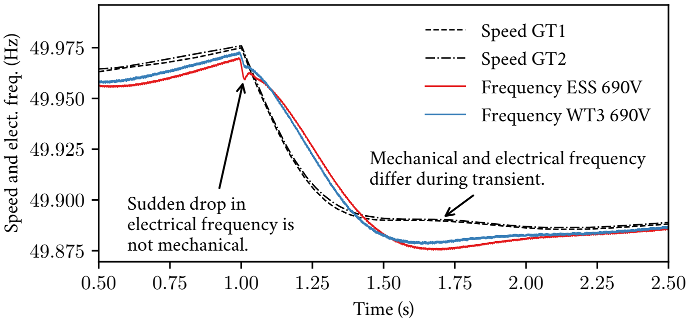

FIGURE 3.8 Case 3, mechanical rotating speed and electrical frequency. To allow the comparison between mechanical and electrical quantities, the mechanical rotation of the GTs has been scaled so 1800 min^{-1} equals 50 Hz.

© Daniel Mota 2023 | Redrawn and recomposed from Publication I | Source code information at Part III.

3.4 DISCUSSION

A centralized hybrid ESS can be used to alleviate the negative consequences of connecting an intermittent energy source to an isolated electrical system. However, this concept poses technological challenges that were identified and discussed in this chapter. Among them, the following challenges can be highlighted.

- **Dc voltage**: the feed-forward scheme described in this chapter may play an important role in a future optimization of the dc-link capacitor bank sizing and, consequently, in the ESSGC cost, weight, and space requirements. However, such an analysis is considered outside the scope of this dissertation.
- **Ac voltage**: the ESS is capable of providing reactive power support reducing voltage sags and swells during transients. Nevertheless, fast interactions between the ESS converters, other large PECs in the platform, and WTs were not assessed in detail in this chapter. This topic will be addressed in chapter 5.
- **Primary reserves**: in the scenario analysed in this chapter, both the GTs and the ESS were providing primary reserves. The consequences of increasingly transferring the primary frequency control from the GTs to the ESS will be further investigated in chapter 5
- **Inertial reserves**: electrical transients can produce fast changes in the ac frequency that are not representative of mechanical changes in the rotational speed of the GTs. These fast changes in the electrical frequency can be

detrimental to the performance of ESDs providing inertial reserves, i.e., with the derivative part of the controller in figure 3.2 active. In chapter 5, a theoretical framework is presented for evaluating the necessity of using, or not using, the derivative controller.

3.5 CONCLUSION

In this chapter, the possibilities provided by a centralized hybrid ESS for alleviating the negative consequences of integrating an offshore WF to the ac grid of an isolated O&G platform were analyzed. A set of structures for providing inertial, primary, and secondary reserves to frequency control and for controlling the internal dc voltage of the ESS was presented. These structures are based on established PID techniques and do not rely on fast communication links between the different converters of the ESS nor with the platform's PMS. The proposed concept shows promising results when assessed through the publicly available models developed for Publications I and II.

3.6 REFERENCES

[1] Reza Hemmati and Hedayat Saboori. Emergence of Hybrid Energy Storage Systems in Renewable Energy and Transport Applications – A Review. *Renewable and Sustainable Energy Reviews* **65**, 11–23 (2016). ISSN 1364-0321. URL https://www.sciencedirect.com/science/article/pii/S1364032116302374. Cited on page(s) 29.

[2] Ned Mohan, Tore M. Undeland, and William P. Robbins. Power Electronics: Converters, Applications, and Design. Wiley New York, USA 2nd ed edition (1995). ISBN 978-0-471-58408-7. Cited on page(s) 32.

[3] IEC 61400-27-1:2015. Wind turbines - Part 27-1: Electrical simulation models - Wind turbines. International Electrotechnical Commission Geneva, Switzerland (February 2015). URL https://webstore.iec.ch/publication/21811, accessed on 2023-02-24. Cited on page(s) 36.

[4] DIgSILENT GmbH. PowerFactory 2020 User Manual. PF2020 r6805 DIgSILENT GmbH Gomaringen, Germany (June 2020). URL https://www.digsilent.de/en/powerfactory-download.html (download for registered users), accessed on 2023-03-17. Cited on page(s) 36, 39.

[5] Seddik Bacha, Iulian Munteanu, and Antoneta Iulinana Bratcu. Power Electronic Converters Modelling and Control with Case Studies. Advanced Textbooks in Control and Signal Processing. Springer London, England (2013). ISBN 978-1-4471-5478-5. URL https://link.springer.com/book/10.1007/978-1-4471-5478-5, accessed on 2023-06-09. Cited on page(s) 36.

[6] Pouyan Pourbeik, *et al.* Dynamic Models for Turbine-Governors in Power System Studies. Technical Report PES-TR1 IEEE Power & Energy Society (January 2013). URL https://site.ieee.org/fw-pes/files/2013/01/PES_TR1.pdf, accessed on 2023-02-17. Cited on page(s) 37.

[7] IEEE Std 421.5-2016. IEEE Recommended Practice for Excitation System Models for Power System Stability Studies. IEEE Power & Energy Society New York, NY, USA (August 2016). DOI 10.1109/IEEESTD.2016.7553421. Cited on page(s) 37.

[8] Saeed Golestan, Josep M. Guerrero, and Juan C. Vasquez. Three-Phase PLLs: A Review of Recent Advances. *IEEE Transactions on Power Electronics* **32** (3), 1894–1907 (2017). ISSN 1941-0107. DOI 10.1109/TPEL.2016.2565642. Cited on page(s) 39.

CHAPTER 4

Current Control in Power Electronic Converters

RESEARCH GOALS AND CONTRIBUTIONS TO THE SCIENTIFIC LITERATURE

This chapter is tied to Research Goal I, which addresses possible causes of instability, and to Research Goal II, which proposes control structures. It focuses on the power electronic converters (PECs)' fast inner current controllers operating in single or dual rotating reference frames. Contribution II from Publication III and Contribution III from Publication IV, as well as passages from Publication V, are compiled in this chapter.

In the previous chapter, the outer-loop control structures for providing ac frequency support, ac voltage and/or reactive power support for an isolated grid fed by traditional synchronous generation, connected to an offshore wind farm (WF) and supported by a converter-interfaced energy storage system (ESS), were presented. The outer-loop controller for the ESS's dc-link voltage was also introduced. The dynamic behavior of these outer loops was assessed omitting a vital part of the control of PECs, namely, the faster inner-loop current controllers. All the outer loops described in chapter 3 provide current references for a faster inner-loop control structure of the PECs. The performance of the outer loops is, therefore, linked to the performance of the inner ones.

Fast inner-loop current controllers operating in rotating reference frames (RRFs) are the focus of this chapter that compiles the main contributions of Publications III and IV. Contents from Publication V have also been included. These main contributions are as follows:

1. An analysis of the root cause of oscillations with the fundamental frequency observed in the dc-link of the ESS when the grid converter (GC) was operated with dual RRF current controllers. These oscillations are directly tied to the transitory exponentially decaying dc currents that appear in three-phase systems with high reactance-resistance ratio (X/R) and the way dual RRF controllers split the positive and negative sequence measurements. An evaluation of the expected range of X/R seen from the energy storage system grid converter (ESSGC) terminals towards the isolated ac grid is also provided.
2. A comparison of the performance of dual RRF controllers employing known

sequence isolation methods and employing a delayed signal cancellation (DSC) technique, described in Publication IV, that is applied directly to the RRFs and is named herein DSC$_{dq}$. This proposed technique removes an intermediate step with filtering in the stationary reference frame (SRF) demanded by the traditional DSC. The DSC$_{dq}$ is also simpler to implement as it does not mix values from different axes of the dq frame as the DSC$_{\alpha\beta}$ does with the values from the $\alpha\beta$ axes.

3. A mathematical proof of the equivalence between the traditional DSC performed in the $\alpha\beta$ frame and the proposed DSC$_{dq}$ applied directly in the dq frame.

The chapter is organized as follows: the current control in RRF is presented in section 4.1; the dual RRF current controllers are introduced in section 4.2; the role of exponentially decaying dc currents in causing oscillations in the dc-link voltage of PECs employing dual controllers is investigated in section 4.3; sequence separation methods are presented in section 4.4; the performance of known sequence separation methods and the DSC$_{dq}$ are compared in section 4.5; and, finally, the concluding remarks are listed in section 4.6.

4.1 CURRENT CONTROL IN A ROTATING REFERENCE FRAME

The isolated electric grid under study in this dissertation employs converter-interfaced generation and loads. To enable the use of traditional proportional and integral (PI) regulators, instead of working with sinusoidal voltages and currents in the natural reference frame (NRF), the controllers of the PECs operate on RRFs [1]. This strategy is known in the industry as vector control and relies on the transformation of measurements between the NRF and RRF ($abc \leftrightarrow dq$). See appendix A for the list of reference frame transformations used throughout this dissertation.

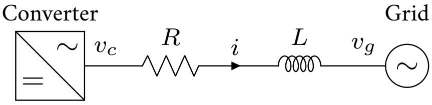

FIGURE 4.1 Idealized single-line diagram of a converter connected to the grid through an RL impedance. The dc side of the converter is not represented.

Figure 4.1 shows a single-line diagram of an idealized PEC connected to an ideal voltage source through a reactor modeled as a resistance R in series with an inductance L. The grid voltage is denoted by v_g, the converter voltage by v_c, and the current flowing from the converter to the grid is denoted by i. The relationship between the current and voltages in the NRF in this idealized system is given by

$$v_g(t) + Ri(t) + L\frac{\mathrm{d}i(t)}{\mathrm{d}t} = v_c(t)$$

which can be expanded into

$$\begin{bmatrix} v_{ga}(t) \\ v_{gb}(t) \\ v_{gc}(t) \end{bmatrix} + R \begin{bmatrix} i_a(t) \\ i_b(t) \\ i_c(t) \end{bmatrix} + L\frac{\mathrm{d}}{\mathrm{d}t} \begin{bmatrix} i_a(t) \\ i_b(t) \\ i_c(t) \end{bmatrix} = \begin{bmatrix} v_{ca}(t) \\ v_{cb}(t) \\ v_{cc}(t) \end{bmatrix}. \tag{4.1}$$

The variable to be controlled in equation (4.1) is the current $[i_a \; i_b \; i_c]^\top$ flowing from the converter to the grid. The grid voltage $[v_{ga} \; v_{gb} \; v_{gc}]^\top$ acts as a disturbance. The converter synthesizes $[v_{ca} \; v_{cb} \; v_{cc}]^\top$ under the command of a current regulator that operates in the RRF. By re-writing the voltage and current measurements from the abc frame into the rotating dq frame with the transformation $\mathcal{T}_+$ from appendix A, equation (4.1) becomes

$$\begin{bmatrix} v_{gd} \\ v_{gq} \end{bmatrix} + R \begin{bmatrix} i_d \\ i_q \end{bmatrix} + \omega L \begin{bmatrix} 0 & -1 \\ 1 & 0 \end{bmatrix} \begin{bmatrix} i_d \\ i_q \end{bmatrix} + L\frac{\mathrm{d}}{\mathrm{d}t} \begin{bmatrix} i_d \\ i_q \end{bmatrix} = \begin{bmatrix} v_{cd} \\ v_{cq} \end{bmatrix} \tag{4.2}$$

where ω is the angular frequency of the grid voltage.

The voltages, currents, and angular frequency in equation (4.2) are functions of time. The the notation (t), however, is omitted for the sake of clarity. The step-by-step algebraic manipulation from equation (4.1) to equation (4.2) is shown in appendix A section A.3.2. Notice that the dq axes are coupled. The current i_q influences the voltages in the d axis, whereas the current i_d influences the q axis.

4.1.1 Decoupling the d and q Axes

The converter voltages $[v_{ca} \; v_{cb} \; v_{cc}]^\top$ are synthesized according to the following reference values $[\overset{*}{v}_{cd} \; \overset{*}{v}_{cq}]^\top$ in the RRF

$$\underbrace{\begin{bmatrix} \overset{*}{v}_{cd} \\ \overset{*}{v}_{cq} \end{bmatrix}}_{\text{Reference}} = \underbrace{\begin{bmatrix} v_{cd\mathrm{PI}} \\ v_{cq\mathrm{PI}} \end{bmatrix}}_{\text{PI regulator}} + \underbrace{\begin{bmatrix} \widehat{v}_{gd} \\ \widehat{v}_{gq} \end{bmatrix}}_{\text{Feed forwarding}} \underbrace{+ \widehat{\omega} L \begin{bmatrix} 0 & -1 \\ 1 & 0 \end{bmatrix} \begin{bmatrix} \widehat{i}_d \\ \widehat{i}_q \end{bmatrix}}_{\text{Decoupling}}. \tag{4.3}$$

These reference values, which are forwarded to the converter pulse-width modulation (PWM) stage [2], are composed of three different parts.

1. Outputs of two PI regulators responsible for controlling i_d and i_q.
2. A feed-forwarding scheme that aims to cancel the influence of v_g.
3. Decoupling terms which are composed by the estimated inductance L between the output of the converter and the point at which the grid voltage v_g is measured and by the measured values of i and ω.

If one assumes for simplification purposes that the converter is sufficiently fast for guaranteeing $[v_{cd}\ v_{cq}]^\top \approx [\overset{*}{v}_{cd}\ \overset{*}{v}_{cq}]^\top$, then equation (4.2) can be written as

$$\begin{aligned}\begin{bmatrix} v_{gd} \\ v_{gq} \end{bmatrix} + R\begin{bmatrix} i_d \\ i_q \end{bmatrix} + \omega L\begin{bmatrix} 0 & -1 \\ 1 & 0 \end{bmatrix}\begin{bmatrix} i_d \\ i_q \end{bmatrix} + L\frac{\mathrm{d}}{\mathrm{d}t}\begin{bmatrix} i_d \\ i_q \end{bmatrix} = & \\ \begin{bmatrix} v_{cd\mathrm{PI}} \\ v_{cq\mathrm{PI}} \end{bmatrix} + \begin{bmatrix} \widehat{v}_{gd} \\ \widehat{v}_{gq} \end{bmatrix} + \widehat{\omega} L\begin{bmatrix} 0 & -1 \\ 1 & 0 \end{bmatrix}\begin{bmatrix} \widehat{i}_d \\ \widehat{i}_q \end{bmatrix}&.\end{aligned}$$

Additionally, if the measurement delays are assumed to be negligible, i.e., $\omega \approx \widehat{\omega}$, $v_g \approx \widehat{v}_g$, and $i \approx \widehat{i}$, then the multiple-input multiple-output (MIMO) system represented by equation (4.2) becomes two independent single-input single-output (SISO) systems, one for each axis of the RRF, which are described by

$$R\begin{bmatrix} i_d \\ i_q \end{bmatrix} + L\frac{\mathrm{d}}{\mathrm{d}t}\begin{bmatrix} i_d \\ i_q \end{bmatrix} = \begin{bmatrix} v_{cd\mathrm{PI}} \\ v_{cq\mathrm{PI}} \end{bmatrix}$$

and result in the following transfer functions

$$\frac{i_d}{v_{cd\mathrm{PI}}}(s) = \frac{1/R}{1 + sL/R} \quad \text{and} \quad \frac{i_q}{v_{cq\mathrm{PI}}}(s) = \frac{1/R}{1 + sL/R}.$$

In the RRF, the system can be modeled by low-pass filters (LPFs) with gain equal to the inverse of R and time constant equal to L/R.

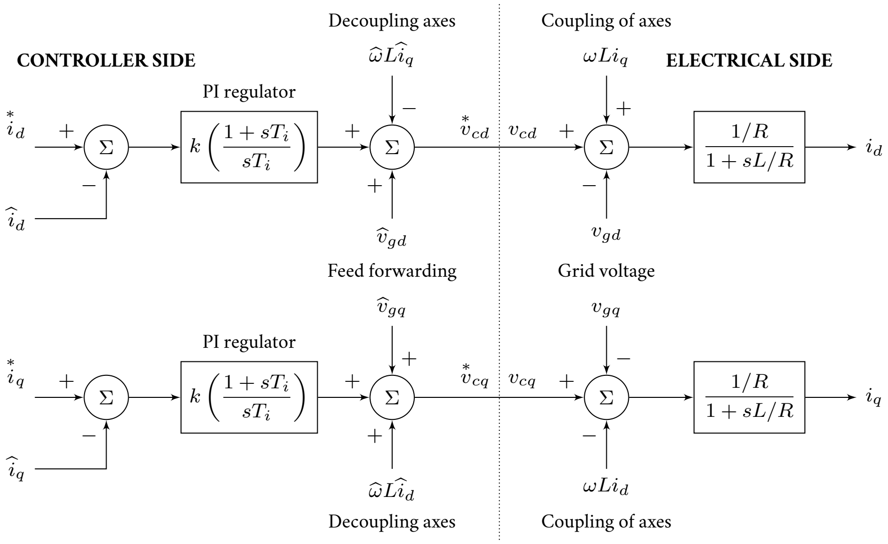

FIGURE 4.2 Current controller in the RRF.

Figure 4.2 presents a block diagram of the converter current controller in the RRF. Current and voltage measurement delays are not represented, neither are the PWM switching dynamics. Notice that PI regulators[1] are represented in the following form

$$G(s) = k\,\frac{1 + sT_i}{sT_i}$$

which is suitable for the application of the Modulus Optimum tuning technique described by Fröhr and Orttenburger [3] with the adaptations for discrete time controllers proposed by Suul *et al.* [4]. The application of these tuning techniques, however, will not be further discussed in this dissertation.

4.2 DUAL RRF CONTROLLERS

The traditional control in the RRF of three-phase voltage source converters (VSCs) assumes that grid voltages are reasonably balanced. However, imbalances may appear in practical applications of PECs. When the grid voltage is not balanced, a second harmonic component appears in the instantaneous active power and hence dc-link voltage of the converter [5]. This degrades the performance and stability of the VSC. The performance of a VSC operating under unbalanced, reduced voltage, or fault conditions can be improved by dual RRF current controllers [6–9].

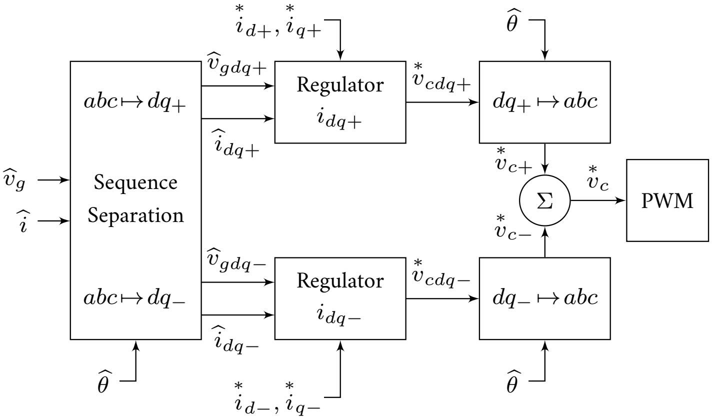

FIGURE 4.3 Dual RRF current controller. The timed dependency (t) of the signals has been omitted for clarity.

© Daniel Mota 2023 | Redrawn and recomposed from Publication III | Source code information at Part III.

Figure 4.3 shows a block diagram representation of a dual controller of a grid connected VSC. The controller operates with two RRFs and handles separately the positive and negative sequence of three-phase voltages and currents. The sequence separation block on the left-hand side of figure 4.3 receives the measured grid voltage $\widehat{v}_g(t)$, measured current flowing out of the converter $\widehat{i}(t)$, and the angle

---

[1] See appendix C for more information on the structure of the PI regulators used throughout this dissertation.

$\widehat{\theta}(t)$ of the grid voltage as inputs . The angle $\widehat{\theta}$ is provided by a phase-locked loop (PLL) measurement device. More information on the inner workings of PLLs can be found in appendix B.

Two outer loops with their own PI regulators (not represented in figure 4.3) control the converter's dc voltage and the reactive power exchange with the grid. The current reference $\overset{*}{i}_{d+}$ controls the converter's dc voltage and $\overset{*}{i}_{q+}$ controls the reactive power exchange with the grid. These outer loops have already been discussed in chapter 3, see figures 3.3 and 3.4. The negative-sequence references ($\overset{*}{i}_{d-}$, $\overset{*}{i}_{q-}$), however, are calculated for mitigating second harmonic oscillations in the active power and dc-link voltage [10, 11] caused by unbalanced operation. When the transformations in appendix A are considered, the negative-sequence current references are given by

$$\begin{bmatrix} \overset{*}{i}_{d-} \\ \overset{*}{i}_{q-} \end{bmatrix} = - \begin{bmatrix} -\widehat{v}_{gd+} & \widehat{v}_{gd+} \\ \widehat{v}_{gq+} & \widehat{v}_{gq+} \end{bmatrix}^{-1} \begin{bmatrix} -\widehat{v}_{gd-} & \widehat{v}_{gq-} \\ \widehat{v}_{gq-} & \widehat{v}_{gd-} \end{bmatrix} \begin{bmatrix} \overset{*}{i}_{d+} \\ \overset{*}{i}_{q+} \end{bmatrix} . \tag{4.4}$$

The structure of the positive (i_{dq+}) and negative sequence current (i_{dq-}) regulators of figure 4.3 is the one presented in figure 4.2. The currents on the controller side of figure 4.2 are representations in the RRF of actual quantities in the process, whereas the currents on the left-hand side are measurements inside the controller. This also applies to the voltages and to the angular frequency. Delays, attenuation, offsets, and phase shifts introduced by analog-to-digital conversions and filtering degrade the performance of the PI regulators and can, potentially, disrupt the feed forwarding and the decoupling schemes. Within this context, it is important to investigate how a common transient phenomenon present in three-phase electrical systems, namely, exponentially decaying dc currents, affects the performance of dual RRF current controllers.

4.3 UNDERSTANDING THE INFLUENCE OF EXPONENTIALLY DECAYING DC CURRENTS IN DUAL RRF CONTROLLERS

For understanding the effects of exponentially decaying dc currents on the control of power converters, it is important to recapitulate a few basic principles. If an ideal three-phase voltage source with the following output

$$v(t) = \begin{bmatrix} v_a(t) \\ v_b(t) \\ v_c(t) \end{bmatrix} = V \underbrace{\begin{bmatrix} \sin(\omega t) \\ \sin(\omega t - 2\pi/3) \\ \sin(\omega t + 2\pi/3) \end{bmatrix}}_{\text{Positive sequence}} \tag{4.5}$$

is connected at time $t = 0\,\mathrm{s}$ to a resistive and inductive (RL) load, the current supplied to the load is

$$i(t) = \frac{V}{\|Z\|}\left(\underbrace{\mathrm{e}^{-t/\tau}\begin{bmatrix}\sin(\varphi)\\ \sin(\varphi + 2\pi/3)\\ \sin(\varphi - 2\pi/3)\end{bmatrix}}_{\text{Exponentially decaying dc}} + \underbrace{\begin{bmatrix}\sin(\omega t - \varphi)\\ \sin(\omega t - \varphi - 2\pi/3)\\ \sin(\omega t - \varphi + 2\pi/3)\end{bmatrix}}_{\text{Positive sequence}}\right) \tag{4.6}$$

where $\varphi = \arctan\left({}^{\omega L}/_{R}\right)$, $\tau = {}^{L}/_{R}$, and $\|Z\| = \sqrt{(\omega L)^2 + R^2}$.

Figure 4.4 shows an example of the voltage v from equation (4.5) with amplitude 0.1 pu that is connected at time $t = 0$ to an RL load with resistance equal to 0.025 pu and reactance equal to 0.5 pu. In addition to the positive sequence three-phase sinusoidal response to the voltage, the currents through the load (figure 4.4b) also feature an exponentially decaying dc characteristic that constitutes neither positive nor negative sequence. These dc components do not form a zero sequence either as their sum is continuously equal to zero. Notice that sinusoidal oscillations appear in the instantaneous powers (figure 4.4c) supplied to the load.

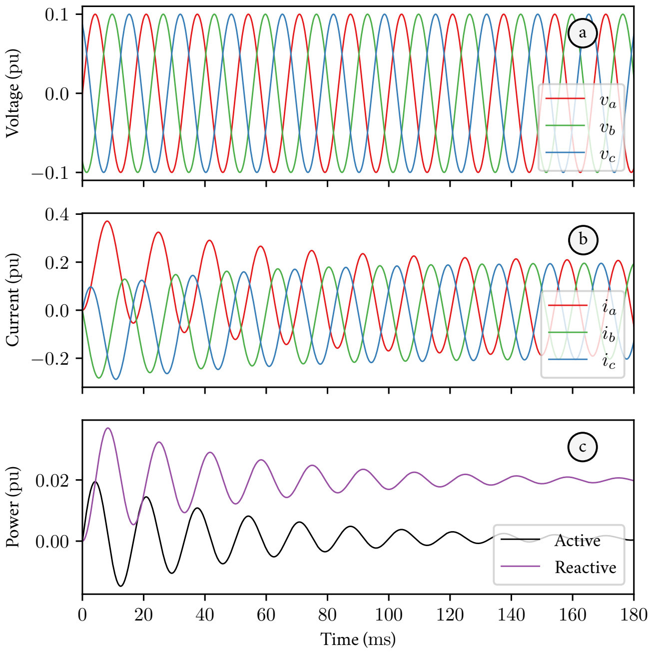

FIGURE 4.4 Exponentially decaying dc components. A three-phase ideal voltage source with amplitude 0.1 pu is suddenly connected at $t = 0$ to an RL load.

Equation (4.7) describes the exponentially decaying dc component of the currents in figure 4.4b.

$$i_{\mathrm{e}}\left(t\right) = \frac{V}{\left\|Z\right\|}\,\mathrm{e}^{-t/\tau}\begin{bmatrix}\sin\left(\varphi\right)\\ \sin\left(\varphi+2\pi/3\right)\\ \sin\left(\varphi-2\pi/3\right)\end{bmatrix} \tag{4.7}$$

When moved into the positive-sequence RRF, and by using $\theta = \omega t$ in the transformation $\mathcal{T}_{+}$ from equation (A.10) in appendix A, i_{e} becomes

$$i_{\mathrm{e}dq+}\left(t\right) = \frac{2}{3}\,\mathcal{T}_{+}\left(\omega t\right)\,i_{\mathrm{e}}\left(t\right) = \frac{V}{\left\|Z\right\|}\,\mathrm{e}^{-t/\tau}\begin{bmatrix}-\cos\left(\omega t+\varphi\right)\\ \sin\left(\omega t+\varphi\right)\end{bmatrix}.$$

When moved into the negative sequence RRF, i_{e} becomes

$$i_{\mathrm{e}dq-}\left(t\right) = \frac{2}{3}\,\mathcal{T}_{-}\left(\omega t\right)\,i_{\mathrm{e}}\left(t\right) = \frac{V}{\left\|Z\right\|}\,\mathrm{e}^{-t/\tau}\begin{bmatrix}\cos\left(\omega t-\varphi\right)\\ -\sin\left(\omega t-\varphi\right)\end{bmatrix}.$$

Notice that i_{e} appears as an exponentially decaying oscillation with the fundamental frequency ω both on the dq_{+} and on the dq_{-} frames.

The instantaneous power dissipated by i_{e} from equation (4.7) in the load can be calculated with quantities in the RRFs or in the NRF with

$$\begin{aligned} p\left(t\right) = \begin{bmatrix}v_a\left(t\right)\\ v_b\left(t\right)\\ v_c\left(t\right)\end{bmatrix}^T \begin{bmatrix}i_a\left(t\right)\\ i_b\left(t\right)\\ i_c\left(t\right)\end{bmatrix} &= \frac{3}{2}\begin{bmatrix}v_{d+}\left(t\right) & v_{q+}\left(t\right)\end{bmatrix}\begin{bmatrix}i_{d+}\left(t\right)\\ i_{q+}\left(t\right)\end{bmatrix}\\ &= \frac{3}{2}\begin{bmatrix}v_{d-}\left(t\right) & v_{q-}\left(t\right)\end{bmatrix}\begin{bmatrix}i_{d-}\left(t\right)\\ i_{q-}\left(t\right)\end{bmatrix}\end{aligned}$$

which result in

$$p\left(t\right) = -\frac{3}{2}\frac{V^2}{\left\|Z\right\|}\mathrm{e}^{-t/\tau}\cos\left(\omega t+\varphi\right). \tag{4.8}$$

Transient dc currents in the abc frame cause an oscillation in the instantaneous power delivered by the voltage source to the load. Active power oscillations directly affect the dc-link voltage of a power converter. If a dual controller is expected to dampen exponentially decaying dc components in the abc frame, it should preserve the fundamental frequency components of the measurements in the dq frames. However, as demonstrated later in section 4.4, a dual sequence current controller relies on filtering out the second harmonic from its RRFs. Unfortunately, completely filtering out the second harmonic while simultaneously maintaining the fundamental with zero attenuation and phase shift cannot be achieved with causal filters [12].

4.3.1 Expected Range of X/R

If not actively damped, the exponentially decaying dc currents caused by a sudden change in the ac voltage of a three-phase system would last for approximately three time constants τ, see equation (4.6). For the purposes of this dissertation, which focuses on the control and stability of an isolated grid supported by a converter-interfaced ESS, it is important to establish the expected range of the X/R seen by the ESSGC.

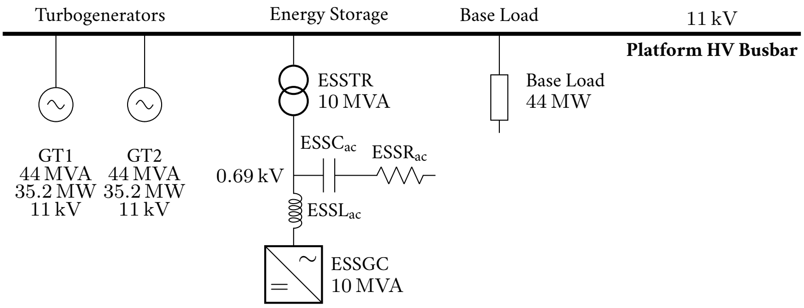

FIGURE 4.5 Simplified single line diagram of the study case used to evaluate the X/R impedance seen from the ac terminals of the GC of the ESS towards the platform main HV busbar.

Figure 4.5 shows an excerpt of the study case analyzed in this dissertation, previously shown in figure 3.5 and later used in figure 5.9. To establish a representative range for the X/R seen from the ac terminals of the ESSGC, a set of conservative simplifications are adopted. The wind farm transformer at the platform is disconnected from the busbar and the base load is modeled as a constant impedance load. In addition to that, the two synchronous generators are modeled as a voltage source behind the transient reactance x'_d in series with the stator resistance r_s and the load is simplified as a fixed resistor r_L. Typical short-circuit impedance and full load losses taken from [13] are employed for x_t and r_t of the ESS's transformer, see table 4.1.

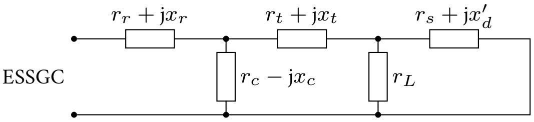

FIGURE 4.6 Single-line diagram for calculation of the X/R seen from the ac terminals of the ESSGC towards the platform's main HV busbar in the scenario illustrated by figure 4.5.

The main contributor to the X/R seen from the ESSGC's ac terminals is the converter-side reactor of the inductive-capacitive-inductive (LCL) filter, ESSL$_{ac}$ in figure 4.5 and x_r in figure 4.6. For MW-sized converters like the ones in [14, 15], paralleled two-level insulated-gate bipolar transistor (IGBT) bridges with individual LCL filters are typically employed. Without losing generality for estimating the range of X/R, the ESSGC can be modeled as one single converter with one single LCL.

The design of LCL filters is well documented in the literature by various authors, for example, Liserre *et al.* [16], Peña-Alzola *et al.* [17], Beres *et al.* [18], and Brantsæter *et al.* [19]. In Publications I, III, VI, and VII and in this dissertation, the criteria described by Brantsæter *et al.* [19] were used for sizing the LCL filter. Within these criteria, the reactance x_r of the ESSGC's main reactor and damping resistance r_c of the capacitive branch (see figure 4.6) depend on the PWM switching frequency F_{sw}. The switching frequency of MW-sized converters [14, 15] is typically below 4 kHz.

Figure 4.7 shows a representative range of values of X/R and x_r as a function of the PWM switching frequency for the study case under analysis in chapters 3 and 5. The impedance seen from the ac terminals of the ESSGC has an X/R in the range of 12 to 20. Sudden changes at the voltage of the ESSGC induce exponentially decaying dc currents with a transient time (3τ) between 100 ms to 200 ms. These dc currents, which are reflected as oscillations with the fundamental frequency in the RRFs, cause oscillations with the fundamental frequency in the active power that can lead to instabilities in the dc-link voltage regulator.

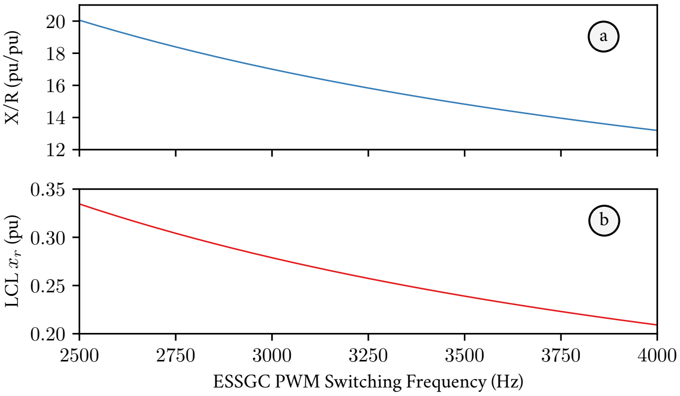

FIGURE 4.7 Representative range for X/R seen from the ESSGC terminals versus the PWM switching frequency for the scenario represented in figure 4.5, i.e., with the WF disconnected. (a) X/R. (b) LCL converter-side reactance.

4.4 SEQUENCE SEPARATION METHODS

When an unbalanced three-phase measurement is moved to the positive-sequence RRF with the transformation $\mathcal{T}_+(\theta)$ in equation (A.11) in appendix A, the positive-sequence content of the measurement becomes dc, whereas the negative-sequence content appears as second harmonic. The opposite happens when this same three-

TABLE 4.1 Representative range of X/R seen from the ESSGC terminals towards the platform ac grid for the study-case employed in chapters 3 and 5 with the WF disconnected.

		Value at (base) in pu	
Parameter		(88 MVA & 11 kV)	(10 MVA & 690 V)
Transient reactance	x'_d	0.299	-
Stator resistance	r_s	0.0242	-
Load resistance	r_L	2.00	-
Transformer reactance	x_t	-	0.060
Transformer resistance	r_t	-	0.005
Capacitor impedance	x_c	-	20
Damping resistor	r_c	-	0.336 to 0.209 (F_{sw} 2.5 to 4 kHz)
Main reactor resistance	r_r	-	0.01

phase measurement is moved to the negative-sequence RRF with $\mathcal{T}_{-}(\theta)$, namely the negative sequence becomes dc and the positive sequence becomes second harmonic. Sequence separation methods, therefore, must remove second-harmonic content from the RRFs. In the following subsections, different sequence-separation methods are presented.

4.4.1 Notch Based Sequence Separation

In 1999, a dual RRF current control scheme was proposed by Song and Nam [10]. In this scheme, notch filters tuned to the second harmonic are employed for removing the opposite sequence measurements from each of the dq frames as illustrated in figure 4.8. The notch angular frequency is set to $\omega_f = 4\pi F_n$ where F_n is the rated frequency of the grid. The damping factor ζ defines the quality of the filter. The lower the damping, the higher the quality. However, higher quality comes at the cost of oscillatory complex conjugated poles [20].

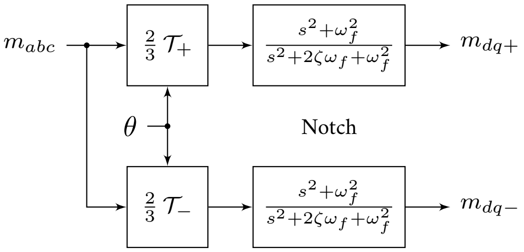

FIGURE 4.8 Notch-filter-based positive and negative sequence separation, adapted from [8, 10, 12, 21]. The measurements m_{abc} stand for either voltages or currents. The angle θ is provided by a PLL, but in this chapter it is assumed to be ideally measured.

© Daniel Mota 2023 | Redrawn and recomposed from Publication III | Source code information at Part III.

Dual-sequence current controllers employing notch filters tuned to the second harmonic applied directly to the RRFs were also employed by Brogan [8], Kocewiak [12], Glasdam [21], and Zhang *et al.* [22].

4.4.2 *DDRRF Sequence Separation*

In 2012, Siemaszko [9] proposed a dual dq controller that employed the decoupled double rotating reference frame (DDRRF)[2] introduced by Rodriguez *et al.* [23]. Figure 4.9 illustrates the DDRRF sequence separation concept. On the top left, the measurement m_{abc} on the abc frame is transformed into the positive sequence dq frame with the transformation $\mathcal{T}_+$. The second harmonic content present in the dq_+ is removed by the LPF with a time constant T_f resulting in the measurement m_{dq+}. Similarly, the LPF at the bottom of the figure isolates the negative sequence component m_{dq-}. According to Rodriguez *et al.* [23], to guarantee a stable and damped response of the sequence separation method, the cutout frequency of the LPF should be lower or equal to $F_n/\sqrt{2}$, where F_n is the fundamental frequency of the grid.

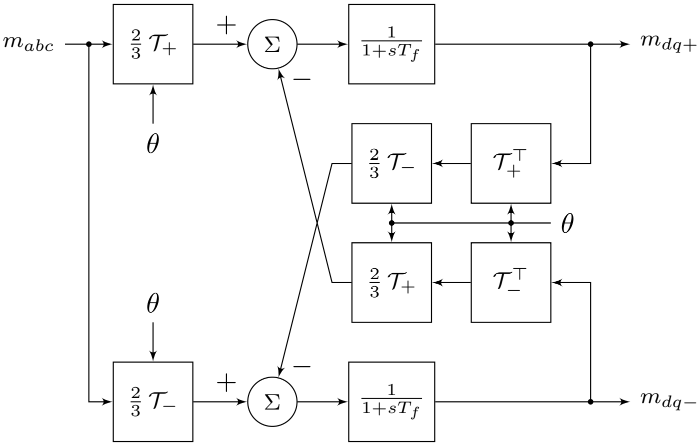

FIGURE 4.9 DDRRF-based sequence separation adapted from [23]. The measurements m_{abc} denote either voltages or currents, m_{dq+} denote the isolated positive sequence content, and m_{dq-} denote the isolated negative sequence content. The angle θ is provided by a PLL, but in this chapter it is assumed to be ideally measured.

© Daniel Mota 2023 | Redrawn and recomposed from Publication III | Source code information at Part III.

In addition to the LPFs, the DDRRF sequence separation method transforms the filtered values m_{dq+} and m_{dq-} back into their opposite sequence frames, as seen by the blocks in series with the transformations $\mathcal{T}_+$ and $\mathcal{T}_-$ in figure 4.9. With the help of the subtraction blocks, these transformed filtered values cancel the

---

[2] DDRRF was originally named DDSRF in [23]. In this dissertation, the "S" of synchronous is replaced by "R" of rotating to avoid confusions with the "S" of the stationary reference frame (SRF, $\alpha\beta$ frame).

"wrong" sequence content present at the output of the transformation blocks on the left-hand side of the figure.

4.4.3 Moving Averages

Moving averages (MAs) with a window equal to half the grid period ($T/2$) can be used to filter the second harmonic of the grid frequency ($2F$). In a digital implementation of an MA filter running in an electronic microprocessor with fixed sampling frequency F_s and fixed sampling time $T_s = F_s{}^{-1}$, the moving average window (MAW) for removing the second harmonic is given by

$$n = \frac{F_s}{2F} = \frac{T}{2T_s}$$

where n represents the number of samples equivalent to half the grid period ($T/2$).

One computationally inefficient way of calculating a moving average in the discrete time domain is to perform a sum of n samples at each new cycle k as in

$$\overline{x}(k) = \frac{1}{n}\sum_{r=0}^{n-1} x(k)z^{-r} \tag{4.9}$$

where $x(k)$ represents a generic variable, $\overline{x}(k)$ its moving average, and n is the number of samples acquired during the past time window of half period of the grid. Notice that the time in the discrete domain is represented by an ever-increasing integer k that is an index and not a proportional gain. Notice also that the terms time, sample, or cycle k referring to an instant kT_s are interchangeably employed in this chapter. In addition to that, the operator that fetches the value of a variable at the rth previous cycle is denoted by z^{-r}.

Orfanidis [24] describes a more efficient way of calculating MAs. If one expands the sum in equation (4.9), multiplies it by

$$\frac{1 - z^{-1}}{1 - z^{-1}}$$

and rearranges the numerator, the result is

$$\overline{x}(k) = \frac{x(k)}{n}\frac{\left(z^0 + \cdots + z^{-n+1}\right) - \left(z^{-1} + \cdots + z^{-n}\right)}{1 - z^{-1}}. \tag{4.10}$$

Most of the terms in equation (4.10) can be canceled, yielding equation (4.11). Figure 4.10 shows one possible block diagram representation of equation (4.11) adapted from [25]. It is important to remark that, even though computationally efficient, equation (4.11) still demands the last n samples of x to be stored in memory.

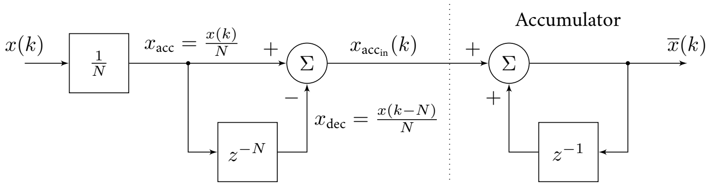

FIGURE 4.10 Computationally efficient MA block built from equation (4.11), adapted from [25].

© Daniel Mota 2023 | Redrawn and recomposed from Publication V | Source code information at Part III.

$$\overline{x}(k) = \frac{x(k)}{n}\frac{1-z^{-n}}{1-z^{-1}} \tag{4.11}$$

Isolated electric systems can be subjected to large frequency excursions, especially during transients. A sequence isolation method based on MAs should not be unreasonably degraded by such variations. For the interested reader, appendix D describes the details proposed in Publication V on how to turn the computationally efficient MA illustrated by figure 4.10 into a frequency adaptive moving average (AMA).

4.4.4 Delayed Signal Cancellation (DSC) in the $\alpha\beta$ Frame

The DSC was employed for sequence isolation by several authors, for instance, Saccomando and Svensson [7], Svensson *et al.* [26], Neves *et al.* [27], and Golestan *et al.* [28]. The DSC implemented by these authors operates in the SRF and is, because of that, denoted by DSC$_{\alpha\beta}$ in this dissertation. It combines values delayed by one quarter of the grid period from one axis of the SRF with current values from the other axis. The DSC$_{\alpha\beta}$ is usually described with complex values in the literature. However, when expressed with vectors of real quantities, the DSC$_{\alpha\beta}$ becomes

$$\begin{bmatrix} m_{\alpha+}(t) \\ m_{\beta+}(t) \end{bmatrix} = \frac{1}{2}\left(\begin{bmatrix} m_{\alpha}(t) \\ m_{\beta}(t) \end{bmatrix} + \begin{bmatrix} 0 & -1 \\ 1 & 0 \end{bmatrix}\begin{bmatrix} m_{\alpha}(t-T/4) \\ m_{\beta}(t-T/4) \end{bmatrix}\right) \tag{4.12}$$

where the vectors $[m_{\alpha}\ m_{\beta}]^{\top}$ are the representations in the SRF of the three-phase measurements, $[m_{\alpha+}\ m_{\beta+}]^{\top}$ contains the isolated positive sequence, and $T/4$ is the time delay with T equal to the period of the fundamental frequency of the grid.

The DSC$_{\alpha\beta}$ can also be adapted for isolating the negative-sequence contents of three-phase voltages and currents. For that, the negative-sequence reference frame can be constructed by assuming a negative grid angular frequency ω, as done by Song and Nam [10], or by swapping the measurements of phases b and c, as done in Publications III and IV. Nevertheless, due to brevity concerns, the mathematical derivation of the DSC$_{\alpha\beta}$ in the negative-sequence reference frame will not be described in this dissertation.

The DSC$_{\alpha\beta}$ adds an extra layer of complexity to the dual current controller shown in figure 4.3. Instead of being transformed directly into the dq frame, the signals have to first be transformed to the $\alpha\beta$ frame, treated with equation (4.12), and then transformed to the RRF. As shown in Publication IV, it is possible to apply the DSC directly to the quantities of the dq frame.

4.4.5 *Delayed Signal Cancellation (DSC) in the dq Frame*

Let the $\alpha\beta$ quantities of the DSC$_{\alpha\beta}$ described in equation (4.12) be written on the dq frame with the transpose of the matrix $\mathcal{P}$ from equation (A.8) in appendix A. The transformation $\mathcal{P}^\top(\theta(t))$ is applied to the $\alpha\beta$ quantities in current time t, whereas $\mathcal{P}^\top(\theta(t-T/4))$ is applied to the delayed quantities from time $(t-T/4)$. The result is, then,

$$\begin{aligned}\mathcal{P}^\top(\theta(t))\begin{bmatrix} m_{d+}(t)\\ m_{q+}(t)\end{bmatrix} = \frac{1}{2}\Bigg(\mathcal{P}^\top(\theta(t))\begin{bmatrix} m_d(t)\\ m_q(t)\end{bmatrix} + \\ + \begin{bmatrix} 0 & -1\\ 1 & 0\end{bmatrix}\mathcal{P}^\top(\theta(t-T/4))\begin{bmatrix} m_\alpha(t-T/4)\\ m_\beta(t-T/4)\end{bmatrix}\Bigg)\end{aligned} \tag{4.13}$$

where the angle $\theta(t)$ employed in the transformation $\mathcal{P}$ is given by

$$\theta(t) = \int_0^t \omega(\tau)\,\mathrm{d}\tau$$

and ω is the angular frequency of the grid. Assuming that ω is reasonably constant, especially within one quarter of the grid period ($T/4$), the current and the delayed values of the angle θ can be approximated to $\theta(t) \approx \omega t$, and $\theta(t-T/4) \approx \omega t - \omega T/4$.

Now, let both sides of equation (4.13) be multiplied by $\mathcal{P}(\omega t)$

$$\begin{aligned}\begin{bmatrix} m_{d+}(t)\\ m_{q+}(t)\end{bmatrix} = \frac{1}{2}\Bigg(\begin{bmatrix} m_d(t)\\ m_q(t)\end{bmatrix} + \\ +\mathcal{P}(\omega t)\begin{bmatrix} 0 & -1\\ 1 & 0\end{bmatrix}\mathcal{P}^{-1}(\omega t-\omega T/4)\begin{bmatrix} m_d(t-T/4)\\ m_q(t-T/4)\end{bmatrix}\Bigg).\end{aligned} \tag{4.14}$$

As the angular frequency of the grid is $\omega = 2\pi F$ and the period of the grid is $T = 1/F$, then $\omega T/4 = \pi/2$. Consequently, the multiplication of the square matrices on the right-hand side of equation (4.14) can be written as

$$
\begin{gathered}
\mathcal{P}(\omega t)\begin{bmatrix}0 & -1\\ 1 & 0\end{bmatrix}\mathcal{P}^{-1}(\omega t-\omega T/4)\\
=\begin{bmatrix}\sin(\omega t) & -\cos(\omega t)\\ \cos(\omega t) & \sin(\omega t)\end{bmatrix}\begin{bmatrix}0 & -1\\ 1 & 0\end{bmatrix}\\
\begin{bmatrix}\sin(\omega t-\pi/2) & \cos(\omega t-\pi/2)\\ -\cos(\omega t-\pi/2) & \sin(\omega t-\pi/2)\end{bmatrix}=\\
\begin{bmatrix}-\cos(\omega t) & -\sin(\omega t)\\ \sin(\omega t) & -\cos(\omega t)\end{bmatrix}\begin{bmatrix}-\cos(\omega t) & (\omega t)\\ -\sin(\omega t) & (\omega t)\end{bmatrix}=\begin{bmatrix}1 & 0\\ 0 & 1\end{bmatrix}.
\end{gathered}
$$

Equation (4.14) results, therefore, in

$$
\begin{bmatrix}m_{d+}(t)\\ m_{q+}(t)\end{bmatrix}=\frac{1}{2}\left(\begin{bmatrix}m_d(t)\\ m_q(t)\end{bmatrix}+\begin{bmatrix}m_d(t-T/4)\\ m_q(t-T/4)\end{bmatrix}\right). \tag{4.15}
$$

Performing the DSC$_{\alpha\beta}$ with equation (4.12) in the $\alpha\beta$ frame and transforming the result to the RRF is equivalent to performing the DSC directly in the dq frame with equation (4.15). This delayed signal cancellation performed directly in the RRF is named DSC$_{dq}$ in this dissertation. In addition to removing the extra layer of signals in the $\alpha\beta$ frame, the DSC$_{dq}$ is simpler to understand and implement as it does not mix values from different axes of the dq frame as the DSC$_{\alpha\beta}$ does with the values from the $\alpha\beta$ axes.

In a way similar to the MA described in section 4.4.3, a sequence isolation method based on the DSC$_{dq}$ should not be unreasonably degraded by ac frequency variations either. The interested reader may find in appendix E the details proposed in Publication IV on how to build a frequency adaptive DSC$_{dq}$. However, for the sake of brevity and to highlight the differences between the sequence isolation methods described in this chapter, it is assumed in the following section that the grid frequency is constant.

4.5 COMPARING SEQUENCE SEPARATION METHODS

In this section, the five sequence separation methods presented in section 4.4 are compared to each other and the performance of dual current controllers employing those methods is evaluated with the use of computer simulations.

4.5.1 Notch-Based versus DDRRF-Based Methods

The performance of the notch-based and DDRRF-based principles is first compared by applying these methods to isolate the sequence contents of the voltages and currents in figure 4.4. The amplitude of the positive sequence voltage is 0.1 pu, the frequency is 60 Hz, the load reactance is 0.5 pu, and the resistance is 0.025 pu. The X/R ratio of the load is at the highest representative range for the scenario analyzed in this dissertation. This highlights the effects of the exponentially decaying dc components without reducing the generality of the results. The grid voltage angular frequency measurement is assumed to be instantaneous and the angle θ (see figures 4.8 and 4.9) is available with zero delay. The goal is to compare the sequence-isolation principles themselves and not grid voltage angle measurement devices (PLLs).

According to Rodriguez *et al.* [23], the cutout frequency of the LPFs employed in the DDRRF should be lower or equal to $F_n/\sqrt{2}$, where F_n is the fundamental frequency of the grid, for guaranteeing a stable and damped response of the method. The cutout frequency is, in this section, set to exactly $F_n/\sqrt{2}$. The damping factor ζ of the notch-based method (see figure 4.8) defines the quality of the second harmonic filtering. The lower the ζ, the higher the quality of the notch filter. Although preliminary computer simulations with $\zeta = \sqrt{2}/2$ showed good results, for a fair comparison with the DDRRF method, a unitary ζ is chosen for the notch filters in this subsection.

Figure 4.11 shows the voltages and currents from figure 4.4 measured and isolated into the positive and negative dq axes with the notch and the DDRRF-based methods. The voltage in the d_+ axis (figure 4.11a) is similar for both methods except for the expected second order characteristic of notch filters. In the q_+ axis (figure 4.11c), the output of the notch-based principle matches the expected value of zero for the voltage. However, the cross-coupling of positive and negative reference frames performed by the DDRRF principle shows its influence in figure 4.11c, where a deviation of almost 0.02 pu is observed in the voltage in the q_+ axis. Although initially featuring a sharper increase in figure 4.11e, the voltage measurement in the d_- axis with the notch-based principle returns to zero faster than the one with the DDRRF principle. In all cases in figures 4.11b, d, f, and h, the phase shifts introduced by the DDRRF principle are the largest. This indicates that the performance of the feed-forwarding and the decoupling of d and q axes in each positive and negative reference frames will be worse for the DDRRF-based dual controller than for the notch-based dual one.

To further evaluate the notch and DDRRF-based methods, the performances of two dual controllers are compared in figure 4.12 by simulating the idealized scenario of a converter connected to the grid through an RL impedance as illustrated previously in figure 4.1. The dc voltage is fixed, i.e., maintained by an ideal voltage source. Initially, the grid voltage is a pure positive sequence with 1 pu. The X/R is at the highest end of the expected value calculated in section 4.3.1 resulting in an unforced decay time of $3\tau = 160$ ms for the exponentially decaying dc components. All PI regulators in both dual controllers are tuned equally. The structure of the regulators is also identical and is given by equation (C.1) in appendix C. All current references are set to zero. Therefore, deviations from zero in the currents and instantaneous power are key performance indicators. The higher

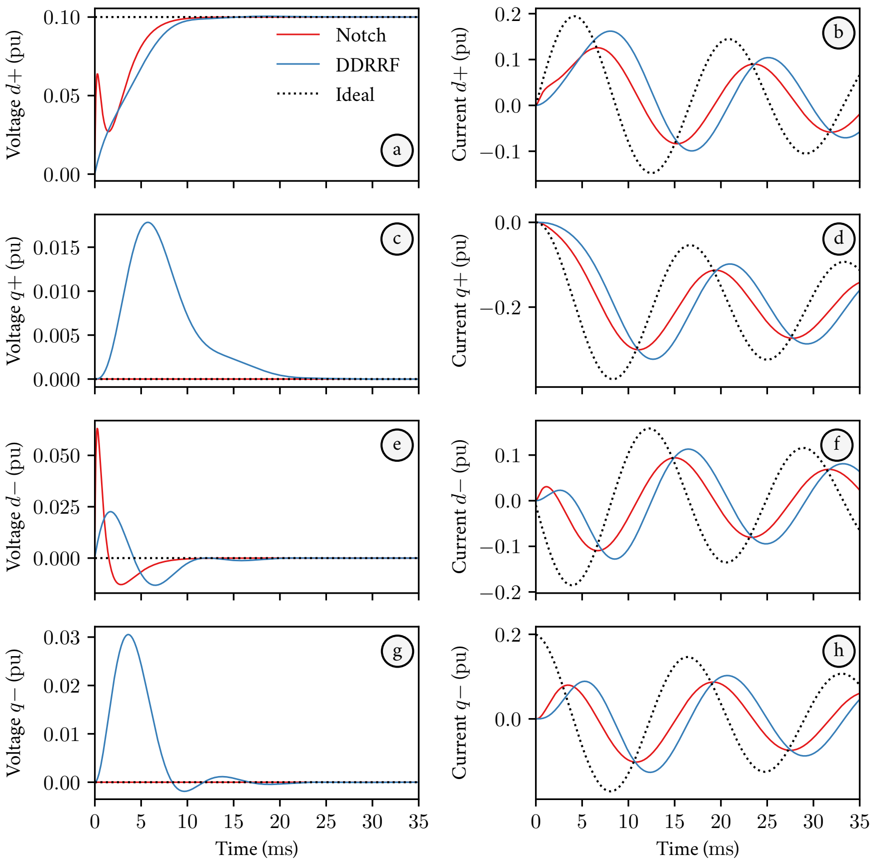

FIGURE 4.11 Comparing notch and DDRRF-based sequence separation method applied to the measurements shown in figure 4.4.

© Daniel Mota 2023 | Redrawn and recomposed from Publication III | Source code information at Part III.

the deviations and the longer their duration, the worse the performance.

Figures 4.12a, c, e, and g show the response of the notch-based regulator and figures 4.12b, d, f, and h show the response of the DDRRF-based regulator to a step on the grid voltage with negative sequence amplitude of 0.2 pu at $t = 500$ ms. The notch-based regulator manages to bring the currents back to zero within 25 ms, whereas the DDRRF-based one does not. The decay of the dc components in the current in figure 4.12f is slower than the one observed in figure 4.12e. For the DDRRF-based regulator, the dc components take more than 150 ms to return to zero. This phenomenon causes the active power (figure 4.12h) to oscillate with 60 Hz.

As expected from the results observed in figure 4.11, the performance in figure 4.12 of the notch-based regulator is better than the DDRRF-based one. The notch-based is able to dampen the dc current components in a considerably

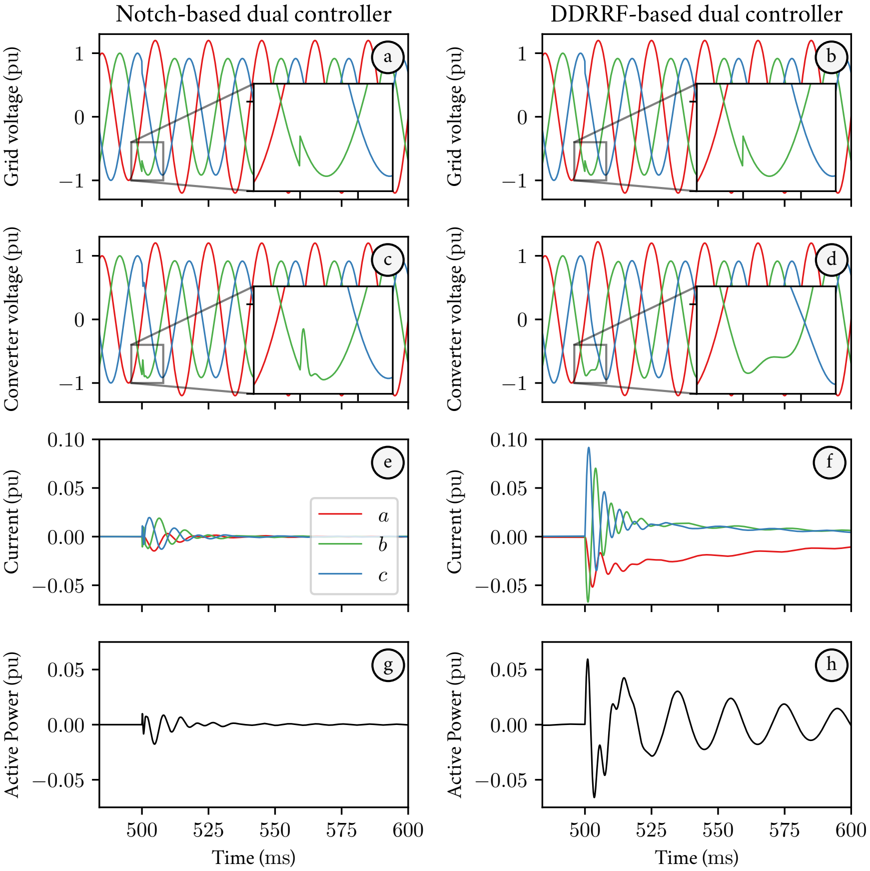

FIGURE 4.12 Comparing the performance dual sequence current controllers employing the notch and the DDRRF-based methods with unbalanced voltage conditions.

© Daniel Mota 2023 | Redrawn and recomposed from Publication III | Source code information at Part III.

shorter time than the unforced decay of $3\tau = 160$ ms, whereas the DDRRF-based is unable to do so. Notice also that the feed-forwarding of the grid voltage behaves differently for the controllers. The notch-based converter mimics the grid voltage better than the DDRRF-based does. This is visible in phase b (solid green) of the converter voltages in figures 4.12c and d right after $t = 500$ ms. The longer phase-shifts introduced by the DDRRF sequence isolation method previously observed in figure 4.11 degrade the overall response of the PI regulators.

4.5.2 Notch versus MA versus DSC

From the perspective of the dq_+ reference frame, the negative sequence content present in the abc frame appears as a second harmonic. Therefore, it is a logical choice to use filters directly in the dq axes to remove the second harmonic and, consequently, isolate positive and negative sequence contents. From the five sequence isolation methods presented in section 4.4, the notch, the MA, and the DSC$_{dq}$ can be directly applied to the dq axes. It is worth recalling that, although applied to the $\alpha\beta$, the DSC$_{\alpha\beta}$ is equivalent to the DSC$_{dq}$.

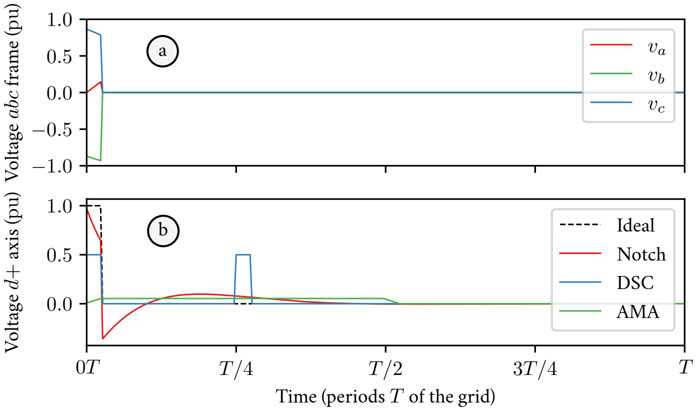

FIGURE 4.13 Comparing sequence isolation methods. (a) Short pulse of a three-phase voltage in the abc-frame. (b) Representation of the voltages in the d_+ axis: ideal in dashed black, notch-based in solid red, DSC-based in solid blue, and MA-based in solid green. The angle of v_a is known and is used for the reference frame transformation.

© Daniel Mota 2023 | Redrawn and recomposed from Publication IV | Source code information at Part III.

To evaluate the performance of the notch, DSC, and MA methods for isolating positive and negative sequences, a simplified computer simulation is devised. A short pulse of a positive-sequence three-phase voltage with amplitude 1 pu appears at time equal to $0T$ in figure 4.13a, where T is the period of the grid. The angular frequency ω and the angle θ of the grid voltage are known and are, therefore, used in the reference frame transformation and filtering. In the d_+ axis, the three-phase short pulse appears as a 1 pu pulse in dashed black in figure 4.13b. The response of the notch filter, shown in solid red, features a prominent undershoot after the grid voltages return to zero. The notch filter damping was set to $\zeta = \sqrt{2}/2$ for this comparison. The response of the DSC, in solid blue, is characterized by two pulses with amplitude 0.5 pu spaced by one quarter of the grid period. The output of the MA, in solid green, increases while the short pulse is present, stays constant until the time reaches $T/2$, and then decays back to zero. From the response of the notch filter, it is possible to deduct that a controller employing this method of sequence isolation would feature overshoots in responses to step transients. The same conclusion cannot be intuitively obtained from the responses of the DSC$_{dq}$ and MA methods.

The ideal measurement in dashed black in figure 4.13b can be considered as the input for three second-harmonic-removal filters: notch, DSC$_{dq}$, and MA.

The latter two are finite impulse response (FIR) filters. Their outputs, instead of decaying asymptotically to zero as in infinite impulse response (IIR) filters, actually reach zero within a finite time. Additionally, the outputs of FIR filters are equal to the weighted sum of their current and previous (delayed) inputs [24]. The number of delayed inputs and their weights can be identified from the filter's response to a unit pulse. Hence, from figure 4.13b, it is possible to deduce the MA and DSC_{dq}'s mathematical descriptions, which are the equations (4.9) and (4.15), respectively. Furthermore, an estimated frequency response of the notch, DSC_{dq}, and MA filters can be obtained if the fast Fourier transform (FFT) of the outputs in figure 4.13b are divided, frequency by frequency, by the FFT of the input (dashed black). This is known as empirical transfer function estimation (ETFE) [29].

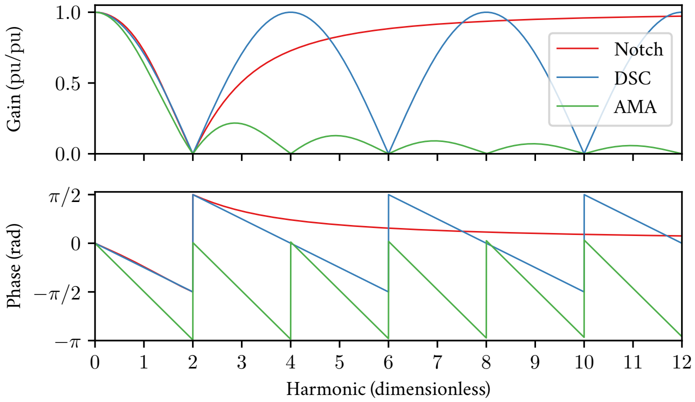

FIGURE 4.14 Frequency response of the notch (red), DSC_{dq} (blue), and MA (green) filters used in the dq frame for isolating the positive and negative sequence content.

© Daniel Mota 2023 | Redrawn and recomposed from Publication IV | Source code information at Part III.

Figure 4.14 shows the frequency responses of the notch, DSC_{dq}, and MA filters applied directly to the d_+ axis for sequence isolation. All three filters have unitary gain and zero phase shift when the frequency is zero. Notice that zero frequency at the d_+ axis is equivalent to the fundamental frequency in the abc frame. Between zero and the second harmonic in the d_+ axis, the gains begin to drop almost identically in conjunction with larger phase shifts. The behavior of the filters differ considerably after the second harmonic. The notch technique removes only the second harmonic, whereas the DSC_{dq} removes from the RRFs all harmonics equal to $4k-2$, with the integer $k \geq 1$. The MA technique, however, filters completely all even harmonics. An analysis of the consequences of these differences in the higher part of the spectrum is considered, nonetheless, beyond the scope of this dissertation.

In section 4.5.1, it was shown that a notch-based dual controller performs better than a DDRRF-based controller due to the larger phase delays introduced in the dq measurements by the latter in the spectrum close the fundamental frequency. In figure 4.14, the MA method clearly features the largest phase delay close to the fundamental. The phase shift of $\pi/2$ rad at the fundamental introduced by the MA will surely degrade the performance of a dual RRF controller operating in grid with high X/R. For this reason, MA-based dual controllers are disregarded in the comparisons in the next subsection.

4.5.3 Notch versus DSC

A comparison of the performance of dual controllers equipped with notch, DSC$_{\alpha\beta}$, and DSC$_{dq}$ sequence isolation methods is presented in this subsection. This is done via computer simulations using the conceptual model of a VSC connected to a three-phase voltage source through a highly inductive impedance employed previously in section 4.5.1. However, the dc link of the converter is now taken into consideration and an outer dc voltage control loop is included. The tuning [4] of the inner PI regulators and the outer one is identical in all cases. A reactive power regulator is not implemented. Saccomando and Svensson [7] showed that dual controllers equipped with notch filters might present a more oscillatory behavior than controllers using DSC. Despite that, notch filters are employed for sequence isolation by authors closely linked to the industry, for instance, Brogan [8] and Brogan *et al.* [30]. For this reason, a controller with notch-based sequence isolation is used as benchmark for the DSC-based ones.

In figure 4.15, initially, the amplitude of the positive sequence of the grid voltage is equal to 1 pu and the amplitude of the negative sequence is equal to 0.1 pu. The outer dc-link voltage regulator and the inner dual-sequence current controller manage to maintain a constant dc voltage at 1 pu despite the unbalance. At the instant $t = 1000$ ms, the positive and negative sequence amplitudes of the grid voltage drop to 0.8 pu and 0.08 pu, respectively. The transient in the grid voltage prompts oscillations in the active and reactive powers during 25 ms. An oscillation in the dc voltage is also observed after the drop in the grid voltage; however, the dc voltage controller manages to dampen it. The difference between the dc voltages of the controllers with DSC$_{\alpha\beta}$ and DSC$_{dq}$ is, with the exception of negligible numerical errors, identical. The performance of the controllers employing both types of DSC is less oscillatory and faster than the controller with the notch-based sequence separation.

4.6 CONCLUSION

Sudden changes to the voltage of three-phase electrical systems with high X/R induce exponentially decaying dc currents in the abc frame. These currents become exponentially decaying sinusoidal signals with the fundamental frequency when moved to the dq frame. They need to be properly measured if a controller is to

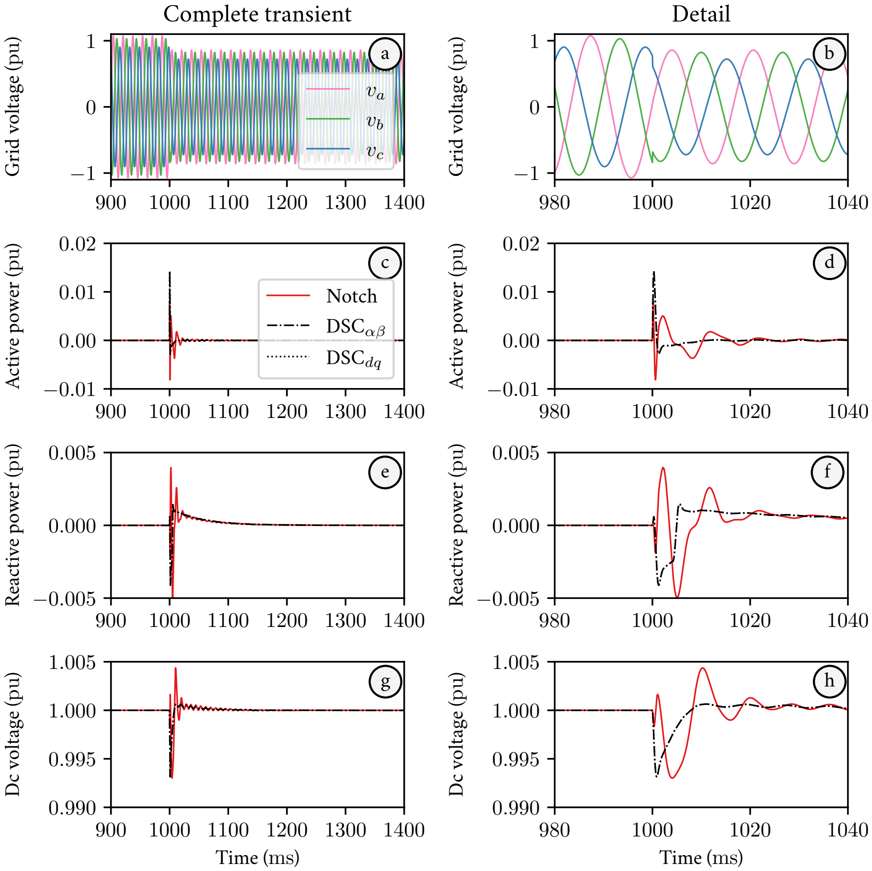

FIGURE 4.15 Comparing converters employing notch, DSC$_{\alpha\beta}$, and DSC$_{dq}$ sequence isolation methods in unbalanced voltage conditions.

© Daniel Mota 2023 | Redrawn and recomposed from Publication IV | Source code information at Part III.

dampen them. Dual dq controllers are thus faced with two conflicting tasks to be performed concurrently in their dq frames: 1) remove the second harmonic to split positive and negative sequences; and 2) preserve the fundamental frequency components of the measurements.

The filtering techniques necessary for a dual dq controller to work introduce phase shifts to the measurement of the exponentially decaying currents. Several sequence isolation methods were compared in this chapter with the help of computer simulations in the time and frequency domains. The methods that introduce excessive phase shifts in the measurements disturb the feed forwarding of the grid voltage and the decoupling of the dq axes during transients degrading the overall performance of the PI regulators, resulting in noticeable oscillations in the active power exchange between converter and grid. These active power variations, ultimately, manifest themselves as undesirable transient oscillations in the dc-link voltage.

The analysis of the problem in the time-domain, with a focus on the effects of exponentially decaying dc currents in three phase systems with high X/R in the dual dq control of power electronic converters, is one of the main contributions presented in the chapter. It provides a valuable insight into the root cause of oscillations in high capacity power converters operating in large electrical systems. In addition to that, a discrete DSC_{dq} algorithm to separate positive and negative sequence measurements directly in the RRF was also described. The mathematical equivalence between the DSC_{dq} and the traditional $\mathrm{DSC}_{\alpha\beta}$ applied in the SRF is demonstrated. The DSC_{dq} technique simplifies the practical implementation of dual-sequence current controllers for grid-connected VSCs, as it eliminates an intermediate filtering step in the SRF demanded by the traditional $\mathrm{DSC}_{\alpha\beta}$.

4.7 REFERENCES

[1] Frede Blaabjerg, Remus Teodorescu, Marco Liserre, and Adrian V. Timbus. Overview of Control and Grid Synchronization for Distributed Power Generation Systems. *IEEE Transactions on Industrial Electronics* **53** (5), 1398–1409 (October 2006). ISSN 1557-9948. DOI 10.1109/TIE.2006.881997. Cited on page(s) 44.

[2] Ned Mohan, Tore M. Undeland, and William P. Robbins. Power Electronics: Converters, Applications, and Design. Wiley New York, USA 2nd ed edition (1995). ISBN 978-0-471-58408-7. Cited on page(s) 45.

[3] Friederich Fröhr and Fritz Orttenburger. Introduction to Electronic Control Engineering. Siemens Aktiengesellschaft; Heyden & Son LTD. Berlin and München, Germany; London, UK (1982). ISBN 0-85501-290-0. Cited on page(s) 47.

[4] Jon Are Suul, Marta Molinas, Lars Norum, and Tore Undeland. Tuning of Control Loops for Grid Connected Voltage Source Converters. In *2008 IEEE 2nd International Power and Energy Conference* Johor Bahru, Malaysia (December 2008). DOI 10.1109/PECON.2008.4762584. Cited on page(s) 47, 64.

[5] Hirofumi Akagi, Edson Hirokazu Watanabe, and Mauricio Aredes. Instantaneous Power Theory and Applications to Power Conditioning. Wiley-Interscience Hoboken, NJ, USA (2007). ISBN 978-0-470-11893-1. URL https://ieeexplore.ieee.org/servlet/opac?bknumber=5236653, accessed on 2023-03-31. Cited on page(s) 47.

[6] P. Rioual, H. Pouliquen, and J. P. Louis. Regulation of a PWM Rectifier in the Unbalanced Network State Using a Generalized Model. *IEEE Transactions on Power Electronics* **11** (3), 495–502 (May 1996). ISSN 1941-0107. DOI 10.1109/63.491644. Cited on page(s) 47.

[7] G. Saccomando and Jan R. Svensson. Transient Operation of Grid-Connected Voltage Source Converter under Unbalanced Voltage Conditions. In *Conference Record of the 2001 IEEE Industry Applications Conference. 36th IAS Annual Meeting (Cat. No.01CH37248)* volume 4 (2001). DOI 10.1109/IAS.2001.955960. Cited on page(s) 47, 56, 64.

[8] Paul Brogan. The Stability of Multiple, High Power, Active Front End Voltage Sourced Converters When Connected to Wind Farm Collector Systems. In *EPE Wind Energy Chapter Seminar* Stafford, UK (April 2010). URL http://www.epe-association.org/epe/seminars/Wind2010, accessed on 2023-03-24 (password protected zip-file). Cited on page(s) 47, 53, 54, 64.

[9] Daniel Siemaszko. Positive and Negative Sequence Control for Power Converters under Weak Unbalanced Networks. In *Electrical Systems for Aircraft, Railway and Ship Propulsion (ESARS)* (October 2012). DOI 10.1109/ESARS.2012.6387479. Cited on page(s) 47, 54.

[10] Hong-Seok Song and Kwanghee Nam. Dual Current Control Scheme for PWM Converter under Unbalanced Input Voltage Conditions. *IEEE Transactions on Industrial Electronics* **46** (5), 953–959 (October 1999). ISSN 1557-9948. DOI 10.1109/41.793344. Cited on page(s) 48, 53, 56.

[11] Sanjay K. Chaudhary, Remus Teodorescu, Pedro Rodriguez, Philip Carne Kjaer, and Ani M. Gole. Negative Sequence Current Control in Wind Power Plants With VSC-HVDC Connection. *IEEE Transactions on Sustainable Energy* **3** (3), 535–544 (July 2012). ISSN 1949-3037. DOI 10.1109/TSTE.2012.2191581. Cited on page(s) 48.

[12] Łukasz Hubert Kocewiak. Harmonics in Large Offshore Wind Farms. *Doctoral thesis*. Department of Energy Technology, Aalborg University, Denmark (February 2012). URL https://vbn.aau.dk/en/publications/harmonics-in-large-offshore-wind-farms, accessed on 2023-03-24. ISBN 978-87-92846-04-4. Cited on page(s) 50, 53, 54.

[13] Siemens AG. GEAFOL cast-resin transformers 100 to 16000 kVA. Catalogue TV1|2007 E50001-K7101-A101-A6-7600 Siemens AG Power Transmission and Distribution Transformers Division (2007). Cited on page(s) 51.

[14] ABB. ACS880-77LC/-87LC/-87CC Wind Turbine Converters. System Description 3AXD50000022022 Rev C ABB Zurich, Switzerland (2020). URL https://search.abb.com/library/Download.aspx?DocumentID=3AXD50000022022&LanguageCode=en&DocumentPartId=1&Action=Launch. Cited on page(s) 51, 52.

[15] Siemens. The Top-Performing Wind Converter Trusted Technology for Maximum Power Yield – SINAMICS W180. Brochure PDLD-B10099-00-7600 Siemens AG Munich, Germany (2017). URL https://assets.new.siemens.com/siemens/assets/api/uuid:26ef63b7cae9657fae9e98618212ba874f3fd729/455_170680_ws_sinamicsw180us.pdf accessed on 2020-09-27, no longer available as of 2023-04-21. Cited on page(s) 51, 52.

[16] Marco Liserre, Frede Blaabjerg, and Antonio Dell'Aquila. Step-by-step design procedure for a grid-connected three-phase PWM voltage source converter. *Tailor & Francis Online International Journal of Electronics* **91** (8), 445–460 (8 2004). ISSN 0020-7217, 1362-3060. DOI 10.1080/00207210412331306186. Cited on page(s) 52.

[17] Rafael Peña-Alzola, Marco Liserre, Frede Blaabjerg, Rafael Sebastián, Jörg Dannehl, and Friedrich Wilhelm Fuchs. Analysis of the Passive Damping Losses in LCL-Filter-Based Grid Converters. *IEEE Transactions on Power Electronics* **28** (6), 2642–2646 (June 2013). ISSN 0885-8993, 1941-0107. DOI 10.1109/TPEL.2012.2222931. Cited on page(s) 52.

[18] Remus Narcis Beres, Xiongfei Wang, Marco Liserre, Frede Blaabjerg, and Claus Leth Bak. A Review of Passive Power Filters for Three-Phase Grid-Connected Voltage-Source Converters. *IEEE Journal of Emerging and Selected Topics in Power Electronics* **4** (1), 54–69 (March 2016). ISSN 2168-6777, 2168-6785. DOI 10.1109/JESTPE.2015.2507203. Cited on page(s) 52.

[19] Henrik Brantsæter, Łukasz Kocewiak, Elisabetta Tedeschi, and Atle Rygg Årdal. Passive Filter Design and Offshore Wind Turbine Modelling for System Level Harmonic Studies. *ELSEVIER Energy Procedia* **80**, 401–410 (2015). ISSN 1876-6102. URL https://ntnuopen.ntnu.no/ntnu-xmlui/handle/11250/2381992. DOI 10.1016/j.egypro.2015.11.444. Cited on page(s) 52.

[20] Zhengmao Ye and Habib Mohamadian. Application of modern control theory on performance analysis of generalized notch filters. In *IEEE 2016 5th International Conference on Modern Circuits and Systems Technologies (MOCAST)* Thessaloniki, Greece (May 2016). DOI 10.1109/MOCAST.2016.7495100. Cited on page(s) 53.

[21] Jakob Bærholm Glasdam. Harmonics in Offshore Wind Power Plants: Application of Power Electronic Devices in Transmission Systems. *Doctoral thesis*. Department of Energy Technology, Aalborg University, Denmark (March 2015). URL https://vbn.aau.dk/ws/portalfiles/portal/316459292/jakob_b_rholm_glasdam.pdf, accessed on 2023-03-24. Cited on page(s) 53, 54.

[22] Song Zhang, Wenhua Wu, Yandong Chend, Jian Luo, Zhixing. He, and Zhiwei Xie. Sequence impedance modeling and characteristic analysis of island inverter with dual sequence control. In *2020 IEEE 9th International Power Electronics and Motion Control Conference (IPEMC2020-ECCE Asia)* pages 400–404 (November 2020). DOI 10.1109/IPEMC-ECCEAsia48364.2020.9368210. Cited on page(s) 54.

[23] Pedro Rodriguez, Josep Pou, Joan Bergas, J. Ignacio Candela, Rolando P. Burgos, and Dushan Boroyevich. Decoupled Double Synchronous Reference Frame PLL for Power Converters Control. *IEEE Transactions on Power Electronics* **22** (2), 584–592 (March 2007). ISSN 1941-0107. DOI: 10.1109/TPEL.2006.890000. Cited on page(s) 54, 59.

[24] Sophocles J. Orfanidis. Introduction to Signal Processing. Prentice Hall Signal Processing Series. Prentice Hall Englewood Cliffs, N.J (1996). ISBN 978-0-13-209172-5. URL www.ece.rutgers.edu/~orfanidi/i2sp, visited on 2023-03-24. Cited on page(s) 55, 63.

[25] Saeed Golestan, Malek Ramezani, Josep M. Guerrero, Francisco D. Freijedo, and Mohammad Monfared. Moving Average Filter Based Phase-Locked Loops: Performance Analysis and Design Guidelines. *IEEE Transactions on Power Electronics* **29** (6) (June 2014). ISSN 1941-0107. DOI 10.1109/TPEL.2013.2273461. Cited on page(s) 55, 56.

[26] Jan Svensson, Massimo Bongiorno, and Ambra Sannino. Practical Implementation of Delayed Signal Cancellation Method for Phase-Sequence Separation. *IEEE Transactions on Power Delivery* **22** (1), 18–26 (January 2007). ISSN 1937-4208. DOI: 10.1109/TPWRD.2006.881469. Cited on page(s) 56.

[27] Francisco A. S. Neves, Marcelo Cabral Cavalcanti, Helber Elias Paz de Souza, Fabrício Bradaschia, Emilio J. Bueno, and Mario Rizo. A Generalized Delayed Signal Cancellation Method for Detecting Fundamental-Frequency Positive-Sequence Three-Phase Signals. *IEEE Transactions on Power Delivery* **25** (3), 1819–1825 (April 2010). DOI 10.1109/TPWRD.2010.2044196. Cited on page(s) 56.

[28] Saeed Golestan, Francisco D. Freijedo, Ana Vidal, Alejandro G. Yepes, Josep. M. Guerrero, and Jesus Doval-Gandoy. An Efficient Implementation of Generalized Delayed Signal Cancellation PLL. *IEEE Transactions on Power Electronics* **31** (2), 1085–1094 (February 2016). ISSN 1941-0107. DOI 10.1109/TPEL.2015.2420656. Cited on page(s) 56.

[29] Lennart Ljung. System Identification: Theory for the User. Prentice Hall PTR Upper Saddle River, NJ 07458, USA second edition (1999). ISBN 978-0-13-656695-3. Cited on page(s) 63.

[30] Paul Brian Brogan, Thyge Knueppel, Andrew Roscoe, and Douglas Elliot. Improved Converter Network Bridge Controller. Patent US 20210021209A1 Siemens Gamesa Renewable Energy AS (January 2021). URL https://uspto.report/patent/app/20210021209, visited on 2023-05-06. Cited on page(s) 64.

Chapter 5

Sharing of Primary Power Reserves in Isolated Grids

Research Goals and Contributions to the Scientific Literature

This chapter is tied to Research Goal II, which proposes control structures, as well as Research Goal III, which validates them in the laboratory. It stems from Research Questions III and IV and focuses on the sharing of primary power reserves for the frequency control in an isolated grid fed by traditional synchronous generation, connected to converter-interfaced generation, and dominated by constant power loads (CPLs). Contribution IV to the scientific literature is presented in this chapter, which compiles the contents of Publication VI.

A critical aspect for operating an electric grid with traditional synchronous generation with a relevant participation of intermittent renewable energy sources (RES) is the continuous compensation of imbalances between consumption and generation. These are counteracted by the activation of distributed power reserves in a hierarchical manner. Primary reserves perform a droop-based control and respond automatically in a time scale of seconds after power imbalances limiting the frequency deviations. Secondary reserves are subordinated to the grid's automatic generation control (AGC) and bring the frequency back to its rated value within seconds to minutes after power imbalances [1]. In the European context, primary reserves are named frequency containment reserves (FCR) and are coordinated nationally by transmission system operators (TSOs) [2].

Three types of FCR have recently been defined for the Nordic synchronous area, which includes the power grids of Finland, Sweden, Norway, and eastern Denmark. These types are [3]:

1. $\mathrm{FCR_N}$: normal operation frequency containment reserves.
2. $\mathrm{FCR_D}$: large disturbance frequency containment reserves.
3. $\mathrm{FCR_I}$: frequency containment reserves for islanded operation.

$\mathrm{FCR_N}$ and $\mathrm{FCR_D}$ cooperate in the interconnected system, whereas $\mathrm{FCR_I}$ are a simplified version of the pair $\mathrm{FCR_{N+D}}$ that are activated only during islanding events. The same provider can supply any of these reserves, depending on the fulfillment of technical requirements, which are evaluated in a qualification process, and the grid operating conditions. Markets under the responsibility of the national TSOs are expected to be established for coordinating the availability and provision of these three types of FCR in the Nordic synchronous area [4–6].

Only the FCR_N are active when the grid frequency is within a given band around the rated value. If the frequency goes outside this band, the FCR_N saturate and the FCR_D are activated. This frequency band is common to the whole grid and is defined by the TSO. When in interconnected mode, an FCR provider may feature two different slopes in its power-frequency droop characteristic, namely, one for operation as FCR_N and another one for operation as FCR_D [3]. For larger frequency variations or in case of large rates of change of frequency, both criteria being defined by the TSO, a primary reserve provider must switch to the FCR_I mode. In this mode, the reserve provider adopts a single slope for its power-frequency droop characteristic [7].

Offshore isolated industrial grids typically employ one of the following strategies for active power sharing between power generators [8–11].

1. All units operate in isochronous mode.
2. One unit operates in isochronous mode while all others operate in droop control.
3. All units operate in droop control with a centralized secondary frequency controller located in the power management system (PMS).

The first strategy demands a fast communication link among the generators implemented via an analog hardwired line or via serial communication. In case of faults in this communication line, the system defaults to the strategies with droop control that are analogous to the FCR_I operation defined for the Nordic synchronous area. It is worth noting that, despite operating in an analogous manner to the Nordic FCR_I, the generators in isolated offshore installations are not required to fulfil grid codes defined by TSOs.

In this chapter, an expansion of the Nordic synchronous area FCR_I concept is proposed together with a theoretical framework for the analysis of the distribution of reserves among multiple providers. The single slope power-frequency droop of the original FCR_I is expanded into a segmented droop with different regions for normal and large disturbance operations. To the best extent of the author's knowledge, the expanded FCR_I concept has not been explored in the offshore industry [8–10]. It has neither been investigated in the literature of isolated offshore oil and gas (O&G) platforms expected to be connected to wind farms (WFs) with the support of energy storage systems (ESSs) [12, 13], without the support of ESSs [14–17], nor with inertial support provided by the wind turbines (WTs) [17]. Moreover, the extended FCR_I concept was not employed in studies on the stability of power-intensive land-based isolated grids fed by hydro, diesel, and coal-based traditional synchronous generation that must balance the intermittency of a considerable wind or photo-voltaic (PV) contribution [18, 19]; it was not employed in the literature on ac microgrids [20–22] either.

This chapter analyzes the stability and performance improvement due to the coordinated distribution of primary power reserves based on the expanded FCR_I concept in the study case using numerical simulations in DIgSILENT PowerFactory 2020 SP2A and experimental validation. The impact of different contributions of the traditional synchronous generators and converter-interfaced devices controlling the grid frequency in the eigenvalues of the system is assessed first. Modal analysis and participation factors [23] are used to associate states with eigenvalues and help identify devices and parameters that strongly influence the system's oscillation modes. Experimental results obtained with real-time simulator (RTS) and power hardware-in-the-loop (PHIL), tests which proved to be efficient tools for analysis and validation of devices and their controls in isolated grids [24], are presented. As demonstrated in section 5.10, when compared to the traditional droop control employed in the offshore O&G industry, the expanded FCR_I provides better performance, especially in regard to frequency regulation and nadir.

The main contributions of this chapter are as follows:

1. It presents an expansion of the Nordic concept of FCR_I and demonstrates with numerical simulations and experimental tests the advantages, from a frequency control perspective, of replacing slower turbogenerators (GTs) by faster converter-interfaced ESSs as the main providers of primary power reserves. Moreover, it shows that this replacement causes a non-critical reduction in the damping of oscillation modes associated with frequency measurement transducers and controllers of constant power devices.
2. It takes into consideration the negative effects caused by CPLs in the electrical grid, an issue commonly overlooked in the literature of power-intensive isolated grids.
3. It performs a comparison with an industry state-of-the-art control strategy that provides valuable insights for the application of the extended FCR_I in increasingly complex islanding scenarios in interconnected systems with traditional synchronous generation, large participation of intermittent RES, and ESSs.

The chapter is organized as follows: the expanded FCR_I concept is presented in section 5.1; CPLs are discussed in section 5.2; the sharing and the coordination of power reserves in an isolated grid are explained in section 5.3; the FCR controllers are introduced in section 5.4; a theoretical approach for the expanded FCR_I concept via modeling and stability analysis is performed in section 5.5; a simplified stability assessment is performed in section 5.6; the study case is described in section 5.7; a validation of the theoretical analysis is then presented in two sections with a detailed stability assessment in section 5.8 and an experimental validation with laboratory PHIL tests in section 5.9; thereafter, a comparison with a state-of-the-art industry method is made in section 5.10; a discussion is made in section 5.11; and, finally, the concluding remarks are listed in section 5.12.

5.1 EXPANDED FREQUENCY CONTAINMENT RESERVES FOR ISOLATED OPERATION (FCR_I)

In the Nordic synchronous area, primary reserve providers are required to have two parameter sets, one for island operation and another one for interconnected operation. In case of an islanding event, the reserve provider must switch to the FCR_I mode and adopt a single slope for its power-frequency droop characteristic [7], as illustrated in figure 5.1. Within this context, an expansion of the single-slope power-frequency droop characteristic of the Nordic FCR_I concept into a segmented one with different regions for normal and large disturbance operation is proposed in this chapter, see figure 5.2. This expanded concept is applied to a study case representing an O&G platform connected to a WF and equipped with an ESS. For simplicity of notation, the normal isolated operation reserves are named FCR_N and the large disturbance reserves for isolated operation are named FCR_D. These new FCR_N and FCR_D for isolated grids are analogous to the ones for interconnected operation defined in [3].

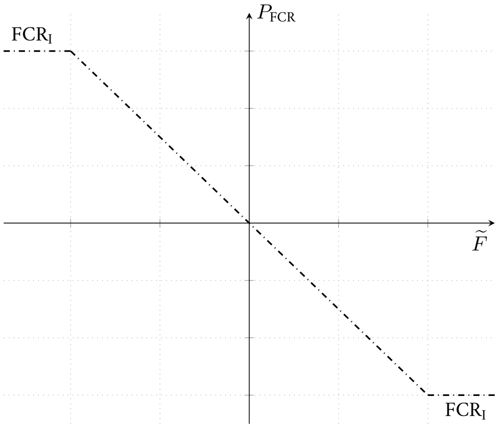

FIGURE 5.1 Original FCR_I characteristic of the system as defined in [7].

© Daniel Mota 2023 | Redrawn and recomposed from Publication VI | Source code information at Part III.

The expanded FCR_I characteristic of the system is illustrated by figure 5.2. The limit $\widetilde{F}_\text{N}$ between the regions of FCR_N and FCR_D activation is defined in terms of the deviation of the measured ac frequency $\widehat{F}$ from its nominal value F_n, namely

$$\widetilde{F} = \widehat{F} - F_n.$$

The FCR_N are active, and the FCR_D are inactive, when

$$|\widetilde{F}| \leq \widetilde{F}_\text{N}.$$

The value of $\widetilde{F}_\text{N}$ is 0.1 Hz (0.2 %) for the Nordic interconnected grid [3]. However, isolated grids usually endure more severe relative power imbalances and resulting

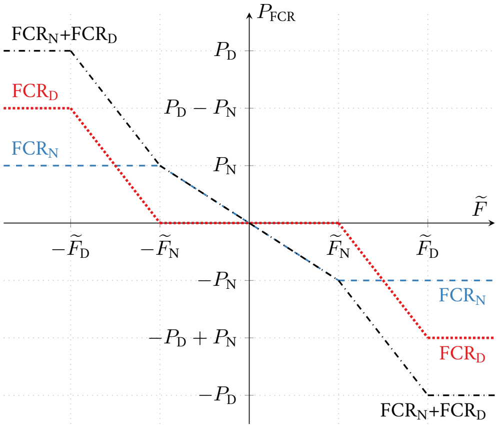

FIGURE 5.2 Expanded FCR$_{\mathrm{I}}$ characteristic of the system, adapted from the FCR$_{\mathrm{N+D}}$ for interconnected operation defined in [3].

© Daniel Mota 2023 | Redrawn and recomposed from Publication VI | Source code information at Part III.

frequency disturbances than a country or continental wide grid. For instance, the recommended practices for the design of electrical power generation in merchant, commercial, and naval vessels [25] define a tolerance of $\pm 3\,\%$ for the "maximum permitted departure from nominal frequency during normal operation, excluding transient and cyclic frequency variations." Hence, a value between 0.2 % and 3 % will later be adopted for $\widetilde{F}_{\mathrm{N}}$ in sections 5.9 and 5.10. The system is considered under a large disturbance when

$$|\widetilde{F}| > \widetilde{F}_{\mathrm{N}}.$$

Under this condition, the FCR$_{\mathrm{N}}$ are saturated at P_{N} and the FCR$_{\mathrm{D}}$ are activated.

5.2 CONSTANT POWER LOADS

WTs as well as solar PV panels can be considered constant power sources (CPSs) as their controllers typically operate in maximum power point tracking; in other words, tracking the optimum power for a given wind speed or solar irradiation [26]. Energy storage devices (ESDs) connected to a common ESS dc link, as the ones studied in Publications I, II, and VI, can also run as CPLs or CPSs. Isolated industrial grids can, moreover, serve a considerable amount of CPLs such as variable frequency drives [27, 28].

Even though constant power loads and sources are known to cause instabilities in dc microgrids [29, 30] and in ac microgrids [31, 32], it is common in studies of the integration of wind power supported by ESSs and by converter-interfaced flexible loads (FLX) [33], as well as those only supported by an ESS [12, 13], to represent the total electrical load of the isolated O&G platform as constant impedance loads

(CZLs). Power electronic oriented studies on CPLs in microgrids [34, 35], moreover, tend to focus on the stability of the converters, not in frequency control nor in the stability of the complete grid. If combined with power electronic converters (PECs), CPL and CPS also give rise to new instability phenomena both in micro and large interconnected grids [24, 36]. Remark that modern type 4 [37] WTs, solar PV farms, ESSs, and some types of loads are all connected to the grid via PECs. Converter driven instabilities, therefore, should not be overlooked when integrating this equipment in isolated grids.

5.3 SHARING AND COORDINATION OF PRIMARY AND SECONDARY RESERVES

The stochastic nature of wind can lead to an increased number of start-stop operations and more variable load profiles for the GTs of an O&G platform connected to a WF resulting in higher wear and tear and an overall degradation of the electric power quality and grid frequency stability [38, 39].Therefore, coordination strategies that allow prioritizing converter-interfaced loads and ESSs instead of GTs as the main source of power for fast frequency control are key to a successful integration of wind power into offshore O&G facilities. In this section, a hierarchical frequency control structure that allows such a prioritization and employs the extended $\mathrm{FCR_I}$ concept is explained.

5.3.1 Secondary Reserves

Figure 5.3 depicts the frequency control structure of the study case's isolated grid where reserve providers play a subordinate role under a centralized PMS. The secondary frequency controller, which is a part of the PMS, is responsible for correcting steady-state errors in the frequency of the isolated grid. It employs a proportional and integral (PI) regulator that reacts to the frequency deviation and generates the total secondary power reference $\overset{*}{P}_{\mathrm{S}}$ which is shared among two GTs and a fuel cell (FC) and electrolyzer (EL) pair. The measured and filtered value of the power delivered by the FC and EL, denoted by $\widehat{P}_{\mathrm{FC}}$ and $\widehat{P}_{\mathrm{EL}}$, respectively, are deducted from the secondary power reference sent to the governors of the GTs, see equation (5.1). Although not represented in figure 5.3, the reserve providers have their own limits for rate of change of power, and the GTs have an extra input for the base load power reference.

$$\overset{*}{P}{}_{\mathrm{S}}^{\mathrm{EL}} = \overset{*}{P}{}_{\mathrm{S}}^{\mathrm{FC}} = \overset{*}{P}_{\mathrm{S}}, \quad \overset{*}{P}{}_{\mathrm{S}}^{\mathrm{GT1}} = \overset{*}{P}{}_{\mathrm{S}}^{\mathrm{GT2}} = \frac{\overset{*}{P}_{\mathrm{S}} - \widehat{P}_{\mathrm{FC}} - \widehat{P}_{\mathrm{EL}}}{2} \tag{5.1}$$

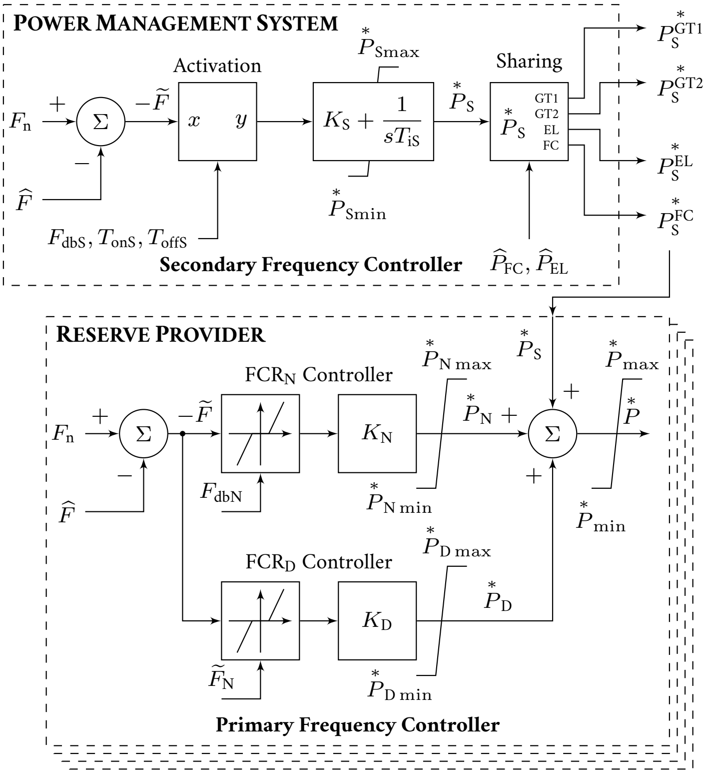

FIGURE 5.3 Hierarchic structure of the ac frequency control

© Daniel Mota 2023 | Redrawn and recomposed from Publication VI | Source code information at Part III.

5.3.2 *Primary Reserves*

The distributed primary frequency control is performed locally at each reserve provider. All FCR$_\mathrm{N}$ providers shall be able to supply their allocated reserve power P_N for a frequency drop of $\widetilde{F}_\mathrm{N}$. Conversely, the providers should absorb P_N for a frequency increase of $\widetilde{F}_\mathrm{N}$. Therefore, the frequency-to-power gain of a FCR$_\mathrm{N}$ provider is

$$K_\mathrm{N} = \frac{P_\mathrm{N}}{\widetilde{F}_\mathrm{N}} \quad \left[\mathrm{W\,Hz^{-1}}\right]. \tag{5.2}$$

When considered for the whole system, this gain is called regulating strength in [3] and frequency bias in [1]. In this dissertation, it will be referred to as FCR gain or frequency-to-power gain. The FCR$_\mathrm{D}$ frequency-to-power gain is defined as

$$K_\mathrm{D} = \frac{P_\mathrm{D} - P_\mathrm{N}}{\widetilde{F}_\mathrm{D} - \widetilde{F}_\mathrm{N}} \quad \left[\mathrm{W\,Hz^{-1}}\right]. \tag{5.3}$$

The total frequency-to-power characteristic of the system is, therefore, a composition of the normal and large disturbance reserves as illustrated in figure 5.2. The

FCR$_\mathrm{D}$ controllers feature a dead band, see figure 5.3, between $\pm\widetilde{F}_\mathrm{N}$, which ensures that only the FCR$_\mathrm{N}$ are activated in normal operation. Notice that gains K_N and K_D do not necessarily have to be equal.

5.4 FCR Controllers

The power contribution of the FCR providers is a function of $\widetilde{F}$. Each provider in figure 5.3 measures the frequency $\widehat{F}$ and subtracts it from the rated frequency F_n. The resulting $-\widetilde{F}$ is fed to two proportional controllers, one for FCR$_\mathrm{N}$ and one for FCR$_\mathrm{D}$. Each controller has its own gain (K), limiters (max, min), and a symmetric dead band (F_dbN and $\widetilde{F}_\mathrm{N}$). The dead-band blocks are symmetric and are implemented as

$$y = \begin{cases} x + F_\mathrm{db}, & \text{if } x < -F_\mathrm{db} \\ 0, & \text{if } -F_\mathrm{db} \leq x \leq F_\mathrm{db} \\ x - F_\mathrm{db}, & \text{if } x > F_\mathrm{db} \end{cases}$$

where x is the input and y is the output of the block. The FCR$_\mathrm{N}$ power reference ($\overset{*}{P}_\mathrm{N}$) and the FCR$_\mathrm{D}$ power reference ($\overset{*}{P}_\mathrm{D}$) are summed to the secondary power reference ($\overset{*}{P}_\mathrm{S}$). Notice that $\overset{*}{P}_\mathrm{S}$ is sent to the providers by the PMS via communication link. The total power reference output ($\overset{*}{P}$) has its own independent maximum and minimum limits.

The PMS allocates a primary reserve quota to each provider based on a security assessment, which takes into consideration the grid operational conditions and the forecasts of loads and RES. To receive a quota, the provider must be able to respond symmetrically to both positive and negative variations in $\widetilde{F}$ and deliver the total assigned reserve power P_N (up or down) when $|\widetilde{F}| = \widetilde{F}_\mathrm{N}$. Based on the assigned reserves, each provider calculates its gains K_N and K_D according to equations (5.2) and (5.3), respectively. Remark that the transient response of each FCR provider does not rely on a fast communication link with the PMS, as the FCR control loops are implemented locally and fast dynamic changes to the power allocation are not expected.

5.4.1 Role of Dead Bands in FCR

The normal operation and large disturbance reserves are properly coordinated by a dead-band block in the FCR$_\mathrm{D}$ providers, shown in figure 5.3. The limit frequency $\widetilde{F}_\mathrm{N}$ is unique for the system and is known by all FCR providers. By adjusting the FCR$_\mathrm{D}$ dead band to $\widetilde{F}_\mathrm{N}$, one guarantees that the large disturbance reserves will only be activated once the FCR$_\mathrm{N}$ are saturated. The limits $\overset{*}{P}_\mathrm{Nmax}$ and $\overset{*}{P}_\mathrm{Nmin}$, of each FCR$_\mathrm{N}$ provider are assumed to be symmetric and their absolute values are equal to P_N. Although not a desirable feature, a non-negligible dead band F_dbN might be necessary for a proper operation of a specific FCR$_\mathrm{N}$ provider. In this case, calculating the gain K_N with equation (5.2) leads to a reduced FCR$_\mathrm{N}$ capacity. If the provider requires a small dead band for proper operation, the effects of the dead band can be compensated locally by calculating the frequency-to-power gain according to equation (5.4) without the intervention of the PMS.

$$K_\mathrm{N} = \frac{P_\mathrm{N}}{\widetilde{F}_\mathrm{N} - F_\mathrm{dbN}} \tag{5.4}$$

Figure 5.4 illustrates the effects of a dead band in the total power delivered by an FCR$_\mathrm{N}$ provider. In addition to not responding when the frequency deviation $\widetilde{F}$ is within the dead band, the FCR$_\mathrm{N}$ provider does not deliver P_N at $\widetilde{F}_\mathrm{N}$, as seen in dotted red. When K_N is calculate with equation (5.4) (dashed blue), the provider delivers its full capacity P_N at $\widetilde{F}_\mathrm{N}$. It is worth noting that the dead band F_dbN is expected to the small. As an example, one can mention the requirements from the North American Electric Reliability Corporation [40], which demand from "equipment capable of providing primary frequency response" to respond to "frequency excursion events measured at the plant point of measurement with a maximum deadband of ±0.036 Hz".

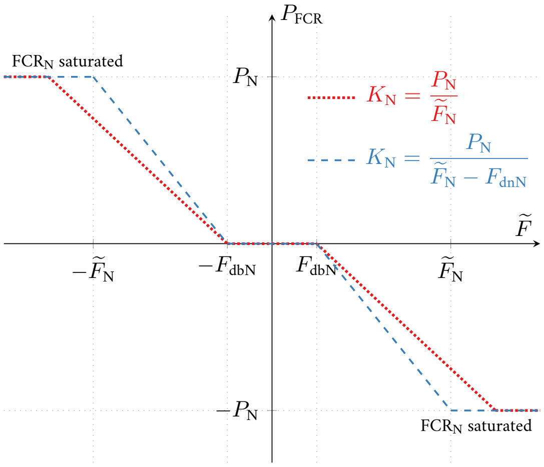

FIGURE 5.4 Effects of the dead band F_dbN in the power delivered by an FCR$_\mathrm{N}$ provider when K_N is calculated with equation (5.2) (dotted red) and equation (5.4) (dashed blue).

© Daniel Mota 2023 | Source code information at Part III.

5.5 THEORETICAL FRAMEWORK FOR A STABILITY ASSESSMENT

Converter interfaced reserves have much faster responses than traditional turbogenerators [41]. The benefits of these faster responses can be evaluated, initially, with the classical rotating mass model [42, 43]. For that, the spinning reserves of the system (the GTs) are aggregated into a single rotating mass with moment of inertia J as done previously in chapter 2 (figure 2.2). The turbines apply torque to increase the angular frequency ω of the rotating mass, whereas the aggregated electrical loads apply torque to reduce ω. The powers in equation (2.1) from chapter 2 can be renamed and rearranged into

$$\omega(t) J \frac{\mathrm{d}\omega(t)}{\mathrm{d}t} = P_{\mathrm{FCR}}(t) + P_{\mathrm{S}}(t) - P_{\mathrm{L}}(t) \tag{5.5}$$

where P_{FCR} is the FCR primary response, P_{S} is the secondary reserve power, and P_{L} is the total load power. Let the following normalizing quantities be introduced:

$$H = \frac{J{\omega_n}^2}{2S_n} \quad \Rightarrow \quad J = \frac{2S_n H}{{\omega_n}^2} = \frac{S_n M}{{\omega_n}^2} \tag{5.6}$$

$$\widetilde{f} = \frac{\omega - \omega_n}{\omega_n} \quad \Rightarrow \quad \omega = \omega_n \left(\widetilde{f} + 1\right) \tag{5.7}$$

$$p_{\mathrm{FCR}} = \frac{P_{\mathrm{FCR}}}{S_n} \quad \Rightarrow \quad P_{\mathrm{FCR}} = p_{\mathrm{FCR}} S_n \tag{5.8}$$

$$\widetilde{p} = \frac{P_{\mathrm{L}} - P_{\mathrm{S}}}{S_n} \quad \Rightarrow \quad P_{\mathrm{S}} - P_{\mathrm{L}} = -S_n \widetilde{p} \tag{5.9}$$

where H is the inertia constant, M is the mechanical starting time, which is equal to twice H, S_n is the system's apparent power, ω_n is the nominal angular frequency, $\widetilde{f}$ is the normalized frequency deviation, p_{FCR} is the normalized power supplied by the frequency containment reserves, and $\widetilde{p}$ is the normalized imbalance of power between the secondary and load. By rewriting the variables in equation (5.5) with the quantities in equations (5.6) to (5.9), one obtains

$$\omega_n \left(\widetilde{f}(t) + 1\right) \frac{S_n M}{{\omega_n}^2} \frac{\mathrm{d}\left(\omega_n \left(\widetilde{f}(t) + 1\right)\right)}{\mathrm{d}t} = S_n\, p_{\mathrm{FCR}}(t) - S_n\, \widetilde{p}(t)$$

which can be simplified into

$$\left(\widetilde{f}(t) + 1\right) M \frac{\mathrm{d}\widetilde{f}(t)}{\mathrm{d}t} = p_{\mathrm{FCR}}(t) - \widetilde{p}(t). \tag{5.10}$$

Figure 5.5 represents equation (5.10) in a block diagram form that can be easily employed in computer simulation software tools as MATLAB Simulink.

A linear small-signal stability analysis of the system represented by equation (5.10) can be performed by assuming that $\widetilde{f}(t) + 1 \approx 1$, in other words,

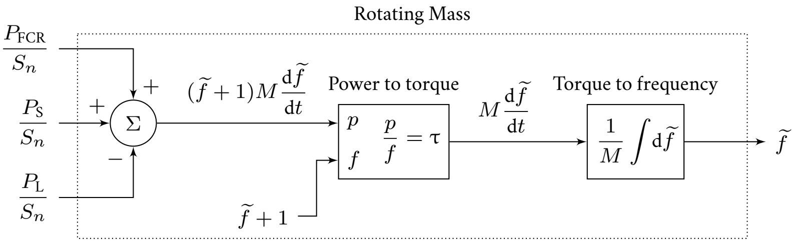

FIGURE 5.5 Block diagram of the nonlinear rotating mass model represented by equation (5.10).

assuming that angular frequency ω is approximately equal to the nominal ω_n. In this case, equation (5.10) can be linearized to

$$M\frac{\mathrm{d}\widetilde{f}(t)}{\mathrm{d}t} = p_{\mathrm{FCR}}(t) - \widetilde{p}(t)$$

which, in the Laplace domain, becomes

$$sM\widetilde{f}(s) = p_{\mathrm{FCR}}(s) - \widetilde{p}(s) \tag{5.11}$$

where s is the complex frequency.

5.5.1 Single Primary Reserve Provider

If the response of the primary power provider is modeled as a low-pass filter (LPF) in the Laplace domain as in

$$p_{\mathrm{FCR}}(s) = -\frac{k}{sT+1}\widetilde{f}(s) \tag{5.12}$$

where k is equal to the normalized primary power delivered per normalized frequency deviation and the time constant T is in seconds, then the balance of power in equation (5.11) becomes

$$sM\widetilde{f}(s) = -\frac{k}{sT+1}\widetilde{f}(s) - \widetilde{p}(s)$$

which can be re-organized into the transfer function $G(t)$ in equation (5.13) with the normalized imbalance of power $\widetilde{p}$ as input and the normalized frequency $\widetilde{f}$ as output.

$$G(s) = \frac{\widetilde{f}(s)}{\widetilde{p}(s)} = -\frac{sT+1}{MTs^2+Ms+k} \tag{5.13}$$

Notice that when T tends to zero, $G(t)$ tends to a first-order LPF. This means that there is no overshoot (no nadir nor zenith) in the response of $\widetilde{f}$ after a power imbalance $\widetilde{p}$. Notice also that the poles of the $G(t)$ are at the complex frequencies given by

$$s = \frac{-M \pm \sqrt{M^2 - 4MTk}}{2MT}.$$

As $M > 0$, $T > 0$, and $k > 0$, the poles of the linearized model always have negative real parts since

$$M > \Re\left(\sqrt{M^2 - 4MTk}\right).$$

The model is, therefore, stable for small disturbances. However, for large disturbances, the nonlinearity represented by the term $(\widetilde{f}(t) + 1)$ in equation (5.10) can lead the system to instability. Poorly damped responses can, furthermore, quickly lead reserve providers to saturation. Thus, it is important to remark the words "linearized" and "small disturbances" as the transfer function $G(s)$ in equation (5.13) is obtained with the assumption that $\omega \approx \omega_n$.

From equation (5.13), it is possible to deduce that constant imbalance of power $\widetilde{p}$ causes a steady-state change in the frequency $\widetilde{f}$ that is inversely proportional to the gain k. It is important to emphasize that the inertia constant H (acceleration time M) does not influence the steady-state error. However, M, T, and k play a role in how fast and how smoothly $\widetilde{f}$ reaches the steady state after a power imbalance. The damping ζ and natural oscillation frequency ω_{nat} of the second order transfer function G can be calculated by algebraic manipulation of equation (5.13). They depend on H, T, and k, as shown in equations (5.14) and (5.15). The higher the inertia constant, the higher the damping and the lower the natural frequency. The longer the actuator time delay, the more oscillatory the system is and the slower ω_{nat} becomes.

$$\zeta = \sqrt{\frac{M}{4kT}} = \sqrt{\frac{H}{2kT}} \tag{5.14}$$

$$\omega_{\text{nat}} = \sqrt{\frac{k}{MT}} = \sqrt{\frac{k}{2HT}} \tag{5.15}$$

The control strategies adopted in this chapter do not include, on purpose, virtual synchronous machines (VSMs). The reasons for that are threefold.

1. The equivalence between frequency droop and VSMs has been pointed out by D'Arco and Suul [44].
2. Enough physical inertia is available in the study cases used in Publications I to III and VI in the form of GTs.
3. The time delay of the actuator controlling the primary reserve power has a considerable impact on the damping of oscillations in the system frequency, as indicated by the second order transfer function $G(s)$ in equation (5.13), ζ in equation (5.14), and ω_{nat} in equation (5.15). The longer the delay of the actuator, the more oscillatory the system becomes.

As demonstrated in this chapter, the primary frequency reserves provided by a fast ESS improve the stability of the system even without the use of VSMs.

When the primary reserve is provided by traditional GTs, the total intrinsic delay of the governor and turbine is in the order of hundreds of milliseconds [45]. However, if the primary reserve is provided by a fast converter-interface ESS, the delay drops by at least one order of magnitude [41]. When T in equation (5.13) approaches zero, the transfer function between the power imbalance and the system frequency tends to a first-order LPF. For the normal operation of an isolated grid, a two-fold advantage is obtained by prioritizing the allocation of primary reserves into fast converter-interfaced ESS and not on slower GTs. Firstly, the GTs are allowed to operate at a more constant power, which reduces the wear and tear of the mechanical parts. Secondly, the system becomes less oscillatory even without a VSM scheme or derivative terms at the ESS reserves.

5.5.2 Multiple Primary Reserve Providers

As discussed previously in section 3.3.3, the frequency $\widetilde{f}(t)$ is assumed to be reasonably identical at any given time t within the whole system. Let the system's n primary power reserve providers be modeled as first-order LPFs as in

$$p_{\mathrm{FCR}}(s) = -\widetilde{f}(s) \sum_{i=1}^{n} \frac{k_i}{sT_i + 1}$$

where the gains k_i are equal to the normalized power provided divided by the normalized frequency deviation and the time constants T_i are in seconds. Then, the balance of power in equation (5.11) can be written as

$$sM\widetilde{f}(s) = -\left(\widetilde{f}(s) \sum_{i=1}^{n} \frac{k_i}{sT_i + 1}\right) - \widetilde{p}(s) \tag{5.16}$$

which can be reorganized into

$$G(s) = \frac{\widetilde{f}(s)}{\widetilde{p}(s)} = \\ -\frac{\prod_{i=1}^{n} (sT_i + 1)}{\left(Ms \prod_{i=1}^{n} (sT_i + 1)\right) + \sum_{j=1}^{n} \left(k_j \prod_{i=1|i\neq j}^{n} (sT_i + 1)\right)}. \tag{5.17}$$

Notice that, in equation (5.17), the variables i and j represent indices and not current nor the complex number j. If the products and sums were to be expanded, equation (5.17) would take the form

$$G(s) = \frac{\widetilde{f}(s)}{\widetilde{p}(s)} =$$
$$= \frac{s^n\left(T_1 T_2 \cdots T_n\right) + s^{n-1}(\cdots) + \cdots + 1}{M s^{n+1}\left(T_1 T_2 \cdots T_n\right) + M s^n(\cdots) + \cdots + \left(k_1 + k_2 + \cdots + k_n\right)}.$$

The transfer function $G(s)$ in equation (5.17) is, therefore, of order $n+1$. It is worth recalling that n is the number of primary reserve providers in the isolated grid. A constant imbalance of power $\widetilde{p}$ causes a steady-state deviation in $\widetilde{f}$ that is inversely proportional to the sum of gains k_i and depends neither on the inertia constant H, nor M, nor on the providers' time delays T_i. This is demonstrated in equation (5.18) by the application of the final value theorem to $G(s)\widetilde{p}(s)$ when the unbalance $\widetilde{p}(s)$ is a step with amplitude p. However, H, M, delays T_i, and gains k_i concurrently affect the location in the complex plane of the poles of $G(s)$; in other words, they influence the damping and natural frequency of the system's oscillation modes.

$$\lim_{t\to\infty} \widetilde{f}(t) = \lim_{s\to 0} sG(s)\widetilde{p}(s) \xrightarrow{\widetilde{p}(s)=\frac{p}{s}} \lim_{t\to\infty} \widetilde{f}(t) = \frac{-p}{\sum\limits_{j=1}^{n} k_j} \tag{5.18}$$

It is, nonetheless, important to remark that the linearized rotating mass model that results in equation (5.17) disregards the involved dynamics of the electrical grid. Although a thorough stability analysis demands a more sophisticated model, this simplified approach gives valuable insights into the roles of the system's inertia, gains, and time delays. The interested reader may find more information on conditions for robust frequency stability of power grids in [46].

5.6 SIMPLIFIED STABILITY ASSESSMENT

It is interesting to assess the stability of the study case with the simplified model given by equation (5.16) when the power reserves are shared between two GTs and the ESS. For that, the normalized p_{FCR} is split into three components, one for the ESS and two for the GTs, as illustrated in figure 5.6. The ESS component is modeled as a first-order LPF with a time constant equal to $T_{\mathrm{ESS}} = 50$ ms. For the GTs, two first-order LPFs are used in series representing the fuel valve and turbine delays. The fuel valve time constant is set to $T_{\mathrm{fv}} = 0.1$ s and the turbine time constant is set to $T_{\mathrm{t}} = 0.4$ s. The rated apparent power of the GTs is 88 MVA, the inertia constant of the system is $H = 2.5$ s and the total load of the isolated grid is 44 MW. The model data is shown in Table 5.1. The total power-to-frequency gain of the FCR is set to $K_{\mathrm{N}} = 12\,\mathrm{MW\,Hz^{-1}}$ and is shared between the GTs and ESS. This gain is reasonably high when compared to the installed GT power of 88 MVA and the electric load of 44 MW. For large interconnected grids in North America, the typical gain in $\mathrm{W\,Hz^{-1}}$ is on the range of 10 % of the peak demand in W [1].

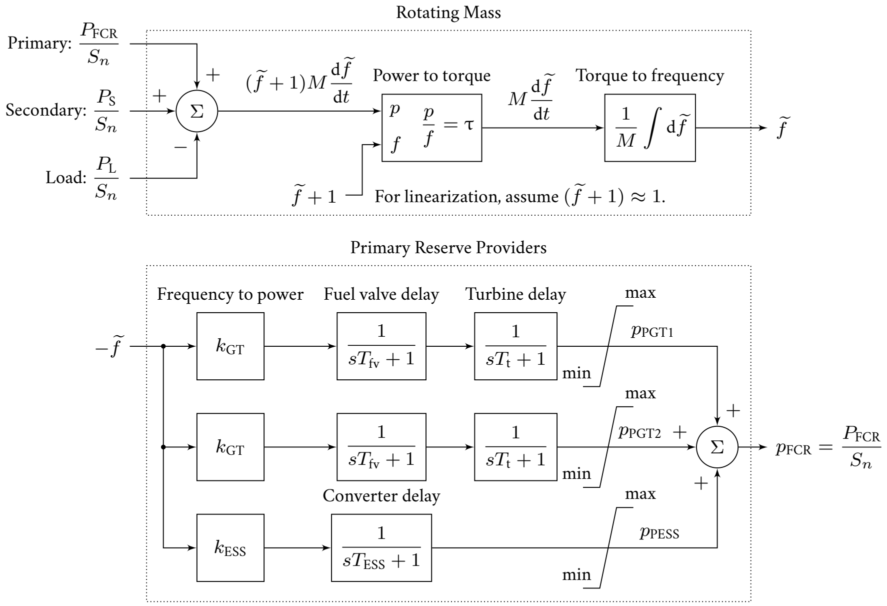

FIGURE 5.6 FCR providers and the rotating mass.

© Daniel Mota 2023 | Source code information at Part III.

Figure 5.7 shows the frequency response of the system after a step load of 1.2 MW obtained with MathWorks MATLAB Simulink R2018a for seven different FCR sharing configurations as listed on Table 5.2. The model and dataset are available at Repository VII. The electric load shown in dashed black in figure 5.7a increases in a step at instant $t = 1$ s. The unbalance of power between load and generation causes the frequency to drop, as seen in figure 5.7b. The providers of FCR respond to the frequency drop by delivering power proportionally to their frequency-to-power gains. The aggregated response of the GTs is shown in figure 5.7c. The response of the ESS is shown in figure 5.7d. The frequency nadir (the minimum value attained after the step) is greatly improved by shifting the primary reserves from the slower GTs to the faster converter-interfaced ESS.

Figure 5.8 shows the eigenvalues of the system obtained with MathWorks MATLAB Simulink R2018a for the seven different FCR sharing configurations employed in the step responses shown in figure 5.7. For all FCR configurations, the eigenvalues associated with the ESS are not oscillatory and lie on the real number axis. The governors are associated with the only oscillatory mode. When only the GTs are supplying FCR, this mode features a natural frequency of $\omega_{\mathrm{nat}} = 1.651\,\mathrm{rad\,s^{-1}}$ and a damping of $\zeta = 0.606$. These are the same ω_{nat} and ζ one would obtain with equations (5.14) and (5.15) if the GTs were aggregated into

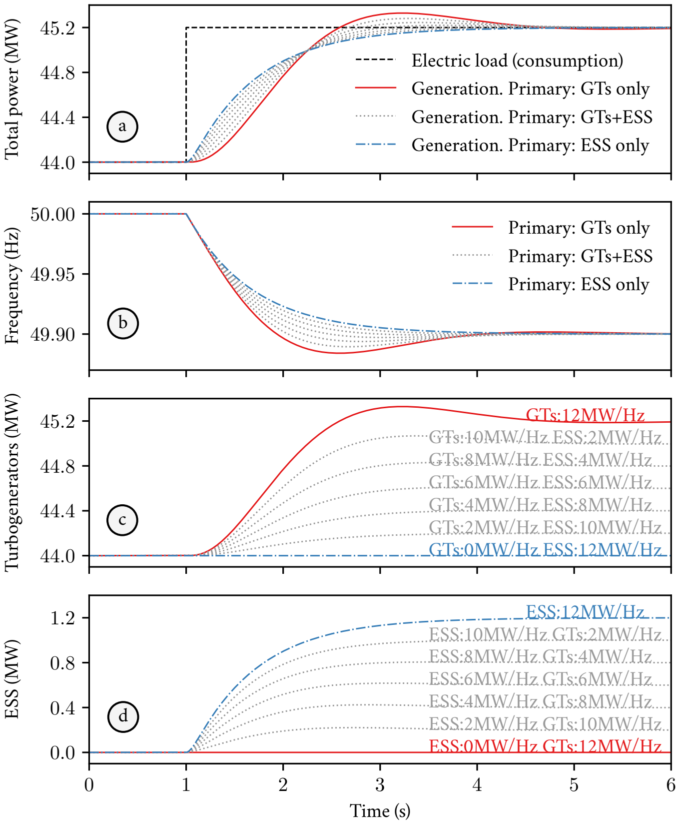

FIGURE 5.7 Response of the model shown in figure 5.6 to a step load of 1.2 MW with different sharing of FCR_N among ESS and GTs.

a single unit modeled with one first-order LPF. Notice, also, that the more the reserves shift towards the ESS, the more the oscillatory mode moves towards the real number axis. When only the ESS provides FCR, the imaginary parts of all eigenvalues are zero.

5.7 STUDY CASE

The study case used in Publication VI and described in this section is based on an existing O&G platform in the North Sea. The platform operates isolated from the continent and is fed, in normal operation, by two 35.2 MW aero-derivative single-cycle GTs. A techno-economical study [39] suggested that a reduction of approximately 30 % of the annual CO_2 emissions can be achieved if the platform were connected to a 12 MW floating offshore WF. The reduction, however, relies

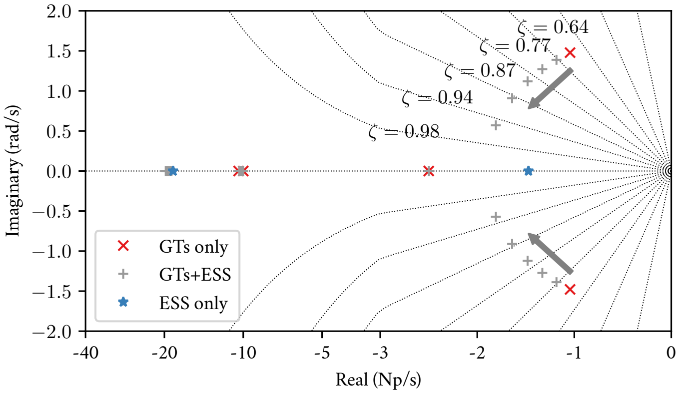

FIGURE 5.8 Eigenvalues with a linearized rotating mass model for a total gain of 12 MW Hz^{-1} and different sharing of $\mathrm{FCR_N}$ among ESS and GTs.

© Daniel Mota 2023 | Redrawn and recomposed from Publication VI | Source code information at Part III.

TABLE 5.1 Simulation data for figures 5.7 and 5.8.

Parameter	Symbol	Value
Total apparent power GTs	S_n	88 MVA
Electric load	P_L	44 MW
Total FCR gain	K_N	12 MW Hz^{-1}
System inertia constant	H	2.5 s
ESS time constant	T_ESS	50 ms
GTs fuel valve time constant	T_fv	0.1 s
GTs turbine time constant	T_t	0.4 s

on the installation of a centralized hybrid ESS with 4 MW proton exchange membrane (PEM) fuel cells and 6 MW PEM electrolyzers. A set of three 4 MW WTs was used as a prospective scenario in the following publications:

- Publication I: for presenting and investigating the behaviour of a set of control structures for the ESS and FLX for regulating the study case's grid frequency, see chapter 3.
- Publication II: for proposing a sizing methodology for the platform's hybrid ESS. The sizing of the ESS is not the focus of this dissertation. However, more information on this topic can be found at [47].
- Publication III: for understanding the effects exponentially decaying dc components on the dual-sequence current control of power electronic converters, see chapter 4.
- Publication VI: the main source of this chapter.

Figure 5.9 shows a single-line diagram of the study case. As explained previously in section 2.4.1, the average electrical load of the platform is 44 MW; therefore, a single 35.2 MW GTs is not able to feed the platform. Additionally, the thermal load of the industrial processes requires one of the GTs to be in operation at all times. Moreover, due to safety concerns, the prospective scenario investigated by Publications I to III and VI assumed that two GTs would still operate simultaneously even with full production from the WF. The premise of two GTs operating at all times is kept in this dissertation.

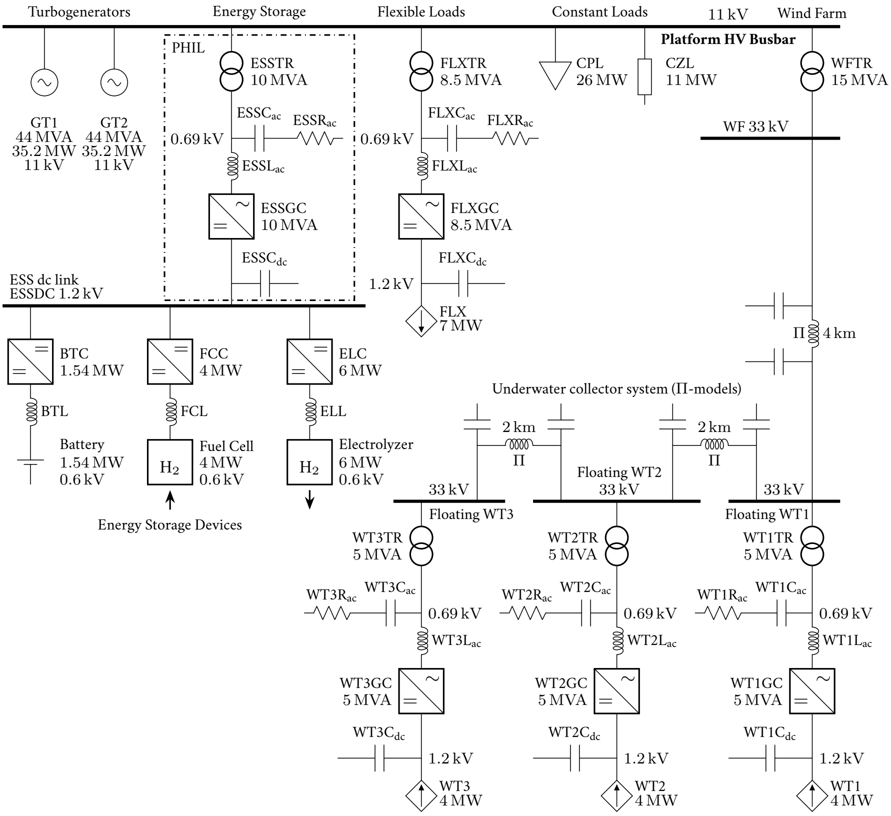

FIGURE 5.9 Single line diagram of the study case's grid.

© Daniel Mota 2023 | Redrawn and recomposed from Publication VI | Source code information at Part III.

The loads of the study case are divided into three groups in figure 5.9. The first group represents the platform's water injection system, whose variable frequency drives can act as flexible loads (FLX) and provide primary frequency control reserves. For simplification purposes, the whole water injection system is grouped under a single 8.5 MVA active-front-end PEC. The second load group aggregates 26 MW of CPL, which are modeled as instantaneous constant power consumers; in other words, there are no delays associated to them. The third group gathers 11 MW of CZL. Both CPL and CZL can be changed in steps for testing the dynamic characteristics of the model.

The FLX are modeled as a single ideal controlled current source connected to a dc link. The current absorbed by this controlled source depends on the power consumed by the flexible loads and the dc-link voltage. Figure 5.10 illustrates the calculation of the reference for the FLX controlled current source. The dc voltage measurement is modeled as a first order LPF with a time constant T_v. The flexible loads grid converter (FLXGC) interfaces the dc link to the platform's ac grid. It operates as a dc voltage controller and, in addition to that, regulates the reactive power exchange with the grid to zero.

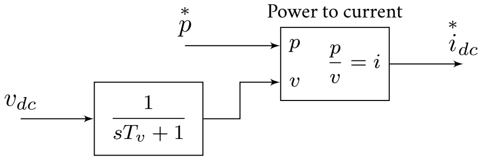

FIGURE 5.10 Current reference calculation for the controlled current sources FLX, WT1, WT2, and WT3 in figure 5.9 that operate as CPL or CPS.

© Daniel Mota 2023 | Redrawn and recomposed from Publication VI | Source code information at Part III.

The WTs with their wind turbine grid converters (WTGCs) are modeled in a similar way to the flexible loads and FLXGC. The turbines, including generator and machine side converter, are simplified to a single controlled current source that supplies constant power even when the dc-link voltage varies. Figure 5.10 illustrates the calculation of the references for the WT controlled current sources. In a way similar to the FLXGC, the WTGCs operate as dc voltage controllers and regulate the reactive power exchange with the grid to zero. As the back-to-back PECs employed in modern type 4 WTs isolate the mechanical oscillation modes from the states on the electrical grid side [48], this simplified representation of the wind turbine units can be adopted.

For counteracting wind variability, a hybrid ESS is employed. A fast ESD composed of a battery and a dc/dc converter provides reserves for the short term wind and load variations. The main goal of the battery is to reduce the burden of the GTs on the fast frequency control. The electrolyzer and fuel cell pair form one single ESD. Energy is stored as hydrogen when there is wind overproduction. Hydrogen is transformed into electricity when there is little production from the WF. Even though the reactive power provided by ESSs can have an important role in avoiding the loss of synchronism of nearby machines in the event of faults [49], the energy storage system grid converter (ESSGC) of the study case keeps the reactive power exchange with the grid equal to zero. In a way similar to the grid converters (GCs) of the FLX and WTs, the ESSGC also runs as a dc voltage controller. The choice of setting the GC as a dc voltage regulator while the ESDs provide power to the dc link has been consistently employed in Publications I, II, and VI. The PowerFactory models developed for Publications I and VI are publicly available at Repositories I and V, respectively.

5.8 DETAILED STABILITY ANALYSIS

The models based on a mechanical rotating mass, which result in the transfer functions in equations (5.13) and (5.17), disregard many of the interactions between the devices of the platform. CPL and converter-driven instabilities are not captured by these transfer functions. To gain an insight into these complex interactions and validate the results of the simplified stability assessment presented in section 5.6, computer simulations were performed with DIgSILENT PowerFactory 2020 SP2A. It is shown that, by prioritizing the fast providers, the overall stability of the system increases. Such analysis is only possible once the model of the power system as a whole is stable. For that, all the regulators of excitation systems, turbine governors, and PECs had to be tuned beforehand. However, due to brevity concerns, the consolidated tuning techniques in line with industrial and academic praxis employed for the various controllers in these devices are not discussed in detail in this dissertation. Nevertheless, more information can be found in the following references.

- Fröhr and Orttenburger [50]: classical tuning techniques for proportional, integral, and derivative (PID) controllers.
- DIgSILENT GmbH [51]: extensive technical documentation of the software tool PowerFactory.
- IEEE Std 421.5-2016 [52]: recommended practices for modeling excitation systems in computer simulation studies.
- Pourbeik *et al.* [45]: dynamic models for turbine-governors in simulations of power system studies.
- Suul *et al.* [53]: application of the classic tuning techniques presented by Fröhr and Orttenburger [50] taking into consideration the discretization errors introduced by modern digital controllers of PECs.
- Golestan *et al.* [54]: a comprehensive review on phase-locked loop (PLL), see also appendix B.

It is important to remark that the models and datasets used for obtaining figures 5.7, 5.8, 5.11, and 5.12 are available at Repository VI.

Figure 5.11a shows seven instances of frequency changes caused by a step load of 1.2 MW. The frequency shown is the one at the platform's main busbar measured with a PLL. The FCR_N sharing is different in each of the seven instances as listed on Table 5.2. The step load is applied at $t = 1$ s. Within the next 4 s, the frequency reaches a new steady state at 49.9 Hz. The response when the GTs are the only FCR_N providers is shown in solid red. In this case, the minimum value reached by the frequency (known as nadir) is 49.886 Hz. The responses when the FCR_N are shared between GTs, battery converter (BTC), and FLX are shown in dotted gray. The dash dotted blue curve denotes the response when only BTC and FLX provide FCR_N. From a frequency control perspective, the system becomes more stable as

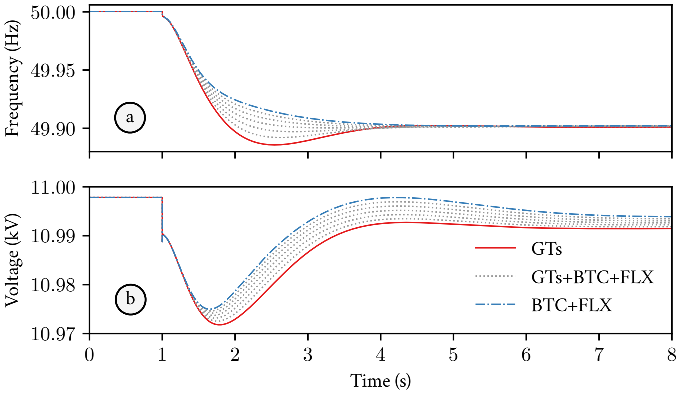

FIGURE 5.11 Response of the detailed PowerFactory model to a step load of 1.2 MW with different sharing of $\mathrm{FCR_N}$ among GTs, BTC, and FLX.

© Daniel Mota 2023 | Redrawn and recomposed from Publication VI | Source code information at Part III.

the $\mathrm{FCR_N}$ contribution is shifted towards the BTC and FLX. These faster primary reserves improve the nadir. It is worth comparing the response in figure 5.11a to the one obtained with the simplified rotating mass model in figure 5.7. Although very similar, the detailed modeling with DIgSILENT PowerFactory 2020 SP2A shows that other complex interactions can destabilize the grid. The response of the main busbar voltage, for instance, becomes slightly less damped (figure 5.11b). The voltage control dynamics of the active front-end converters ESSGC and FLXGC should always be considered in a thorough stability analysis.

When the steady state is reached in the simulations shown in figure 5.11, the eigenvalues of the system are calculated (automatically by PowerFactory [55]) together with the participation factors of each state in each eigenvalue. The result is shown in figure 5.12. See table 5.2 for information regarding chart legend and markers. The devices whose internal states have a participation factor higher than 50 % are named on the side of some specific eigenvalues. The real and imaginary axes are partially linear and partially logarithmic in figure 5.12a. Both axes of figures 5.12b and 5.12c are linear. Constant damping (ζ) lines are plotted to help identifying the more oscillatory eigenvalues. The system is stable in all configurations and, as expected, all eigenvalues have negative real parts.

Figure 5.12a shows an overview of the complex plane. The negative half of the imaginary axis is mostly omitted as oscillatory modes appear as complex conjugate eigenvalues. The eigenvalue related to the BTC and battery main reactor (BTL) leave the real number axis and reach a damping of $\zeta = 0.94$ with a natural frequency of 22 $\mathrm{rad\,s^{-1}}$ when the reserves are exclusively supplied by the BTC and FLX. The modes related to fuel cell converter (FCC) and fuel cell main reactor (FCL) are marked with FCC,FCL and the ones related to the electrolyzer converter (ELC)

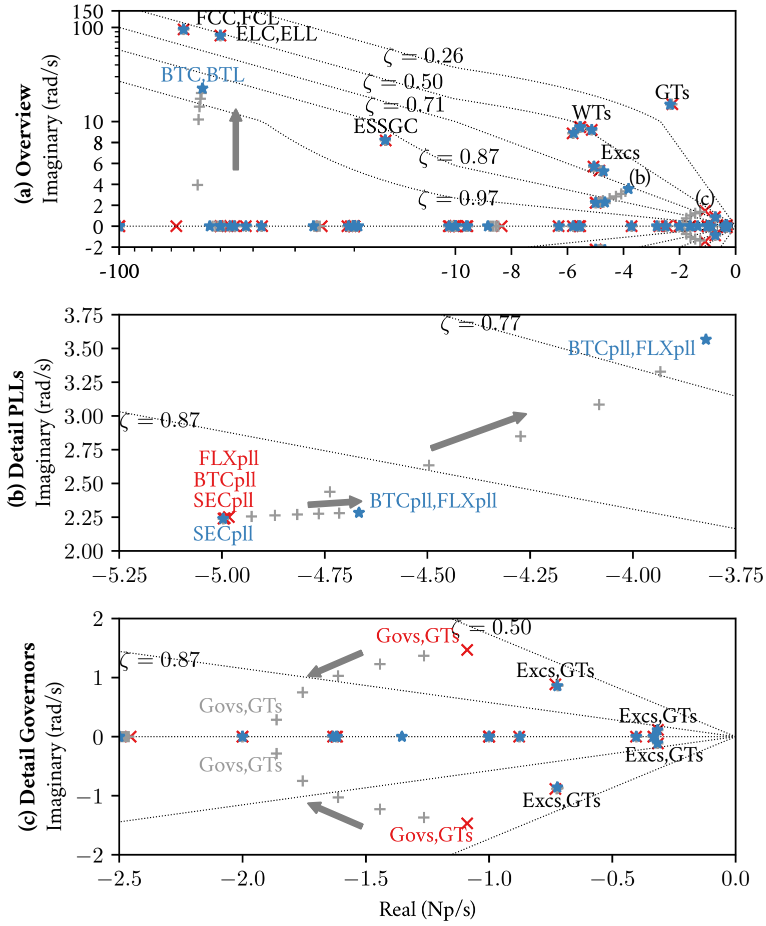

FIGURE 5.12 Eigenvalues with detailed PowerFactory model for a gain of 12 MW Hz^{-1} and different sharing of FCR_N among GTs, BTC, and FLX.

© Daniel Mota 2023 | Redrawn and recomposed from Publication VI | Source code information at Part III.

and electrolyzer main reactor (ELL) are marked with ELC,ELL. The eigenvalues related to the wind turbines including their converters are clustered together and are marked with WTs. The modes associated with the FCC, ELC, and WTs are not affected by the FCR_N sharing. They are, nevertheless, influenced by the tuning of the controllers of their PECs. However, due to brevity concerns, the influence of controller tuning in the location of these eigenvalues will not be investigated in this dissertation. It is worth noting, though, that FCC, ELC, WTs, and BTC operate as constant power devices. Other eigenvalues worth remarking are the ones associated with the excitation system of the synchronous machines (Excs), the ones related to the grid converter of the ESS (ESSGC), and the ones related to internal states of the turbogenerators (GTs).

Figure 5.12b shows a detail of the complex plane with eigenvalues related to the frequency measurement (performed with PLLs) of the flexible loads (FLXpll), battery converter (BTCpll), and secondary frequency controller (SECpll). When the reserves are provided by the GTs only, three eigenvalues are clustered close to the point $-5 + \mathrm{j}2.25$. Each of those eigenvalues is related to one frequency measurement device. Once the $\mathrm{FCR_N}$ is shifted from the GTs to the FLX and BTC, two eigenvalues start to move towards less damped regions of the complex plane. States of the PLLs of the BTC and FLX have a participation factor above 50 % in these eigenvalues. The eigenvalue related to the secondary frequency controller PLL, however, is not affected by the sharing of $\mathrm{FCR_N}$.

TABLE 5.2 $\mathrm{FCR_N}$ sharing values and chart information for figures 5.7, 5.8, 5.11, and 5.12.

Chart legends		GTs	GTs+BTC+FLX					BTC+FLX
GT1,2	K_N [MW/Hz]	6	5	4	3	2	1	0
BTC	K_N [MW/Hz]	0	1	2	3	4	5	6
FLX	K_N [MW/Hz]	0	1	2	3	4	5	6
Line style		solid red —	dotted gray ······					dash-dotted blue —·—
Marker		×	+					⋆

Figure 5.12c presents a detailed view including the oscillation modes associated with the governors and turbogenerators (Govs,GTs). The dynamic of this mode coincides with the one observed in figure 5.8. As indicated by the gray + markers, the less the GTs provide $\mathrm{FCR_N}$, the more this eigenvalue moves towards the real number axis. The other oscillatory eigenvalues in figure 5.12c are not affected by changes to the $\mathrm{FCR_N}$ sharing. They are associated with internal states of the excitation systems (Excs) and turbogenerators (GTs).

It is important to remark that eigenvalue analyses rely on approximating a nonlinear system, which should be at the steady-state operating point of interest, to a time-invariant linear model [56]. The analyses performed in section 5.6 and in this section are inadequate for predicting system stability after large perturbations that excite nonlinear features, force controllers to switch parameter sets, or result in changes to the grid topology. Therefore, eigenvalue analyses cannot be employed to evaluate the transition period while the $\mathrm{FCR_D}$ are already activated and the $\mathrm{FCR_N}$ are not yet fully settled at their maximum contribution due to actuator delays. To enable the study of the dynamic response to large disturbances of the expanded $\mathrm{FCR_I}$ proposed in this chapter, including the effects of nonlinearities as saturations and dead bands, a reduced-scale PHIL test setup is implemented. This setup is validated in Section 5.9. The response to a large disturbance that forces $\mathrm{FCR_N}$ and $\mathrm{FCR_D}$ to interact is shown in section 5.10.

5.9 VALIDATION OF THE PHIL TEST SETUP

In this section, the PowerFactory model used in section 5.8 is compared to a model running in a RTS [57] in a scaled-down PHIL test setup at the National Smart Grid Laboratory (NSGL) at NTNU, as seen in figure 5.13. This test setup is also employed for comparing the performances obtained with the proposed extended FCR_I concept and with a state-of-the art technique employed in power-intensive isolated industrial grids.

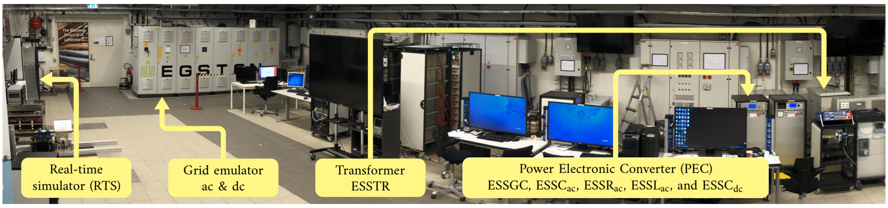

FIGURE 5.13 PHIL setup at the National Smart Grid Laboratory at NTNU.

© Daniel Mota 2023 | Redrawn and recomposed from Publication VI | Source code information at Part III.

The hardware under test is composed of the ESSGC, dc link capacitance, and inductive-capacitive-inductive (LCL) filter. These devices are marked with a dashed rectangle in figure 5.9. Their connections to the ac and dc grid emulator [58] are illustrated in figure 5.14. The ac grid emulator runs as a controlled voltage source and is connected to the high-voltage (HV) side of the energy storage system transformer (ESSTR). The dc grid emulator runs as a controlled current source and feeds the dc link of the ESS with the net current coming from the ESDs. The scaling of the hardware under test is presented in Table 5.3.

Three test cases are devised for the experimental results.

Case 1 — FCR_N provided only by the GTs .
Case 2 — FCR_N shared between BTC and GTs .
Case 3 — FCR_N shared between BTC and FLX. .

For all three cases, the following conditions apply:

- the total available FCR_N is $P_\text{N} = 3\,\text{MW}$,

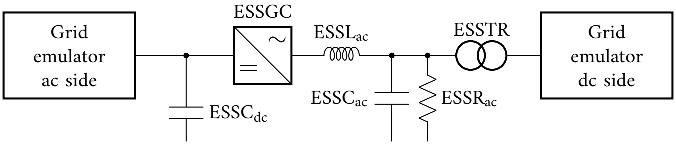

FIGURE 5.14 Single-line diagram of the scaled-down PHIL test rig.

© Daniel Mota 2023 | Redrawn and recomposed from Publication VI | Source code information at Part III.

- the $\mathrm{FCR_D}$ are provided only by the GTs, the boundary for normal and large disturbance operation is $\widetilde{F}_\mathrm{N} = 1\,\mathrm{Hz}$,
- and the total $\mathrm{FCR_D}$ gain is $6\,\mathrm{MW\,Hz^{-1}}$ concentrated only in the GTs.

Notice that the value of $\widetilde{F}_\mathrm{N}$ represents 2 % of the rated system frequency, which is larger than the 0.2 % limit required for the Nordic region [3] but lower than 3 % defined for normal operation in the recommended practices for maritime vessels [25].

In this subsection, a step load of 3 MW is chosen as test transient for comparing the scaled-down PHIL setup against the PowerFactory model. As noted in Publication II, this is the maximum expected load variation under normal operational conditions with 99.9 % of probability for the platform. The step load is divided between CPL and CZL proportionally to their rated values. For all three cases in this subsection, the $\mathrm{FCR_N}$ providers operate with a 0.25 % frequency dead band and their frequency-to-power gains are compensated with equation (5.4). The frequency-to-power characteristic for case 3 considering the dead bands of the $\mathrm{FCR_N}$ providers is shown in figure 5.15. The battery converter (BTC, in dashed red) and the flexible loads (FLX, dotted blue) supply 1.5 MW when the frequency deviation is $\widetilde{F} = 1\,\mathrm{Hz}$. The turbogenerators GT1 (dashed gray) and GT2 (dotted gray) only provide $\mathrm{FCR_D}$; therefore, they only contribute if the frequency deviation is $|\widetilde{F}| > 1\,\mathrm{Hz}$. It is worth mentioning that, given the choices of P_N and $\widetilde{F}_\mathrm{N}$, a step load of 3 MW does not activate the large disturbance reserves.

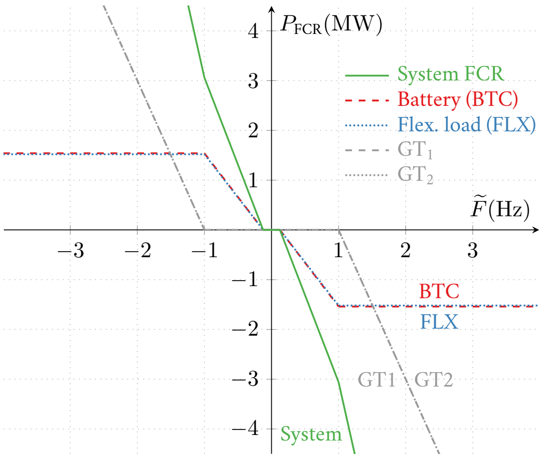

FIGURE 5.15 $\mathrm{FCR_{N+D}}$ characteristic of case 3 considering the dead bands of $F_\mathrm{dbN} = 0.25\,\%$ used in section 5.9.

© Daniel Mota 2023 | Source code information at Part III.

The comparison of the PowerFactory model and the PHIL setup is shown in figure 5.16. The results obtained with power hardware-in-the-loop are marked with “PHIL”. The ones obtained with PowerFactory are marked with “SW”. Initially,

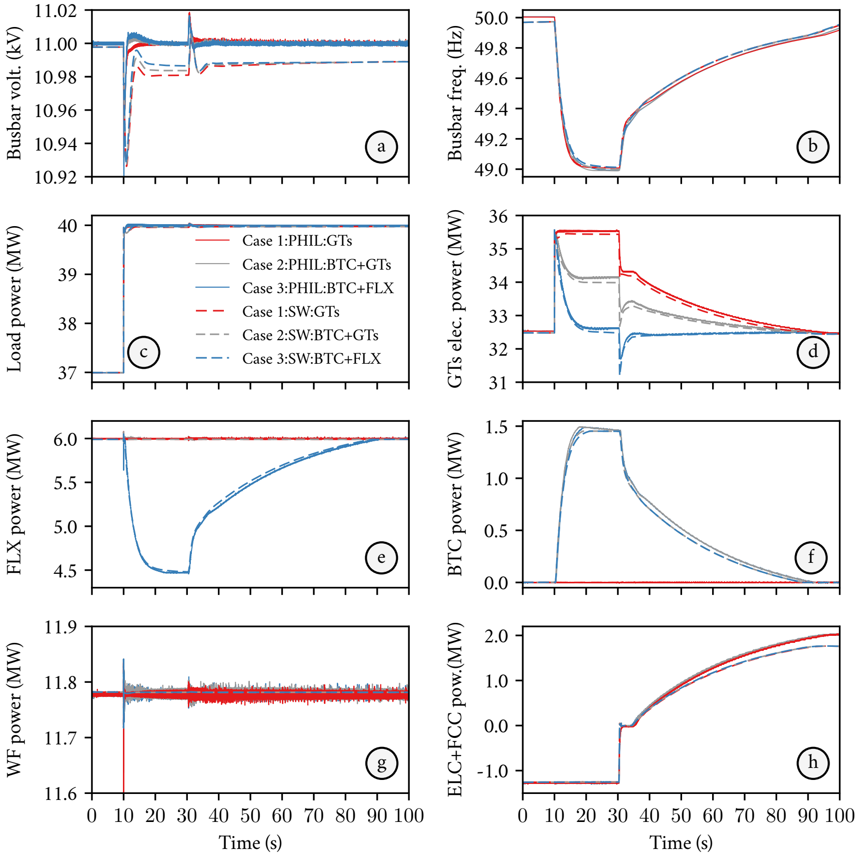

FIGURE 5.16 Validation of the PHIL setup and PowerFactory model (marked as SW). Responses to 3 MW step loads with three different sharing of FCR_N. For clarity purposes, the WTs mechanical power is fixed and the action of the secondary controller after the frequency changes is delayed.

© Daniel Mota 2023 | Redrawn and recomposed from Publication VI | Source code information at Part III.

the system is in steady state; the total production from the GTs (figure 5.16d) and WF (figure 5.16g) is larger than the total consumption by the load (figure 5.16c) and flexible loads (figure 5.16e). The overproduction of power is stored by the slow ESD composed of the electrolyzer and fuel cell (figure 5.16h). At instant $t = 10$ s, the step load of 3 MW is applied (figure 5.16c). The initial transient caused by the step load is noticeable at the busbar voltage (figure 5.16a) and at the total power supplied by the WF (figure 5.16g). The imbalance of power of 3 MW is, initially, fully covered by the GTs (figure 5.16d) and causes the ac frequency to drop (figure 5.16b). When the FCR_N are shared between BTC and GTs (Case 2), the burden on the GTs is quickly halved. For case 3, when the FCR_N are provided exclusively by the BTC and FLX, the power of the flexible loads (figure 5.16e) is reduced proportionally with the frequency deviation. This, together with the power delivered by the batteries (figure 5.16f), drives the generator power back to the level of before the step. The secondary frequency controller is activated at $t = 30$ s. The ELC is quickly shut-down and the FCC (figure 5.16h) slowly starts to supply power regulating the frequency back to the nominal.

There are a few discrepancies between the results obtained with the PHIL setup and the PowerFactory simulations that are worth commenting on, mainly in the voltage dynamics and fuel cell power. In figure 5.16a, a different voltage dynamic and a small voltage drop is observed in the PowerFactory results. The reasons for that are twofold. For the PowerFactory, a detailed model 2.2 from [59] is used for each generator, the reactive power sharing of the PMS is not modeled, and the voltage regulators of the two generators operate with reactive current droop. Therefore, after the step load at $t = 10$ s, the busbar voltage drops by approximately 20 V. For the PHIL results, the two GTs are aggregated into one single variable-voltage-behind-reactance model that considers the effects of the field winding and disregards the damper windings. The voltage regulator of this single aggregated generator runs with zero reactive current droop. Therefore, after a short transient, the excitation system of aggregated generator in the RTS model brings the busbar voltage back to nominal.

The difference in ELC/FCC power observed in figure 5.16h after instant $t = 50$ s is due to higher losses in the scaled-down hardware devices (ESSGC, ESSL$_\mathrm{ac}$, and ESSTR) that are not present in the PowerFactory simulations. Normalized resistive losses in laboratory equipment such as transformers, reactors, and converters tend to be higher than the normalized losses in their full-scale counterparts. Therefore, the real-time simulated fuel cell must produce more power than the one from the PowerFactory model to compensate for the extra losses. A compromise between reducing losses and matching reactance and capacitance values in pu must be made for a scaled-down PHIL test. The matching of scaled-down laboratory converters in PHIL test beds with their large counterpart full-scale converters is addressed in detail in chapter 6.

5.10 EXTENDED FCR$_\mathrm{I}$ VERSUS INDUSTRY STATE-OF-THE-ART

In this section, the extended FCR$_\mathrm{I}$ concept proposed in Publication VI is compared to the industry state-of-the-art droop with a centralized secondary frequency controller. Case 3 is selected for this benchmarking. The dead bands previously adopted for the FCR$_\mathrm{N}$ providers are now set to 10 mHz. For the traditional droop scenario, the total frequency-to-power gain of 3 MW Hz^{-1} is divided among the primary reserve providers in the following manner: each turbogenerator GT is assigned with 0.5 MW Hz^{-1}, the battery converter (BTC) is assigned with 1 MW Hz^{-1}, and the flexible loads (FLX) are assigned with a total of 1 MW Hz^{-1}. The turbulence effects on the WTs are now considered as they were in Publication II, see also Repositories II and VI.

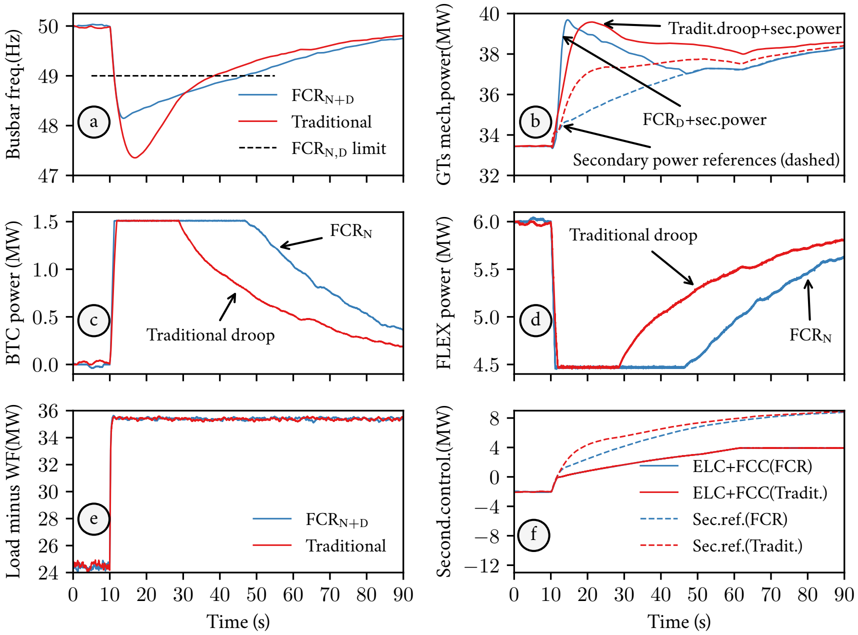

FIGURE 5.17 Comparison between the extended FCR_I concept and the industry state-of-the-art droop. Responses to a loss of 11 MW production from the WF. FCR_{N+D} case 3 in blue, traditional droop in red. The secondary controller responds to the frequency changes without intentional delays. Effects of wind turbulence in the power delivered by the WTs are considered.

© Daniel Mota 2023 | Redrawn and recomposed from Publication VI | Source code information at Part III.

Figure 5.17 shows the comparison of the performance of the traditional droop method and the FCR_{N+D} case 3. At $t = 10$ s, 11 MW of wind power production is lost, as seen in Figure 5.17e. The PI regulator of the secondary power controller reacts to the frequency variation without intentional delays and changes the secondary power reference causing the ELC and FCC to respond (figure 5.17f). The difference between the required secondary power and the measured delivered power by the ELC and FCC is sent as reference to the GTs, as specified in equation (5.1). For that reason, the mechanical power delivered by the turbines to the synchronous generators (figure 5.17b) contains both the droop and the secondary power response. The FCR_{N+D} case 3 prioritizes the BTC and FLX as providers in normal operation. The 11 MW production loss leads those FCR_N providers to saturation (Figure 5.17c,d) when the frequency crosses 49 Hz (Figure 5.17a). A possible shortage of power caused by the saturation, however, is automatically covered by activation of the FCR_D from the GTs. By defining $\widetilde{F}_N$ and calculating the gains K_N and K_D with equation (5.2) and equation (5.3), one ensures that an eventual saturation of the FCR_N providers is automatically covered by the activation of the FCR_D.

5.11 DISCUSSION

The main advantage of the extended FCR_I concept when compared to the traditional droop method is the flexibility provided for the selection of which units will be responsible for normal operation reserves and which ones will be responsible for the large disturbance reserves. Additionally, the proposed concept enables the choice of different frequency-to-power gains for the different operating conditions in isolated grids. It is also important to remark that the same provider can participate as both types of reserves depending on technical or economical reasons.

The provision of primary reserves by the faster ESS and FLX lessens the burden of the slower GTs with frequency control, which leads to reduced wear and tear of the turbine governors, reduced nitrogen oxides (NO_x) and CO_2 emissions, and an improved overall electric power quality in the platform. Although the higher participation of the faster reserves results in a more damped response of the frequency after sudden load changes, there is a non-critical increase in the oscillations at the main busbar voltage. Therefore, interactions between the excitation system of the GTs and the reactive power control of the ESSGC need special attention. Additionally, the tuning of the ESS and FLX frequency measurement devices needs to be carefully performed as the oscillation modes associated with them move towards less damped regions of the complex plane when the contributions of these providers increase. Nevertheless, the eigenvalue analysis and dynamic simulations performed with PowerFactory and the results obtained with the PHIL test setup indicate that the benefits, from a grid stability perspective, outweigh the disadvantages of increasing the share of converter interfaced FCR_N reserves for primary frequency control in isolated grids.

As the total allocated reserve power is maintained by the PMS, a higher participation of the battery in the primary frequency control means a higher FCR gain in the BTC and a lower gain in the governors. This results in the increased damping of an oscillation mode associated with governors and GTs, whereas oscillation modes associated with the BTC and BTL become less damped. While the reduction in damping of the BTC and BTL modes is not critical, as ζ is still larger than 0.87, the increased damping of governors and GTs modes is much more expressive, from $\zeta = 0.64$ to the real number line. Notwithstanding, there is a series of modes with ζ close to or lower than 0.5 that are associated with constant power devices such as the fuel cell, electrolyzer, and WTs. Different tuning strategies for the controllers of these devices influence the location in the complex planes of these oscillation modes. However, an assessment of such tuning strategies is considered outside the scope of this dissertation.

5.12 CONCLUSION

In this chapter, the Nordic synchronous system concept of frequency containment reserves for isolated operation (FCR$_{\mathrm{I}}$) was expanded and subdivided into two categories. This strategy of categorized FCR$_{\mathrm{I}}$ was applied to the study case of an isolated complex industrial system that is fed by traditional GTs and a WF, dominated by CPLs, equipped with fast flexible converter-interfaced loads, and supported by an ESS. The analyses performed in this work took into consideration the detrimental effects of the CPLs and demonstrated that the overall stability of the system increased by shifting the primary power reserves from the slow GTs to the fast ESS and converter-interfaced loads. This also allowed the GTs of the study case to operate at a more constant power, which has the potential to reduce wear and tear in the turbine governors. While the reduction in the damping of oscillation modes associated with the CPLs and the PECs were not critical, the oscillation mode associated with the slow turbine governors were considerably damped when ESS and converter-interfaced reserves were prioritized. The results presented in this chapter were supported by computer simulations, made publicly available, and PHIL tests. They demonstrate the versatility of the expanded FCR$_{\mathrm{I}}$ concept for coordinating fast primary power reserves in autonomous grids with increased participation of non-synchronous intermittent RES.

TABLE 5.3 Scaled down PHIL and full size converter data.

Device	Quantity	Full-Scale Converter (SW PowerFactory)		Scaled-Down Converter (PHIL)	
ESSGC (ac side)	Apparent power	10 MVA	1 pu	14.3 kVA	1 pu
	Voltage	690 V	1 pu	115 V	1 pu
	Current	8367 A	1 pu	72 A	1 pu
	PWM frequency	5 kHz		7 kHz	
ESSGC (dc side)	Voltage	1200 V		200 V	
	Current	8333 A		71.7 A	
ESSTR (from LV)	Transformer ratio	11 kV / 690 V		400 V / 400 V	
	Short-circuit inductance	12.1 µH	0.08 pu	316 µH	0.108 pu
	Short-circuit resistance	238 µΩ	0.005 pu	49.37 mΩ	0.0535 pu
ESSL$_{\mathrm{ac}}$	Main reactor inductance	25.8 µH	0.17 pu	500 µH	0.17 pu
	Main reactor resistance	952 µΩ	0.02 pu	20 mΩ (estimated)	0.0217 pu
ESSC$_{\mathrm{ac}}$	Capacitance	3.343 mF	0.05 pu	50 µF	0.0145 pu
ESSR$_{\mathrm{ac}}$	Damping resistance	18.16 mΩ (series)	0.381 pu	47 kΩ (parallel)	50 967 pu
ESSC$_{\mathrm{dc}}$	Capacitance	69.4 mF	$H = 5$ ms†	14 mF	$H = 19.5$ ms†

† H equals the energy in the capacitor at rated dc voltage divided by the converter rated apparent power.

5.13 REFERENCES

[1] Erik Ela, Michael Milligan, and Brendan Kirby. Operating Reserves and Variable Generation. Technical Report NREL/TP-5500-51978 National Renewable Energy Lab. (NREL) Golden, Colorado, USA (August 2011). DOI 10.2172/1023095. Cited on page(s) 69, 75, 83.

[2] EU. Establishing a Guideline on Electricity Transmission System Operation. Commission regulation (EU) 2017/1485. European Union (2017). URL https://eur-lex.europa.eu/eli/reg/2017/1485/oj, accessed on 2023-01-09. Cited on page(s) 69.

[3] ENTSO-E. Technical Requirements for Frequency Containment Reserve Provision in the Nordic Synchronous Area. Grid Code Version Pending Approval of Legal Methodology ENTSO-E Brussels, Belgium (June 2022). URL https://www.statnett.no/globalassets/for-aktorer-i-kraftsystemet/marked/reservemarkeder/fcr-technical-requirements-2022-06-27.pdf, accessed 2022-08-03. Cited on page(s) 69, 70, 72, 73, 75, 93.

[4] Poria Hasanpor Divshali and Corentin Evens. Optimum Operation of Battery Storage System in Frequency Containment Reserves Markets. *IEEE Transactions on Smart Grid* **11** (6), 4906–4915 (November 2020). ISSN 1949-3061. DOI 10.1109/TSG.2020.2997924. Cited on page(s) 70.

[5] Ksenia Poplavskaya and Fabian Leimgruber. Analysis of the Swedish FCR-N market design - effects of transition to marginal pricing and free bidding. Technical Report Commissioned by Svenska kraftnät AIT Austrian Institute of Technology GmbH Wien, Austria (January 2021). URL https://www.svk.se/contentassets/22a7164df5c2415d9c2a8f69c08498f8/svk_report_analysis_of_fcr-n_market_design.pdf, accessed on 2023-02-17. Cited on page(s) 70.

[6] Niklas Modig, Robert Eriksson, Pia Ruokolainen, Jon Nerbø Ødegård, Simon Weizenegger, and Thomas Dalgas Fechtenburg. Overview of Frequency Control in the Nordic Power System. Technical Report ENTSO-E Brussels, Belgium (March 2022). URL https://www.epressi.com/media/userfiles/107305/1648196866/overview-of-frequency-control-in-the-nordic-power-system-1.pdf, accessed on 2023-02-17. Cited on page(s) 70.

[7] Statnett. Funksjonalitet for Separatdriftsregulering/Deteksjon (FCR-I) og Dødbånd. Technical Note Dokument ID: 2375815 Statnett AS Oslo, Norway (October 2018). URL https://www.statnett.no/globalassets/for-aktorer-i-kraftsystemet/systemansvaret/soknad-om-idriftsettelse-av-anlegg-fos--14/funksjonalitet-for-separatdriftsregulering-og-deteksjon.pdf, accessed on 2023-06-09. Cited on page(s) 70, 72.

[8] Gary Olson. Paralleling Dissimilar Generators: Part 3 – Load Sharing Compatibility. White paper Power topic #9017 Cummins Inc. (2010). URL https://mart.cummins.com/imagelibrary/data/assetfiles/0056549.pdf, accessed on 2023-03-03. Cited on page(s) 70.

[9] Woodward. DSLC-2 Digital Synchronizer and Load Control. Manual 37443J DSLC-2 Rev.J Woodward GmbH Stuttgart, Germany (February 2022). URL https://wss.woodward.com/manuals/PGC/DSLC_MSLC_series/DSLC-2/01_Technical_Manuals/37443J_TM-DSLC-2.pdf, accessed on 2023-03-03. Cited on page(s) 70.

[10] Woodward. easYgen-3000XT Series Genset Control. Manual Release 2.13-0, Document ID: B37580, Revision L, Build 52604 Woodward GmbH Stuttgart, Germany (October 2022). URL https://wss.woodward.com/manuals/PGC/easYgen-3000XT_series/easYgen-3400XT-3500XT-P1/01_Technical_Manuals/B37580_TM_easYgen-3400-3500-XT-P1_L.pdf, accessed on 2023-03-03. Cited on page(s) 70.

[11] Krishnanjan Gubba Ravikumar, Brandon Bosley, Ty Clark, and Julio Garcia. Generation Control System: Using Isochronous Load-Sharing Principles With Gas and Steam Turbine Generators. *IEEE Industry Applications Magazine* **25** (2) (March 2019). ISSN 1558-0598. DOI 10.1109/MIAS.2018.2875127. Cited on page(s) 70.

[12] Jing Zhong Tee, Kian Hou Tan, Idris Li Hong Lim, Keliang Zhou, and Olimpo Anaya-Lara. Integration of offshore wind with O&G platforms with an energy storage system. In *2019 IEEE PES Innovative Smart Grid Technologies Europe (ISGT-Europe)* Bucharest, Romania (September 2019). ISBN 978-1-5386-8218-0. DOI 10.1109/ISGTEurope.2019.8905500. Cited on page(s) 70, 73.

[13] Tee Jing Zhong, Idris Li Hong Lim, and Jin Yang. Energy management strategy designed for offshore oil rig with offshore wind. In *2022 IEEE 16th International Conference on Compatibility, Power Electronics, and Power Engineering (CPE-POWERENG)* Birmingham, United Kingdom (June 2022). DOI 10.1109/CPE-POWERENG54966.2022.9880886. Cited on page(s) 70, 73.

[14] D. Hu, X. Zhao, Xu Cai, and Jianfeng Wang. Impact of Wind Power on Stability of Offshore Platform Power Systems. In *2008 Third International Conference on Electric Utility*

Deregulation and Restructuring and Power Technologies Nanjing, China (April 2008). DOI 10.1109/DRPT.2008.4523677. Cited on page(s) 70.

[15] Atle Rygg Årdal, Salvatore D'Arco, Raymundo E. Torres-Olguin, Tore Undeland, and Kamran Shrarifabadi. Parametric sensitivity of transients in an islanded system with an offshore wind farm connected to an oil platform. In *Proceedings of the 2011 14th European Conference on Power Electronics and Applications* Birmingham, UK (August 2011). IEEE. ISBN 978-90-75815-15-3. URL https://ieeexplore.ieee.org/document/6020683, accessed on 2023-03-03. Cited on page(s) 70.

[16] Atle Rygg Årdal, Tore Undeland, and Kamran Sharifabadi. Voltage and frequency control in offshore wind turbines connected to isolated oil platform power systems. *ELSEVIER Energy Procedia* **24** (January 2012). ISSN 1876-6102. DOI 10.1016/j.egypro.2012.06.104. Cited on page(s) 70.

[17] Atle Rygg Årdal, Kamran Sharifabadi, Oyvind Bergvoll, and Vidar Berge. Challenges with integration and operation of offshore oil gas platforms connected to an offshore wind power plant. In *2014 Petroleum and Chemical Industry Conference Europe* Amsterdam, Netherlands (June 2014). DOI 10.1109/PCICEurope.2014.6900054. Cited on page(s) 70.

[18] Gauthier Delille, Bruno Francois, and Gilles Malarange. Dynamic Frequency Control Support by Energy Storage to Reduce the Impact of Wind and Solar Generation on Isolated Power System's Inertia. *IEEE Transactions on Sustainable Energy* **3** (4), 931–939 (10 2012). ISSN 1949-3029, 1949-3037. DOI 10.1109/TSTE.2012.2205025. Cited on page(s) 70.

[19] Yi Liu, Wenjuan Du, Liye Xiao, Haifeng Wang, and Siqi Bu. Sizing Energy Storage Based on a Life-Cycle Saving Dispatch Strategy to Support Frequency Stability of an Isolated System With Wind Farms. *IEEE Access* **7** (November 2019). ISSN 2169-3536. DOI 10.1109/ACCESS.2019.2953766. Cited on page(s) 70.

[20] Jong-Yul Kim, Jin-Hong Jeon, Seul-Ki Kim, Changhee Cho, June Ho Park, Hak-Man Kim, and Kee-Young Nam. Cooperative Control Strategy of Energy Storage System and Microsources for Stabilizing the Microgrid during Islanded Operation. *IEEE Transactions on Power Electronics* **25**, 3037–3048 (December 2010). ISSN 1941-0107. DOI 10.1109/TPEL.2010.2073488. Cited on page(s) 70.

[21] Tahoura Hosseinimehr, Arindam Ghosh, and Farhad Shahnia. Cooperative control of battery energy storage systems in microgrids. *ELSEVIER International Journal of Electrical Power & Energy Systems* **87**, 109–120 (May 2017). ISSN 0142-0615. DOI 10.1016/j.ijepes.2016.12.003. Cited on page(s) 70.

[22] Ling Ai Wong, Vigna K. Ramachandaramurthy, Phil Taylor, J.B. Ekanayake, Sara L. Walker, and Sanjeevikumar Padmanaban. Review on the optimal placement, sizing and control of an energy storage system in the distribution network. *ELSEVIER Journal of Energy Storage* **21**, 489–504 (February 2019). ISSN 2352152X. DOI 10.1016/j.est.2018.12.015. Cited on page(s) 70.

[23] Francisco M. Gonzalez-Longatt and José Luis Rueda, editors. PowerFactory Applications for Power System Analysis. Power Systems. Springer International Publishing New York, USA (2014). ISBN 978-3-319-12957-0 978-3-319-12958-7. DOI 10.1007/978-3-319-12958-7. Cited on page(s) 71.

[24] Mostafa Farrokhabadi, *et al.* Microgrid Stability Definitions, Analysis, and Examples. *IEEE Transactions on Power Systems* **35** (1) (January 2020). ISSN 1558-0679. DOI: 10.1109/TPWRS.2019.2925703. Cited on page(s) 71, 74.

[25] IEEE Std 45.1-2017. IEEE Recommended Practice for Electrical Installations on Shipboard–Design. IEEE Industry Applications Society New York, NY, USA (August 2017). DOI 10.1109/IEEESTD.2017.8007394. Cited on page(s) 73, 93.

[26] Remus Teodorescu, Marco Liserre, and Pedro Rodriguez. Grid Converters for Photovoltaic and Wind Power Systems | IEEE eBooks | IEEE Xplore. Wiley-IEEE Press (December 2010). ISBN 978-0-470-05751-3. DOI 10.1002/9780470667057. Cited on page(s) 73.

[27] Håvard Devold. Oil and Gas Production Handbook, an Introduction to Oil and Gas Production, Transport, Refining and Petrochemical Industry. ABB Oil

and Gas Oslo, Norway 3.0 edition (2013). ISBN 978-82-997886-3-2. URL https://library.e.abb.com/public/34d5b70e18f7d6c8c1257be500438ac3/Oil%20and%20gas%20production%20handbook%20ed3x0_web.pdf, accessed on 2023-02-17. Cited on page(s) 73.

[28] Razieh Nejati Fard and Elisabetta Tedeschi. Integration of Distributed Energy resources into Offshore and Subsea Grids. *CPSS Transactions on Power Electronics and Applications* **3** (March 2018). ISSN 2475-742X. DOI 10.24295/CPSSTPEA.2018.00004. Cited on page(s) 73.

[29] Shiguo Luo. A Review of Distributed Power Systems Part I: DC Distributed Power System. *IEEE Aerospace and Electronic Systems Magazine* **20** (8) (August 2005). ISSN 1557-959X. DOI: 10.1109/MAES.2005.1499272. Cited on page(s) 73.

[30] Alexis Kwasinski and Chimaobi N. Onwuchekwa. Dynamic Behavior and Stabilization of DC Microgrids With Instantaneous Constant-Power Loads. *IEEE Transactions on Power Electronics* **26** (3) (March 2011). ISSN 1941-0107. DOI 10.1109/TPEL.2010.2091285. Cited on page(s) 73.

[31] Duminda P. Ariyasinghe and D. Mahinda Vilathgamuwa. Stability Analysis of Microgrids with Constant Power Loads. In *2008 IEEE International Conference on Sustainable Energy Technologies* (November 2008). DOI 10.1109/ICSET.2008.4747017. Cited on page(s) 73.

[32] Nathaniel Bottrell, Milan Prodanovic, and Timothy C. Green. Dynamic Stability of a Microgrid With an Active Load. *IEEE Transactions on Power Electronics* **28** (11), 5107–5119 (November 2013). ISSN 1941-0107. DOI 10.1109/TPEL.2013.2241455. Cited on page(s) 73.

[33] Santiago Sanchez, Elisabetta Tedeschi, Jesus Silva, Muhammad Jafar, and Alexandra Marichalar. Smart load management of water injection systems in offshore oil and gas platforms integrating wind power. *IET Renewable Power Generation* **11** (9), 1153–1162 (7 2017). ISSN 1752-1416, 1752-1424. DOI 10.1049/iet-rpg.2016.0989. Cited on page(s) 73.

[34] Suresh Singh, Aditya R. Gautam, and Deepak Fulwani. Constant power loads and their effects in DC distributed power systems: A review. *ELSEVIER Renewable and Sustainable Energy Reviews* **72** (May 2017). ISSN 1364-0321. DOI 10.1016/j.rser.2017.01.027. Cited on page(s) 74.

[35] Eklas Hossain, Ron Perez, Adel Nasiri, and Ramazan Bayindir. Stability improvement of microgrids in the presence of constant power loads. *ELSEVIER International Journal of Electrical Power & Energy Systems* **96** (March 2018). ISSN 0142-0615. DOI 10.1016/j.ijepes.2017.10.016. Cited on page(s) 74.

[36] Nikos Hatziargyriou, *et al.* Definition and Classification of Power System Stability – Revisited & Extended. *IEEE Transactions on Power Systems* **36** (4), 3271–3281 (July 2021). ISSN 1558-0679. DOI: 10.1109/TPWRS.2020.3041774. Cited on page(s) 74.

[37] IEC 61400-27-1:2015. Wind turbines - Part 27-1: Electrical simulation models - Wind turbines. International Electrotechnical Commission Geneva, Switzerland (February 2015). URL https://webstore.iec.ch/publication/21811, accessed on 2023-02-24. Cited on page(s) 74.

[38] Magnus Korpås, Leif Warland, Wei He, and John Olav Giæver Tande. A case-study on offshore wind power supply to oil and gas rigs. *ELSEVIER Energy Procedia* **24** (January 2012). ISSN 1876-6102. DOI 10.1016/j.egypro.2012.06.082. Cited on page(s) 74.

[39] Luca Riboldi, Erick F. Alves, Marcin Pilarczyk, Elisabetta Tedeschi, and Lars O. Nord. Optimal Design of a Hybrid Energy System for the Supply of Clean and Stable Energy to Offshore Installations. *Frontiers in Energy Research* **8**, 346 (December 2020). ISSN 2296-598X. doi: 10.3389/fenrg.2020.607284. DOI 10.3389/fenrg.2020.607284. Cited on page(s) 74, 84.

[40] Andrew Arana, *et al.* Fast Frequency Response Concepts and Bulk Power System Reliability Needs, NERC Inverter-Based Resource Performance Task Force (IRPTF). White Paper North American Electric Reliability Corporation (NERC) Atlanta, GA, USA (March 2020). URL https://www.nerc.com/comm/PC/InverterBased%20Resource%20Performance%20Task%20Force%20IRPT/Fast_Frequency_Response_Concepts_and_BPS_Reliability_Needs_White_Paper.pdf, accessed on 2023-01-09. Cited on page(s) 77.

[41] Jingyang Fang, Hongchang Li, Yi Tang, and Frede Blaabjerg. On the Inertia of Future More-Electronics Power Systems. *IEEE Journal of Emerging and Selected Topics in Power Electronics* **7** (4), 2130–2146 (12 2019). ISSN 2168-6777, 2168-6785. DOI 10.1109/JESTPE.2018.2877766.

Cited on page(s) 78, 81.

[42] Prabha Kundur, Neil J. Balu, and Mark G. Lauby. Power System Stability and Control. EPRI power system engineering series. McGraw-Hill New York, USA (1994). ISBN 978-0-07-035958-1. Cited on page(s) 78.

[43] Jan Machowski. Power System Dynamics: Stability and Control. Wiley Chichester, U.K. 2nd edition (2008). ISBN 978-1-119-96505-3. Cited on page(s) 78.

[44] Salvatore D'Arco and Jon Are Suul. Equivalence of Virtual Synchronous Machines and Frequency-Droops for Converter-Based MicroGrids. *IEEE Transactions on Smart Grid* **5** (1) (January 2014). ISSN 1949-3061. DOI 10.1109/TSG.2013.2288000. Cited on page(s) 80.

[45] Pouyan Pourbeik, *et al.* Dynamic Models for Turbine-Governors in Power System Studies. Technical Report PES-TR1 IEEE Power & Energy Society (January 2013). URL https://site.ieee.org/fw-pes/files/2013/01/PES_TR1.pdf, accessed on 2023-02-17. Cited on page(s) 81, 88.

[46] Erick Alves, Gilbert Bergna-Diaz, Danilo Brandao, and Elisabetta Tedeschi. Sufficient Conditions for Robust Frequency Stability of AC Power Systems. *IEEE Transactions on Power Systems* **36** (3) (May 2021). ISSN 1558-0679. DOI 10.1109/TPWRS.2020.3039832. Cited on page(s) 82.

[47] Erick Fernando Alves. Optimization of Energy Storage for Frequency Control in Autonomous AC Power Systems – Frameworks for Planning and Operation. *Doctoral thesis*. NTNU (2023). URL https://ntnuopen.ntnu.no/ntnu-xmlui/handle/11250/3067209, accessed on 2023-07-02. ISBN: 9788232658671. ISSN: 2703-8084. Cited on page(s) 85.

[48] Linash P. Kunjumuhammed, Bikash C. Pal, Colin Oates, and Kevin J. Dyke. Electrical Oscillations in Wind Farm Systems: Analysis and Insight Based on Detailed Modeling. *IEEE Transactions on Sustainable Energy* 7 (1), 51–62 (January 2016). ISSN 1949-3037. DOI 10.1109/TSTE.2015.2472476. Cited on page(s) 87.

[49] Alvaro Ortega and Federico Milano. Stochastic transient stability analysis of transmission systems with inclusion of energy storage devices. *IEEE Transactions on Power Systems* **33** (1) (January 2018). ISSN 1558-0679. DOI 10.1109/TPWRS.2017.2742400. Cited on page(s) 87.

[50] Friederich Fröhr and Fritz Orttenburger. Introduction to Electronic Control Engineering. Siemens Aktiengesellschaft; Heyden & Son LTD. Berlin and München, Germany; London, UK (1982). ISBN 0-85501-290-0. Cited on page(s) 88.

[51] DIgSILENT GmbH. PowerFactory 2020 User Manual. PF2020 r6805 DIgSILENT GmbH Gomaringen, Germany (June 2020). URL https://www.digsilent.de/en/powerfactory-download.html (download for registered users), accessed on 2023-03-17. Cited on page(s) 88.

[52] IEEE Std 421.5-2016. IEEE Recommended Practice for Excitation System Models for Power System Stability Studies. IEEE Power & Energy Society New York, NY, USA (August 2016). DOI 10.1109/IEEESTD.2016.7553421. Cited on page(s) 88.

[53] Jon Are Suul, Marta Molinas, Lars Norum, and Tore Undeland. Tuning of Control Loops for Grid Connected Voltage Source Converters. In *2008 IEEE 2nd International Power and Energy Conference* Johor Bahru, Malaysia (December 2008). DOI 10.1109/PECON.2008.4762584. Cited on page(s) 88.

[54] Saeed Golestan, Josep M. Guerrero, and Juan C. Vasquez. Three-Phase PLLs: A Review of Recent Advances. *IEEE Transactions on Power Electronics* **32** (3), 1894–1907 (2017). ISSN 1941-0107. DOI 10.1109/TPEL.2016.2565642. Cited on page(s) 88.

[55] Sergio Pizarro-Gálvez, Héctor Pulgar-Painemal, and Víctor Hinojosa-Mateus. Parameterized Modal Analysis Using DIgSILENT Programming Language. In Francisco M. Gonzalez-Longatt and José Luis Rueda, editors, *PowerFactory Applications for Power System Analysis* pages 221–248. Springer International Publishing (2014). ISBN 978-3-319-12958-7. DOI 10.1007/978-3-319-12958-7_10. Cited on page(s) 89.

[56] Katsuhiko Ogata. Modern Control Engineering. Prentice-Hall Electrical Engineering Series. Instrumentation and Controls Series. Prentice-Hall Boston, USA 5th edition (2010). ISBN 978-0-13-615673-4. Cited on page(s) 91.

[57] OPAL. OP4510 System Description. Hardware products documentation OPAL-RT TECHNOLOGIES Montreal, Canada (2023). URL https://wiki.opal-rt.com/display/HDGD/

OP4510+V2+System+Description, accessed on 2023-03-10. Cited on page(s) 92.

[58] EGSTON. COMPISO System Unit (CSU). Operator Manual CSU X00-XGAMPX EGSTON Power Electronics GmbH Klosterneuburg, Austria (2018). URL https://www.egstonpower.com/wp-content/uploads/2020/06/CSU100-1GAMP6_Product-Folder.pdf, accessed on 2023-03-10. Cited on page(s) 92.

[59] IEEE Std 1110-2019 (Revision of IEEE Std 1110-2002). IEEE guide for synchronous generator modeling practices and parameter verification with applications in power system stability analyses. IEEE New York, USA (March 2020). DOI 10.1109/IEEESTD.2020.9020274. ISBN 978-1-5044-6290-7. Cited on page(s) 95.

CHAPTER 6

Scaling Method for Power Hardware-in-the-Loop Test Beds

RESEARCH GOALS AND CONTRIBUTIONS TO THE SCIENTIFIC LITERATURE

This chapter is tied to the Research Goal III, which validates in the laboratory the control structures proposed in this dissertation. It stems from Research Question V and focuses on a scaling method for matching specific characteristics of laboratory power electronic converters (PECs) used in power hardware-in-the-loop (PHIL) tests to the characteristics of real-life full-scale converters. Contribution V to the scientific literature is presented in this chapter, which compiles the contents of Publication VII.

Power hardware-in-the-loop (PHIL) testing bridges the gap between laboratory prototypes and real operational devices. It represents a sensible step before deployment of an electric power component in the real world [1]. The applications of PHIL span high performance motor drives [2], microgrids [3], renewable energy [4], and control of high-power converters [5]. In most cases, the device under test (DUT) is a power conversion equipment in a laboratory setup interfaced through power amplifiers with a simulated complex system in a real-time simulator (RTS). The easiest scenario is when the system under study and the PHIL test bed are of similar voltage and power levels. This, however, is rare as most of the DUTs in academic or industrial laboratories are low-voltage (LV) equipment with limited voltage and current capabilities adhering to standard safety practices, whereas the power systems emulated are of higher power and voltage levels sometimes in the kV and MW ranges. Due to these practical limitations, scaled-down converters (SDCs) are commonly used as DUTs to emulate real full-size converters (FSCs) [6–8]. However, an accurate scaling and interface methodology is essential for a realistic PHIL simulation. Without an accurate scaling, the benefits of choosing only controller hardware-in-the-loop (CHIL) simulations [9–12] or offline digital simulation can outweigh those of PHIL due to simplicity in implementation.

On one hand, traditional methods utilize rated values of voltages, currents, and power of the SDC to directly normalize and scale it to the FSC. Luo *et al.* [7], for instance, studied frequency regulation support by emulating a 300 MW wind farm with a 3 kW permanent-magnet synchronous generator (PMSG) connected to a reduced scale back-to-back power electronic converters (PECs). The entire wind farm was modeled as a controllable current source passed through a low-pass filter (LPF) (100 Hz cut-off) leaving behind the harmonics. Li *et al.* [6] employed a scaled-down 3 kW modular multilevel converter (MMC) to emulate a 1500 MW full-scale MMC using average models neglecting the switching harmonics. Type 3 and 4 [13] wind turbines of 2 MW and 600 kW, respectively, were emulated with 75 kVA PECs by Huerta *et al.* [8]. Those authors modeled the high-power system with a controlled power source and mentioned the advantage of using similar inductive filters in both the simulated and physical systems but did not discuss eventual mismatches caused by improper scaling. The scaling methods employed by Li *et al.* [6], Luo *et al.* [7], Huerta *et al.* [8], Torres-Olguin *et al.* [14], and Belhaouane *et al.* [15], moreover, assumed power flow only at the fundamental frequency. Thus, stability studies of the PHIL simulation with the SDCs may not fully conform with their high power systems as the harmonic interactions with the grid have been simplified. This is due to the impedance mismatches in the inductive-capacitive-inductive (LCL) filter as well as the different switching frequency of the SDC when compared with FSC. Given the limited assortment of available SDCs, it is a challenge to find specific sets of converters, transformers, and inductive-capacitive (LC) filters that reasonably represent the FSC.

On the other hand, Ren *et al.* [16] and Ren *et al.* [17] report issues in interfacing methods related to parasitic resonance between the impedances of the DUT and grid simulators, mismatch in reconstructed real voltage over its simulated signal, and problems with phase delays. These issues are typically solved by modifying, as part of the interfacing algorithms, either the hardware or software impedance. Although the focus of this chapter is not on interfacing algorithms, it is worth mentioning that some impedance-based interface algorithms alter the power circuit of the SDC [18] and that this could further deteriorate the representation of the SDC as FSC for high-frequency transients including the ones related to pulse-width modulation (PWM) switching. Most of the PHIL results [14, 19, 20] do not present outcomes that match voltages and currents at the switching frequency range of the FSC. Hence, there is a research gap in validating SDCs as replicas of FSCs for both line frequency and harmonic interactions with PHIL simulations.

In summary, there is no one-size-SDC-fits-all solution for establishing an accurate PHIL test bench. No two SDCs of different converter sizes, no LCL filters, and no make of line transformers with direct scaling at the rated voltage and current produce identical PHIL results representing the same FSC. It is noteworthy that, to the extent of the author's knowledge, the flexibility of varying the base kVA ratings of SDCs is often ignored and rarely discussed in the literature. Hence, the harmonic-invariant scaling method (HISM), proposed in Publication VII and described in this chapter, exploits the base kVA rating of an SDC to scale up and match the performance of the FSC, not only at line frequency but also for harmonic interactions up to the switching frequency. In other words, the voltage and current waveforms of the SDC when scaled up accurately match the FSC's in the spectrum between the fundamental and the switching frequency. This is the main strength of the proposed method, which features a script to vary SDC base values of voltages and currents (in turn base kVA rating) and selects the base value that gives the best match with the FSC.

This chapter describes the following contributions presented originally in Publication VII:

1. Guidelines for performing PHIL simulations that can be adapted to academic and industrial laboratories.
2. Novel harmonic-invariant scaling method (HISM) to exploit the base kVA rating of SDC for an accurate match with FSC.
3. Simplified scripts for scaling the converter, along with models and raw data, that are made publicly available at the Repository VI.

This chapter is organized as follows: the scaled-down PHIL test bench at the National Smart Grid Laboratory (NSGL) used for Publication VII is presented in Section 6.1. The mismatch in pu values when the SDC is operated at nominal rating is highlighted in Section 6.2. The proposed HISM is presented as a systematic procedure using a flowchart in Section 6.3. In Section 6.4, the HISM is applied to a practical example representing a 5 MVA battery energy storage system (BESS) power conversion equipment [21] with an SDC in the laboratory. The theoretical analysis is, then, validated by comparing offline digital simulations and PHIL results in Section 6.5.

6.1 SCALED-DOWN PHIL TEST BED

Figure 6.1 shows the single line diagram of the PHIL setup. On the left-side, the dc-grid emulator is connected to the dc link of the converter. The capacitor at the dc link is denoted by C_{dc} and the voltage across this capacitor is named V_{dc}. The current flowing into the dc-side of the PEC is named I_{dc}. The dc-grid emulator operates as a controlled voltage source. On the right-side, the ac-grid emulator is connected to the converter transformer, which stands for one of the inductances of the LCL filter. The short-circuit impedance of the transformer is denoted by L_t (inductive part) and R_t (resistive part). The values of the short-circuit inductance and resistance are the ones seen from the converter side terminals of the transformer. The ac-grid emulator operates as a controlled voltage source. The voltage at the middle of the LCL filter is named V_{ac}. The capacitive branch of the LCL filter is represented by C_{dc}. The converter reactor is modeled by the inductance L_r with a parasitic resistance R_r. The current leaving the converter towards the reactor is denoted by I_{ac}.

The superscript fs denotes quantities related to the FSC and the superscript sd denotes quantities of the SDC. Capital letters refer to quantities in the International System of Units (SI), whereas lowercase letters are employed for normalized (i.e.,

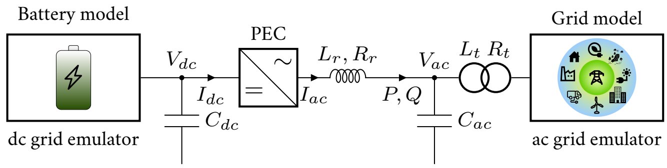

FIGURE 6.1 Scaled-down PHIL test rig.

© Daniel Mota 2023 | Redrawn and recomposed from Publication VII | Source code information at Part III.

divided by a base value) quantities. The described scaling method, moreover, does not change time. Hence, quantities in seconds and hertz are unaffected. Therefore, the following values are assumed equal for both full-size and scaled-down systems:

1. Rated ac frequency F_n in Hz,
2. Correspondent angular frequency $\omega_n = 2\pi F_n$ in rad s^{-1}.
3. Switching frequency F_{sw} in Hz of the converters.

Note that laboratory SDCs are able to operate at higher switching frequencies (5-10 kHz) [22] than MW-sized real-life converters (on the range of 3 kHz) [21]. It is, however, simple to lower the SDC switching frequency in the laboratory.

6.2 NORMALIZATION OF FSC AND SDC

The goal of the scaling is to match the normalized quantities describing the FSC and SDC. To begin with, a set of normalizing bases for the quantities in the ac and dc sides must be defined and applied to both full-scale and scaled-down converters. Firstly, base values for apparent power (S_b) and ac voltage (V_{bac}) and current (I_{bac}) are defined:

$$S_b = \sqrt{3}\, V_{bac}\, I_{bac}\ [\text{VA}]. \tag{6.1}$$

For the FSC, S_b^{fs}, V_{bac}^{fs}, and I_{bac}^{fs} are typically defined as the rated values of the converter designed for an application. However, for a ready-to-use or laboratory SDC, either absolute maxima mentioned on the nameplate or derated values as provision for overloading capacities are chosen for S_b^{sd}, V_{bac}^{sd}, and I_{bac}^{sd}. The pu bases for the impedance (Z_b), inductance (L_b), and ac capacitance (C_b) are defined by the choices made for V_{bac} and I_{bac}:

$$Z_b = \frac{V_{bac}}{\sqrt{3}\, I_{bac}}\ [\Omega],\quad L_b = \frac{V_{bac}}{\omega_n \sqrt{3}\, I_{bac}}\ [\text{H}],\quad C_b = \frac{\sqrt{3}\, I_{bac}}{\omega_n V_{bac}}\ [\text{F}]. \tag{6.2}$$

It is worth recalling that ω_n is equal for both full-scale and scaled-down converters. Also, for simplicity, the power bases on the ac and dc sides are assumed equal, i.e., the converter losses are ignored and the power factor is assumed to be unity.

$$S_b = V_{bdc}\, I_{bdc} = \sqrt{3}\, V_{bac}\, I_{bac}. \tag{6.3}$$

The main purpose of the dc-link capacitance is to serve as an energy buffer. It keeps the dc-link voltage relatively constant during transient unbalances in power exchange through the converter. For normalization, an option is to use an analogous of the inertia constant H of synchronous machines [23], which is defined as the kinetic energy stored in the rotor divided by the machine's apparent power. For the converters, the analogous H is equal to the energy stored in the capacitor at rated dc voltage divided by the converter's rated apparent power.

$$H = \frac{C_{dc} {V_{bdc}}^2}{2\ S_b} \quad [\mathrm{s}] \tag{6.4}$$

Table 6.1 shows the quantities before and after normalization, computed with equations (6.1) to (6.4), for an FSC and a laboratory ready-to-use SDC. It can be clearly seen that the normalized quantities for the SDC computed both at nameplate values and close to rated values have a mismatch compared to the FSC.

TABLE 6.1 Mismatch in pu values between an SDC scaled at nameplate and at close to rated values and an FSC.

Quantity	**Full-Scale Converter**	**Scaled-Down Converter (Nameplate values)**	**Scaled-Down Converter (Close to rated values)**
Power S_b	5 MVA	70 kVA	45 kVA
Voltage V_{bac}	690 V	400 V	363 V
Current I_{bac}	4184 A	100 A	72 A
Voltage V_{bdc}	1100 V	650 V	579 V
Current I_{bdc}	4546 A	100 A	78 A
Reactor L_r	77.5 µH 0.256 pu	500 µH 0.068 pu	500 µH 0.054 pu
Transformer ratio	13.8 kV / 690 V	400 V / 400 V	363 V / 363 V
Transformer L_t	24.2 µH 0.08 pu	316 µH 0.043 pu	316 µH 0.034 pu
Transformer R_t	0.476 mΩ 0.005 pu	49.4 mΩ 0.021 pu	49.4 mΩ 0.017 pu
Capacitance C_{ac}	1.8 mF 0.055 pu	50 µF 0.036 pu	50 µF 0.046 pu
LCL resonance F_{res}	863.7 Hz	1.61 kHz	1.61 kHz
Capacitance C_{dc}	20 mF $H = 2.42$ ms	14 mF $H = 42.3$ ms	14 mF $H = 52.8$ ms

6.3 HARMONIC INVARIANT SCALING METHOD (HISM)

It is fairly common for laboratories to feature sets of ready-to-use converters that can be chosen as SDCs to represent specific FSCs in different PHIL setups. However, the direct scaling of these converters can lead to large discrepancies in pu values of components of the FSC and SDC. As it is not always feasible to procure a tailor-made SDC for each and every PHIL setup, it is essential to develop a matching procedure between available SDCs and an FSC. To address this problem, the HISM that minimizes mismatches by searching for optimal sets of pu base values within the SDC kVA range was proposed in Publication VII. A summarized version of this method is shown in figure 6.2. The mismatches are assessed for combinations of V_{bac}^{sd} and I_{bac}^{sd} assuming that those are bounded by minimum and maximum values.

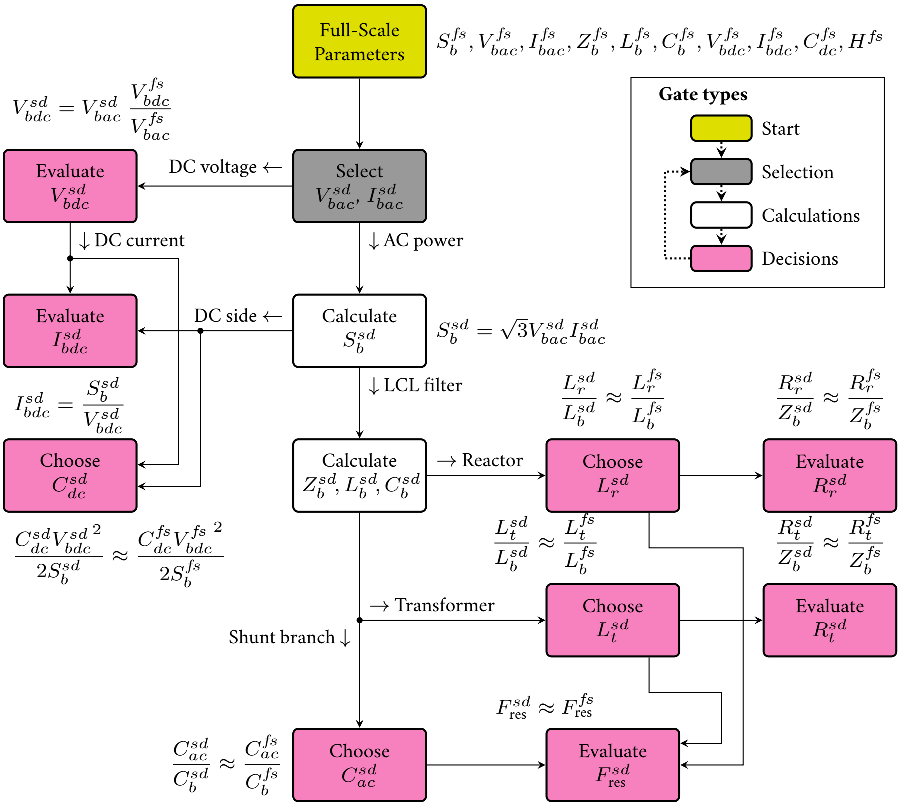

FIGURE 6.2 Method for matching scaled-down and full-scale converters.

© Daniel Mota 2023 | Redrawn and recomposed from Publication VII | Source code information at Part III.

6.3.1 Select Pair V_{bac}^{sd}, I_{bac}^{sd} and Evaluate V_{bdc}^{sd} and I_{bdc}^{sd}

Firstly, select V_{bac}^{sd} according to the following constraints:

1. Operational range of the ac grid emulator.
2. Turns ratio and rated voltage of the converter transformer.
3. Rating of the SDC and LCL devices.
4. Converter minimum operating voltage for detection and synchronization using phase-locked loop (PLL).

The choice of V_{bac}^{sd} also determines the dc base voltage V_{bdc}^{sd}, as seen in equation (6.5).

$$V_{bdc}^{sd} = V_{bac}^{sd} \frac{V_{bdc}^{fs}}{V_{bac}^{fs}} \quad [\mathrm{V}] \tag{6.5}$$

Notice that the FSC voltages V_{bdc}^{fs} and V_{bac}^{fs} are predetermined and not variables within the method. Additionally, the resulting V_{bdc}^{sd} from equation (6.5) must be within the operating range of the SDC, as well as within the range of the dc grid emulator.

Secondly, select an appropriate base current I_{bac}^{sd} for the SDC taking into consideration the following constraints:

1. Rated currents of the transformer.
2. Rated current of the LC filter devices.
3. Rated current of the SDC.
4. Possible overloaded cases to be analyzed in the PHIL tests.

The selected pair (V_{bac}^{sd},I_{bac}^{sd}) yields the base apparent power S_b^{sd} for the SDC, see equation (6.1), which can be lower than the rated (nameplate) value of the SDC. Moreover, the pair of ac voltage and current determines I_{bdc}^{sd} with equation (6.3) and the impedance bases on the LV side of the scaled-down transformer with equation (6.2). Now, the components of the LCL filter can be selected.

6.3.2 Converter Reactor L_r^{sd} and R_r^{sd}

In this step, the converter-side L of the LCL-filter is chosen. The inductance in pu of the converter reactor (l_r) of the SDC is compared with that of the FSC. In practice, there will be a mismatch between l_r^{sd} and l_r^{fs} particularly in cases of limited availability of SDC reactors. If l_r^{sd} could be freely chosen, it should be made equal to l_r^{fs}.

The following equation expresses the inductance in pu of the converter reactor of the SDC and FSC:

$$l_r^{sd}[\text{pu}] = \frac{L_r^{sd}[\text{H}]}{L_b^{sd}[\text{H}]} \approx l_r^{fs}[\text{pu}] = \frac{L_r^{fs}[\text{H}]}{L_b^{fs}[\text{H}]}. \tag{6.6}$$

When L_b^{sd} in equation (6.6) is rewritten with L_b from equation (6.2), l_r^{sd} becomes

$$l_r^{sd}[\text{pu}] = L_r^{sd}\omega_n\sqrt{3}\,\frac{I_{bac}^{sd}}{V_{bac}^{sd}}. \tag{6.7}$$

As it can be seen from equation (6.7), the values of the base voltage and current influence l_r^{sd}. Thus, if L_r^{sd} cannot be changed, then V_{bac}^{sd} and I_{bac}^{sd} can be altered to bring l_r^{sd} closer to l_r^{fs}.

The resistance of the SDC's converter reactor in pu should be approximately equal to that of the FSC. This is expressed in the following equation:

$$r_r^{sd}[\text{pu}] = \frac{R_r^{sd}[\text{H}]}{Z_b^{sd}[\text{H}]} \approx r_r^{fs}[\text{pu}] = \frac{R_r^{fs}[\text{H}]}{Z_b^{fs}[\text{H}]}. \tag{6.8}$$

When Z_b^{sd} in equation (6.8) is rewritten with Z_b from equation (6.2), r_r^{sd} becomes

$$r_r^{sd}[\text{pu}] = R_r^{sd}\sqrt{3}\,\frac{I_{bac}^{sd}}{V_{bac}^{sd}}. \tag{6.9}$$

The resistance in pu of the SDC converter reactor can rarely be chosen freely as it largely depends on the quality, in efficiency terms, of the reactor. Nevertheless, a mismatch between resistances in pu is usually expected as kVA-range laboratory reactors can have lower efficiencies, i.e., higher relative resistive losses, than industry-grade large scale reactors. Furthermore, as seen in equations (6.7) and (6.9), if the pu bases are adapted to increase l_r^{sd}, the resistance r_r^{sd} also increases. Thus, a compromise must be made between matching the inductances and matching the resistances of the converter reactors of the SDC and FSC.

The ripple current in pu can also be used for matching the reactors of the SDC and FSC. One should aim to make the ripple current in pu for both the scaled-down and full-scale converters to be as similar as possible. The peak-to-peak ripple in the converter reactor current (ΔI_r^{sd}) is given by [24]:

$$\Delta I_r^{sd}[\text{A}] = \frac{V_{bdc}^{sd}}{8\,L_r^{sd}\,F_{\text{sw}}}. \tag{6.10}$$

By substituting V_{bdc}^{sd} from equation (6.5) and by normalizing ΔI_r^{sd} with the peak value of I_{bac}^{sd}, one obtains:

$$\Delta i_r^{sd}[\text{pu}] = \frac{\Delta I_r^{sd}}{\sqrt{2}\,I_{bac}^{sd}} = \frac{1}{8\sqrt{2}\,L_r^{sd}F_{\text{sw}}}\,\frac{V_{bac}^{sd}}{I_{bac}^{sd}}\,\frac{V_{bdc}^{fs}}{V_{bac}^{fs}}. \tag{6.11}$$

Even when the converter reactor can easily be swapped, the set of available reactors in a laboratory is usually limited. Therefore, the flexibility of adapting base voltage V_{bac}^{sd} and base current I_{bac}^{sd} should be used to match ripple currents in pu for the SDC and FSC. It is, however, important to notice in equation (6.11) that the ratio $V_{bdc}^{fs}/V_{bac}^{sd}$ is fixed by the FSC design.

6.3.3 Converter Transformer L_t^{sd} and R_t^{sd}

There is usually not much flexibility in choosing the SDC transformer, i.e., the grid-side L of LCL, in a laboratory as the set of ready-to-use transformers tends to be limited. Also, procuring tailor-made scaled-down transformers might not be economically feasible within some project budgets. Therefore, one must try to match the converter transformer pu inductance of the SDC and FSC by choosing the base voltage and current of the SDC.

The following equations express the pu value of the inductance and resistance of the SDC and the FSC:

$$l_t^{sd}[\text{pu}] = \frac{L_t^{sd}[\text{H}]}{L_b^{sd}[\text{H}]} \approx l_t^{fs}[\text{pu}] = \frac{L_t^{fs}[\text{H}]}{L_b^{fs}[\text{H}]} \tag{6.12}$$

$$r_t^{sd}[\text{pu}] = \frac{R_t^{sd}[\Omega]}{Z_b^{sd}[\Omega]} \approx r_t^{fs}[\text{pu}] = \frac{R_t^{fs}[\Omega]}{Z_b^{fs}[\Omega]}. \tag{6.13}$$

In general, the goal should be achieving similar pu values for the inductances of the SDC and FSC transformers. Likewise, a similar pu value should be the aim for the transformer resistance. However, it will be difficult to have a close match between the transformer resistances of the SDC and FSC as the efficiency of an LV low-power transformer in the laboratory is usually lower than that of a high-voltage (HV) high-power transformer [25].

When L_b^{sd} in equation (6.12) and Z_b^{sd} in equation (6.13) are rewritten with the bases in equation (6.2), the following equations are obtained:

$$l_t^{sd}[\text{pu}] = L_t^{sd}\omega_n\sqrt{3}\,\frac{I_{bac}^{sd}}{V_{bac}^{sd}} \tag{6.14}$$

$$r_t^{sd}[\text{pu}] = R_t^{sd}\sqrt{3}\,\frac{I_{bac}^{sd}}{V_{bac}^{sd}}. \tag{6.15}$$

It can be seen from equations (6.14) and (6.15) that the base voltage and current can be chosen to match the pu inductance and pu resistance of the SDC transformer with those of the FSC. However, it should be noted that the choice that matches pu inductances will likely lead to a mismatch in pu resistances. Thus, a trade-off between the mismatches in inductance and resistance must be made.

6.3.4 Shunt Branch of the LCL C_{ac}^{sd}

The normalized capacitance of the SDC LCL filter should be made as similar as possible to that of the FSC, i.e.,

$$c_{ac}^{sd}[\text{pu}] = \frac{C_{ac}^{sd}[\text{F}]}{C_b^{sd}[\text{F}]} \approx c_{ac}^{fs}[\text{pu}] = \frac{C_{ac}^{fs}[\text{F}]}{C_b^{fs}[\text{F}]}. \tag{6.16}$$

By using equation (6.2) and re-writing equation (6.16) into equation (6.17), one notices that c_{ac}^{sd} is proportional to V_{bac}^{sd} and inversely proportional to I_{bac}^{sd}.

$$c_{ac}^{sd}[\text{pu}] = C_{ac}^{sd}\,\frac{\omega_n}{\sqrt{3}}\,\frac{V_{bac}^{sd}}{I_{bac}^{sd}} \tag{6.17}$$

When it is impractical to change $C_{ac}^{sd}[\text{F}]$, $c_{ac}^{sd}[\text{pu}]$ can be matched with $c_{ac}^{fs}[\text{pu}]$ by adapting the SDC base voltage and base current. Notice, however, that the ratio of bases in equation (6.17) is the inverse of the ones in equations (6.7), (6.9), (6.14), and (6.15). Therefore, a choice of bases that increases c_{ac}^{sd}, decreases l_r^{sd} and l_t^{sd}.

6.3.5 Evaluate Resonance Frequency F_{res}^{sd}

The LCL resonance frequency can be calculated using the following equation [24]:

$$F_{\text{res}}^{sd}[\text{Hz}] = \frac{1}{2\pi}\sqrt{\frac{L_t^{sd} + L_r^{sd}}{L_t^{sd} L_r^{sd} C_{ac}^{sd}}} \approx F_{\text{res}}^{fs}[\text{Hz}] = \frac{1}{2\pi}\sqrt{\frac{L_t^{fs} + L_r^{fs}}{L_t^{fs} L_r^{fs} C_{ac}^{fs}}}. \tag{6.18}$$

In general, the resonance frequency of the SDC should be approximately equal to that of the FSC.

6.3.6 Converter Dc-Link Capacitance C_{dc}^{sd}

The H constant of the SDC as defined in equation (6.4) should ideally be made equal to the one of the FSC. When changes to the SDC capacitor bank are not feasible, the values of V_{bdc}^{sd} and S_b^{sd} can be adapted to improve the match of H. It is important to remark that H should be carefully scaled when the real-life converter is expected to regulate the dc-voltage through an active current loop. In such cases, a proper modeling of interactions between the converter controller and the dc-capacitance is critical. However, H is not as critical when the FSC dc-link is fed by an active source like a battery as in the scenario depicted in figure 6.1.

6.3.7 Application Strategies

It is clear from the previous subsections that the mismatches in the inductance of the converter reactor, the capacitance in the LCL, the constant H of the dc-link capacitance, and transformer reactance can be minimized by varying the base voltage V_{bac}^{sd} and base current I_{bac}^{sd}, thus the base VA rating of SDC. The process begins by sweeping in small steps the base current from a minimum to a maximum value for a given base voltage. Once the full range of the base current has been explored for this given base voltage, another current sweep is performed for an incremented value of the base voltage. At every base pair, the mismatch in the parameters is calculated. This process continues until the mismatch has been evaluated at all possible combinations of base voltages and base currents. Depending on the application purpose of the PHIL simulation, a two-fold strategy must be adapted to choose the right solution.

Strategy 1 — Minimizing the mismatch on one normalized quantity
Mismatch error in one normalized quantity is calculated at all possible combinations of base voltage V_{bac}^{sd} and base current I_{bac}^{sd}. For multiple solutions around the predefined mismatch error, a base voltage V_{bac}^{sd} and a base current I_{bac}^{sd} that make the maximum VA rating are selected for the better utilization of the SDC.

Strategy 2 — Trade-off minimization of mismatch on all the normalized quantities
As it may be practically impossible to minimize the mismatch on all the normalized quantities without physical replacement of any component, a higher predefined mismatch error is considered and the pair of base voltage V_{bac}^{sd} and current I_{bac}^{sd} that makes the maximum VA rating is selected.

The following section presents the application of the HISM's first strategy with a practical example of a BESS power conversion stage.

6.4 PRACTICAL EXAMPLE - BESS

The design parameters for the FSC shown in Table 6.1 are based on a practical grid-scale BESS [21] that can be employed for various grid ancillary services such as frequency and voltage support, peak shaving of distributed generation, etc. It is impractical to invest in deploying the entire power conversion system in the laboratory, especially for studies related to PWM techniques, harmonic penetration into the grid, and impact on power quality. The PHIL system presented in figure 6.1 can easily be made to represent a practical BESS. This is done by controlling the dc and ac emulators to respond as a battery bank and as an electric grid, respectively, and by physically representing the FSC with the SDC, as shown in figure 6.1.

Based on mathematical computations of the proposed methodology (strategy 1) in section 6.3.7, a script was developed for computing an error estimate of the normalized quantities between SDC and FSC while varying base values of voltage (50 V to 363 V) and current values (5 A to 72 A) simultaneously. A surface plot in figure 6.3 with varying base current and base voltage shows the error in the normalized value of l_r^{sd} compared to l_r^{fs} along with a predefined mismatch error plane of 5 %. The following two cases are chosen for analysis:

Case 1 — base current close to rated SDC but with reduced base voltage.
Case 2 — base voltage and current close to SDC rated.

Two data points for case 1 and one data point for case 2 are shown on the plot in figure 6.3. Further analysis will be focused around these cases. Case 1 points to a set of base values in a region where the predefined mismatch error plane is intersected. Two data points shown for case 1 present an interesting scenario where both base values of currents are maximum and equal. However, it is worth recalling here that strategy 1 aims to select the base values that yield the maximum VA rating of the SDC. Hence, the choice for case 1 is made as

$$V_{bac}^{sd} = 81\,\mathrm{V} \quad \text{and} \quad I_{bac}^{sd} = 72\,\mathrm{A}.$$

Hence, using HISM, the base VA rating of SDC for case 1 is adjusted to

$$\sqrt{3} \times 81\,\mathrm{A} \times 72\,\mathrm{A} = 10.1\,\mathrm{kVA}.$$

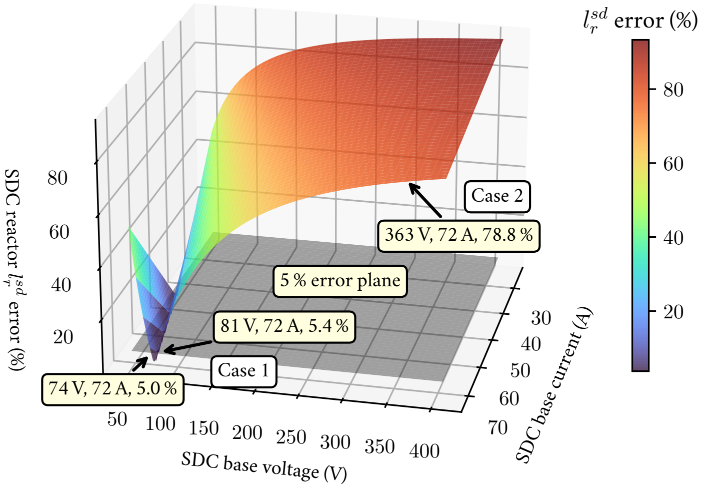

FIGURE 6.3 HISM applied to the converter reactor.

© Daniel Mota 2023 | Redrawn and recomposed from Publication VII | Source code information at Part III.

This minimizes the error on the inductance in pu of the converter reactor (l_r).

From figure 6.3, base values close to the rated quantities of the SDC are chosen for case 2, namely

$$V_{bac}^{sd} = 363\,\text{V} \quad \text{and} \quad I_{bac}^{sd} = 72\,\text{A}.$$

This results in the following base for the SDC apparent power:

$$\sqrt{3}\times 363\,\text{A}\times 72\,\text{A} = 45.3\,\text{kVA}.$$

Based on the application requirement, the user can freely decide between strategies 1 and 2 while using the HISM.

The performances of the SDCs using HISM based selection (case 1) and close-to-rated-value scaling (case 2) are benchmarked against the computer simulation of a practical BESS FSC in the following section.

6.5 SIMULATED AND PHIL RESULTS

The PHIL tests with the SDC are performed at the NSGL, see figure 6.4. An oscilloscope with a bandwidth of 20 MHz, no extra filtering or smoothing, is employed for measuring two of the phase-to-ground voltages across the shunt capacitor and the current across two phases of the converter reactor, which are indicated by V_{ac} and I_{ac} in figure 6.1, respectively.

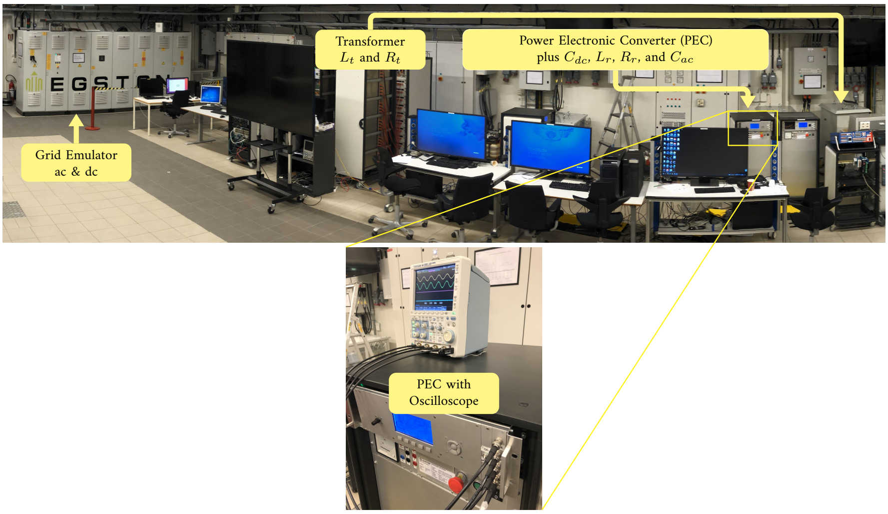

FIGURE 6.4 National Smart Grid Laboratory at NTNU. The oscilloscope on the top of the converter was used for the measurements shown in figure 6.5.

© Daniel Mota 2023 | Source code information at Part III.

The measurements of phase a, scaled up to FSC levels, are presented in figures 6.5a and b. The active and reactive power (figures 6.5c and d) are calculated from the scaled up three-phase voltages and currents. They represent the power flow at the point indicated by P,Q in figure 6.1. A moving average (MA) filter with a window equal to 20 ms is applied to the power measurements. The voltages, active power, and reactive power, obtained with case 1 (green) and case 2 (red) are similar to the ones obtained with a computer simulation (black) of the FSC. However, the switching ripple in the current across L_r for case 2 is clearly worse than the one of case 1. To properly analyze the distortions and ripple in the voltages and currents, the fast Fourier transform (FFT) is employed.

Figure 6.6 shows the FFT of voltages and currents presented in figure 6.5. A time window of 200 ms, i.e., 10 grid cycles, is chosen for the FFT, which yields a resolution of 5 Hz in the frequency spectrum. The frequency axis is linear between zero and 100 Hz and logarithmic between 100 Hz and 10 kHz. The amplitude of the fundamental frequency (50 Hz) of the voltage and current are similar for the FSC computer simulation (black), SDC case 1 (green), and case 2 (red). The distortions caused by the PWM switching in the range of 3 kHz are highlighted by insets. Case 1 greatly matches the magnitude of switching harmonics when compared to case 2 and to the computer simulation of the FSC.

For a better assessment, the total demand distortion (TDD) of the currents are calculated according to IEC 61000-4-7:2002 [26] with the interharmonic components in the spectrum up to 10 kHz grouped at their respective closest integer harmonic of 50 Hz. As seen in table 6.2, the SDC case 1 manages to match the TDD

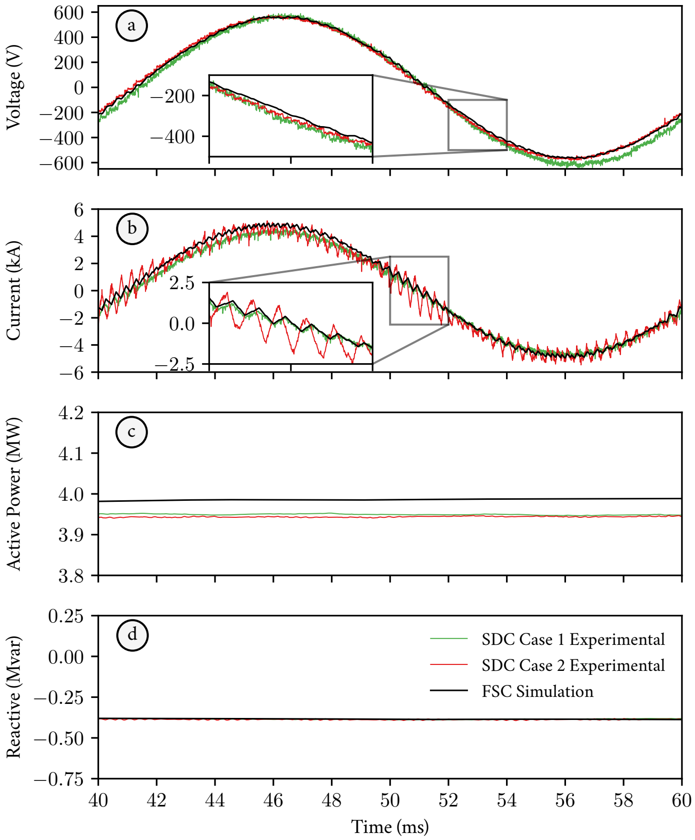

FIGURE 6.5 Computer simulation and PHIL results.

© Daniel Mota 2023 | Redrawn and recomposed from Publication VII | Source code information at Part III.

of the FSC. Both are below the limit of 5 % established by IEEE Std 519-1992 [27], whereas, the SDC case 2 amplifies the switching frequency components and thus the TDD, wrongly representing the FSC in the PHIL simulation. It is worth remarking that, in the laboratory test, the current is measured at the converter terminals, i.e., before the shunt capacitance and grid-side inductance of the LCL filter. IEEE Std 519-1992 [27], however, defines the TDD limit for the current delivered at the point of common connection.

TABLE 6.2 TDD of the converter currents in figure 6.5b.

	SDC case 1	SDC case 2	FSC
TDD	2.456 %	9.401 %	2.462 %

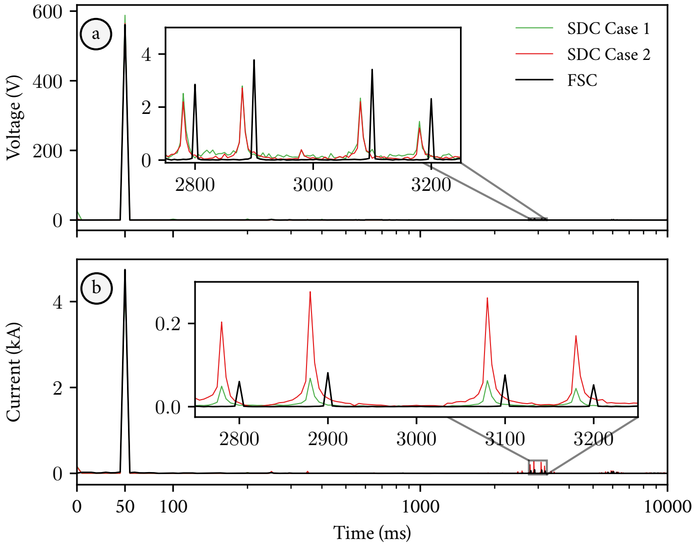

FIGURE 6.6 FFT of the voltages and currents from figure 6.5.

© Daniel Mota 2023 | Redrawn and recomposed from Publication VII | Source code information at Part III.

6.6 CONCLUSION

Reduced scale PHIL tests in academic or industrial laboratories can greatly reduce the burden of building high-power converter prototypes in early technology readiness level (TRL) stages. However, as any other modeling technique, the depth of detail in which the laboratory SDC mimics the real-life FSC must be adapted to the phenomena one intends to investigate with the PHIL tests. When power quality and harmonic disturbances are under scrutiny, a proper match of the converter PWM frequency and the LCL filter should be guaranteed. In this chapter, a method that aims to reproduce the distortions and harmonic content of real-life power converters in the laboratory by adapting the pu bases of preexisting scaled-down equipment is presented. The performance of the method in question, named HISM, was tested by comparing the harmonic content of the output current of a simulated FSC with the measured ones of an SDC in a PHIL setup. The HISM, as demonstrated in this chapter, can be used by researchers to avoid being misled towards controller stability issues when higher ripple currents are seen during PHIL simulations. In fact, such issues could be caused by bad scaling methods as seen in case 2 results in section 6.5. In summary, the HISM provides the means to better reproduce the harmonic distortions and power quality phenomena of real-life full-size power converters in PHIL tests, reducing the need for customization of available laboratory power converters.

6.7 REFERENCES

[1] Andrew J. Roscoe, Andrew Mackay, Graeme M. Burt, and J. R. McDonald. Architecture of a Network-in-the-Loop Environment for Characterizing AC Power-System Behavior. *IEEE Transactions on Industrial Electronics* **57** (4), 1245–1253 (April 2010). ISSN 1557-9948. DOI 10.1109/TIE.2009.2025242. Cited on page(s) 105.

[2] Nimananda Sharma, Georgios Mademlis, Yujing Liu, and Junfei Tang. Evaluation of Operating Range of a Machine Emulator for a Back-to-Back Power-Hardware-in-the-Loop Test Bench. *IEEE Transactions on Industrial Electronics* **69** (10), 9783–9792 (October 2022). ISSN 1557-9948. DOI 10.1109/TIE.2022.3142421. Cited on page(s) 105.

[3] Panos C. Kotsampopoulos, Vasilis A. Kleftakis, and Nikos D. Hatziargyriou. Laboratory Education of Modern Power Systems Using PHIL Simulation. *IEEE Transactions on Power Systems* **32** (5), 3992–4001 (September 2017). ISSN 1558-0679. DOI 10.1109/TPWRS.2016.2633201. Cited on page(s) 105.

[4] Mandip Pokharel and Carl Ngai Man Ho. Stability Analysis of Power Hardware-in-the-Loop Architecture With Solar Inverter. *IEEE Transactions on Industrial Electronics* **68** (5), 4309–4319 (May 2021). ISSN 1557-9948. DOI 10.1109/TIE.2020.2984969. Cited on page(s) 105.

[5] Ranjan Sharma, Qiuwei Wu, Seung Tae Cha, Kim H. Jensen, Tonny W. Rasmussen, and Jacob Østegaard. Power hardware in the loop validation of fault ride through of VSC HVDC connected offshore wind power plants. *Journal of Modern Power Systems and Clean Energy* **2** (1), 23–29 (March 2014). ISSN 2196-5420. DOI 10.1007/s40565-014-0049-z. Cited on page(s) 105.

[6] Binbin Li, Zigao Xu, Shengbo Wang, Linjie Han, and Dianguo Xu. Interface Algorithm Design for Power Hardware-in-the-loop Emulation of Modular Multilevel Converter Within High-Voltage Direct Current Systems. *IEEE Transactions on Industrial Electronics* **68** (12), 12206–12217 (December 2021). ISSN 1557-9948. DOI 10.1109/TIE.2020.3040682. Cited on page(s) 105, 106.

[7] Kui Luo, Wenhui Shi, Yongning Chi, Qiuwei Wu, and Weisheng Wang. Stability and Accuracy Considerations in the Design and Implementation of Wind Turbine Power Hardware in the Loop Platform. *CSEE Journal of Power and Energy Systems* **3** (2), 167–175 (June 2017). ISSN 2096-0042. DOI 10.17775/CSEEJPES.2017.0021. Cited on page(s) 105, 106.

[8] Francisco Huerta, Ronald Lister Tello, and Milan Prodanovic. Real-Time Power-Hardware-in-the-Loop Implementation of Variable-Speed Wind Turbines. *IEEE Transactions on Industrial Electronics* **64** (3), 1893–1904 (March 2017). ISSN 1557-9948. DOI 10.1109/TIE.2016.2624259. Cited on page(s) 105, 106.

[9] Wei Li, Géza Joos, and Jean Belanger. Real-Time Simulation of a Wind Turbine Generator Coupled With a Battery Supercapacitor Energy Storage System. *IEEE Transactions on Industrial Electronics* **57** (4), 1137–1145 (April 2010). ISSN 1557-9948. DOI 10.1109/TIE.2009.2037103. Cited on page(s) 105.

[10] Guoqing Li, Di Zhang, Yechun Xin, Shouqi Jiang, Weiru Wang, and Jiahui Du. Design of MMC Hardware-in-the-Loop Platform and Controller Test Scheme. *CPSS Transactions on Power Electronics and Applications* **4** (2), 143–151 (June 2019). ISSN 2475-742X. DOI 10.24295/CPSSTPEA.2019.00014. Cited on page(s) 105.

[11] Xu Zhang, Xiaorong Xie, Jan Shair, Hui Liu, Yu Li, and Yunhong Li. A Grid-Side Subsynchronous Damping Controller to Mitigate Unstable SSCI and Its Hardware-in-the-loop Tests. *IEEE Transactions on Sustainable Energy* **11** (3), 1548–1558 (July 2020). ISSN 1949-3037. DOI 10.1109/TSTE.2019.2930289. Cited on page(s) 105.

[12] Everson Mattos, Lucas C. Borin, Caio R. D. Osório, Gustavo G. Koch, Ricardo C. L. F. Oliveira, and Vinícius F. Montagner. Robust Optimized Current Controller Based on a Two-Step Procedure for Grid-Connected Converters. *IEEE Transactions on Industry Applications* (October 2022). ISSN 1939-9367. DOI 10.1109/TIA.2022.3211251. Cited on page(s) 105.

[13] IEC 61400-27-1:2015. Wind turbines - Part 27-1: Electrical simulation models - Wind turbines.

International Electrotechnical Commission Geneva, Switzerland (February 2015). URL https://webstore.iec.ch/publication/21811, accessed on 2023-02-24. Cited on page(s) 106.

[14] Raymundo E. Torres-Olguin, Atsede G. Endegnanew, and Salvatore D'Arco. Power-hardware-in-the-loop approach for emulating an offshore wind farm connected with a VSC-based HVDC. In *2017 IEEE Conference on Energy Internet and Energy System Integration (EI2)* Beijing, China (November 2017). DOI: 10.1109/EI2.2017.8245735. Cited on page(s) 106.

[15] Mohamed Moez Belhaouane, Khaled Almaksour, Lampros Papangelis, Oleg Gomozov, Frédéric Colas, Thibault Prévost, Xavier Guillaud, and Thierry Van Cutsem. Implementation and Validation of a Model Predictive Controller on a Lab-Scale Three-Terminal MTDC Grid. *IEEE Transactions on Power Delivery* **37** (3), 2209–2219 (June 2022). ISSN 1937-4208. DOI 10.1109/TPWRD.2021.3107485. Cited on page(s) 106.

[16] Wei Ren, Michael Steurer, and Thomas L. Baldwin. Improve the Stability and the Accuracy of Power Hardware-in-the-Loop Simulation by Selecting Appropriate Interface Algorithms. *IEEE Transactions on Industry Applications* **44** (4), 1286–1294 (July 2008). ISSN 1939-9367. DOI: 10.1109/TIA.2008.926240. Cited on page(s) 106.

[17] Wei Ren, *et al.* Interfacing Issues in Real-Time Digital Simulators. *IEEE Transactions on Power Delivery* **26** (2), 1221–1230 (April 2011). ISSN 1937-4208. DOI 10.1109/TPWRD.2010.2072792. Cited on page(s) 106.

[18] Il Do Yoo and A. M. Gole. Compensating for Interface Equipment Limitations to Improve Simulation Accuracy of Real-Time Power Hardware In Loop Simulation. *IEEE Transactions on Power Delivery* **27** (3), 1284–1291 (July 2012). ISSN 1937-4208. DOI 10.1109/TPWRD.2012.2195335. Cited on page(s) 106.

[19] Yu Wang, Mazheruddin H. Syed, Efren Guillo-Sansano, Yan Xu, and Graeme M. Burt. Inverter-Based Voltage Control of Distribution Networks: A Three-Level Coordinated Method and Power Hardware-in-the-Loop Validation. *IEEE Transactions on Sustainable Energy* **11** (4), 2380–2391 (October 2020). ISSN 1949-3037. DOI 10.1109/TSTE.2019.2957010. Cited on page(s) 106.

[20] Yusi Liu, Chris Farnell, Kenny George, H. Alan Mantooth, and Juan Carlos Balda. A scaled-down microgrid laboratory testbed. In *2015 IEEE Energy Conversion Congress and Exposition (ECCE)* pages 1184–1189 Montreal, Canada (September 2015). DOI 10.1109/ECCE.2015.7309825. Cited on page(s) 106.

[21] ABB Hitachi. PS1000 480Vac Power Conversion System Data Sheet. Data Sheet 4CAE000862 Rev. F ABB / Hitachi Energy Zurich, Switzerland (September 2022). URL https://library.abb.com/d/4CAE000862, accessed on 2023-02-24. Cited on page(s) 107, 108, 115.

[22] Sandeep Anand, Rajesh Singh Farswan, and B. G. Fernandes. Unique power electronics and drives experimental bench (pedeb) to facilitate learning and research. *IEEE Transactions on Education* **55** (4), 573–579 (June 2012). DOI 10.1109/TE.2012.2200681. Cited on page(s) 108.

[23] Prabha Kundur, Neil J. Balu, and Mark G. Lauby. Power System Stability and Control. EPRI power system engineering series. McGraw-Hill New York, USA (1994). ISBN 978-0-07-035958-1. Cited on page(s) 109.

[24] Henrik Brantsæter, Łukasz Kocewiak, Elisabetta Tedeschi, and Atle Rygg Årdal. Passive Filter Design and Offshore Wind Turbine Modelling for System Level Harmonic Studies. *ELSEVIER Energy Procedia* **80**, 401–410 (2015). ISSN 1876-6102. URL https://ntnuopen.ntnu.no/ntnu-xmlui/handle/11250/2381992. DOI 10.1016/j.egypro.2015.11.444. Cited on page(s) 112, 114.

[25] EU 548/2014. Commission Regulation (EU) No 548/2014 of 21 May 2014 on implementing Directive 2009/125/EC of the European Parliament and of the Council with regard to small, medium and large power transformers. European Commission Brussels, Belgium (May 2014). URL https://eur-lex.europa.eu/eli/reg/2014/548/oj, accessed on 2023-02-25. Cited on page(s) 113.

[26] IEC 61000-4-7:2002. Electromagnetic compatibility (EMC) - Part 4-7: Testing and Measurement Techniques - General Guide on Harmonics and Interharmonics Measurements and Instrumentation, for Power Supply Systems and Equipment Connected Thereto. International

Electrotechnical Commission Geneva, Switzerland (ago 2002). URL https://webstore.iec.ch/publication/4226, accessed on 2023-03-03. Cited on page(s) 117.

[27] IEEE Std 519-1992. IEEE Recommended Practices and Requirements for Harmonic Control in Electrical Power Systems. Institute of Electrical and Electronics Engineers New York, NY, USA (June 1992). DOI 10.1109/IEEESTD.1993.114370. Cited on page(s) 118.

CHAPTER 7

Conclusion

This PhD dissertation compiled the contributions to the scientific literature that were published in academic conferences and journals during the pursuit of the goals of my doctoral research. Although the sequence of chapters, contributions, and publications illustrated previously in figure 1.3 in chapter 1 may have given the impression that my doctoral path was completely preplanned from start to finish, there were, as always, unpredictable aspects along the way. As in any endeavor, time constraints forced me to choose which topics were more critical and deserved immediate investigation, which ones should be temporarily set aside, and which ones should be classified as future work. To conclude this dissertation, my doctoral pursuit is put into perspective from its beginnings with the Research Questions, passing through the Contributions, and aiming at future research topics.

7.1 RESULTS OF THE PURSUIT OF RESEARCH GOAL I

The Research Goal I of my doctoral work was to identify and address possible causes of converter-induced instabilities in a power-intensive isolated grid fed by traditional synchronous generation, connected to converter-interfaced intermittent renewable energy sources (RES), and supported by fast-acting converter-interfaced loads and by an energy storage system (ESS). As mentioned in section 2.1, converter-driven instabilities arise from the interactions that different control loop layers of power electronic converters (PECs) have with each other, other converters, or other equipment in the grid. In the pursuit of the Research Goal I (see figure 7.1), four phenomena that may lead to converter-driven instabilities were investigated, namely:

1. exponentially decaying dc components that appear during transients in three-phase electric systems with high reactance-resistance ratio (X/R);
2. phase-shifts introduced by measurement and sequence isolation algorithms employed by the controllers of PECs;
3. oscillations introduced by constant power loads and sources;
4. oscillations introduced by converter synchronization algorithms (phase-locked loop (PLL)).

In Publication III, the effects of exponentially decaying dc components in the

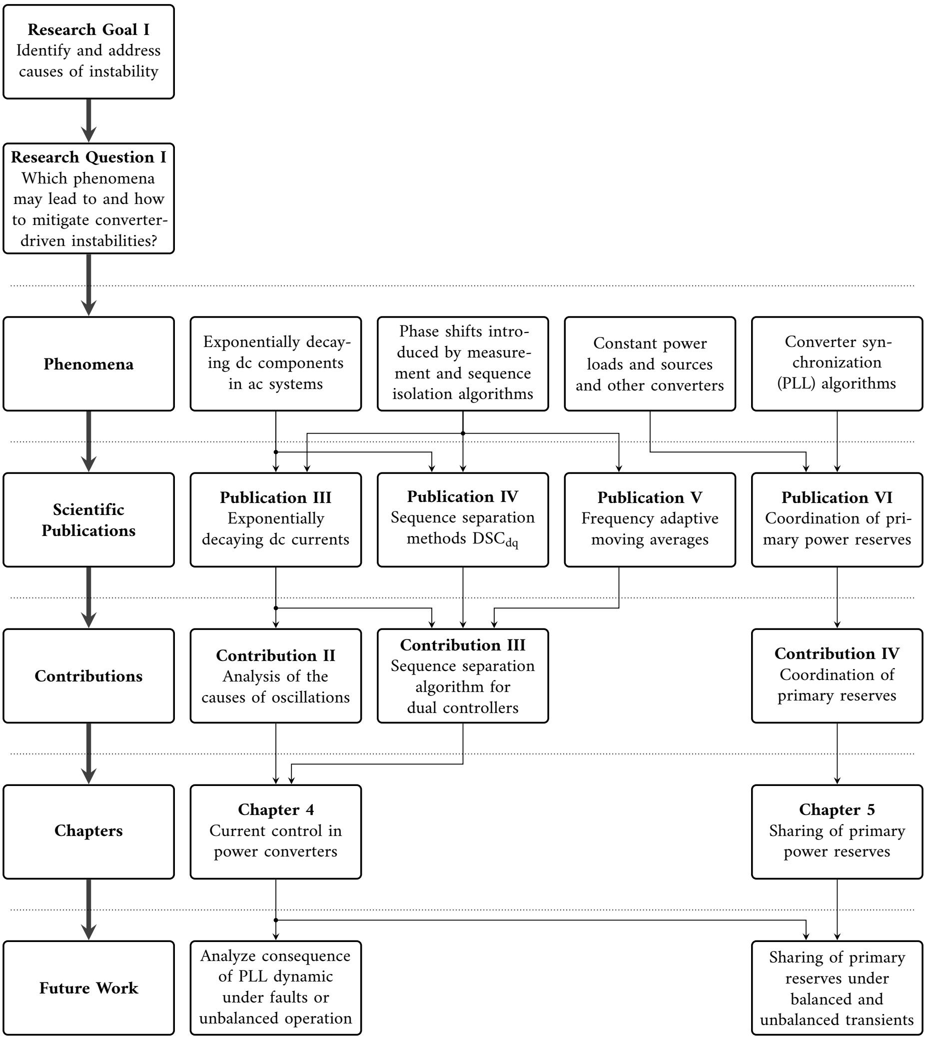

FIGURE 7.1 Results of the pursuit of Research Goal I and suggestions for future work.

stability of PECs that operate in dual rotating reference frames (RRFs) and rely on the separation of positive and negative sequence contents of the grid voltages and currents were assessed. In Publication IV, a sequence isolation method based on the delayed signal cancellation (DSC) applied directly to the RRF was described. This method was compared to other ones available in the scientific literature. The contents of Publications III and IV were compiled in chapter 4. To complement this chapter, a frequency adaptive moving average (MA) filter proposed in Publication V was also assessed as means of isolating positive and negative sequence content in RRFs. For the interested reader, the intricacies of performing adaptive moving averages (AMAs) discussed in Publication V are summarized in appendix D. The conclusions derived from chapter 4 were obtained with computer simulations of one single converter connected to an ideal voltage source through a resistive and inductive impedance. The dynamic of the PLL were purposefully disregarded to highlight the differences in the performance of the various sequence isolation methods.

In addition to PLL dynamics, converter-driven instabilities can also be instigated by interactions among different converters of the grid. Including the PLL dynamics and assessing interactions among converters were the main motivations to build the computer simulation model employed in Publication I, the results of which were compiled in chapter 3. Although the main converters that feed the platform's high-voltage ac grid were included in the model, only simplified constant impedance representations were used for the platform loads. However, a substantial part of the platform loads is interfaced to the grid via PECs that operate as constant power loads (CPLs) and those are known to cause instabilities. For that reason, the instability issues brought by CPLs were addressed in Publication VI and compiled in chapter 5. It is worth remarking that the computer simulation and power hardware-in-the-loop (PHIL) tests employed in Publication VI only used step loads and sudden loss of wind as transients, i.e., no severe faults were simulated. Investigating the study case during and immediately after severe transients, for instance, three-phase, two-phase, and single-phase short-circuit faults, was considered future work.

7.2 RESULTS OF THE PURSUIT OF RESEARCH GOAL II

The Research Goal II of my doctoral work was to propose robust control structures to guarantee the stability of isolated grids with synchronous and non-synchronous intermittent RES that are supported by converter-interfaced ESSs. Three research questions arose during the pursuit of this goal, as illustrated in figure 7.2. Those questions were the following:

- Research Question II — How to build a robust control structure for the provision of primary and secondary frequency control reserves in isolated grids equipped with converter-interfaced ESSs?
- Research Question III — How to share fast power reserves for frequency control?
- Research Question IV — What are the consequences for the stability of the grid of prioritizing faster converter-interface ESSs as primary reserve providers instead of slower turbogenerators (GTs)?

In addition to Research Questions II and III, a set of constraints were established aiming for system modularity. This included prioritizing independence from fast communication links among the converters of the ESS and independence from a fast communication link with the grid power management system (PMS). With this in mind, traditional proportional, integral, and derivative (PID) regulators were chosen as the base for the control structures. Although a derivative branch is present in the control structure described in chapter 3, it was demonstrated theoretically and experimentally with simulations and PHIL tests in chapter 5 that the grid frequency control could be improved even without it. This was achieved by prioritizing the faster converter-interfaced ESS instead of the slower GTs as providers of primary power reserves

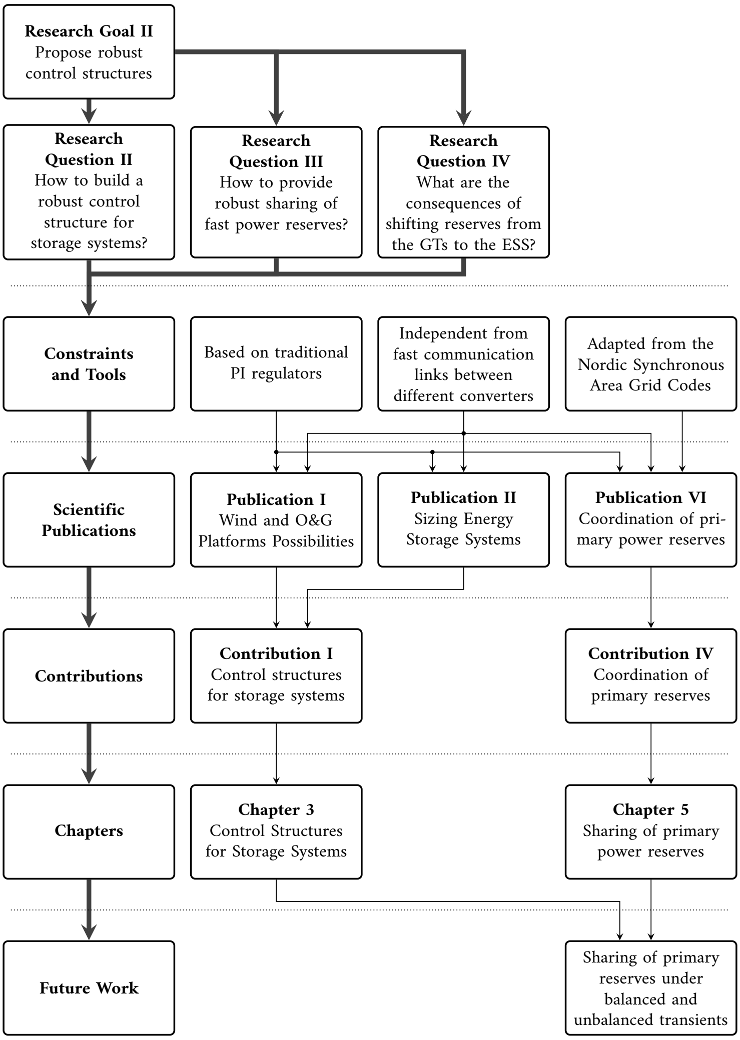

FIGURE 7.2 Results of the pursuit of Research Goal II and suggestions for future work.

© Daniel Mota 2023 | Source code information at Part III.

In the quest to answer Research Question IV, the recently published requirements for frequency containment reserves (FCR) for the Nordic synchronous system were employed as an inspiration. Although not required, the turbogenerators of the offshore isolated grids under study in this dissertation operate in an analogous way to the Nordic frequency containment reserves for isolated operation (FCR_I). Controlling the frequency of such complex grids, which may feature converter-interfaced ESSs and flexible loads (FLX) that can be used as primary reserve providers, motivated the proposition of the expanded FCR_I concept described in chapter 5. The original Nordic FCR_I was expanded from a single power-frequency droop curve into a segmented one with different regions for normal operation reserves (FCR_N) and large disturbance reserves (FCR_D). The expanded FCR_I concept, i.e., Contribution IV, allowed for prioritizing the converter-interfaced primary reserves as FCR_N while assigning the mechanical actuated turbogenerators mainly for FCR_D. This lessened the burden of the slower GTs with frequency control, which may lead to the reduced wear and tear of the turbine governors. Employing the expanded FCR_I improved the overall electric power quality in the platform. The eigenvalue analysis, dynamic simulations, and PHIL presented in chapter 5 indicated that the benefits, from a grid stability perspective, outweighed the disadvantages of increasing the share of converter-interfaced FCR_N reserves for primary frequency control in isolated grids. Nevertheless, as remarked previously in section 7.1, the PLL dynamics and the overall response of the converter-interfaced reserves to severe faults as short-circuits, balanced or unbalanced, were not investigated.

7.3 Pursuit of the Research Goal III

The Research Goal III was to validate the control structures proposed in chapter 3 experimentally in the laboratory with reduced scale PHIL tests. The pursuit of this goal is summarized in figure 7.3. In chapter 5, reduced-scale PHIL tests were used to evaluate the benefits of employing a segmented droop strategy that allowed prioritizing faster converter-interfaced power reserves instead of the slower GTs, i.e., the Contribution IV of this work. To perform these tests, a method for matching the specific characteristics of the full-scale converter to the reduce-scale laboratory one began to take shape. However, to emulate all the characteristics of an MVA-range full-size converter (FSC) with a laboratory kVA-range scaled-down converter (SDC) proved difficult. Meanwhile, it was noticed that specific characteristics of the FSC could be better reproduced with adaptations to the pu bases of the SDC. This led, in the first moment, to the scaling adopted for the PHIL tests shown in chapter 5 (see table 5.3 in page 98).

Varying the base current and voltage of a laboratory converter with the goal of matching its inductive-capacitive-inductive (LCL) filter and dc-link capacitance to a full-scale converter, while minimizing the need to physically change existing components was not straightforward. Changes that helped in matching the pu

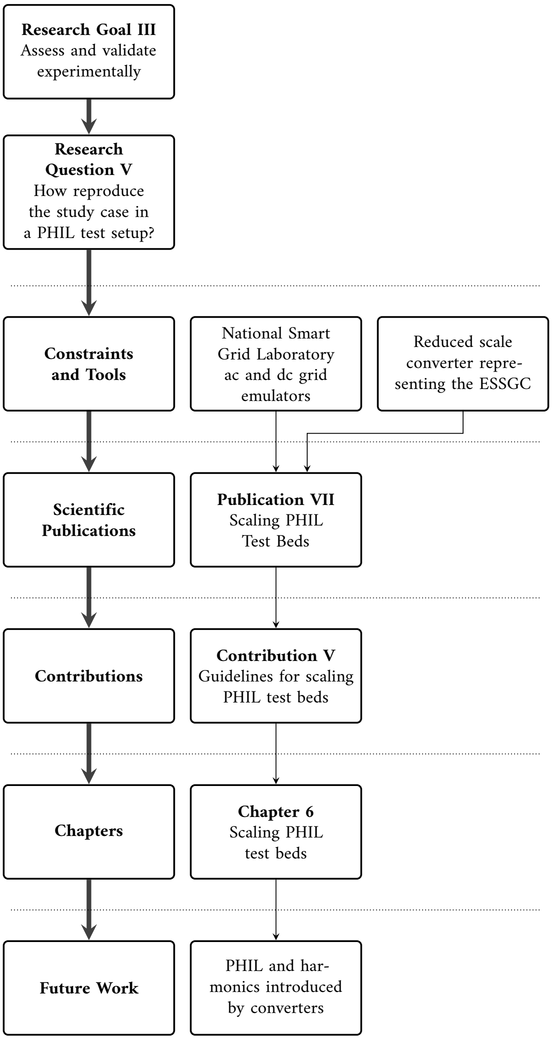

FIGURE 7.3 Results of the pursuit of Research Goal III and suggestions for future work.

© Daniel Mota 2023 | Source code information at Part III.

value of one part of the LCL filter increased the differences in pu of another part. For that reason, the Research Question V became relevant during the preparation and execution of the laboratory tests used for validation in Publication VI. In addition to that, and aiming for a future work, a scaling method that allowed for reproducing harmonic disturbances introduced by the pulse-width modulation (PWM) switching began to be sketched. This resulted in Publication VII, which proposed Contribution V of this doctoral work. Nevertheless, the control structures for converter-interfaced ESS described in chapter 3, the dual sequence current controllers employing the sequence isolation method described in chapter 4, and the power reserve sharing for isolated grids with synchronous and nonsynchronous generation proposed in chapter 5 were not thoroughly tested in a PHIL test bed that takes fully into consideration the PWM switching harmonics introduced by the converters. This future research topic, and the other ones suggested in sections 7.1 and 7.2, will be summarized in the following section.

7.4 FUTURE WORK

In sections 7.1 to 7.3, the pursuit of the three goals established for my doctoral research and the resulting contributions to the scientific literature were discussed. However, each of these sections ended in suggestions for future work, which can be summarized as follows.

- **Investigate the consequences of PLL dynamics under faults and during severe temporary unbalanced operation.**
  The generators of the study case analyzed in this dissertation are designed for operating with a maximum of 8 % of negative-sequence current. This means that the permanent operation with large unbalanced loads connected to the platform's main high-voltage (HV) busbar would not be allowed by the generator's electric protection system. However, unbalanced conditions may appear temporarily due to faulty operation of the grid devices. Negative-sequence current injection might be demanded from the energy storage system grid converter (ESSGC) that feeds the platform's main busbar. It is therefore important to analyze the behaviour of the ESSGC under severe grid faults. More specifically, assessing the consequences of the PLL dynamics in the performance of the current controllers discussed in chapter 4 is suggested as a future research topic.
- **Explore the performance of converter-interfaced primary reserves during and immediately after severe balanced and unbalanced transients.**
  In this dissertation, the sharing of primary frequency reserves among traditional synchronous machines and converter-interfaced devices as battery energy storage systems and fast flexible loads was investigated with the help of computer simulations and PHIL laboratory tests. The transients chosen for testing the dynamic response when different types of equipment were prioritized as primary reserve providers included fast (step) changes to the isolated grid's loads and sudden loss of power generated by the wind farm (WF). All these transients were balanced; in other words, the changes to each of the three-phases of the system were equal. No temporary load unbalances were introduced. No asymmetrical severe faults such as phase-to-phase of phase-to-ground short circuits were chosen as testing scenarios. It is, therefore, important to investigate how well the converter-interfaced ESS would perform under such scenarios.

- **Research the consequences of harmonics introduced by PECs with properly matched reduced scale PHIL setups.**
  As discussed in chapter 6, most of PHIL tests present outcomes that do not match voltages and currents at the PWM switching frequency range of the FSCs. Although the harmonic-invariant scaling method (HISM) described in this dissertation provides the means to better reproduce these harmonic disturbances, the PHIL tests employed to validate the strategy for sharing fast primary power reserves in power-intensive isolated grids proposed in chapter 5 did not match SDC and FSC's PWM switching frequencies. It is important, therefore, to further investigate the possibilities of properly reproducing the harmonic phenomena introduced by a larger participation of non-synchronous converter-interfaced generation and consumption in PHIL setups.

7.5 ON THE GENERALITY OF THE FINDINGS

Although much of this dissertation was anchored in a specific application, i.e., a study case of an oil and gas (O&G) platform isolated from the continent, the theoretical frameworks adopted in this doctoral work were as general as possible. The findings, insights, and conclusions presented in this work are applicable to other scenarios where medium and large isolated grids with synchronous dispatchable sources face the challenges of integrating variable RES.

7.6 FINAL PERSONAL REMARKS

In his lectures at Santa Barbara in 1959, Huxley [1] recalled reading a remark on the nature of basic research by Albert von Szent-Györgyi Nagyrápolt, who had won a Nobel Prize in 1937 for "his discoveries in connection with the biological combustion processes, with special reference to vitamin C and the catalysis of fumaric acid" [2].

> *"When I first came to this country ten years ago, I had the greatest difficulty to find means for my basic research. People asked me, what are you doing, what is it good for? I had to say, it is no good at all. Then they asked, then exactly what are you going to do? I had to answer, I don't know, that is why it is research..."*

Although this PhD dissertation is an example of applied research, not basic, I recall a similar feeling as the one experienced by Szent-Györgyi. After 17 years working in the industry with control and automation equipment for hydropower generation, I was back in academia and was asking myself what I was supposed to be investigating and what kind of scientific contributions I was expected to produce. Processing all the information necessary to begin a PhD project can be overwhelming. As a starter, a set of goals was defined with the help of my supervisor and co-supervisor. Then, I began investigating the frontiers of the research on the control and stability of isolated grids with synchronous and non-synchronous generation. These investigations led to the research questions described in chapter 1. The attempts to answer these questions resulted in seven publications. The five main contributions of these publications are compiled in the chapters of this dissertation. Notwithstanding, there is one additional goal of a PhD research that was not explicitly named until now, and that is to give one the opportunity to learn and develop the skills necessary for performing research. I believe I seized this opportunity. Finally, I would like to thank the readers for reaching these final remarks. If you have time, take a look at appendices A to E as well. I hope you have enjoyed the ride.

7.7 REFERENCES

[1] Aldous Huxley. The Human Situation, Lectures at Santa Barbara. Collections of lectures on topics relating to religion, art, philosophy and mysticism. Delphine Lettau, Howard Ross & the online Distributed Proofreaders Canada (1959). URL https://www.fadedpage.com/showbook.php?pid=20210612, visited on 2023-05-05. Cited on page(s) 130.

[2] Nobel Foundation. The Nobel Prize in Physiology or Medicine 1937. (online) The Nobel Prize Outreach AB (June 2023). URL https://www.nobelprize.org/prizes/medicine/1937/summary/, visited on 2023-04-05. Cited on page(s) 130.

End of Part I - Main Matter

◆

Part II

APPENDICES

Appendix A

Reference Frames and Transformations

The following reference frames for representing three-phase quantities are used in this dissertation.

Natural reference frame (NRF), also referred to as the abc frame.
Stationary reference frame (SRF), also named the $\alpha\beta$ frame.
Rotating reference frame (RRF), also called the dq frame.

A.1 Natural Reference Frame

Figure A.1 illustrates voltages and currents represented in the NRF.

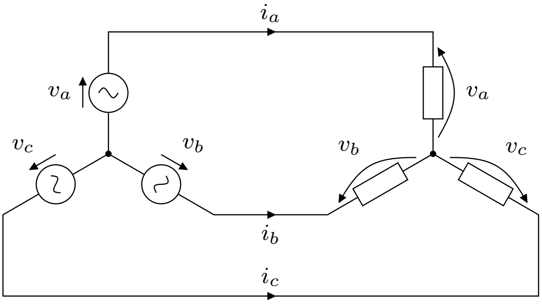

Figure A.1 Three-phase circuit with voltages and currents in the NRF.

© Daniel Mota 2023 | Source code information at Part III.

Let $v(t)$ be defined as

$$v(t) = \begin{bmatrix} v_a(t) \\ v_b(t) \\ v_c(t) \end{bmatrix} = V \begin{bmatrix} \sin(\omega t) \\ \sin(\omega t - 2\pi/3) \\ \sin(\omega t + 2\pi/3) \end{bmatrix} \tag{A.1}$$

where V is the amplitude of the sinusoidal voltage and ω is the angular frequency. Notice that v_a, v_b, and v_c are expressed with sine functions, not cosine functions, and that the phase of v_a is zero.

Let $i(t)$ be defined as

$$i(t) = I \begin{bmatrix} \sin(\omega t - \varphi) \\ \sin(\omega t - 2\pi/3 - \varphi) \\ \sin(\omega t + 2\pi/3 - \varphi) \end{bmatrix} \tag{A.2}$$

where I is the amplitude and φ is the phase shift between the sinusoidal currents i and the sinusoidal voltages v.

If the v were to feed a series-connected resistive and inductive (RL) impedance, then the phase φ of i flowing through the impedance would be

$$\varphi = \arctan\left(\frac{\omega L}{R}\right).$$

In the following sections, the transformations between different reference frames will be applied to this set of voltages and currents.

A.2 STATIONARY REFERENCE FRAME $\alpha\beta$

In this dissertation, quantities are transformed from the NRF into the SRF and back with an amplitude invariant Clark transformation [1, 2]. The energy storage system (ESS) and power electronic converters (PECs) studied in this work are connected to the grid via ungrounded delta-wye transformers, which block the flow of zero-sequence currents between grid and converter; therefore, the axis γ which relates to the zero sequence is disregarded in the transformations used throughout this dissertation.

A.2.1 Positive Sequence

The transformations between the abc and $\alpha\beta_+$ frames is performed with the matrix

$$\mathcal{C}_+ = \begin{bmatrix} 1 & -1/2 & -1/2 \\ 0 & \sqrt{3}/2 & -\sqrt{3}/2 \end{bmatrix}. \tag{A.3}$$

Notice the relationship, which will be useful later in this appendix, between the matrix $\mathcal{C}_+$ and its transpose:

$$\frac{2}{3}\,\mathcal{C}_+ {\mathcal{C}_+}^\top = \begin{bmatrix} 1 & 0 \\ 0 & 1 \end{bmatrix}. \tag{A.4}$$

The $abc \mapsto \alpha\beta_+$ transformation is given by

$$\begin{bmatrix} m_{\alpha+}(t) \\ m_{\beta+}(t) \end{bmatrix} = \frac{2}{3}\,\mathcal{C}_+ \begin{bmatrix} m_a(t) \\ m_b(t) \\ m_c(t) \end{bmatrix} \tag{A.5}$$

where the variables m_a, m_b, and m_c represent the instantaneous measurements of either phase-to-neutral voltages or line currents, and the subscripts α_+ and β_+ stand for the axes of the SRF. The $\alpha\beta_+ \mapsto abc$ transformation is performed with

$$\begin{bmatrix} m_a(t) \\ m_b(t) \\ m_c(t) \end{bmatrix} = \mathcal{C}_+{}^\top \begin{bmatrix} m_{\alpha+}(t) \\ m_{\beta+}(t) \end{bmatrix}. \tag{A.6}$$

If the transformation in equation (A.5) is applied to v from equation (A.1), then the result is

$$\begin{bmatrix} v_{\alpha+}(t) \\ v_{\beta+}(t) \end{bmatrix} = \frac{2}{3}\mathcal{C}_+ V \begin{bmatrix} \sin(\omega t) \\ \sin(\omega t - 2\pi/3) \\ \sin(\omega t + 2\pi/3) \end{bmatrix} = V \begin{bmatrix} \sin(\omega t) \\ -\cos(\omega t) \end{bmatrix}.$$

The amplitude V from the voltage in equation (A.5) is maintained in the positive sequence SRF; therefore, the transformation described by equation (A.5) is known as amplitude invariant. Although not used in this dissertation, if the reader intends to use the power invariant transformation instead, the coefficient $2/3$ should be replaced by $\sqrt{2/3}$.

A.2.2 Negative Sequence

The transformations between the abc and the $\alpha\beta_-$ frames are performed in this dissertation by replacing the matrix $\mathcal{C}_+$ in equations (A.5) and (A.6) with the matrix $\mathcal{C}_-$ from equation (A.7).

$$\mathcal{C}_- = \mathcal{C}_+ \begin{bmatrix} 1 & 0 & 0 \\ 0 & 0 & 1 \\ 0 & 1 & 0 \end{bmatrix} = \begin{bmatrix} 1 & -1/2 & -1/2 \\ 0 & -\sqrt{3}/2 & \sqrt{3}/2 \end{bmatrix} \tag{A.7}$$

A.3 ROTATING REFERENCE FRAME

The RRF rotates synchronously with the angular frequency ω of a given three-phase voltage v, usually the one at the middle point of the converters' inductive-capacitive-inductive (LCL) filter, see chapter 4. Quantities can be transformed from the SRF to the RRF and back with the Park transformation [2, 3]. The RRF frames represent the three-phase quantities with direct (d), quadrature (q), and zero-sequence components. However, as with the SRF, the zero sequence in the RRF is disregarded in this dissertation.

The transformations between the SRF and the RRF are performed with the matrix

$$\mathcal{P}(\theta) = \begin{bmatrix} \sin(\theta) & -\cos(\theta) \\ \cos(\theta) & \sin(\theta) \end{bmatrix} \tag{A.8}$$

where the angle $\theta(t)$ is given by

$$\theta(t) = \int_0^t \omega(\tau)\,\mathrm{d}\tau$$

and ω is the angular frequency with which the RRF rotates. The angle θ is measured with a phase-locked loop (PLL) device, see appendix B for more details. Assuming a constant angular frequency, the angle θ can then be replaced by ωt resulting in

$$\mathcal{P}(\omega t) = \begin{bmatrix} \sin(\omega t) & -\cos(\omega t) \\ \cos(\omega t) & \sin(\omega t) \end{bmatrix}.$$

It is worth noticing that

$$\begin{aligned} \mathcal{P}(\omega t)\frac{\mathrm{d}}{\mathrm{d}t}\mathcal{P}^\top(\omega t) = \omega & \begin{bmatrix} \sin(\omega t) & -\cos(\omega t) \\ \cos(\omega t) & \sin(\omega t) \end{bmatrix} \\ & \begin{bmatrix} \cos(\omega t) & -\sin(\omega t) \\ \sin(\omega t) & \cos(\omega t) \end{bmatrix} = \omega \begin{bmatrix} 0 & -1 \\ 1 & 0 \end{bmatrix}. \end{aligned} \tag{A.9}$$

The relationship between $\mathcal{P}$ and the time derivative of its transpose will be useful later in this appendix in section A.3.2.

A.3.1 Positive Sequence Rotating Reference Frame

The transformations between the NRF and the positive-sequence RRF are performed with the matrix

$$\begin{aligned} \mathcal{T}_+(\theta) &= \mathcal{P}(\theta)\,\mathcal{C}_+ = \\ &= \begin{bmatrix} \sin(\theta) & \sin(\theta - 2\pi/3) & \sin(\theta + 2\pi/3) \\ \cos(\theta) & \cos(\theta - 2\pi/3) & \cos(\theta + 2\pi/3) \end{bmatrix}. \end{aligned} \tag{A.10}$$

The complete $abc \mapsto \alpha\beta_+ \mapsto dq_+$ transformation is given by

$$\begin{aligned} \begin{bmatrix} m_{d+}(t) \\ m_{q+}(t) \end{bmatrix} = \mathcal{P}(\theta) \begin{bmatrix} m_{\alpha+}(t) \\ m_{\beta+}(t) \end{bmatrix} = \mathcal{P}(\theta) \left(\frac{2}{3}\,\mathcal{C}_+ \begin{bmatrix} m_a(t) \\ m_b(t) \\ m_c(t) \end{bmatrix} \right) = \\ = \frac{2}{3}\,\mathcal{T}_+(\theta) \begin{bmatrix} m_a(t) \\ m_b(t) \\ m_c(t) \end{bmatrix} \end{aligned} \tag{A.11}$$

where the variables m_a, m_b, and m_c represent the instantaneous measurements of either phase-to-neutral voltages or line currents, and the subscript d_+ stands for direct and q_+ for quadrature. It is worth remarking the relationship between the matrix $\mathcal{T}_+$ and its transpose

$$\frac{2}{3}\,\mathcal{T}_+(\theta)\,\mathcal{T}_+{}^\top(\theta) = \begin{bmatrix} 1 & 0 \\ 0 & 1 \end{bmatrix}. \tag{A.12}$$

The complete $dq_+ \mapsto \alpha\beta_+ \mapsto abc$ transformation is given by

$$\begin{aligned}\begin{bmatrix} m_a(t) \\ m_b(t) \\ m_c(t) \end{bmatrix} &= \mathcal{C}_+{}^\top \begin{bmatrix} m_{\alpha+}(t) \\ m_{\beta+}(t) \end{bmatrix} = \mathcal{C}_+{}^\top \left(\mathcal{P}^\top(\theta) \begin{bmatrix} m_{d+}(t) \\ m_{q+}(t) \end{bmatrix} \right) \\ &= \mathcal{T}_+{}^\top(\theta) \begin{bmatrix} m_{d+}(t) \\ m_{q+}(t) \end{bmatrix} .\end{aligned} \tag{A.13}$$

If the transformation in equation (A.11) is applied to v from equation (A.1) with θ synchronized to the angle of v_a, in other words, the remainder of division of the angle ωt by 2π is equal to the remainder of the division of the angle θ by 2π

$$\omega t \bmod 2\pi = \theta \bmod 2\pi$$

then, the result is

$$\begin{bmatrix} v_{d+}(t) \\ v_{q+}(t) \end{bmatrix} = \frac{2}{3} \mathcal{T}_+(\omega t)\, V \begin{bmatrix} \sin(\omega t) \\ \sin(\omega t - 2\pi/3) \\ \sin(\omega t + 2\pi/3) \end{bmatrix} = \begin{bmatrix} V \\ 0 \end{bmatrix} .$$

The amplitude V in the NRF is maintained in the positive sequence RRF. Therefore, the transformation described by equation (A.11) is known as amplitude invariant. Three-phase quantities in the NRF become constant values in the RRF. This allows for the use of traditional proportional, integral, and derivative (PID) controllers.

If the transformation in equation (A.11) with $\mathcal{T}_+$ synchronized to voltage v from equation (A.1) is applied to current i from equation (A.2), then the result is

$$\begin{bmatrix} i_{d+}(t) \\ i_{q+}(t) \end{bmatrix} = \frac{2}{3} \mathcal{T}_+(\omega t)\, I \begin{bmatrix} \sin(\omega t - \varphi) \\ \sin(\omega t - 2\pi/3 - \varphi) \\ \sin(\omega t + 2\pi/3 - \varphi) \end{bmatrix} = \begin{bmatrix} I \cos\varphi \\ -I \sin\varphi \end{bmatrix} .$$

Notice that the current amplitude I appears in both direct and quadrature axes multiplied either by the cosine or by the negative sine of the phase shift φ. Whenever i is in phase with v, the amplitude of i appears only in the d_+ axis. Whenever the phase shift is $\pm\pi/2$, the amplitude of i appears only in the q_+ axis. Given the choice of representing v with sine functions, not cosine ones, and the synchronization choice made for $\mathcal{T}_+$ in this dissertation, the direct axis d_+ relates to the active power, whereas the quadrature axis q_+ relates to reactive power measurements.

A.3.2 An RL circuit represented in the RRF dq_+

The relationship between the current and voltages in the idealized circuit from figure A.2 is described in the NRF by

$$\begin{bmatrix} v_{ga}(t) \\ v_{gb}(t) \\ v_{gc}(t) \end{bmatrix} + R \begin{bmatrix} i_a(t) \\ i_b(t) \\ i_c(t) \end{bmatrix} + L \frac{\mathrm{d}}{\mathrm{d}t} \begin{bmatrix} i_a(t) \\ i_b(t) \\ i_c(t) \end{bmatrix} = \begin{bmatrix} v_{ca}(t) \\ v_{cb}(t) \\ v_{cc}(t) \end{bmatrix} . \tag{A.14}$$

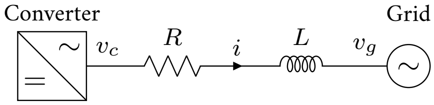

FIGURE A.2 Idealized single-line diagram of a converter connected to the grid through an RL impedance (copy of figure 4.1 from chapter 4 placed here for convenience).

© Daniel Mota 2023 | Source code information at Part III.

By rewriting equation (A.14) in the dq_+ frame with equation (A.13) and assuming that $\mathcal{T}_+$ is synchronized with v_{ca}, one obtains

$$\mathcal{T}_+{}^\top(\omega t)\begin{bmatrix} v_{gd+}(t) \\ v_{gq+}(t) \end{bmatrix} + R\,\mathcal{T}_+{}^\top(\omega t)\begin{bmatrix} i_{d+}(t) \\ i_{q+}(t) \end{bmatrix} + \\ + L\frac{\mathrm{d}}{\mathrm{d}t}\left(\mathcal{T}_+{}^\top(\omega t)\begin{bmatrix} i_{d+}(t) \\ i_{q+}(t) \end{bmatrix}\right) = \mathcal{T}_+{}^\top(\omega t)\begin{bmatrix} v_{cd+}(t) \\ v_{cq+}(t) \end{bmatrix}$$

which, after multiplying by $2\mathcal{T}_+/3$, can be re-written as

$$\begin{bmatrix} v_{gd+}(t) \\ v_{gq+}(t) \end{bmatrix} + R\begin{bmatrix} i_{d+}(t) \\ i_{q+}(t) \end{bmatrix} + \\ + \underbrace{\frac{2}{3}\mathcal{T}_+(\omega t)\,L\frac{\mathrm{d}}{\mathrm{d}t}\left(\mathcal{T}_+{}^\top(\omega t)\begin{bmatrix} i_{d+}(t) \\ i_{q+}(t) \end{bmatrix}\right)}_{\text{derivative term}} = \begin{bmatrix} v_{cd+}(t) \\ v_{cq+}(t) \end{bmatrix}. \tag{A.15}$$

The derivative term in equation (A.15) can be expanded into

$$\frac{2}{3}L\mathcal{T}_+(\omega t)\left(\left(\frac{\mathrm{d}}{\mathrm{d}t}\mathcal{T}_+{}^\top(\omega t)\right)\begin{bmatrix} i_{d+}(t) \\ i_{q+}(t) \end{bmatrix} + \mathcal{T}_+{}^\top(\omega t)\frac{\mathrm{d}}{\mathrm{d}t}\begin{bmatrix} i_{d+}(t) \\ i_{q+}(t) \end{bmatrix}\right)$$

which, by using equations (A.10) and (A.12), becomes

$$\frac{2}{3}L\mathcal{P}(\omega t)\mathcal{C}_+\mathcal{C}_+{}^\top\left(\frac{\mathrm{d}}{\mathrm{d}t}\mathcal{P}^\top(\omega t)\right)\begin{bmatrix} i_{d+}(t) \\ i_{q+}(t) \end{bmatrix} + L\frac{\mathrm{d}}{\mathrm{d}t}\begin{bmatrix} i_{d+}(t) \\ i_{q+}(t) \end{bmatrix}.$$

Therefore, by using equations (A.4) and (A.9), it is possible to conclude that the relationship between the currents and voltages in the idealized circuit in figure A.2 can be described in the RRF as

$$\begin{bmatrix} v_{gd+}(t) \\ v_{gq+}(t) \end{bmatrix} + R\begin{bmatrix} i_{d+}(t) \\ i_{q+}(t) \end{bmatrix} + \omega L\begin{bmatrix} 0 & -1 \\ 1 & 0 \end{bmatrix}\begin{bmatrix} i_{d+}(t) \\ i_{q+}(t) \end{bmatrix} + L\frac{\mathrm{d}}{\mathrm{d}t}\begin{bmatrix} i_{d+}(t) \\ i_{q+}(t) \end{bmatrix} = \begin{bmatrix} v_{cd+}(t) \\ v_{cq+}(t) \end{bmatrix}$$

which features a coupling between the dq_+ axes. The value of $-\omega L i_{q+}$ affects the quantities in the d_+ axis, whereas the value of $\omega L i_{d+}$ affects the q_+ axis.

A.3.3 Negative Sequence Rotating Reference Frame

A measurement $[m_a \; m_b \; m_c]^\top$ in the NRF can be moved to the negative sequence RRF if the middle and right columns of $\mathcal{T}_+$ are swapped

$$\mathcal{T}_- = \mathcal{T}_+ \begin{bmatrix} 1 & 0 & 0 \\ 0 & 0 & 1 \\ 0 & 1 & 0 \end{bmatrix}$$

resulting in

$$\mathcal{T}_-(\theta) = \begin{bmatrix} \sin(\theta) & \sin(\theta + 2\pi/3) & \sin(\theta - 2\pi/3) \\ \cos(\theta) & \cos(\theta + 2\pi/3) & \cos(\theta - 2\pi/3) \end{bmatrix}. \tag{A.16}$$

This is equivalent to swapping the measurements of phases b and c.

The $abc \mapsto dq_-$ transformation is given by

$$\begin{bmatrix} m_{d-}(t) \\ m_{q-}(t) \end{bmatrix} = \frac{2}{3} \mathcal{T}_-(\omega t) \begin{bmatrix} m_a(t) \\ m_b(t) \\ m_c(t) \end{bmatrix} \tag{A.17}$$

where the subscript d_- stands for direct and q_- for quadrature axis. The $dq_- \mapsto abc$ transformation is performed with

$$\begin{bmatrix} m_a(t) \\ m_b(t) \\ m_c(t) \end{bmatrix} = \mathcal{T}_-^\top(\omega t) \begin{bmatrix} m_{d-}(t) \\ m_{q-}(t) \end{bmatrix}. \tag{A.18}$$

If the transformation in equation (A.17) is applied to v from equation (A.1) with $\mathcal{T}_-$ synchronized to the voltage v, then the result is

$$\begin{bmatrix} v_{d-}(t) \\ v_{q-}(t) \end{bmatrix} = \frac{2}{3} \mathcal{T}_-(\omega t) \, V \begin{bmatrix} \sin(\omega t) \\ \sin(\omega t - 2\pi/3) \\ \sin(\omega t + 2\pi/3) \end{bmatrix} = \begin{bmatrix} -V\cos(2\omega t) \\ V\sin(2\omega t) \end{bmatrix}.$$

The positive sequence voltage v from equation (A.1) appears in the negative sequence RRF as two sinusoidal signals with amplitude V and twice the angular frequency ω. Conversely, any negative sequence voltage content in the NRF appears as second harmonic content on the dq_+ reference frame. A similar line of reasoning applies when the positive sequence current i from equation (A.2) is moved to the dq_-.

In summary, positive sequence content in the NRF becomes constant in the dq_+ frame. However, if transformed into the dq_- frame, it appears as second harmonic. Conversely, the negative sequence content in the NRF becomes constant in the dq_- and second harmonic in the dq_+ frame.

A.4 REFERENCES

[1] Edith Clarke. Circuit Analysis of A-C Power Systems volume I of *General Electric series.* John Wiley and Sons New York, USA (1943). Cited on page(s) 136.

[2] Colm J. O'Rourke, Mohammad M. Qasim, Matthew R. Overlin, and James L. Kirtley. A Geometric Interpretation of Reference Frames and Transformations: Dq0, Clarke, and Park. *IEEE Transactions on Energy Conversion* **34** (4), 2070–2083 (2019). ISSN 1558-0059. DOI 10.1109/TEC.2019.2941175. Cited on page(s) 136, 137.

[3] Robert H. Park. Two-reaction Theory of Synchronous Machines Generalized Method of Analysis-part I. *Transactions of the American Institute of Electrical Engineers* **48** (3), 716–727 (July 1929). ISSN 2330-9431. DOI 10.1109/T-AIEE.1929.5055275. Cited on page(s) 137.

APPENDIX B

Geometric Representations of Three-Phase Quantities and the PLL

This appendix is based on the work published in Portuguese by Matakas Junior [1], which provides a comprehensive explanation of the representation of three-phase systems with spacial three-dimensional vectors and the inner workings of a phase-locked loop (PLL). For more information on the history of reference frame transformations for three-phase quantities, their different variants, and their geometrical foundations, see also [2].

A PLL device generates an internal voltage that tracks a measured three-phase voltage. Although the reference frames in which the internal and the measured voltages are compared vary in the literature, the goal of this appendix is to explain the PLL inner workings within the natural reference frame (NRF) itself without changing to the stationary reference frame (SRF) or rotating reference frame (RRF). For that, it is important to introduce a three-dimensional representation for three-phase measurements.

B.1 GEOMETRIC REPRESENTATIONS OF THREE-PHASE MEASUREMENTS

Let a set of three orthogonal unitary vectors

$$\overrightarrow{a} = \begin{bmatrix} 1 \\ 0 \\ 0 \end{bmatrix}, \quad \overrightarrow{b} = \begin{bmatrix} 0 \\ 1 \\ 0 \end{bmatrix}, \quad \overrightarrow{c} = \begin{bmatrix} 0 \\ 0 \\ 1 \end{bmatrix}$$

be the bases for a three-dimensional space with three axes a, b, and c. Let a vector v starting at the origin of the three-dimensional space be defined by three phase-to-neutral voltage measurements

$$v\left(t\right) = v_a\left(t\right)\overrightarrow{a} + v_b\left(t\right)\overrightarrow{b} + v_c\left(t\right)\overrightarrow{c} = \begin{bmatrix} v_a\left(t\right) \\ v_b\left(t\right) \\ v_c\left(t\right) \end{bmatrix}.$$

As an example, a vector v in the abc-space is illustrated in figure B.1.

Every vector $v(t)$ that fulfills $v_a\left(t\right) + v_b\left(t\right) + v_c\left(t\right) = 0$ lies in a specific plane of the three-dimensional space, which is named null zero-sequence in this

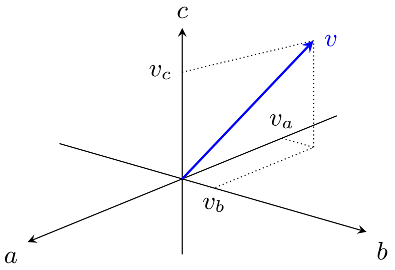

FIGURE B.1 Three-dimensional space for representing three-phase measurements.

© Daniel Mota 2023 | Source code information at Part III.

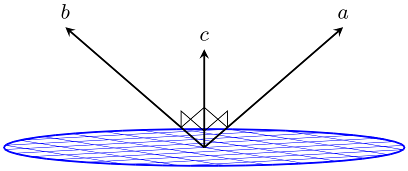

FIGURE B.2 Null-zero-sequence plane in the abc-space, in blue, where all vectors v with $v_a(t) + v_b(t) + v_c(t) = 0$ are located; the axis c points towards the reader.

© Daniel Mota 2023 | Source code information at Part III.

appendix and is illustrated in figure B.2. This means that all balanced three-phase quantities that take the form of

$$v(\theta) = \begin{bmatrix} v_a(\theta) \\ v_b(\theta) \\ v_c(\theta) \end{bmatrix} = V \begin{bmatrix} \sin(\theta - \varphi) \\ \sin(\theta - 2\pi/3 - \varphi) \\ \sin(\theta + 2\pi/3 - \varphi) \end{bmatrix} \tag{B.1}$$

where V is the amplitude, are located entirely in the null zero-sequence plane.

If the angle θ is defined as

$$\theta(t) = \int_0^t \omega(\tau)\, \mathrm{d}\tau$$

then v from equation (B.1) spins in the null zero-sequence plane with the angular frequency ω.

B.2 THE PLL TRACKS A THREE-PHASE VOLTAGE WITH A DOT PRODUCT

Let the voltage v_{PLL} be the internal three-phase voltage of the PLL

$$v_{\mathrm{PLL}}(\widehat{\theta}) = \begin{bmatrix} v_{\mathrm{PLL}a}(\widehat{\theta}) \\ v_{\mathrm{PLL}b}(\widehat{\theta}) \\ v_{\mathrm{PLL}c}(\widehat{\theta}) \end{bmatrix} = \begin{bmatrix} \cos(\widehat{\theta}) \\ \cos(\widehat{\theta} - 2\pi/3) \\ \cos(\widehat{\theta} + 2\pi/3) \end{bmatrix} \tag{B.2}$$

where $\widehat{\theta}$ is an estimate of the angle θ of the voltage v in equation (B.1). The angle $\widehat{\theta}$ is equal to the remainder of the integral in time of the PLL internal variable $\widehat{\omega}$ divided by 2π, i.e.,

$$\widehat{\theta}(t) = \left(\int_0^t \widehat{\omega}(t)\, \mathrm{d}t \right) \bmod 2\pi. \tag{B.3}$$

Notice that $\widehat{\omega}$ is the estimated value of the angular frequency ω of the voltage v. Both the balanced three-phase voltages v and v_{PLL} spin around the origin of the abc-space, as illustrated in figure B.3.

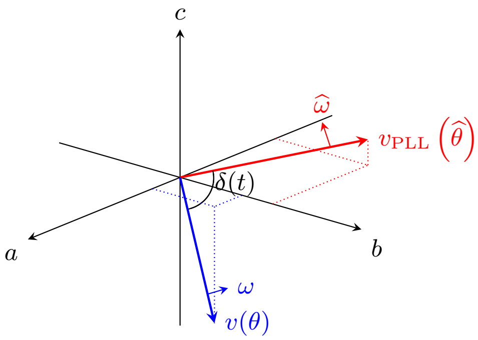

FIGURE B.3 Two balanced three-phase voltages, v from equation (B.1) and v_{PLL} from equation (B.2), at a given instant t in the abc-space. The voltages spin in the null zero-sequence plane, not drawn in this figure, with angular frequencies ω and $\widehat{\omega}$.

Let an error variable ε be defined by the dot product between the voltages v from equation (B.1) and v_{PLL} from equation (B.2)

$$\begin{aligned}\varepsilon(t) = v(\theta) \cdot v_{\mathrm{PLL}}\left(\widehat{\theta}\right) &= \\ &= \begin{bmatrix} v_a(\theta) & v_b(\theta) & v_c(\theta) \end{bmatrix} \begin{bmatrix} v_{\mathrm{PLL}a}(\widehat{\theta}) \\ v_{\mathrm{PLL}b}(\widehat{\theta}) \\ v_{\mathrm{PLL}c}(\widehat{\theta}) \end{bmatrix} = V \cos(\delta(t))\end{aligned}$$

where δ is the angle between the vectors v and v_{PLL} in the three-dimensional space illustrated in figure B.3. Notice that, for a nonzero amplitude V of the vector v, the error ε is only equal to zero when the angle δ is

$$\delta = \frac{(2k-1)\pi}{2}$$

where k is an integer, in other words, when v_{PLL} and v are perpendicular to each other.

To make its internal voltage v_{PLL} track the voltage v, the PLL acts on the controlled variable $\widehat{\omega}$ from equation (B.3) in the following manner:

- if $\varepsilon > 0$, increase $\widehat{\omega}$,
- if $\varepsilon < 0$, decrease $\widehat{\omega}$.

By doing so, assuming that $\widehat{\omega}$ is reasonably close to the angular frequency ω, the PLL forces its internal voltage v_{PLL} to lead v by $\pi/2$ rad. Notice that there are two equilibrium points for v_{PLL}. One is $\pi/2$ rad ahead of v, the other one is $\pi/2$ rad behind v. However, due to the cosinusoidal characteristic of ε, the latter is not a stable equilibrium point.

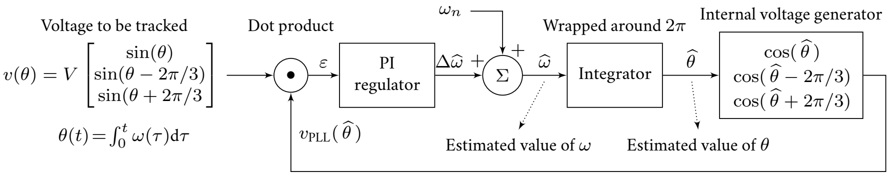

FIGURE B.4 Generic PLL expressed in the *abc*-space.

© Daniel Mota 2023 | Source code information at Part III.

Figure B.4 shows a block diagram of a generic PLL built in the *abc*-frame with the principles presented in this appendix. The voltage $v(\theta)$ to be tracked by the PLL is shown on the left side. The logic of increasing or decreasing the internal estimated value of the angular frequency is performed by a proportional and integral (PI) controller. The angle $\widehat{\theta}$ is calculated with equation (B.3). Other versions of the PLL available in the literature [3] perform the same fundamental operations illustrated in figure B.4, but transformed to different reference frames.

B.3 REFERENCES

[1] Lourenço Matakas Junior. Implementação de Controladores para Conversores Trifásicos, sem Transformações de Coordenadas: Análise Geométrica Através de Vetores Espaciais. *Tese de Livre Docência*. Universidade de São Paulo São Paulo (May 2012). DOI 10.11606/T.3.2012.tde-18052012-163756. Cited on page(s) 143.

[2] Colm J. O'Rourke, Mohammad M. Qasim, Matthew R. Overlin, and James L. Kirtley. A Geometric Interpretation of Reference Frames and Transformations: Dq0, Clarke, and Park. *IEEE Transactions on Energy Conversion* **34** (4), 2070–2083 (2019). ISSN 1558-0059. DOI 10.1109/TEC.2019.2941175. Cited on page(s) 143.

[3] Saeed Golestan, Josep M. Guerrero, and Juan C. Vasquez. Three-Phase PLLs: A Review of Recent Advances. *IEEE Transactions on Power Electronics* **32** (3), 1894–1907 (2017). ISSN 1941-0107. DOI 10.1109/TPEL.2016.2565642. Cited on page(s) 146.

APPENDIX C

PI Regulators and Anti-Windup

Figure C.1 shows the general structure of the proportional and integral (PI) regulators adopted throughout this dissertation where:

x = input of the regulator,
y = output of the regulator,
k_g, k_p = proportional gains,
T_i = integrator time,
x_f = input for feed-forwarding or for a derivative part,
x_w, y_w = input and output of the anti-windup block,
$y_{\max}$, $y_{\min}$ = maximum and minimum limits (dynamic or static),
y_u = unlimited output of the regulator,
s = complex frequency.

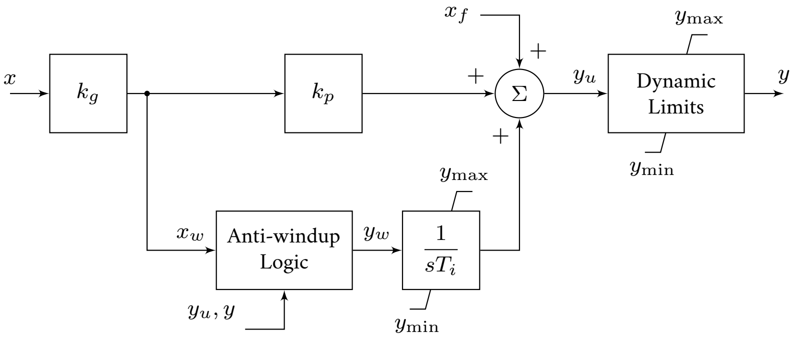

FIGURE C.1 PI regulator with limiters and anti-windup.

© Daniel Mota 2023 | Source code information at Part III.

C.1 LINEAR REPRESENTATION OF THE PI REGULATOR

Equation (C.1) shows the transfer function of the PI regulator in figure C.1 when the feed-forwarding input, anti-windup logic, and dynamic limits are disregarded.

$$G(s) = k_g \left(k_p + \frac{1}{sT_i} \right) \tag{C.1}$$

This transfer function is flexible and can represent the PI in different ways by considering, for instance, $k_g = 1$, which results in

$$G(s) = k_p + \frac{1}{sT_i}.$$

By considering $k_p = 1$, equation (C.1) can also represent the PI as

$$G(s) = k_g \left(\frac{sT_i + 1}{sT_i} \right).$$

This latter form, as adopted by Fröhr and Orttenburger [1], allows the setting of T_i for compensating the dominant pole of systems with one large time constant independently of the proportional gain k_g.

C.2 DYNAMIC LIMITS AND ANTI-WINDUP

The dynamic limit block at the output of the PI in figure C.1 can represent fixed and/or variable maximum and minimum values, as well as maximum allowed rates of change. The wind-up of a PI regulator happens when its integrator keeps on integrating even when the unlimited output y_u reaches a dynamic limit, in other words, when $y_u \neq y$. To avoid wind-up, the following strategy is adopted in this dissertation.

$$y_w = \begin{cases} 0 & \text{if } y_u > y \text{ and } x_w > 0, & \text{@ top, block integration up.} \\ x_w & \text{if } y_u > y \text{ and } x_w < 0, & \text{@ top, allow integration down.} \\ x_w & \text{if } y_u = y, & \\ x_w & \text{if } y_w < y \text{ and } x_w > 0, & \text{@ bottom, allow integration up.} \\ 0 & \text{if } y_w < y \text{ and } x_w < 0, & \text{@ bottom, block integration down.} \end{cases}$$

C.3 REFERENCES

[1] Friederich Fröhr and Fritz Orttenburger. Introduction to Electronic Control Engineering. Siemens Aktiengesellschaft; Heyden & Son LTD. Berlin and München, Germany; London, UK (1982). ISBN 0-85501-290-0. Cited on page(s) 148.

APPENDIX D

Frequency Adaptive Moving Averages

The grid frequency of low-inertia power systems is subjected to large excursions specially during transients. Thus, a filtering method based on moving averages (MAs) within multiples of submultiples of the grid period should not be unreasonably degraded by such variations. This appendix presents the frequency adaptive moving average (AMA) described in Publication V, which is based on the computationally efficient calculation from equation (4.11) and built with circular buffers.

D.1 FREQUENCY ADAPTIVE MOVING AVERAGE

Figure D.1 illustrates the proposed AMA method. On the left-hand side, the current input value $x(k)$ is divided by the moving average window (MAW) $n(k)$, which is defined as

$$n(k) = \text{round}\left(\frac{F_s}{F(k)}\right) \tag{D.1}$$

where F_s is the sampling frequency with which the AMA is processed, $F(k)$ is the variable frequency one intends to remove from the spectrum of the signal $x(k)$, the function "round" returns the closest integer to $F_s/F(k)$, and the ever-increasing integer k represents the discrete time kT_s where $T_s = {F_s}^{-1}$.

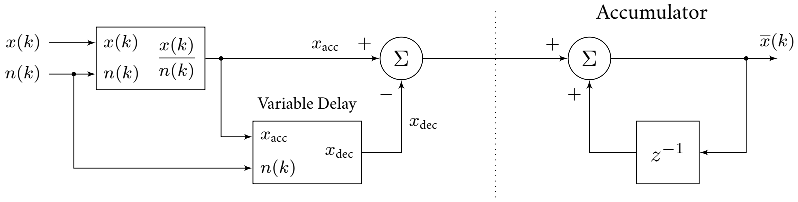

FIGURE D.1 Frequency adaptive moving average.

The value of $x(k)/n(k)$ in figure D.1, denoted by x_{acc}, is sent to the right-hand side of the AMA block to be accumulated. Simultaneously, an old value of x_{acc} from a time in the past $k - n(k)$ is sent to the right-hand side for decumulation. This value, meant for decumulation, is denoted by x_{dec}. All values of $x(k)/n(k)$

are accumulated at the instant k and must be decumulated at a later instant $k+n$. This is a key principle into designing an AMA block.

D.2 VARIABLE DELAY BLOCK

Figure D.1 illustrates the circular buffer that implements the variable delay block shown in figure D.2. Orfanidis [1] provides more information on the hardware realization of such buffers. The length of the circular buffer (N) needs to be large enough to store all samples of x/n when F is at the minimum expected value.

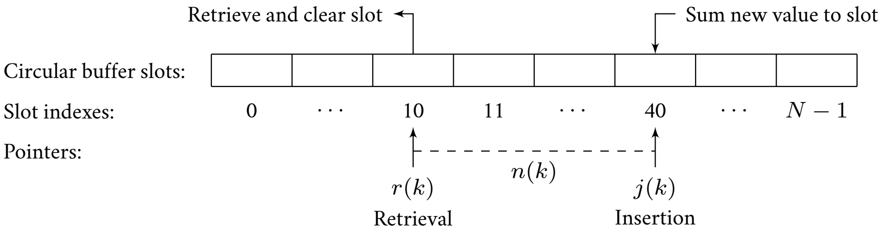

FIGURE D.2 Circular buffer and pointers that implement the variable time delay block in figure D.1.

© Daniel Mota 2023 | Source code information at Part III.

The circular buffer in figure D.2 incorporates two pointers:

$r(k)$: the retrieval pointer marks the slot from which the old value of x/n is to be retrieved. It moves along the buffer according to

$$r(k) = k \mod N$$

where $k \bmod N$ is equal to the remainder of the division of k by N.

$j(k)$: the insertion pointer marks the slot where the current value of x/n is to be stored. It is purposefully named j for avoiding the confusion with the current i. It moves along the circular buffer according to

$$j(k) = (k + n(k)) \mod N.$$

Notice that the retrieval pointer $r(k)$ moves continuously forward one slot of the circular buffer at each new cycle k. The insertion pointer $j(k)$ is pushed $n(k)$ slots ahead of $r(k)$. It is the insertion pointer, not the retrieval one, that is forced to jump or stay put whenever the $n(k)$ changes. In addition to that, the following conditions are enforced:

1) at the insertion slot, the new value of x/n is summed to any preexisting value already present in the slot;
2) the retrieval slot is set to zero after the old value of x/n is retrieved from it.

Every value entering the variable time delay block in figure D.1 is ensured to be set for decumulation only once even when the frequency to be filtered F varies causing the MAW to change. No values of x/n are decumulated twice, and no values are lost either when the frequency varies.

D.3 WEIGHTED ADAPTIVE MOVING AVERAGE

A discrete AMA filter with a window of n samples removes from the spectrum of the signal at its input the frequencies equal to and multiple of $(nT_s)^{-1}$, where T_s is the sampling period with which the filter is processed [2, p. 341]. Let $F = T^{-1}$ be the frequency one intends to filter with a discrete AMA. When T is not an exact multiple of nT_s, the AMA does not block completely the frequency F and its harmonics [3]. To mitigate this problem, a weighting method proposed by Svensson *et al.* [4] for delayed signal cancellation (DSC) filters was used in Publication V. The resulting AMA filter was named weighted adaptive moving average (WAMA).

The output of a WAMA filter, $\overline{x}_w(k)$ in equation (D.2), is equal to the weighted sum of the outputs of two AMA filters. The first one, $\overline{x}_c(k)$, uses a window equal to the value of $n(k)$ rounded up to the closest integer, as shown by equation (D.3). The second one, $\overline{x}_f(k)$, rounds the window down to the closest integer as shown in equation (D.4). The function "ceiling" is used for rounding up and "floor" for rounding down to the closest integer. It is important to remark that a WAMA filter uses twice as much memory than a single AMA.

$$\overline{x}_w(k) = (n(k) - n_f(k))\,\overline{x}_c(k) + (1 - n(k) + n_f(k))\,\overline{x}_f(k) \tag{D.2}$$

$$n_c(k) = \text{ceiling}\left(\frac{F_s}{F(k)}\right) \tag{D.3}$$

$$n_f(k) = \text{floor}\left(\frac{F_s}{F(k)}\right) \tag{D.4}$$

D.4 REFERENCES

[1] Sophocles J. Orfanidis. Introduction to Signal Processing. Prentice Hall Signal Processing Series. Prentice Hall Englewood Cliffs, N.J (1996). ISBN 978-0-13-209172-5. URL www.ece.rutgers.edu/~orfanidi/i2sp, visited on 2023-03-24. Cited on page(s) 150.

[2] Richard G. Lyons. Understanding Digital Signal Processing. Prentice Hall PTR Upper Saddle River, NJ 07458, USA (2001). ISBN 0-201-63467-8. Cited on page(s) 151.

[3] Naji Ama, Rayra Destro, Wilson Komatsu, Fuad Kassab, and Lourenco Matakas. PLL performance under frequency fluctuation-compliance with standards for distributed generation connected to the grid. In *2013 IEEE PES Conference on Innovative Smart Grid Technologies (ISGT Latin America)* pages 1–6 São Paulo, Brazil (April 2013). DOI 10.1109/ISGT-LA.2013.6554374. Cited on page(s) 151.

[4] Jan Svensson, Massimo Bongiorno, and Ambra Sannino. Practical Implementation of Delayed Signal Cancellation Method for Phase-Sequence Separation. *IEEE Transactions on Power Delivery* **22** (1), 18–26 (January 2007). ISSN 1937-4208. DOI: 10.1109/TPWRD.2006.881469. Cited on page(s) 151.

APPENDIX E

Frequency Adaptive Delayed Signal Cancellation

The grid frequency of low-inertia power systems is subjected to large excursions specially during transients. Thus, the delayed signal cancellation (DSC) applied directly to the dq frame discussed in chapter 4 should not be unreasonably degraded by such variations. In this appendix, the frequency adaptive DSC_{dq} proposed in Publication IV is described.

The digital implementation of the frequency adaptive DSC_{dq} demands the discretization of the time-varying delay $T(t)/4$, where T is the period of the grid voltage. In the discrete time domain, the number of samples $n(k)$ equivalent to $T(t)/4$ is given by

$$n(k) = \frac{T(k)}{4T_s} = \frac{F_s}{4F(k)} \tag{E.1}$$

where F_s is the sampling frequency with which the DSC_{dq} algorithm is processed, T_s is the sampling time, and the ever-increasing integer k represents the discrete time kT_s. The discrete implementation of the DSC_{dq} equation (4.15) from chapter 4 in only one axis of the dq frame becomes

$$y(k) = \frac{x(k)}{2}\left(1 + z^{-n(k)}\right), \tag{E.2}$$

where x denotes the input of the filter, y the output, and the operator $z^{-n(k)}$ fetches the value of the variable x at the instant $k - n(k)$.

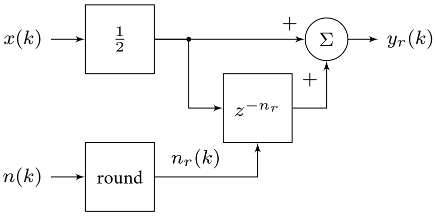

FIGURE E.1 Frequency adaptive DSC_{dq} with rounded $n(k)$.

© Daniel Mota 2023 | Redrawn and recomposed from Publication IV | Source code information at Part III.

A time-varying grid frequency produces noninteger values of n that must be truncated or rounded. Figure E.1 shows a block diagram representation of a frequency adaptive DSC_{dq} based on equation (E.2) that rounds $n(k)$ to the closest integer. To understand the consequences of this approximation, the calculated frequency responses of two DSC$_{dq}$ filters are presented in figure E.2. The filters run at $F_s = 18$ kHz and have delays of $n_c = 75$ (red) and $n_f = 74$ (blue). The frequencies in which they feature zero gain are 120 Hz for n_c and 121.622 Hz for the given n_f. For any frequencies in between those ones, the gain is non-zero. As a result, a small content of the opposite sequence will pass through the DSC$_{dq}$ filters if the grid frequency is between 60 and 60.811 Hz. Recall that the lower F_s is, the wider the gap between frequencies with zero gain of two DSC$_{dq}$ filters with contiguous delays.

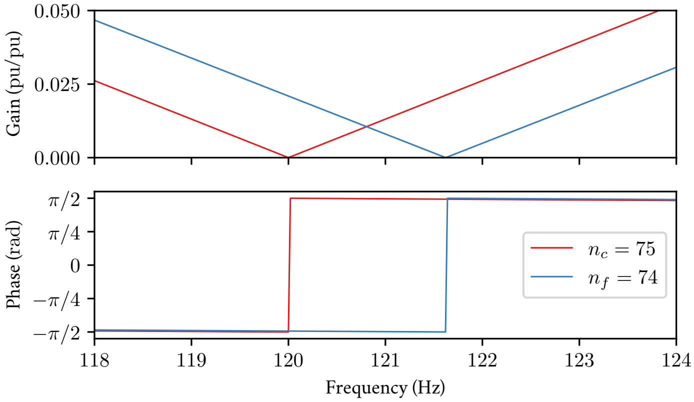

FIGURE E.2 Detail of the frequency response of two DSC$_{dq}$ filters running at 18 kHz with delays of 74 and 75 samples.

© Daniel Mota 2023 | Redrawn and recomposed from Publication IV | Source code information at Part III.

The phases of the two filters with $n_c = 75$ and $n_f = 74$ in figure E.2 are almost equal to π radians between 120 Hz and 121.622 Hz. This fact is also noticeable in the time domain. Figure E.3a shows the computer simulation of frequency-varying three-phase voltages with a positive sequence amplitude of 1 pu and a negative sequence amplitude of 0.1 pu. The frequency of the three-phase voltages is known and is used for calculating the time delay n with its ceiling and floor values (figure E.3b). The angle of the positive sequence fundamental is also known and is used as input to the transformations between the abc and dq frames. On figure E.3c, the d_+ measurements are shown. The amplitude of the second harmonic oscillations in the measurement with n_c, denoted by v_{d+c}, increases as the value of n drifts from n_c. Concurrently, the amplitude of the oscillations in the measurement v_{d+f} decreases as the value of n approaches n_f. The same effect is observed in the quadrature measurements in figure E.3d.

The responses observed in figures E.2 and E.3 indicate that the outputs of the filters with the ceiling and floor of n can be weighted according to

$$y_w(k) = \gamma(k)y_f(k) + (1 - \gamma(k))y_c(k) \tag{E.3}$$

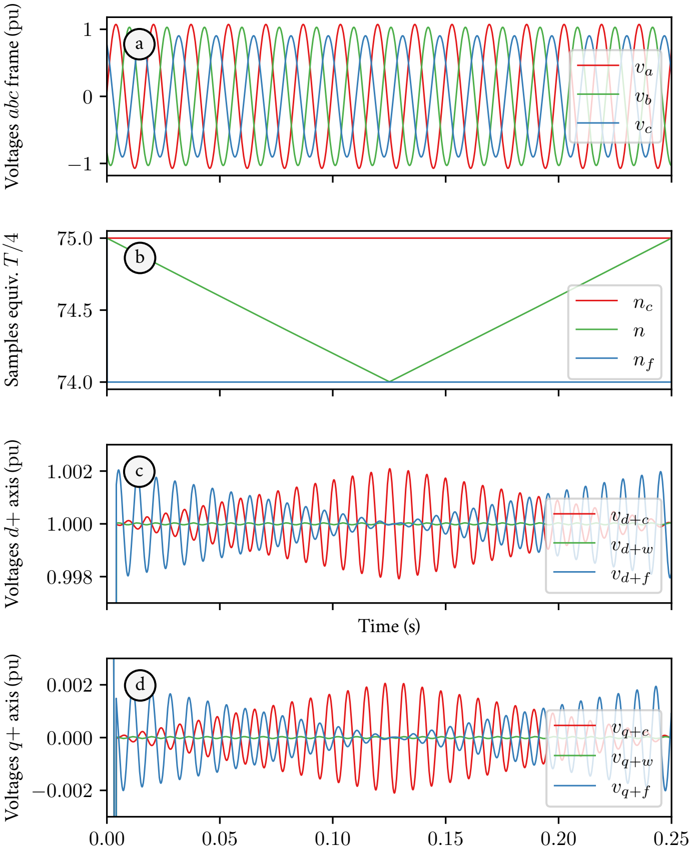

FIGURE E.3 Mitigating discretization errors in the DSC$_{dq}$ filter. (a) Unbalanced three-phase voltages with varying frequency represented in the abc frame. (b) Moving average window corresponding to $T/4$ expressed in number of samples n and the ceiling and floor values. (c) Voltage measurement in the d_+ axis calculated with ceiling (v_{d+c}) and floor (v_{d+f}) values of n and with the weighted average (v_{d+w}) of those two. (d) Voltage measurements in the q_+ axis.

© Daniel Mota 2023 | Redrawn and recomposed from Publication IV | Source code information at Part III.

where y_w is the weighted average output (denoted by the subscript w in figures E.3c and d),
y_f is the the result of equation (E.2) with the floor of n,
y_c is the result with the ceiling of n.

The weight factor $\gamma(k)$ is given by

$$\gamma(k) = n_c(k) - n(k).$$

It is important to recall that n is constantly updated according to equation (E.1). The weighted average described by equation (E.3) was proposed by Svensson *et al.* [1]

for the DSC$_{\alpha\beta}$. Notice that this method reduces but does not completely remove the second harmonic present in the dq_+ axes of figures E.3c and d (denoted as v_{d+w} and v_{q+w} in solid green) .

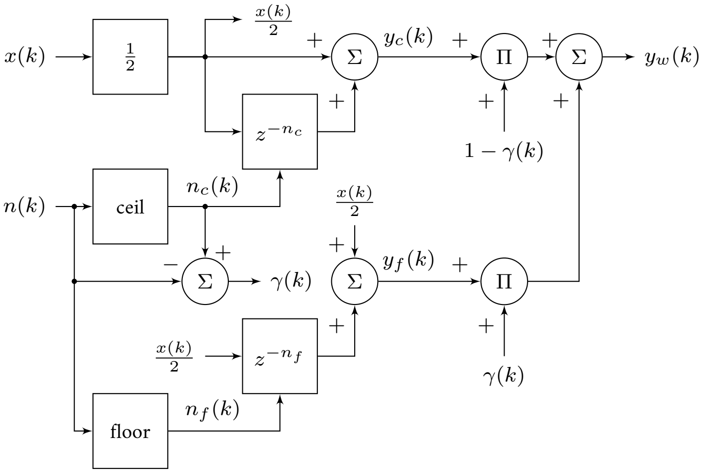

FIGURE E.4 Weighted average frequency adaptive DSC$_{dq}$. Block diagram representation of equation (E.3).

© Daniel Mota 2023 | Redrawn and recomposed from Publication IV | Source code information at Part III.

Figure E.4 shows a block diagram representation of equation (E.3). The delay operators z^{-n_c} and z^{-n_f} are typically implemented with circular buffers [2]. It is natural to assume that calculating $y_w(k)$ as illustrated by figure E.4 requires twice the amount of memory one would need for calculating $y(k)$ with just the rounded value of n as in figure E.1. Indeed, this is not the case. The length of the DSC's circular buffers is determined by the longest expected delay, i.e., the lowest acceptable grid frequency. A pointer, which moves continuously forward through the circular buffer, indicates where the new value of $x(k)/2$ is to be stored, replacing a value that became too old. This pointer can be called the insertion one. Other two pointers, the retrieval ones, lag behind the insertion pointer, indicating from where the old values $x(k-n_c)/2$ and $x(k-n_f)/2$ are to be retrieved. The two filtered values y_c and y_f in equation (E.3) are, thus, calculated with one single circular buffer with two contiguous retrieval pointers running in parallel. The interested reader is invited to inspect the proposed algorithm in detail at the Repository III.

E.1 REFERENCES

[1] Jan Svensson, Massimo Bongiorno, and Ambra Sannino. Practical Implementation of Delayed Signal Cancellation Method for Phase-Sequence Separation. *IEEE Transactions on Power De-*

livery **22** (1), 18–26 (January 2007). ISSN 1937-4208. DOI: 10.1109/TPWRD.2006.881469. Cited on page(s) 155.

[2] Sophocles J. Orfanidis. Introduction to Signal Processing. Prentice Hall Signal Processing Series. Prentice Hall Englewood Cliffs, N.J (1996). ISBN 978-0-13-209172-5. URL www.ece.rutgers.edu/~orfanidi/i2sp, visited on 2023-03-24. Cited on page(s) 156.

End of Part II - Appendices

Part III

LISTS AND SUPPLEMENTARY INFORMATION

Figure Source Data

Whenever possible, the raw data, models used for obtaining the data, and Python source codes for drawing the figures in this dissertation are made publicly available at the following repositories:

- Repository VII – DOI 10.5281/zenodo.8282628.
  Source data and Python code for drawing the figures.

- Repository VIII – DOI 10.5281/zenodo.8282714
  Source code for figures drawn with LaTeX TikZ & PGF.

The sources are listed by the file names, which are unique and can be searched within the repositories. Figure 1.1 is purposefully omitted from the list below.

CHAPTER 1 — INTRODUCTION

Figure 1.2 | Research methodology 7
LaTeX source: Metodologia.tex.

Figure 1.3 | Chapters, Contributions, and Publications 13
LaTeX source: ContChapPub.tex.

CHAPTER 2 — BACKGROUND

Figure 2.1 | Generalized isolated grid 18
LaTeX source: TheGrid.tex.

Figure 2.2 | Rotating mass model 19
LaTeX source: RotatingMass.tex.

Figure 2.3 | Phases of frequency control 20
Python source: Intro_FreqRespPhases.py.
Raw data: SimpleMass_RawData.csv.
Model: SimpleMass.slx.

Figure 2.4 | Time scale of phenomena in electrical systems 22
LaTeX source: TimeScalePhenomenaElSys.tex.

Figure 2.5 | Simplified single-line diagram of the study case 22
LaTeX source: Grid_SimplifiedSingleLine.tex.

CHAPTER 3 — CONTROL STRUCTURES FOR ESSs

Figure 3.1 | Schematic diagram of a hybrid energy storage system 30
LaTeX source: HESSDiagram.tex.

Figure 3.2 | Grid frequency control with the ESS 32
LaTeX source: HESSFreqControl.tex.

Figure 3.3 | Control of the dc voltage 34
LaTeX source: HESSDCVoltControl.tex.

Figure 3.4 | Control of the ac voltage in the ESS 35
LaTeX source: HESSACVoltControl.tex.

Figure 3.5 | Single line diagram of the study case 36
LaTeX source: HESSGridSingleLine.tex.

Figure 3.6 | ESS providing inertia and primary reserves 38
Python source: ChHESS_PowFactFreqControl.py.
Raw data case 1: 20211206_Case01_PCC.csv.
Raw data case 2: 20211206_Case02_PCC.csv.
Raw data case 3: 20211206_Case03_PCC.csv.
Model: 20201211_OMAE_BaseModel.pfd.

Figure 3.7 | Feed-forwarding and the dc voltage control 39
Python source: ChHESS_PowFactDCVolt.py.
Raw data case 3 with feed forwarding: 220211206_Case03_ESS.csv.
Raw data case 3 without feed forwarding: 20211206_Case04_ESS.csv.
Model: 20201211_OMAE_BaseModel.pfd.

Figure 3.8 | Case 3, mechanical and electrical frequency 40
Python source: ChHESS_PowFactDCVolt.py.
Raw data case 3 with feed forwarding: 20211206_Case03_Freq.csv.
Model: 20201211_OMAE_BaseModel.pfd.

CHAPTER 4 — CURRENT CONTROL IN POWER CONVERTERS

Figure 4.1 | Idealized diagram of a converter connected to the grid 44
LaTeX source: IdealizedConvSingleLine.tex.

Figure 4.2 | Current controller in the RRF 46
LaTeX source: PECInnerController.tex.

Figure 4.3 | Dual RRF current controller 47
LaTeX source: PECDualCurrControl.tex.

Figure 4.4 | Exponentially decaying dc components 49
Python source: ChPEC_Underst_Bench_ABC.py.
Raw data: BenchABC.csv.

Figure 4.5 | Single line diagram of the study case 51
LaTeX source: PECXRSingleLineDiagram.tex.

Figure 4.6 | Single-line diagram for X/R calculation 51
LaTeX source: PECXRImpedanceDiagram.tex.

Figure 4.7 | Representative range for X/R 52
Python source: ChPEC_XRvsFsw.py.py.

Figure 4.8 | Notch-filter-based sequence separation 53
LaTeX source: PECNotchSeparation.tex.

Figure 4.9 | DDRRF-based sequence separation 54
LaTeX source: PECDoubleDecoupSeparation.tex.

Figure 4.10 | Moving average block 56
LaTeX source: PECMovingAverage.tex.

Figure 4.11 | Notch and DDRRF-based methods 60
Python source: ChPEC_Underst_Bench.py.
Raw data: BenchVoltPos.csv, BenchVoltNeg.csv, BenchCurrPos.csv, BenchCurrNeg.csv.

Figure 4.12 | Converters with notch and DDRRF-based isolation 61
Python source: ChPEC_Underst_Comparison.py.
Raw data: Comp_viabcpqui_Neg_DDRRF.csv, Comp_viabcpqui_Neg_notch.csv.

Figure 4.13 | Short pulse and sequence isolation methods 62
Python source: ChPEC_DSC_ShortPulse_FFT.py.
Raw data: ShortPulse_Raw.txt.
Simulink model: ShortPulse.slx.
Simulink script: ShortPulse_Script.slx.

Figure 4.14 | Frequency responses of sequence isolation methods 63
Same source code and source data as for figure 4.13.

Figure 4.15 | Converters with notch and DSC methods 65
Python source: ChPEC_DSC_Comparison.py.
Raw data: Application_Unb_Notch.txt. Application_Unb_DSCab.txt. Application_Unb_DSCdq.txt.

CHAPTER 5 — SHARING OF PRIMARY POWER RESERVES

Figure 5.1 | Original $\mathrm{FCR_I}$ 72
LaTeX source: FCRI.tex.

Figure 5.2 | Expanded $\mathrm{FCR_I}$ 73
LaTeX source: FCR_N_D_System.tex.

Figure 5.3 | Hierarchic structure of the frequency control 75
LaTeX source: FrequencyControl_PMS_FCR.tex.

Figure 5.4 | $\mathrm{FCR_N}$ compensation for dead band 77
LaTeX source: FCRNdeadbandComp.tex.

Figure 5.5 | Nonlinear rotating mass model 79
LaTeX source: NonLinRotMassBlockDiag.tex.

Figure 5.6 | FCR providers and the rotating mass 83
LaTeX source: PrimPowTwoGTsOneESS.tex.

Figure 5.7 | Step load with simplified model 84
Python source: ChFreq_Steps_1_2MW_MATLAB_7csv.py.
Raw data: matstep_1_2MW_run_1.csv to matstep_1_2MW_run_7.csv.
Model: SPrimRes_sharing.slx.
Script: PrimRes_sharing_steps_1_2MW_Script.m.

Figure 5.8 | Eigenvalues with simplified model 85
Python source: ChFreq_Eigen_MATLAB_7csv.py.
Raw data: mateigen_run_1.csv to mateigen_run_7.csv
Model: SPrimRes_sharing.slx.
Script: PrimRes_sharing_eigen_Script.m.

Figure 5.9 | Single line diagram of the study case's grid 86
LaTeX source: Grid_DetailedSingleLine.tex.

Figure 5.11 | Step load with detailed model 89
Python source: ChFreq_Steps_1_2MW_PowerFactory_7csv.py.
Raw data: timedomain_00.csv to timedomain_06.csv
Model: 202208_RMS_Tests.pfd.
Script: ChFreq_Steps_1_2MW_PowerFactory_RunModel.py.

Figure 5.12 | Eigenvalues with detailed model 90
Python source: ChFreq_Eigen_PowerFactory_7csv.py.
Raw data: eigenvalues_00.csv to eigenvalues_06.csv
Model: 202208_RMS_Tests.pfd.
Script: ChFreq_Steps_1_2MW_PowerFactory_RunModel.py.

Figure 5.13 | PHIL setup at the National Smart Grid Laboratory 92
LaTeX source: FCRSmartGridLab.tex.
Contains a picture from the author's archive.

Figure 5.14 | Scaled-down PHIL test rig 92
LaTeX source: FCRPHILSingleLine.tex.

Figure 5.15 | FCR characteristic with dead bands of Case 3 93
LaTeX source: FCRNdbDGT12ESSFlex.tex.

Figure 5.16 | Validation of the PHIL setup and PowerFactory 94
Python source: ChFreq_Steps_PowerFactory_vs_RTLAB.py.
Raw data (PowerFactory): simulationdata_00.csv to simulationdata_02.csv.
Raw data (RTS): PHIL_3MW_FCRN_BTCFLEX.mat, PHIL_3MW_FCRN_BTCGTs.mat, PHIL_3MW_FCRN_GTs.mat. Large "mat" files have been bundled into "7-zip" files due to repository limitations.

Figure 5.17 | FCR_I versus industry state-of-the-art droop 96
Python source: ChFreq_WindChange_FCR_vs_Traditional.py.
Raw data: PHIL_Wind_12_6m_s_FCR.mat, PHIL_Wind_12_6m_s_Trad.mat. Large "mat" files have been bundled into "7-zip" files due to repository limitations.

Chapter 6 — Scaling Method for PHIL Test Beds

Figure 6.1 | Scaled-down PHIL test rig 108
LaTeX source: PHILPracticalExample.tex.
Contains icons from www.flaticon.com.

Figure 6.2 | Method for matching converters 110
LaTeX source: PHILScalingMethod.tex.

Figure 6.3 | HISM applied to the converter reactor 116
Python source: ChPHIL_Levels_20221122.py.

Figure 6.4 | National Smart Grid Laboratory at NTNU 117
LaTeX source: PHILSmartGridLab.tex.
Contains pictures from the author's archive.

Figure 6.5 | Computer simulation and PHIL results 118
Python source: ChPHIL_MATLAB_PHIL.py.
Raw data: P_08_Q_0375Mvar_5usstep.mat, C1.CSV, and C3.CSV.

Figure 6.6 | FFTs of the voltages and currents 119
Same source code and raw data as in figure 6.5.

Chapter 7 — Conclusion

Appendix A — Reference Frames and Transformations

Appendix B — Geometric Representations and the PLL

Appendix C — PI Regulators and Anti-Windup

Appendix D — Frequency Adaptive Moving Averages

Appendix E — Frequency Adaptive DSC

Figure E.2 | Frequency response of two DSC filters 154
Python source: ChPEC_DSC_FFTTwoContiguous.py.
Raw data: FreqAdaptiveFFT_Raw.txt.
Model: FreqAdaptiveFFT.slx
Model script: FreqAdaptiveFFT_Script.m

Figure E.3 | Mitigating discretization errors in the DSC filter 155
Python source: ChPEC_DSC_FrequencyAdaptive.py.
Raw data: FreqAdaptive_Raw.txt.
Model: FreqAdaptive.slx
Model script: FreqAdaptive_Script.m

Figure E.4 | Weighted average frequency adaptive DSC 156
LaTeX source: AppDSCdqWeighted.tex.

List of Figures

CHAPTER 1

CHAPTER 2

CHAPTER 3

CHAPTER 4

CHAPTER 5

CHAPTER 6

CHAPTER 7

APPENDIX A

APPENDIX B

APPENDIX C

APPENDIX D

APPENDIX E

List of Tables

CHAPTER 4

CHAPTER 5

CHAPTER 6

Abbreviations and Acronyms

ac	Alternate current. x, 6, 9, 15, 17–20, 29–35, 37, 40, 41, 43, 50–53, 58, 70, 72, 73, 75, 87, 92, 94, 98, 107, 108, 110, 111, 115, 125
AGC	Automatic generation control. 19–21, 69
AMA	Adaptive moving average. 56, 124, 149–151
ASME	American Society of Mechanical Engineers. 11
BC	Battery converter. 31–33
BESS	Battery energy storage system. 107, 115, 116
BTC	Battery converter. 88–97
BTL	Battery main reactor. 89, 97
CHIL	Controller hardware-in-the-loop. 105
CPD	Constant power device. 33
CPL	Constant power load. 10, 14, 17, 23, 24, 69, 71, 73, 74, 86–88, 93, 98, 125
CPS	Constant power source. 73, 74, 87
CZL	Constant impedance load. 17, 24, 36, 37, 73, 86, 93
dc	Direct current. x, 6, 9, 24, 29–34, 36, 37, 39–41, 43, 44, 47–50, 52, 53, 59, 60, 64, 66, 73, 85, 87, 92, 98, 107–111, 114, 115, 123, 127
DDRRF	Decoupled double rotating reference frame. 54, 58–61, 63
DSC	Delayed signal cancellation. 9, 10, 44, 56–58, 62–66, 124, 151, 153–156
DUT	Device under test. 105, 106
EL	Electrolyzer. 74
ELC	Electrolyzer converter. 89, 90, 95, 96
ELL	Electrolyzer main reactor. 90
ESD	Energy storage device. 3, 9, 24, 29–34, 36, 40, 41, 73, 87, 92, 94
ESS	Energy storage system. 3, 6, 8–10, 14, 17, 21, 22, 24, 25, 29–32, 34–37, 39–41, 43, 51, 70–74, 81–85, 87, 89, 90, 92, 95, 97, 98, 123, 125–129, 136
ESSGC	Energy storage system grid converter. 6, 9, 23, 33, 35, 37, 40, 43, 51–53, 87, 98, 129
ESSTR	Energy storage system transformer. 92, 98
ETFE	Empirical transfer function estimation. 63
FC	Fuel cell. 74
FCC	Fuel cell converter. 37, 89, 90, 95, 96
FCL	Fuel cell main reactor. 89

FCR	Frequency containment reserves. FCR_N denotes normal operation. FCR_D denotes large disturbance operation. FCR_I denotes islanded operation. 10, 20, 69–78, 82–85, 88–98, 127
FCR_N	Normal operation FCR. 91
FFT	Fast Fourier transform. 63, 117, 119
FIR	Finite impulse response. 63
FLX	Flexible loads. 17, 24, 73, 85–97, 127, 129
FLXGC	Flexible loads grid converter. 87
FSC	Full-size converter. 105–109, 111–119, 127, 130
GC	Grid converter. 10, 22, 30, 31, 33–37, 43, 51, 87, 89, 90, 92, 95, 97
GHG	Greenhouse gas. 4
GT	Turbogenerator or gas turbine. 3–6, 10, 17, 21, 23, 32, 33, 36, 37, 39, 40, 71, 74, 78, 80–98, 125–127
HISM	Harmonic-invariant scaling method. 106, 107, 109, 115, 116, 119, 130
HV	High-voltage. 23, 24, 29, 36, 37, 39, 51, 92, 113, 129
IEEE	Institute of Electrical and Electronics Engineers. 11
IGBT	Insulated-gate bipolar transistor. 51
IIR	Infinite impulse response. 63
L	Inductive. 111, 112
LC	Inductive-capacitive. 106, 111
LCL	Inductive-capacitive-inductive. 29, 30, 32, 34, 35, 51, 52, 92, 106, 107, 109–114, 118, 119, 127, 128, 137
LowEmission	LowEmission Research Centre. 3, 5–7
LPF	Low-pass filter. 33, 46, 54, 59, 79–82, 84, 87, 106
LV	Low-voltage. 39, 98, 105, 111, 113
MA	Moving average. 55, 56, 58, 62–64, 117, 124, 149
MAW	Moving average window. 55, 149, 151
MIMO	Multiple-input multiple-output. 46
MMC	Modular multilevel converter. 106
NCS	Norwegian continental shelf. 3–5
NO_x	Nitrogen oxides. 4, 5, 97
NRF	Natural reference frame for three-phase quantities (abc). 44, 45, 50, 135, 136, 138, 139, 141, 143
NSGL	National Smart Grid Laboratory in Trondheim, Norway. 6, 8, 92, 107, 116, 117
NTNU	*Norges teknisk-naturvitenskapelige universitet*. Norwegian University of Science and Technology. ix, 3, 6, 92, 117
O&G	Oil and gas. 3–5, 7, 22, 29, 41, 70–74, 84, 130
PEC	Power electronic converter. 5, 9, 10, 14, 15, 18, 21, 23, 24, 32, 36, 40, 43, 44, 47, 74, 86–88, 90, 98, 105–107, 123–125, 130, 136
PEM	Proton exchange membrane. 24, 85
PhD	Philosophiae Doctor. ix, 3, 5–8, 12, 13, 22, 123, 130, 131

PHIL	Power hardware-in-the-loop. 6, 9, 10, 14, 71, 91–95, 97, 98, 105–109, 111, 114–116, 118, 119, 125–127, 129, 130
PI	Proportional and integral. 33–35, 44, 45, 47, 48, 59, 61, 64, 65, 74, 96, 146–148
PID	Proportional, integral, and derivative. 6, 9, 23, 30, 31, 41, 88, 126, 139
PLL	Phase-locked loop. 39, 40, 48, 53, 54, 59, 88, 91, 110, 123, 125, 127, 129, 138, 143–146
PMS	Power management system. 6, 9, 20, 21, 30, 31, 33, 41, 70, 74, 76, 77, 95, 97, 126
PMSG	Permanent-magnet synchronous generator. 105
pu	Per unit. Dimensionless "unit" of a variable that has been divided by a base value. 15, 20, 33, 34, 37, 49, 53, 59, 60, 62, 64, 95, 98, 107–109, 111–113, 116, 119, 127, 128, 154
PV	Photo-voltaic. 5, 18, 70, 73, 74
PWM	Pulse-width modulation. 22, 23, 32, 36, 45, 47, 52, 98, 106, 115, 117, 119, 128–130
RES	Renewable energy sources. 5, 6, 8, 14, 18, 29, 69, 71, 76, 98, 123, 125, 130
RL	Resistive and inductive. 44, 49, 59, 136, 140
RMS	Root mean square. 34, 35
RoCoF	Rate of change of frequency. 20
RRF	Rotating reference frame. 9, 14, 15, 34, 36, 43–48, 50, 52–54, 57, 58, 63, 64, 66, 124, 135, 137–141, 143
RTS	Real-time simulator. 6, 71, 92, 95, 105, 165
SDC	Scaled-down converter. 105–119, 127, 130
SI	International System of Units. 107
SINTEF	SINTEF Energy Research. 3
SISO	Single-input single-output. 46
SOC	State of charge. 33
SRF	Stationary reference frame ($\alpha\beta$). 9, 10, 44, 54, 56, 66, 135–137, 143
TDD	Total demand distortion. 117, 118
TRL	Technology readiness level. 119
TSO	Transmission system operator. 20, 69, 70
VSC	Voltage source converter. 47, 66
VSM	Virtual synchronous machine. 80, 81
WAMA	Weighted adaptive moving average. 151
WF	Wind farm. 3, 7, 17, 21–24, 29, 41, 43, 52, 53, 70, 72, 74, 84, 86, 87, 94, 96, 98, 129
WT	Wind turbine. 21, 22, 24, 36, 37, 39, 40, 70, 73, 74, 85, 87, 90, 95–97
WTGC	Wind turbine grid converter. 35, 87
X/R	Reactance-resistance ratio. 9, 10, 43, 51–53, 59, 64, 66, 123

Symbols

A list of symbols and operators used in this doctoral dissertation is presented below. Ambiguities and double meanings of symbols and operators have been avoided as much as possible. However, some symbols might have more than one meaning. The following diacritics are used throughout the text to assign special meanings for the symbols:

$\overset{*}{x}$	Reference value for the variable x.
$\widetilde{x}$	Variation about a given steady-state of x.
$\widehat{x}$	Measured value of a physical quantity x.
$\overline{x}$	Average value of samples of x acquired within a time window.

Mathematical operators

Capitalized and lowercase letters, as well as stylized characters, are used to represent mathematical operators.

ceiling	Closest integer above or equal to: $\text{ceiling}(3.14) = 4$. 151, 154, 155
$\mathcal{C}$	Matrix for transformations between NRF and SRF. Subscript $+$ denotes positive sequence frame. Subscript $-$ denotes negative sequence frame. 136–140
d	Infinitesimal variation as in $\mathrm{d}x$. 19, 31, 45, 46, 57, 78, 79, 138–140, 144, 145
Δ	Finite variation as in Δx. 112
$\cdot$	Dot product of two column vectors: $x \cdot y = x^{\top} y$. 145
floor	Closest integer below or equal to: $\text{floor}(3.14) = 3$. 151, 154, 155
mod	Remainder of the division: $3\pi/2 \mod \pi = \pi/2$. 139, 145, 150
$\times$	Multiplication symbol only used for avoiding ambiguities. 115, 116
$\mathcal{P}$	Matrix for transformations between SRF and RRF. 57, 58, 137–140
$\Re$	Real part of a complex number. 80
round	Rounds to the nearest integer. 149
$\mathcal{T}$	Matrix for transformations between NRF and RRF. Subscript $+$ denotes positive sequence frame. Subscript $-$ denotes negative sequence frame. 45, 50, 52–54, 138–141

$\top$	Transpose of a matrix. 45, 46, 56, 57, 136–141
z	Fetches the value of a variable at a discrete time kT_s in the past. May be expressed as z^{-kT} or simply by z^{-k}. 55, 56, 153, 156

Latin Variables and Constants

Lowercase and capitalized Latin letters are used to represent variables and constants.

abc	Axes of the NRF. 44, 45, 50, 54, 56, 61–64, 117, 135–139, 141, 143–146, 154, 155
C	Capacitance. Subscript b denotes base value. Superscript sd denotes SDC. Superscript fs denotes FSC. 108, 113
C_{ac}	Capacitance. Lowercase denotes pu value. Superscript sd denotes SDC. Superscript fs denotes FSC. 109, 113, 114
C_{dc}	Capacitance. Superscript sd denotes SDC. Superscript fs denotes FSC. 30, 31, 107, 109
dq	Axes of the RRF. xiv, 44, 45, 50, 53, 54, 57–59, 62–66, 135, 137, 153, 154
dq_+	Positive sequence RRF. 50, 54, 59, 61–63, 138–141, 154–156
dq_-	Negative sequence RRF. 50, 59, 141
E	Energy. 31
e	Euler's number: $\mathrm{e} = \lim\limits_{n\to\infty}\left(1+\frac{1}{n}\right)^n$. 49, 50
F	Frequency. Subscript n denotes nominal value. Subscript s denotes sampling. Subscript sw denotes PWM switching. 52–55, 57, 59, 72, 73, 76, 77, 93, 108, 112, 149–151, 153, 154
f	Frequency in pu. 32, 78–82
F_{db}	Frequency dead band. Subscript N denotes FCR$_{\mathrm{N}}$. 76, 77, 93
$\widetilde{F}_{\mathrm{D}}$	Maximum expected frequency variation in FCR$_{\mathrm{D}}$ operation. 75
$\widetilde{F}_{\mathrm{N}}$	Frequency variation boundary for the activation of FCR$_{\mathrm{N}}$ and FCR$_{\mathrm{D}}$. 72, 73, 75–77, 93, 96
F_{res}	Resonance frequency. Superscript sd denotes SDC. Superscript fs denotes FSC. 109, 114
G	Transfer function. 47, 79–82, 147, 148
H	Inertia constant. For synchronous machines it is equal to the kinetic energy stored in the rotor at rated mechanical angular frequency divided by the machine's rated apparent power. For PECs it is equal to the energy stored in the dc-link capacitor at rated voltage divided by the converter's rated apparent power. 78, 80, 82, 85, 98, 109, 114

i	Current. Single phase or three-phase in the NRF. May be capitalized. 44–47, 49, 50, 136, 139, 141, 150
i,j,k,r	Integer number. 55, 56, 81, 82, 145, 149–151, 153–156
I_{ac}	Ac current. Subscript b denotes base value. Superscript sd denotes SDC. Superscript fs denotes FSC. 107–116
i_{bt}	Battery current in pu. 32, 33
I_{dc}	Dc current. Lowercase denotes pu. Subscript b denotes base value. Superscript sd denotes SDC. Superscript fs denotes FSC. 31, 107–109, 111
i_{dq}	Current in the RRF. 45, 46
i_{dq+}	Current in the positive sequence RRF. 48, 50, 139, 140
i_{dq-}	Current in the negative sequence RRF. 48, 50
i_{e}	Exponentially decaying dc currents in the NRF. 50
$i_{\mathrm{e}dq+}$	Exponentially decaying dc currents represented in the positive sequence RRF. 50
$i_{\mathrm{e}dq-}$	Exponentially decaying dc currents represented in the negative sequence RRF. 50
I_{es}	Dc current from the ESDs. May also be in lowercase. 31, 33, 34, 39
I_{r}	Reactor current. May also be lowercase. Superscript sd denotes SDC. Superscript fs denotes FSC. 112
i_{rdq}	Current in the RRF at the reactor of the GC. 33–35, 37
J	Moment of inertia. 19, 20, 78
j	$=\sqrt{-1}$. 81, 91
k	Gain. Subscripts i and j denote indexed gain. Subscripts p and g denote proportional gains in a PID. Subscript d denotes derivative gain. 32, 33, 47, 63, 79–82, 147, 148
$K_{\mathrm{N,D}}$	FCR gain. Subscript N denotes FCR$_{\mathrm{N}}$. Subscript D denotes FCR$_{\mathrm{D}}$. 75–77, 82, 85, 91, 96
L	Inductance. Subscript b denotes base value. Superscript sd denotes SDC. Superscript fs denotes FSC. 44–46, 49, 108, 111, 113, 136, 139, 140
L_r	Reactor inductance. Lowercase denotes pu. Superscript sd denotes SDC. Superscript fs denotes FSC. 107, 109, 111–117
L_t	Transformer inductance. Lowercase denotes pu. Superscript sd denotes SDC. Superscript fs denotes FSC. 107, 109, 113, 114
M	Mechanical starting time equal to twice the inertia constant H. 78–82
m	Values in the NRF. 53, 54, 136–139, 141
$m_{\alpha\beta}$	Values in the SRF. 56, 57
$m_{\alpha\beta+}$	Values in the positive sequence SRF. 56, 136–139

m_{dq}	Values in the RRF. 57, 58
m_{dq+}	Values in the positive sequence RRF. 54, 57, 58, 138, 139
m_{dq-}	Values in the negative sequence RRF. 54, 141
N, n	Integer number. 55, 56, 81, 82, 149–151, 153–156
P, p	Power. 50, 76, 78–82, 117
P_{D}	$\mathrm{FCR_D}$ power. 75, 76
P_{FCR}	FCR power. 78, 79, 81, 82
$P_{m,e,\mathrm{L}}$	Power. Subscript m denotes mechanic. Subscript e denotes electric. Subscript L denotes load. 19, 78, 85
P_{N}	$\mathrm{FCR_N}$ power. 73, 75–77, 92, 93
P_{S}	Secondary power reserve. Lowercase denotes pu. 33, 74, 76, 78
$P_{\mathrm{S}}^{\mathrm{EL}}$	Electrolyzer secondary power reserve. 74
$P_{\mathrm{S}}^{\mathrm{FC}}$	Fuel cell secondary power reserve. 74
$P_{\mathrm{S}}^{\mathrm{GT1}}$	GT1 secondary power reserve. 74
$P_{\mathrm{S}}^{\mathrm{GT2}}$	GT2 secondary power reserve. 74
Q	Reactive power. 117
R	Resistance. 44–46, 49, 136, 139, 140
r	Resistance in pu. Subscript s denotes stator. Subscript L denotes load. Subscript t denotes transformer. Subscript c denotes capacitive branch. Subscript r denotes reactor. 51–53
R_r	LCL reactor parasitic series resistance. Lowercase denotes pu. Superscript sd denotes SDC. Superscript fs denotes FSC. 107, 111, 112
R_t	LCL transformer short-circuit resistance. Lowercase denotes pu. Superscript sd denotes SDC. Superscript fs denotes FSC. 107, 109, 113
S	Apparent power. Subscript b denotes base value. Subscript n denotes nominal value. Superscript sd denotes SDC. Superscript fs denotes FSC. 78, 85, 108, 109, 111, 114
s	Complex frequency in the Laplace domain. 46, 47, 79–82, 147, 148
T	Time. Subscript i and j denote indexed constant. Subscript i can also refer to the integrator of a PID controller. Subscript d denotes a filter time for a derivative branch. Subscript f denotes filter. Subscript s denotes sampling. Subscript v denotes voltage. 32, 33, 47, 54–58, 62, 79–82, 87, 147–149, 151, 153, 155
$T_{\mathrm{ESS,fv,t}}$	Time constants of the simplified rotating mass model with multiple $\mathrm{FCR_N}$ providers. 82, 85

t	Time. 19, 20, 31, 37, 45–50, 56–58, 60, 61, 64, 78–83, 88, 95, 96, 135–141, 143–145, 153
v	Voltage. Single phase or three-phase in the NRF. 48–50, 62, 135–137, 139, 141, 143–146
V_{ac}	Ac voltage. Subscript b denotes base value. Superscript sd denotes SDC. Superscript fs denotes FSC. 32, 107–116
v_{ac}	Ac voltage in pu. 34, 35
$v_{\alpha\beta+}$	Voltage in the positive sequence SRF. 137
v_c	Converter voltage in the NRF. 44, 45, 139, 140
v_{cdq}	Converter voltage in the RRF. 45, 46
v_{cdq+}	Converter voltage in the positive sequence RRF. 140
$v_{cdq\mathrm{PI}}$	Converter PI regulator output voltage in the RRF. 45, 46
V_{dc}	Dc voltage. Lowercase denotes pu. Subscript b denotes base value. Superscript sd denotes SDC. Superscript fs denotes FSC. 31–33, 107–112, 114
v_{dq+}	Voltage in the positive sequence RRF. 50, 139
v_{dq-}	Voltage in the negative sequence RRF. 50, 141
v_g	Grid voltage in the NRF. 35, 44–47, 139
v_{gdq}	Grid voltage in the RRF. 45, 46
v_{gdq+}	Grid voltage in the positive sequence RRF. 48, 140
v_{gdq-}	Grid voltage in the negative sequence RRF. 48
v_{PLL}	Internal PLL three-phase voltage in the NRF. 144–146
x	Internal variables of a AMA filter. Subscript acc denotes value for accumulation. Subscript dec denotes value for decumulation. Subscript c denotes value obtained with the ceiling of of the MAW. Subscript f denotes average obtained with the floor of the MAW. Subscript w denotes weighted AMA. 149, 151
x	Reactance in pu. x'_d denotes the transient direct axis reactance of a synchronous machine. Subscript L denotes load. Subscript t denotes transformer. Subscript c denotes capacitor. Subscript r denotes reactor. 51–53
x, y, z	Generic variables. 32, 55, 56, 76, 147–151, 153–156
Z	Impedance. Subscript b denotes base value. Superscript sd denotes SDC. Superscript fs denotes FSC. 49, 50, 108, 111–113

Greek variables and constants

Variables and constants are also represented in Greek letters.

α,β,γ,δ,φ	Angle. 49, 50, 136, 139, 144, 145, 154, 155
$\alpha\beta$	Axes of the SRF. xiv, 44, 54, 56–58, 62, 135
$\alpha\beta_+$	Axes of the positive sequence SRF. 136–139
$\alpha\beta_-$	Axes of the negative sequence SRF. 137
ε	Error. 145, 146

ζ	Damping coefficient. 53, 59, 62, 80, 83, 89, 97
θ	Angle tracked by a PLL. 48, 50, 52–54, 57, 59, 62, 137–139, 141, 144–146
π	Well known transcendental constant. 53, 57, 58, 64, 135–139, 141, 144–146, 154
τ	Time. 49–52, 57, 59, 61, 138, 144
$\mathrm{\tau}$	Torque. Subscript e denotes electrical. Subscript m denotes mechanical. 19
ω	Angular frequency. Subscript n denotes nominal value. Subscript f denotes filter. Subscript nat denotes natural oscillation frequency. 19, 45, 46, 48–50, 53, 56–58, 62, 78–80, 83, 108, 111, 113, 135–141, 144–146

COLOPHON

Typeset with LaTeX in B5 paper 176 mm × 250 mm. Based on a template by Andreas Liudi Mulyo (https://andreasliudimulyo.github.io/#latex). Main text contained within 120 mm × 205 mm, with 1:1 horizontal (top:bottom) and vertical (left:right) margin ratios. Width of margin notes is 10 mm.

Color palette employed throughout the text: part page background, chapters' names, and cross references `RGB:0,70,148`, headings `RGB:125,0,45`, chapter summary `RGB:255,248,220`, and figure caption background `RGB:231,231,231`.

Graphics generated with LaTeX TikZ & PGF package or with Python Matplotlib. T. Emil Rivera-Thorsen's color palette (gist.github.com/thriveth/8560036) adopted for charts: red `RGB:228,26,28`, green `RGB:77,175,74`, blue `RGB:55,126,184`, pink `RGB:247,129,191`, yellow `RGB:222,222,0`, purple `RGB:152,78,163`, and gray `RGB:153,153,153`.

Final Version compiled on 2023-11-29 15:18 (UTC+00:00).

ISBN 978-82-326-7604-0 (printed ver.)
ISBN 978-82-326-7603-3 (electronic ver.)
ISSN 1503-8181 (printed ver.)
ISSN 2703-8084 (online ver.)

NTNU
Norwegian University of
Science and Technology